UNIVERSITY OF LIVERPOOL

Environmental Effects in Molecular Electronics

Thesis submitted in accordance with the requirements of the University of Liverpool for the degree of Doctor of Philosophy by

Andrea Vezzoli

May 2015

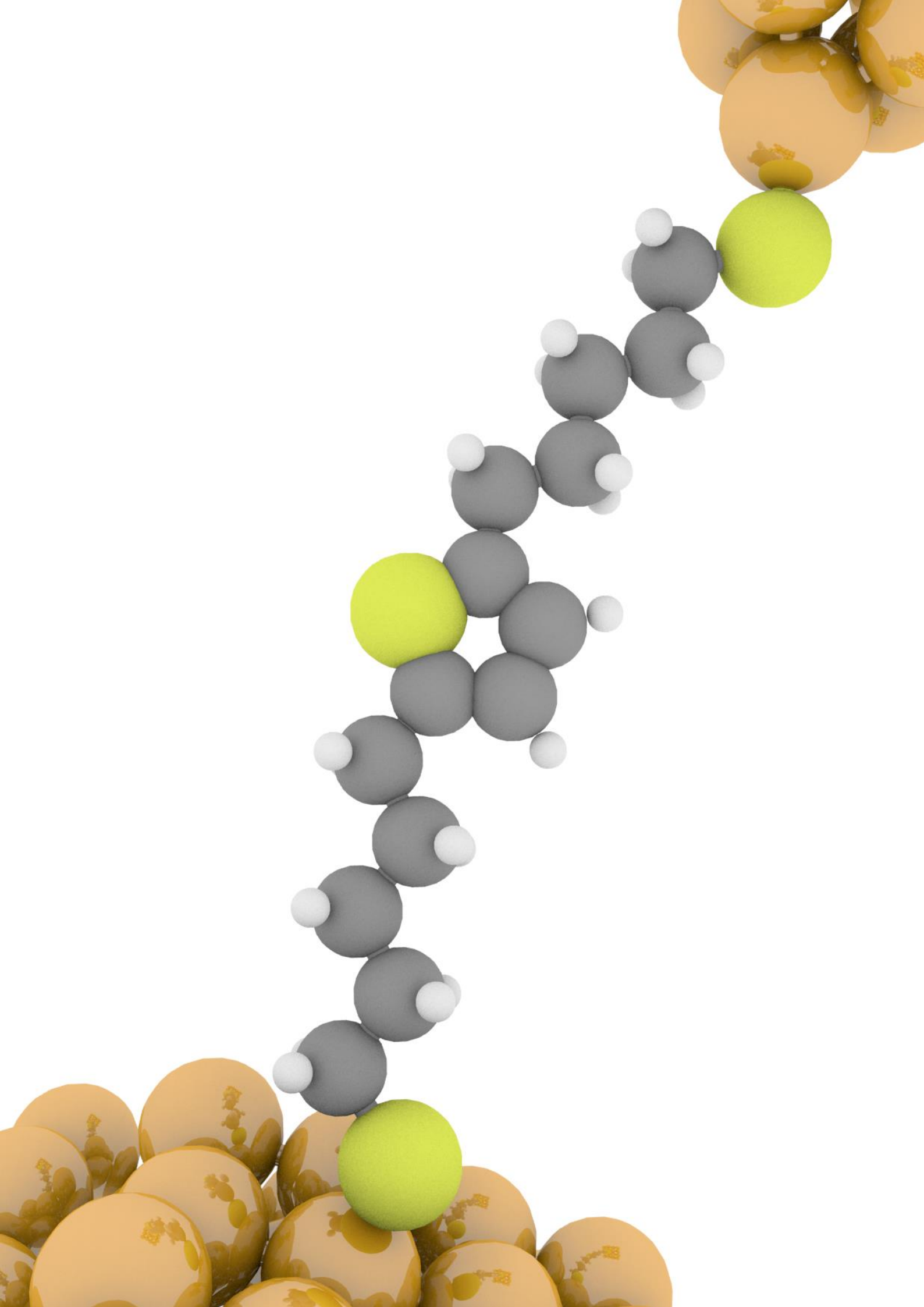

Abstract

Researchers have looked at the possibility of using single molecules as functional building blocks in electronics circuits since the 1970s. The field of molecular electronics, despite its experimental and theoretical challenges, has continued to grow incessantly from a simple scientific curiosity to an emerging field with hundreds of publications per year. Thanks to the development of scanning probe microscopy a variety of techniques currently used to characterise the electrical properties of single molecules has been developed, and molecular systems mimicking the behaviour of traditional electronic components, such as transistors or rectifiers, have been prepared.

Despite the obvious fact that supramolecular interactions must play a role in the charge transfer process, only a small number of reports on the subject have been published. In this thesis a set of molecular wires with an oligothiophene central unit, sandwiched between two insulating chains, has been used to probe the effect of such interactions on molecular conductance using several scanning tunnelling microscopy techniques. It has been found that the side-chain length has little effect on molecular conductance, but the presence of water in the surrounding environment triggers an increase in conductance and a switch in the behaviour from activationless to thermally-activated. Furthermore, upon exposure to electron-withdrawing small molecules, these oligothiophene molecular wires form charge transfer complexes, with conductance enhanced by a factor up to 100. Measurements performed in UHV confirmed the observed behaviour, and theoretical calculations were performed to explain it in the coherent tunnelling regime. A gateway state arising from coupling of the molecular backbone to the sulfur contacts accounts for the observed shallow decay of conductance with length, while shifting of transport resonances upon interaction with water and the appearance of interference features upon charge transfer complexation explained the temperature dependence and the conductance enhancement, with experimental observation closely matched by DFT calculations.

Table of Contents

List of Figures

Chapter 1

Chapter 2

Chapter 3

Chapter 4

Chapter 5

Chapter 6

Appendix A

Appendix B

List of Tables

Chapter 1

Chapter 2

Chapter 3

Chapter 4

Chapter 5

Appendix A

List of Acronyms and Abbreviations

Ac	Acetyl
ADT	Alkanedithiols
AFM	Atomic Force Microscope
BDT	Benzene-1,4-dithiol
CHL	Chloranil (tetrachloro-*p*-benzoquinone)
CI	Chemical Ionisation
CT	Charge Transfer
DBTCE	1,2-dibromotetrachloroethane
DCM	Dichloromethane
DDT	1,10-decanedithiol
DFT	Density Functional Theory
DHP	Dihydropyran
DIPA	Di*iso*propylamine
DMF	*N,N*-Dimethylformamide
DNT	2,4-Dinitrotoluene
DPPE	1,2-Bis(diphenylphosphino)ethane
DPPP	1,3-Bis(diphenylphosphino)propane
DTB	Double Tunnelling Barrier
EI	Electron Ionisation
FET	Field-effect Transistor
HOMO	Highest Occupied Molecular Orbital
HRMS	High Resolution Mass Spectrometry
IR	Infrared
ITO	Indium-Tin Oxide
IUPAC	International Union of Pure and Applied Chemistry
LUMO	Lowest Unoccupied Molecular Orbital

MCBJ	Mechanically Controlled Break Junction
MI	Matrix Isolation
MS	Mass Spectrometry
NBS	*N*-Bromosuccinimide
NDR	Negative Differential Resistance
NEGF	Non-Equilibrium Green's Function
NMR	Nuclear Magnetic Resonance
ONI	Oligonaphtalenefluoreneimine
OPE	Oligophenyleneethynylene
OPI	Oligophenyleneimine
OPT	Oligophenylenetriazole
OPV	Oligophenylenevinylene
P3AT	Poly(3-alkylthiophene)
P3HT	Poly(3-hexylthiophene)
PEDOT	Poly(3,4-Ethylenedioxythiophene)
[Ph]	Phenyl
RT	Room Temperature
SAM	Self Assembled Monolayer
SIESTA	Spanish Initiative for Electronic Simulations with Thousands of Atoms
SMC	Single Molecule Conductance
SMEAGOL	Spin and Molecular Electronics in Atomically-Generated Orbital Landscapes
SPM	Scanning Probe Microscope
STM	Scanning Tunnelling Microscope
STM-BJ	Scanning Tunnelling Microscope – Break Junction
STS	Scanning Tunnelling Spectroscopy
[T]	Thiophene
[T2]	α-Bithiophene (2,2'-bithiophene)
[T3]	α-Terthiophene (2,2':5',2"-terthiophene)

TCB	1,2,4-Trichlorobenzene
TCNE	Tetracyanoethylene
TCNQ	Tetracyanoquinodimethane
TMS	Trimethylsilyl
TMXYL	Tetramethylxylyldithiol
THF	Tetrahydrofuran
THP	Tetrahydropyran
TTF	Tetrathiafulvalene
TVS	Transition Voltage Spectroscopy
UHV	Ultra High Vacuum
UV-Vis	Ultraviolet – Visible
[V]	Viologen (4,4'-bipyridinium)
VT	Variable Temperature

Introduction

CHAPTER 1

The scientific man does not aim at an immediate result. He does not expect that his advanced ideas will be readily taken up. His work is like that of the planter: for the future. His duty is to lay the foundation for those who are to come, and point the way. He lives and labours and hopes.

Nikola Tesla, 1934.

In a seminal paper[1] in 1965 Intel co-founder Gordon E. Moore observed that, over the brief history of integrated circuits to that point, the number of transistors had doubled approximately every two years, while their cost had fallen, and his prediction that this would continue took the name of Moore's law. This law is strongly linked to many capabilities of digital electronic devices (such as processing speed, memory capacity, sensors, etc.). He predicted that the trend would continue for at least ten years, but it held true until the end of the 20th century, when some reports of its current slowing down were published.[2,3]

Structural limitations of the materials used in modern semiconductors and technical limitations of the lithographic process used to pattern and build transistor arrays are slowing the miniaturisation process needed to improve performances, portability and energy consumption of modern electronic devices. This issue has been addressed in different research fields in the last decade, such as spintronics, photonics and the subject of this thesis, namely *molecular electronics*, the use of single molecules as electronic devices.

1.1 History of Molecular Electronics

Two seminal works published in the 1970s paved the foundation of the field of molecular scale electronics. In 1971, Bernhard Mann and Hans Kuhn managed reproducibly to measure the conductance of fatty acid monolayers by evaporating various metal electrodes on top of Langmuir-Blodgett - formed films.[4] Many attempts had been made to measure alkyl chain conductance before, but the earlier attempts resulted in noisy and non-reproducible results[5] or probing of multilayer system.[6,7] The care they put in their experimental setup allowed them to obtain a consistent set of data, and they were able clearly to demonstrate the tunnelling mechanism of charge transport in such systems. In 1974 Aviram and Ratner hypothesised about a rectifying molecule[8] that could be employed in monolayer electronic devices. This molecule contains a donor tetrathiafulvalene (TTF) group and an acceptor tetracyanoquinodimethane (TCNQ) group, separated by an insulating bridge to prevent direct coupling of their π levels. This molecular bridge was designed to mimic the p-n junctions of common solid state rectifiers.

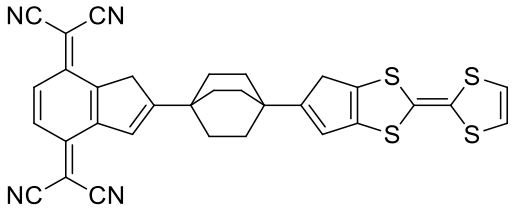

Figure 1.1: TTF-TCNQ molecular rectifier proposed through theoretical considerations by Aviram and Ratner in 1974.

Owing to the relative energies of the HOMO and LUMO orbitals on either side of the molecule, only a small bias would be required for electrons to flow from the metal Fermi energy to the LUMO of the acceptor and from the HOMO of the donor to the other metal Fermi energy, permitting tunnelling across the barrier, but a much larger bias would be required to align the HOMO of the acceptor with the metal Fermi energy and the LUMO of the donor with the other metal, so overall, the molecule would act as a diode. In 1974 measurement of electrical properties of single molecules was just a dream, but the technology to allow them would arrive in 1981 with the invention of scanning tunnelling microscope (STM) by Binnig and Rohrer at IBM Zürich.[9]

Aviram *et al.* used a scanning tunnelling microscope to measure the *I-V* characteristics of an asymmetrical hemiquinone-catechol molecule in a pioneering 1988 paper,[10] finding switching and rectifying properties. They prepared a self-assembled monolayer (SAM) on a Au(111) on mica surface by immersion in a solution containing the thiol-capped hemiquinone-catechol and took measurements using a Pt tip to obtain *I-V* scans in various regions of the surface.

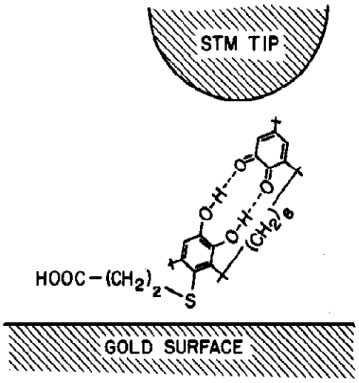

Figure 1.2: Structure of the hemiquinone-catechol molecule used in the Aviram study. *Reprinted from ref. 10.*

Where the surface was very flat the *I-V* trace was just a slightly asymmetric Au/Pt junction, but a dramatically different characteristic was observed in rough areas, where molecules are adsorbed. As the voltage was scanned in the negative direction, the current peaked at approximately -200 mV, saturating the preamplifier. This phenomenon only occurred in negative scans, indicating a rectifying behaviour similar to the one predicted in 1974. In this case it is proposed that the catechol moiety acts as electron donor and the hemiquinone as acceptor. Arguably, the result itself may not be spectacular, but the possibility to perform such measurements inspired new research in the field, showing the capabilities of STM instruments and their application to test the electrical properties of a small number of molecules packed in a self-assembled monolayer.

The first experiment on electron transfer through a *single* molecular junction was reported in 1997 by Reed *et al.,*[11] with the development of a new method that allowed them to measure the conductance of benzene-1,4-dithiol (BDT). They stretched a length of gold wire in a solution of BDT in tetrahydrofuran until breakage occurred. That resulted in the formation of two tips of atomic sharpness covered with a SAM of BDT. The solvent was then left to evaporate in Ar atmosphere and the two tips were brought together (by means of a piezo-controlled bendable substrate) while measuring the current flow and performing *I-V* scans. The invention of this technique, now generally known as mechanically controlled break junction (MCBJ), is regarded as a breakthrough in the field of molecular electronics, allowing chemists and physicist to study electron transport through molecular systems at the most fundamental level.

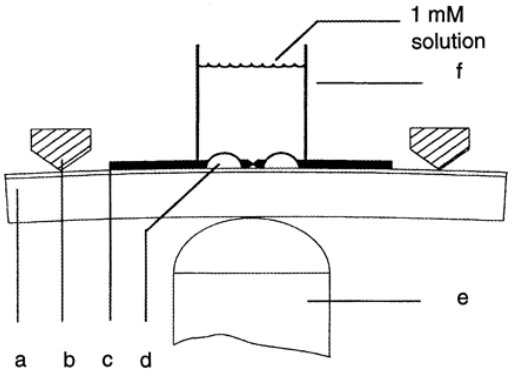

Figure 1.3: A schematic of the mechanically controlled break junction with the bending beam (a), the counter supports (b), the notched gold wire (c), the glued contacts (d), the piezo element (e) and the glass tube containing the solution (f). *Reprinted from ref. 11.*

Many different methods to characterise metal¦*molecule*¦metal junctions have been developed in the last 15 years, but the field of single molecule electronics can be considered to still be at an early stage, particularly regarding potential technological exploitation. The high variability of conductance observed in the current experiments must be decreased before molecular devices can realistically seek technological applications and the theoretical modelling of experiments is still struggling at explaining some key phenomena. The development of modern STM-based techniques (discussed later and employed in this thesis) accelerated the study and characterisation of molecular wires but, as Mark Ratner put it in a 2013 Nature commentary "*the field of molecular electronics can be traced back to 1971, but molecular electronics is a vibrant and dynamic area of science and technology, and numerous challenges and opportunities lie ahead*".[12]

1.2 History and Principles of Scanning Tunnelling Microscopy

In 1972 Young, Ward and Scire built a machine, called *topographiner*[13] that allowed them to visualise a scanning image of a conductive surface. This instrument is now widely recognised as the first example of a scanning probe microscope, and it used a field emitter (a tungsten tip) to scan the surface while measuring the current flowing through the sample. The instrument, albeit crude, was capable of a vertical resolution of 3 nm and a lateral resolution of 400 nm, and they estimated an ultimate resolution of 0.3 nm perpendicular to the surface (limited by noise) and 20 nm on the x-y plane (limited by field emitter tip radius). In the same paper Young predicted that it could be possible to achieve better resolution by using the tunnel effect, but the 1970s technology did not allow him to build such an instrument. In 1981 Binnig and Rohrer built a working scanning tunnelling microscope at the IBM Zürich research laboratories, fulfilling Young's predictions of higher resolution. In the paper they published in 1982[14] the STM was used to achieve atomic resolution on the vertical axis, showing monoatomic steps during the scanning of $CaIrSn_4$ (110) and Au surfaces.

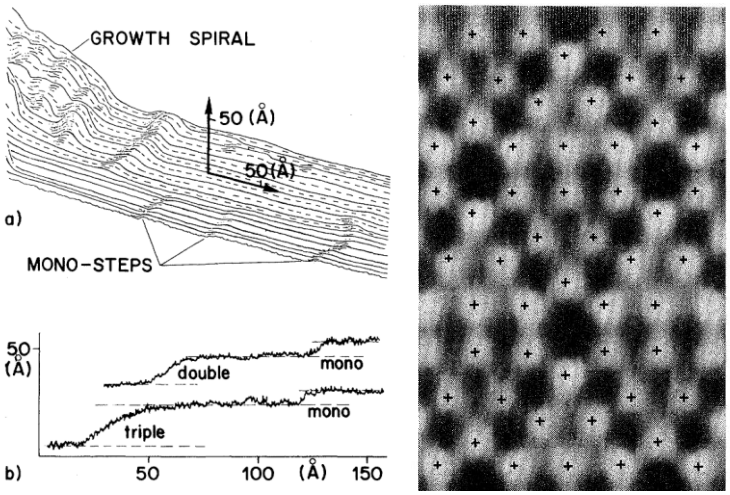

Figure 1.4: Left: evidence of monoatomic steps during the first STM experiments. Right: 7x7 reconstruction of Si(111) surface, showing atomic resolution. *Reprinted from refs. 14-15*

While the vertical resolution achieved with the original STM was excellent, lateral resolution could be greatly improved, and the first atomic resolution image was obtained in 1983 on a Si(111) surface, showing the 7x7 reconstruction.[15] Since then, atomic resolution has been achieved on a great number of substrates.[16,17] More than 30 years from its invention, STM is still one of the most important surface characterisation techniques and can be used to image[18] and manipulate[19] atoms and molecules on a conductive surface in several different environments, including air, vacuum, and liquid solvent, over a vast range of temperatures.

A schematic diagram of an STM is shown in Figure 1.5. The tip is first brought as near as possible to the substrate under visual observation and a bias is applied between the STM tip and the substrate (V_{BIAS}). A stepper motor is then used to approach the tip to the surface until electrons tunnel and the desired current (I_0) is reached: the tip-substrate separation is usually between 5 and 15 Å at this point. The piezo drive is then responsible for precise control of the movement of the tip on the three axes in the tunnelling regime.

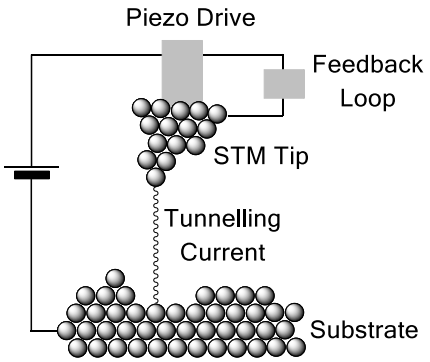

Figure 1.5: Schematic diagram of an STM.

There are two methods of imaging a surface: in constant current mode, the feedback loop maintains the current while scanning and the output is a plot of the movement of the tip. In constant height mode, suitable for very flat surfaces, the feedback loop maintains the height of the tip while scanning, and the output is therefore a plot of current.

1.2.1 Quantum Tunnelling

In quantum mechanics, quantum tunnelling is a phenomenon where a particle (e.g. an electron) violates the principles of classical mechanics by penetrating a potential barrier with higher energy than the kinetic energy of the particle. Tunnelling emerges formally as a solution of the Schrödinger equation,[20,21] for a particle coming from left to right towards a constant potential energy barrier V:

$$-\frac{\hbar^2}{2m}\frac{d^2\psi}{dx^2} + V\psi = E\psi \qquad \textit{Equation 1.1}$$

Outside the potential barrier $V = 0$ and the general solution of the Schrödinger equation is

$$\psi = Ae^{ikx} + Be^{-ikx} \qquad \textit{Equation 1.2}$$

Where k is the wave vector

$$k = \frac{\sqrt{2mE}}{\hbar} \qquad \textit{Equation 1.3}$$

Inside the barrier, considering particles with energy E lower than the barrier V, $V - E$ is positive and the general solution of the Schrödinger equation is

$$\psi = Ce^{\kappa x} + De^{-\kappa x} \qquad \textit{Equation 1.4}$$

Where κ is a decay constant

$$\kappa = \frac{\sqrt{2m(V-E)}}{\hbar} \qquad \textit{Equation 1.5}$$

On the right, after having passed the barrier, the electron is again outside the potential barrier, so $V = 0$ and the general solution to the Schrödinger equation is

$$\psi = A'e^{ikx} + B'e^{-ikx} \qquad \textit{Equation 1.6}$$

The acceptable solutions must obey some boundary conditions, in particular they must be continuous at the edge of the barrier (at $x = 0$ and $x = L$ for a barrier of width L) and their slopes must be continuous too:

$$A + B = C + D$$
$$Ce^{\kappa L} + De^{-\kappa L} = A'e^{ikL} + B'^{e^{-ikL}}$$
$$ikA - ikB = \kappa C - \kappa D$$
$$\kappa Ce^{\kappa L} - \kappa De^{-\kappa L} = ikA'e^{ikL} - ikB'e^{-ikL}$$

Equation 1.7

We can set $B' = 0$ as there will be no particles coming towards the barrier on the right side of it. The probability that a particle is travelling towards the barrier from the left side is proportional to $|A|^2$, and the probability that it is travelling to the right after the barrier is $|A\rangle^2$. The ratio of these two probabilities is called the transmission probability T, which takes the expression

$$T = \left\{1 + \frac{(e^{\kappa L} - e^{-\kappa L})^2}{16\varepsilon(1-\varepsilon)}\right\}^{-1} \qquad \textit{Equation 1.8}$$

Where $\varepsilon = E/V$. For sufficiently high and wide barriers ($\kappa L >> 1$) the transmission probability can be simplified to

$$T \approx 16\varepsilon(1-\varepsilon)e^{-2\kappa L} \qquad \textit{Equation 1.9}$$

Therefore there is an exponential decay of the transmission probability with the thickness of the barrier and with $m^{1/2}$. Particles of low mass are more able to tunnel through barriers and that is the reason why tunnelling is an important phenomenon for electrons, and only occasionally encountered for protons (but nevertheless important in some reactions). At the same time, during an STM experiment, the current flow will be proportional to $e^{-2\kappa L}$ or $e^{-\beta L}$ where L is the distance between the tip and the surface and β is the decay constant (sometimes called attenuation factor).

1.3 Charge Transport through Molecular Wires

The tunnelling model described in the previous section refers to the simplest model of vacuum tunnelling between two metals across a one-dimensional potential barrier. When a molecule is wired between the two electrodes this simple model cannot be applied because many other variables, such as structure and chemical composition,[22] redox properties[23] or length of the molecule,[24,25] can impact the mechanism of charge transport.

1.3.1 Coherent Transport

A mechanism of charge transport is called *coherent* if the electron maintains its phase information during the process (e.g. there is a definite phase relationship between the amplitudes corresponding to the electron before and after the potential barrier). When a bias voltage is applied between the substrate and the STM tip, the relative Fermi energy levels (E_F) of the two metal leads change accordingly, as can be seen in Figure 1.6.

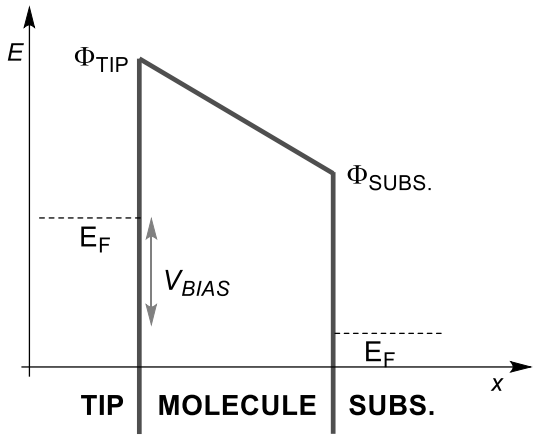

Figure 1.6: Metal¦molecule¦metal junction with a voltage applied (tip negative)

This bias causes the energy levels of the tip to be raised by $E(V_{BIAS})$ and the electrons in the occupied levels of the tip (between E_F and $E_F + E(V_{BIAS})$) can tunnel through the potential barrier (the molecule) into the unoccupied levels of the substrate. In this scenario, with no molecular orbital near the Fermi level, two possible mechanism of tunnelling are possible. Direct tunnelling occurs when V_{BIAS} is smaller than the barrier height Φ, and Fowler-Nordheim tunnelling occurs when the bias voltage applied is larger than the barrier height. The two mechanisms have different transport characteristics: in the Fowler-Nordheim case, the effective barrier width is smaller due to the high bias, its shape is distorted into a triangular form and the tunnelling current is therefore larger than in the direct case.[21] Another type of coherent electron transport is thermionic emission, where high temperatures excite the electrons to energies higher than the potential barrier, thus allowing them to surmount it. While still a coherent mechanism of charge transport, thermionic emission is not a type of tunnelling and is not seen in STM measurements, although it still retains significance in molecular electronics of semiconductors.[26]

Conduction Mechanism	Characteristic Behaviour	
Direct Tunnelling	$J \approx Vexp\left(-\frac{2d}{\hbar}\sqrt{2m\Phi}\right)$	*Equation 1.10*
Fowler-Nordheim Tunnelling	$J \approx V^2 exp\left(-\frac{4d\sqrt{2m}\Phi^{3/2}}{3q\hbar V}\right)$	*Equation 1.11*
Thermionic Emission	$J \approx T^2 \exp\left(-\frac{\Phi - q\sqrt{qV/4\pi\varepsilon d}}{kT}\right)$	*Equation 1.12*

Table 1.1: Possible coherent transport mechanisms in the absence of molecular orbitals near the Fermi level of the metal electrodes. J is the current density, d is the barrier width, T is the temperature, V is the applied bias and Φ is the barrier height. *After ref. 26.*

When the molecule has an orbital that can aid charge transport despite being far from the Fermi level of the electrodes, a fourth coherent mechanism can be observed: super-exchange. Super-exchange can be seen as a two-step tunnelling (tip → molecule → substrate), but the charge carrier does not remain on the molecular bridge long enough to experience dephasing by nuclear motions (hence the correct nomenclature coherent super-exchange).[27] Therefore the molecular orbitals are used solely as a coupling medium and do not actively participate in the electron transfer process.

1.3.2 Resonant Tunnelling

An interesting structure in quantum physics is the double tunnelling barrier (DTB). If two barriers are placed in sequence then one would expect the transmission across both barriers to be less than across just one barrier, in the same way as classical resistors lined up in a series work. However, the physical size of the DTB devices can be close to the de Broglie wavelength of the tunnelling electron, making the electron transport subject to the laws of quantum mechanics. In electron tunnelling there are always two components to a wave: the transmitted part, which passes the tunnelling barrier, and the reflected part, which does not penetrate the barrier and moves in the opposite direction. In a nanoscale device, with two tunnelling barriers spaced a few Angstroms apart, the reflected wave from the second barrier can interfere with the transmitted wave from the first barrier, increasing or decreasing the amplitude inside the potential well (thus *resonant*). A particular case, where the energy of the well matches the energy level from which the particles are injected, leads to the double barrier being totally transparent for particle transmission, allowing ballistic charge transport.[28] The

phenomenon can be either *coherent* (the particle has the same phase before and after tunnelling) or *incoherent* (dephasing occurs due to sequential tunnelling steps), but the two mechanisms are experimentally indistinguishable.[29] Apart from ballistic transport, resonant tunnelling can cause a phenomenon called "negative differential resistance" (NDR), where an increase in the current results in a *decrease* in voltage, in conflict with Ohm's law. This is due again to interferences (constructive and destructive) between the incoming and reflected waves inside the quantum well, that can increase or decrease the transmission probability for certain energies of the incoming particles.[30]

The first device constructed which demonstrated an NDR signature of resonant tunnelling was an inorganic GaAlAs¦GaAs¦GaAlAs DTB system, incorporated in a lightly doped GaAs matrix[31]. In molecular electronics, large NDR effects have been recently seen for molecular system containing a 9,10-dihydroanthracene core: the break in conjugation causes a splitting in the energy levels of the molecular wire, thus creating two different tunnelling barriers. At certain biases, resonant transport is suppressed due to level misalignment and the current decreases with voltage. Effects of this magnitude in single molecules, however, have only been seen at very low temperatures (6 K in the latter study).

1.3.3 Hopping

An example of incoherent charge transport mechanism is hopping. Hopping usually happens in long molecular wire, where the time it takes for the electron (or the hole) to travel through is enough for inelastic interactions to occur. The electrons "hops" through different fragments of the molecular wire spending a finite amount of time ($\approx 10^{-11}$ s) on each of them, and the charge carrier is therefore dephased due to interactions with the molecular backbone.

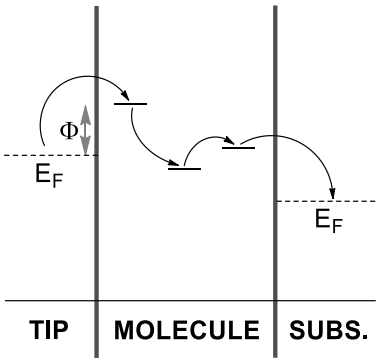

Figure 1.7: Incoherent charge carrier hopping through different energy levels of a molecular wire.

Hopping is essentially a redox mechanism and requires thermal activation for the electron to overcome the difference Φ in energy between E_F of the electrode and the level of the receiving fragment: it is therefore temperature dependent, following equation 1.13.[32]

$$J \propto Vexp\left(\frac{-\Phi}{k_B T}\right) \qquad \textit{Equation 1.13}$$

Hopping mechanisms show rates of charge transfer, k_{ET}, given by

$$k_{ET} \propto N^{-\eta} \qquad \textit{Equation 1.14}$$

where η lies between 1 and 2, and N is the number of hopping steps, as opposed to the exponential decay typical of tunnelling mechanism. The nature of the contact groups anchoring the molecule to the electrodes has less influence on the measured conductance.[33]

1.3.4 Transition between charge transport mechanisms

Choi *et al.* observed a change in the slope of the attenuation factor β when the molecular length of an oligophenyleneimine (OPI) molecular wire reaches 4 nm and attributed it to a change in the transport mechanism from direct, coherent tunnelling to incoherent hopping. As further confirmation, they also measured the conductance of such molecular wires at different temperatures: the shorter oligomer (OPI 4, 3.5 nm) showed no temperature dependence, while the longer ones (OPI 6, 4.7 nm and OPI 10, 7.3 nm) showed thermally-activated behaviour, with molecular conductance increasing with temperature.[34]

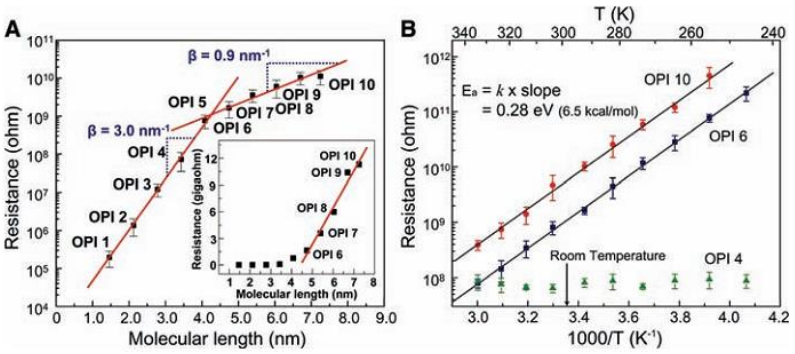

Figure 1.8: Logarithmic resistance vs length plot (panel A) and Arrhenius plot (panel B) of OPI series. 2 different values of β were observed, as the transport regime change from tunnelling to hopping when the molecular wire gets longer. The Arrhenius plot shows activation energy E_a of 0.28 eV for the longer molecular wires, while the short one has activationless transport mechanism. *Reprinted from ref. 34.*

A similar transition between tunnelling and hopping as the length of the molecular wire grows has also been seen, among others, in oligonaphthalenefluoreneimine[24] (ONI - critical length ≈ 5 nm), oligophenylenetriazole[35] (OPT - critical length ≈ 6 nm) and oligophenyleneethynylene[36] (OPE – critical length ≈ 2.5 nm) systems.

Temperature dependence alone, however, cannot be taken as a signature of hopping transport mechanism: a very short sulphur end-functionalised tercyclohexylidene showed thermal activation above 150 K[37] and a series of oligoporphyrin molecular wires[38] showed thermal activation in the range 298 – 373 K.

A thermally activated behaviour has been observed in single redox molecules (perylene derivatives) and yet another explanation was given:[23] the presence of a redox-active moiety allows a two-step incoherent tunnelling process, where the electron spends a finite amount on time on the molecule, effectively reducing and then re-oxidising it. The model, originally developed by Kuznetsov and Ulstrup[39] involves a vibrational relaxation of the orbital hosting the electron and is therefore thermally activated, with the natural logarithm of conductance proportional to T^{-1} in a manner similar to hopping.

1.3.5 Double Tunnelling Barriers in Molecular Electronics

The double tunnelling barrier configuration has been explored in molecular electronics, but signatures of resonant tunnelling (NDR or ballistic transport) have been reported in very few articles.[40–42] However, the presence of a barrier indentation (potential well) improves the charge transport. For instance, a viologen (4,4'-bipyridinium) moiety sandwiched between two mercaptohexyl barriers has a group B conductance of 0.5 nS,[43] roughly four times higher than dodecanedithiol (*i.e.* two back-to-back mercaptohexyl barriers with no well; 0.12 nS)[44]. Furthermore, viologen is a redox-active moiety and can be oxidised by an external bias to a more conductive state, with a conductance of 2.8 nS (roughly 20 times higher than dodecanedithiol): the viologen radical cation acts as a particularly deep well.[45]

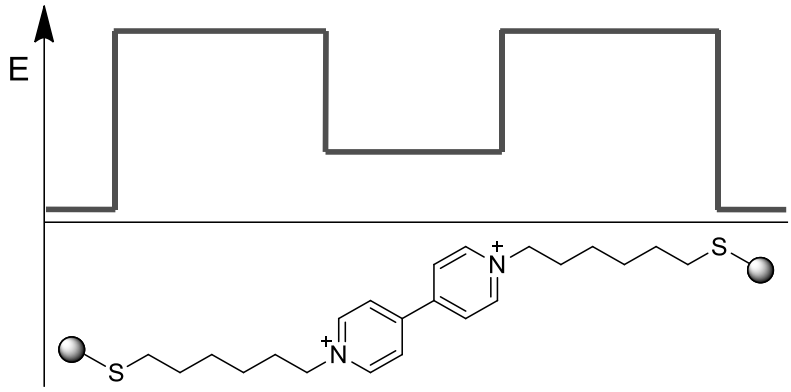

Figure 1.9: Example of a DTB molecule with a viologen well and energy diagram at zero bias. Counterions are not shown for clarity.

This increase of conductance has been related to the change in the energy levels of the molecule with respect to E_F when approaching the reduction potential. The molecular orbital moves towards E_F upon reduction, and charge transport is therefore more efficient. The orbital energy of a moiety can also be tuned by varying its electron density, through the attachment of electron-withdrawing or electron-donating groups. Leary *et al.* observed that, for a DTB molecular junction containing a phenyl well, the more electron rich the benzene ring, the higher the conductance.[46]

1.3.6 Charge transport through a single molecular resonance

The simplest model that can be used to approximate the electron flow in a molecular device consists of two electrodes (1 and 2), with a small voltage applied between them, and a single energy level ε lying between them.[47] As discussed previously in section 1.3.1, the presence of an external bias changes the electrochemical potential of the electrodes to, respectively, μ_1 and μ_2. If $\mu_1 > \varepsilon > \mu_2$ we can write the current through this device as

$$I = \frac{e}{\hbar}\frac{\Gamma_1\Gamma}{\Gamma_1+\Gamma_2}[f_1(\varepsilon) - f_2(\varepsilon)] \qquad \textit{Equation 1.15}$$

where Γ is the coupling of the energy level ε to the electrodes and $f(\varepsilon)$ is the Fermi function $f_1(\varepsilon) = 1/(1+\exp\frac{\varepsilon-\mu_1}{k_BT})$ and $f_2(\varepsilon) = 1/(1+\exp\frac{\varepsilon-\mu_2}{k_BT})$. At sufficiently low temperatures so that $f_1(\varepsilon) - f_2(\varepsilon) = 1$, and with $\Gamma_1 = \Gamma_2 = \Gamma$, the equation can be rewritten to

$$I = \frac{e\Gamma}{2\hbar} \qquad \textit{Equation 1.16}$$

This suggests that it could be possible to pump unlimited current through this one-level device by just increasing the coupling strength of ε to the electrodes. However, it has been demonstrated that the maximum conductance of a one-level device (such as a gold point contact) is equal to the quantum of conductance G_0. This happens because the process of coupling a level to the electrodes causes a broadening of the level itself, with part of its energy to spread outside the range between μ_1 and μ_2, where current flows. Therefore, Γ can be seen as a function describing the level broadening due to the coupling between the two electrodes and the central energy level ε. The actual current is reduced below what we expect from equation 1.16, to approach a constant value independent of the strength of the coupling to the contacts.

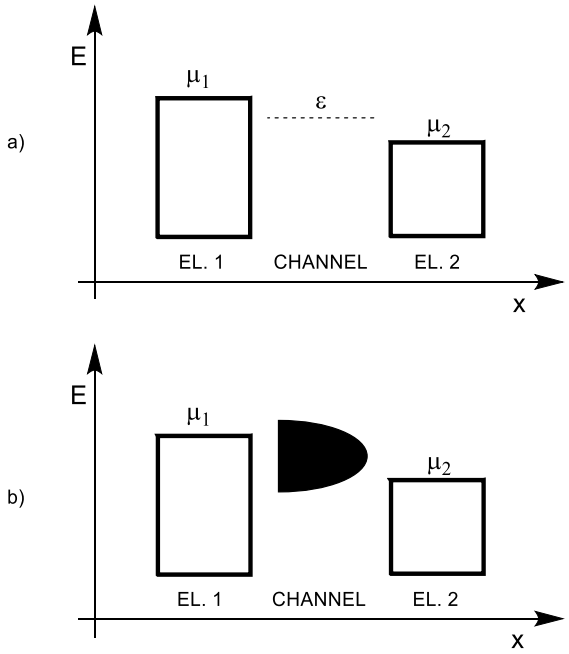

Figure 1.10: a) A channel with a small voltage applied across it, causing a splitting of the electrodes electrochemical potentials $\mu_1 > \varepsilon > \mu_2$. b) The process of coupling to the channel broadens the level, spreading part of its energy outside the range between μ_1 and μ_2, where current flows.

An important effect arising from this formalism is that, as long as the thermal energy k_BT is much lower than ε and Γ, the current is temperature-independent. As the temperature increases, the high-energy tail of the Fermi distribution starts to overlap with the broadened level and the current increases exponentially with temperature.[37,38]

1.4 SPM-SMC Techniques

Starting from the pioneering work of Reed *et al.* a plethora of methods to fabricate metal¦*single molecule*¦metal junctions and to measure their electrical properties has been proposed and introduced at the beginning of the XXI century. Junctions have been prepared by electromigration of gold wires in 2000,[48] but the technique allows little control on the junction geometry and width, and the process of electromigration itself can cause artifacts that are hard to distinguish from the true molecular behaviour. The advent of scanning probe microscope (SPM) based techniques made the measurement of electron flow through single molecules easier and more reproducible.

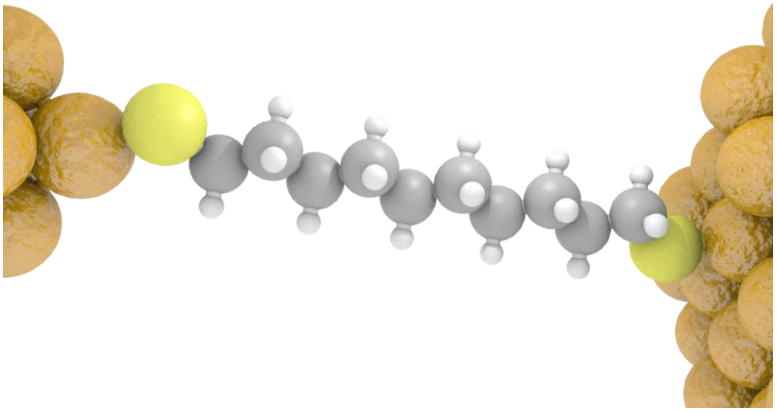

Figure 1.11: A simple molecular wire (decanedithiol) sandwiched between a gold (111) terrace (right) and a gold tip (left) as common geometry in single molecule conductance measurements.

1.4.1 Matrix Isolation Technique

In 2001, Cui *et al.* published a new method to achieve electrical characterisation of single molecules[49]. They used monolayers of octanethiol on Au(111) in which they inserted octanedithiol molecules and exposed the so obtained mixed SAM to a solution of gold nanoparticles. The nanoparticles bind to the free thiol moiety of the octanedithiol and they are subsequently gently touched with a conductive, gold-coated atomic force microscope (AFM) tip/cantilever assembly and *I-V* traces are recorded. They found five different curves, representative of integer multiples of a fundamental curve, that they related to the number of molecules actually contacting the nanoparticle. A statistical analysis, conducted on 4000 traces obtained from the same number of individual contacted nanoparticles, verified their ideas. About 25% of the curves corresponded to the *single* molecule peak.

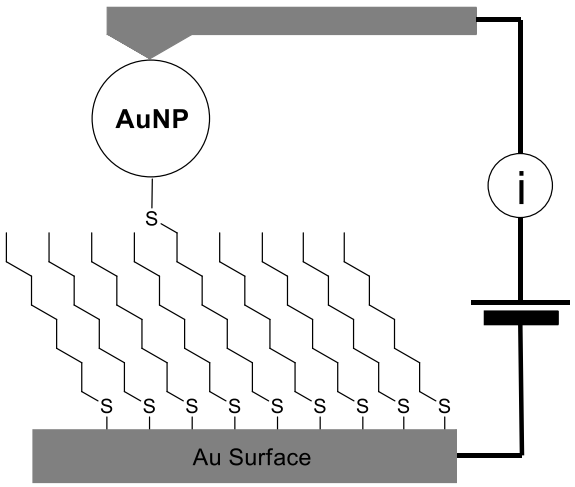

Figure 1.12: Matrix isolated dithiol contacted with a Au nanoparticle held in the cantilever-substrate gap as described in Cui *et al.*

The technique, however, requires a long and elaborate sample preparation and the measured conductance can be complicated by Coulomb blockade effect due to the distinct size of the nanoparticles and their contact resistance with the AFM cantilever.[50]

1.4.2 STM – Break Junction Technique

In 2003 Xu and Tao[51] published a paper in which they used a modified STM to create molecular junctions by repeatedly crashing a Au tip into a Au surface and retracting it in the presence of a molecular target such as alkanedithiols or bipyridine. As the tip is retracted from the gold surface, a number of "quantum steps" near multiple of G_0 (quantum of conductance, $2e^2/h$) due to the formation of an atom-thick gold wire can be seen before the breakage of the final Au-Au bond. As the tip is further retracted, molecules present in solution can bridge the surface-tip gap and new step-like features, characteristic of charge transport through integer number of molecules, can be seen. The molecular junction will then break, resulting in an abrupt decrease in current. Combining a number of these current-distance traces in statistical histograms shows peaks at integer multiple of a value, that is believed to be the conductance through a *single* molecule.

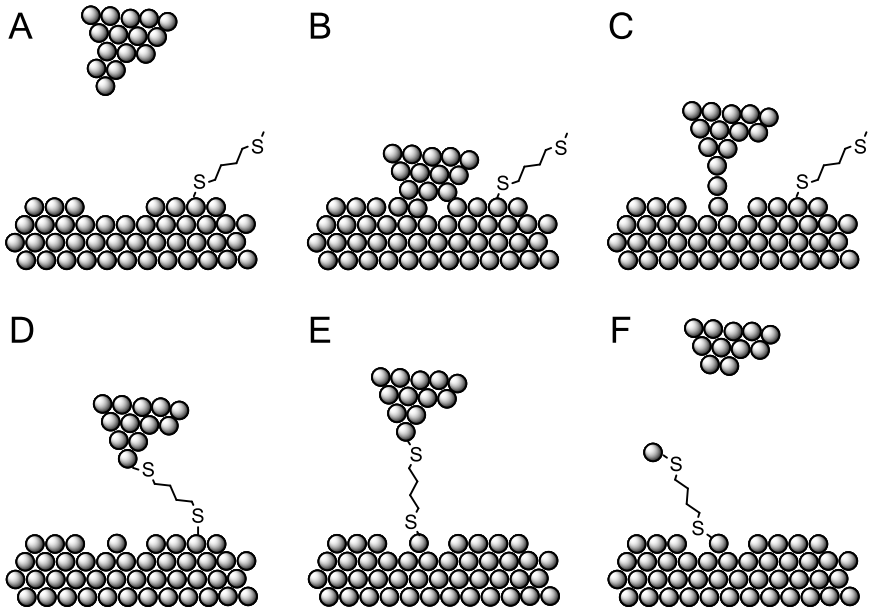

Figure 1.13: Schematics of a *STM-BJ* experiment: the tip is crashed on the gold surface (B) in the presence of molecular wires (butanedithiol in this panel) and subsequently retracted. A monoatomic gold wire is pulled from the surface (C) and eventually breaks, so a molecule can bridge the tip-substrate gap (D). As the tip is further withdrawn, the molecular wire will adopt an elongated configuration, until the junction will finally break (F).

This technique (*STM-BJ*, acronym for scanning tunnelling microscope – break junction), requires little sample preparation and relatively simple instrumentation: it is now the most widely used to characterise single molecule junctions.

1.4.3 Non-contact STM techniques

A similar technique, *I(z)*, has been developed by Haiss *et al.*[43] involving the use of an STM to contact single molecules adsorbed on a Au(111) surface with a Au tip and measuring the current flow while the tip is retracted. The main difference between this technique and the *STM-BJ* developed by Xu and Tao is that there is no physical contact between the tip and the substrate. As a result the geometry of the tip is left unchanged during the experiment, resulting in sharper histograms and the possibility to periodically monitor the Au surface with high resolution images. In the same paper the possibility to exert electrochemical control on molecular wires containing redox-active groups is discussed, showing that viologen-containing molecules have a conductance dependant on the applied bias.[43] Haiss *et al.* also developed another technique, called the *I(t)* method, to measure single molecule conductance using the spontaneous formation of molecular wires.[52] A STM gold tip is held at constant tip-substrate

separation over a submonolayer of molecules capped with suitable contacts and, at optimal tip-substrate distance, the molecular wires bridge the gold-to-gold gap and this result in characteristic current jumps that usually last for a very short period of time and are characteristic of molecular conductance. Recently, a new STM non-contact technique has been developed by Pires *et al.*[53] and involves the collection of a large number of *I-V* curves (*vide infra*) while retracting a gold STM tip in very small steps (0.5 Å – *I(v,z)* technique). Molecular conductance can be extrapolated from the slope of the *I-V* curves, but its major advantage is that it enables observation of the complete *I-V* behaviour of a single molecule, thus pointing out possible rectifying or negative differential resistance (NDR) behaviour.

1.4.5 Scanning Tunnelling Spectroscopy

Scanning Tunnelling Spectroscopy (STS) is the study of the tunnelling current as a function of the bias voltage. It is generally performed as single point spectroscopy, which means holding the tip at a defined position by freezing the voltage applied to the *x, y* and *z* piezos, disabling the feedback loop and sweeping the tip-substrate voltage between two specified values while recording the tunnelling current. After the spectra acquisition, the bias voltage is returned to the starting value and the feedback loop is switched on[54]. The resulting data, plotted as *I-V* curves (current-voltage characteristic) contains information about the electrical behaviour of the junction. Single molecules have been characterised using this method by imaging the surface first and then placing the tip over an isolated molecule. If a molecule is only adsorbed on the surface, however, the junction will be asymmetric with a tunnelling barrier between the tip and the molecule, and contamination of the tip-molecule gap can lead to irreproducible results. Molecular wires bridging the tip-substrate gap, on the other hand, offer a way to perform STS on symmetric junctions and have been used in both break-junction[11,55,56] and STM-based methods.[49,51] *I-V* curves with varying shape are generally obtained using STS (Figures 1.13 and 1.14). As illustrated in these figures, tunnelling between two metals results in linear current-voltage characteristics, while tunnelling through semiconducting systems shows a non-linear behaviour. Non-doped semiconductors generally have a linear regime at low bias followed by a change of slope at larger biases, while doped semiconductors also show rectification, at positive bias when p-doped and at negative bias when n-doped.

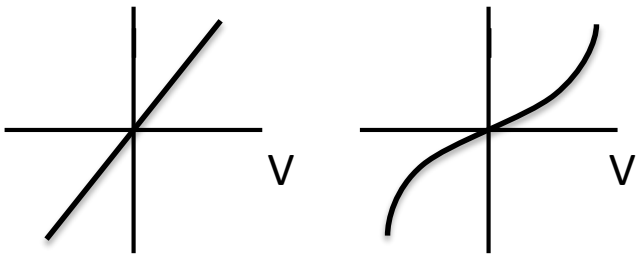

Figure 1.14: *I-V* characteristics expected for a metal (left) and a semiconductor (right).

Another type of *I-V* behaviour seen for semiconductor junctions and for some molecules is known as Negative Differential Resistance (NDR): at a particular bias value the slope of the curve becomes negative (Figure 1.15). This means that, as the bias is increased, the current across the junction will fall, due to an energy level in the junction moving out of alignment with the metal E_F, thus having a lower transmission probability[41].

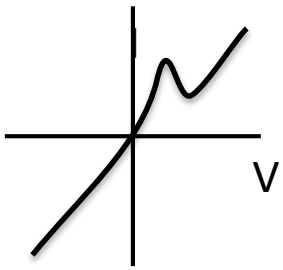

Figure 1.15: NDR Effect in an *I-V* curve.

1.4.4 Contact Nature and Geometry

Several metals[57–60] have been employed in the fabrication of metal¦*single molecule*¦metal junctions, but gold remains so far the most widely used. This is due to its intrinsic resistance to oxidation, making it easy to bridge molecules to the metal without adventitious oxides on the surface. Furthermore, many functional groups have strong affinity to gold enabling the formation of stable contacts that facilitate electron transport. Sulfur and nitrogen are by far the most used contacts, in a variety of functional groups: thiols,[11] thioethers,[61] thioesters,[62] thiophenes,[63] dithiocarbamates,[64] pyridines,[51] cyanides[65] and amines.[66] Among the contact groups employed less frequently are fullerenes,[67] selenols,[68] phosphines,[69] carboxylic acids,[70] TMS-ethynyl,[71] dihydrobenzo[b]thiophene,[72] π-stacked benzene rings[73] and diazonium salts,[74] that can be reduced *in situ* to form direct Au-C bonds. Other methods of obtaining direct Au-C contact have been the deprotection of TMS-acetylenes on the surface[75] and the spontaneous

cleavage of trimethyltin groups in the presence of Au.[76] The nature of contact groups can alter the value of the measured conductance according to the Landauer formula:[77]

$$G(\mu) = G_0 \sum_n T_n(\mu) \qquad \textit{Equation 1.17}$$

Where the quantum of conductance G_0 is the conductance of a one-dimensional wire of metal atoms and is given by:

$$G(0) = \frac{2e^2}{h} \approx 77.6\,\mu S \qquad \textit{Equation 1.18}$$

The total conductance is, therefore, the sum of the transmission eigenvalues T_n for all the molecular wire transport channels, including the ones referring to the metal¦*molecule*¦metal contacts. The higher conductance demonstrated by molecules with Au-S contacts than Au-N is because the transmission probability through the contact channel is higher for thiols (0.81) than for amines (0.19).[78]

Molecules bearing sulfur-capped contact groups showed three different conductance values during experiments.[79] The consensus here is that these conductance groups arise from the formation of contacts with different geometry at each end of the molecule. It has been suggested that the A, or low conductance group is observed when the molecule is adsorbed on a flat, terraced surface on one end and a single undercoordinated (tip-type) Au adatom at the other. When the molecule is adsorbed at a step-edge at one, or both ends, then the B (or medium) and C (or high) contact groups are respectively observed.

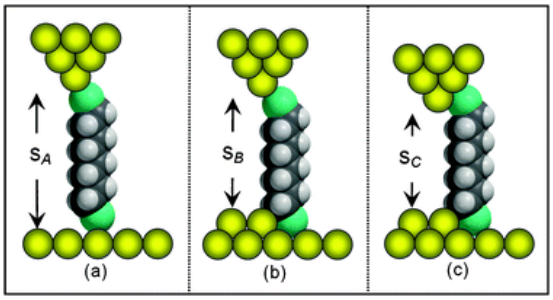

Figure 1.16: Different contact geometries for sulfur-capped molecules in a junction. (a) shows the molecule with both thiolate contacts adsorbed on flat surface and single atoms, in a low-conductive geometry. In (b) the bottom contact is adsorbed on a defective, stepped site, and in (c) both contacts are adsorbed on such sites, in increasingly conductive geometries.
Reprinted from ref. 79.

Doing measurements with different experimental conditions can favour the occurrence of one conductance group over the others: smooth surfaces and non-contact techniques (such as *I(z)* and *I(t)*) that tend to leave the gold substrate unaltered promote A or B type junctions, while highly corrugated surfaces and *STM-BJ* technique promote B or C type junctions[80,81].

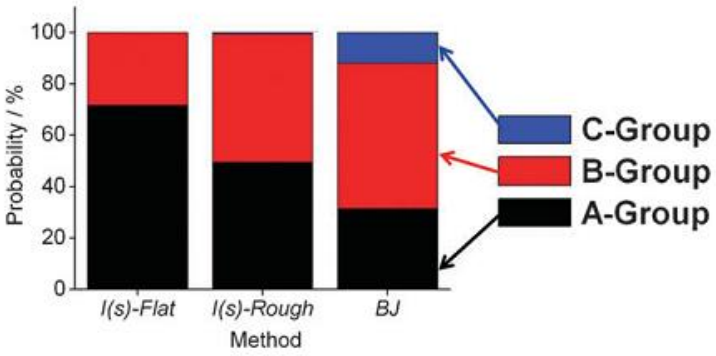

Figure 1.17: A representation of the distribution of conductance groups across two different techniques on substrates of differing roughness. *Reprinted from ref. 81.*

The strong nature of the S-Au bond causes a large charge delocalisation at the two Au | molecule interfaces, leading to a "gateway" state. This is an intermediary state coupling the metallic lead to the molecular backbone.[82,83] If the calculated transmission probability T is plotted as a function of energy E (transmission curve), the thiol contacts produce a resonance about 1 eV from the Au Fermi level[84], thus generally causing an increase in conductance compared with other contact moieties.

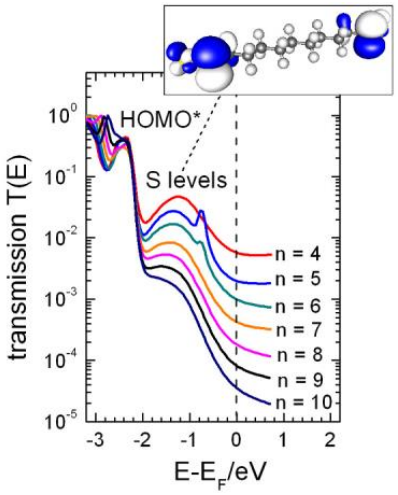

Figure 1.18: Transmission curves for a series of alkanedithiols having n(CH_2) between 4 and 10. The S-Au "gateway" state is clearly visible in the shorter molecular wire. *Reprinted from ref. 84.*

1.5 Thiophenes

Thiophene, also called thiofuran, is a heterocyclic compound with general formula C_4H_4S. It is a flat five-membered ring, an aromatic compound and, like benzene, commonly participates in substitution reactions although theoretical calculations suggest that the degree of aromaticity is lower. At room temperature, it is a colourless liquid with a pleasant odor reminiscent of benzene, and the ring structure is flat in a distorted pentagonal shape: the bond angle at the sulfur is 91°, the C-C-S angle is 112° and the C-C-C angle is 113°. Bond lengths are distorted too, with C-S bond 1.74 Å, and C-C bond 1.35 (near to the sulfur atom) and 1.44 Å (opposite to the sulfur atom)[85]. It is commonly found as a contaminant in petroleum, in concentrations up to 1-3%, both as free thiophene and as fused-rings compounds, such as benzothiophene and dibenzothiophene.

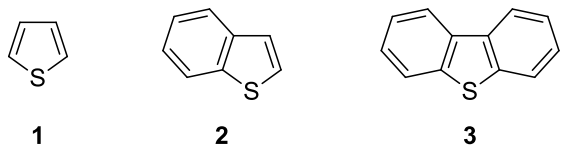

Figure 1.19: Typical thiophene-based contaminants found in petroleum: thiophene (1), benzothiophene (2) and dibenzothiophene (3).

The presence of an electron-rich heteroatom imparts thiophene with unusual susceptivity to attack by electrophiles. Halogens firstly attack the 2 and 5 position and perhalogenation is easily accomplished to obtain C_4X_4S (X = Cl, Br, I). Thiophene brominates 10^7 times faster than benzene.[86] At the same time, thiophene is very susceptible to lithiation (by reaction with *n*-BuLi) to give 2-lithiothiophene and 2,5-dilithiothiophene, useful precursors to a variety of derivatives.[87]

1.5.1 Thiophene Uses and Applications

Thiophene is an important building block in many agrochemical and pharmaceutical compounds, and it can often replace the benzene ring of a biologically active compound without loss of activity.[88] Thiophene oligomers can also be found in nature: 2,2':5',2"-terthiophene is a pigment in African marigolds and has a biological activity as an insecticide[89] / biocide[90] because it sensitizes the formation of singlet oxygen, and several substituted bi- and terthiophenes occur naturally in plants such as the *Echinops Grijisii.*[91]

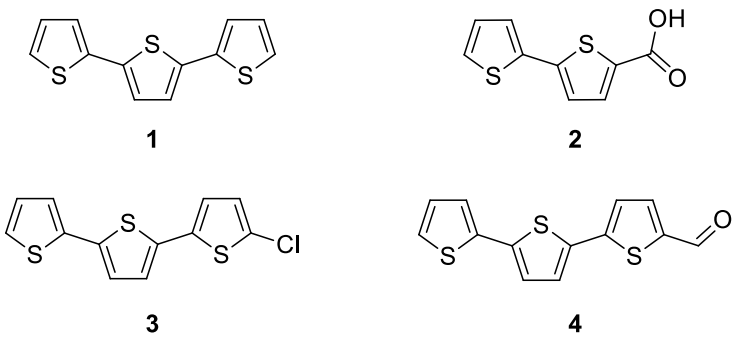

Figure 1.20: Examples of naturally-occurring thiophene oligomers and derivatives: 2,2':5',2"-terthiophene (1), 2,2'-bithiophene-5-carboxylic acid (2), 5-chloro-2,2':5',2"-terthiophene (3) and 2,2':5',2"-terthiophene-5-carboxaldehyde (4).

The main use of thiophene derivatives, oligomers and polymers, however, is in the semi-conductor and photovoltaic industry: the extended conjugated system (alternation of single and double bonds), stabilised by the presence of an electronegative element, results in some remarkable electrical properties of this class of polymers, such as very high field effect mobility.[92] In particular, poly(3-alkylthiophene) (P3AT) was one of the first contenders as a high-mobility semiconductor for organic field-effect transistor (FET), and after the first report in the late 1980s by Assadi *et al.*[93] (on poly(3-hexylthiophene), P3HT) a great interest was stirred in the field.[94] These remarkable properties arise from the dense and highly ordered packing of neighbouring polythiophene chains in π-stacked, lamellar structures. Charge transport is therefore fast both through the polymer chain (due to the polymer structure) and *between* neighbouring chains (due to supramolecular organisation), with field effect mobility close to 0.1 $cm^2\ V^{-1}\ s^{-1}$ for highly regioregular head-to-tail P3HT.[95] Doping of the polymer (injection of charges in the polymer backbone by electrochemical or chemical means) further increases this value, up to 20 times higher.[96]

Apart from simple poly(alkylthiophenes), several other substituted polythiophenes have been studied, and some found commercial applications. As example, AGFA developed a series of PEDOT (poly(3,4-ethylenedioxythiophene) based polymers, marketed under the name of Orgacon™, that are employed as antistatic coatings in the photographic film industry and as flexible conductive thin films, as alternatives to the brittle ITO (Indium-Tin Oxide).

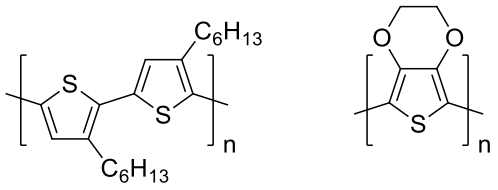

1 2

Figure 1.21: Examples of substituted polythiophenes: regioregular head-to-tail P3HT (1) and PEDOT (2)

Oligo- and polythiophenes are therefore well known as good conducting organic molecules, with hole transporting ability increasing with the number of monomer units in the oligomer series. Terthiophene, for instance, has a lower oxidation potential than bithiophene, which in turn has a lower potential than thiophene since the longer the oligomer, the better the charge delocalisation across the conjugated system. Changes in the energies of the highest occupied and lowest unoccupied molecular orbitals (HOMO and LUMO) and the difference between them (H-L gap) from one oligomer to the next becomes negligible beyond 6-8 monomer units.[97] Therefore sexithiophene has almost the same H-L gap and energies as polythiophene (≈ 2 eV).[98]

1.5.2 Thiophenes in Molecular Electronics

Given the remarkable electric properties of its oligomers and polymers, thiophene has been used as a moiety in molecular wires in several experiments. Xu and Tao, the original developers of the *STM-BJ* technique, used oligothiophene molecular wires to test the effect of an electrochemical gate on molecular conductance.[99] Using methylthio-terminated terthiophene and quaterthiophene oligomers in a four electrode STM cell they found that the conductance of the molecule at zero gate bias actually *increase* with the number of thiophene rings, in a manner contrary to expectations from classical tunnelling behaviour. They attributed this unusual length-dependence to a smaller HOMO-LUMO gap and, therefore, a closer position of the HOMO to the Fermi levels of the probing electrodes, for the quaterthiophene molecule. Furthermore, they could repeatedly switch the two molecules between a high and low conductance state oxidising them using the electrochemical gate.

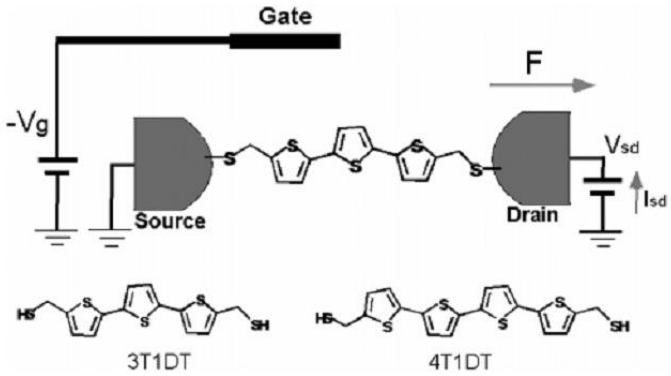

Figure 1.22: Schematic illustration of Xu and Tao experimental setup. They used Au electrodes as source and drain (Au surface and tip), a Pt counter electrode and a Ag quasi-reference electrode in 0.1 M $NaOCl_4$ as electrolyte. *Reprinted from ref. 99.*

Yamada *et al.* used the break junction technique to measure the conductance of very long SCN-terminated oligoalkylthiophenes (from a 5- up to a 14-mer), finding evidence of a tunnelling mechanism for the whole oligomer series, with an observed decay constant $\beta = 0.1$ $Å^{-1}$ [100]. It is remarkable that the pentamer had a lower conductance than expected from the decay constant: this is consistent with HOMO-LUMO calculations that predict a decrease of the gap value from the monomer to sesquithiophene, the latter having almost the same gap value as polythiophene. Therefore the exponential decay observed by Yamada *et al.* and the increase in conductance observed by Xu and Tao both fit in the same theory. Leary *et al.*[62] studied a series of thiohexyl-capped oligothiophenes and found the same behaviour, but a different explanation is proposed: combining measurements in different media, molecular dynamics simulations and DFT calculations they found that water can significantly affect the junction conductance. In the presence of water the conductance increase across the oligothiophene series as measured by Xu and Tao, while in a dry atmosphere the conductance follows an exponential decay with an attenuation factor $\beta = 0.54$ $Å^{-1}$. DFT calculations using the nonequilibrium Green's function (NEGF) show that the presence of water triggers a shift of the LUMO resonance towards the Fermi energy, thus increasing conductance. Crucially, the longer molecules showed greater gating effect due to the presence of a larger number of water molecules coordinated to the oligothiophene system, compensating for the reduction in conductance as function of length.

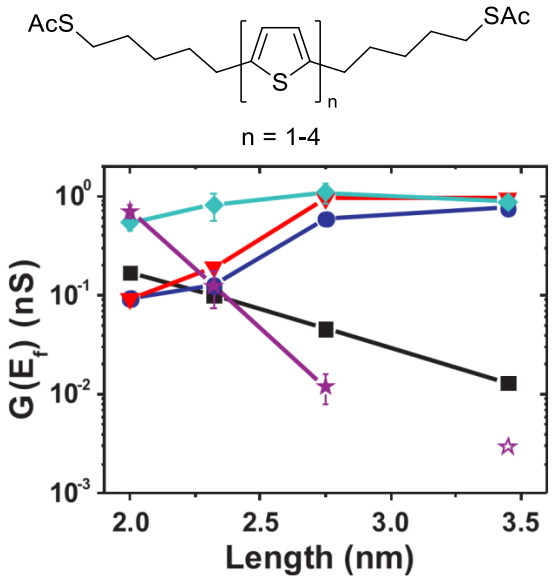

Figure 1.23: Structure of molecular wires employed in the study and comparison between calculated and experimental conductance. Experimentally measured in air (light blue diamonds), measured in dry Ar (purple stars), calculated in vacuum (black squares) and calculated in the presence of water (red triangles and blue dots). *Reprinted from ref. 62.*

Using fully conjugate oligothiophene molecular wires, with methyl sulfide contacts[101] (different from thiols in the geometry of the Au-S bond), a different behaviour was found. Conductance exponentially decreases with the oligothiophene length, as expected in tunnelling theory, until the number of thiophene rings reaches four: quaterthiophene has been found more conductive than terthiophene and sexithiophene much less conductive than expected from the tunnelling decay constant. This unusual trend has been attributed by Capozzi *et al.* to different conformers present in the junctions: quaterthiophene is the first oligomer in the series to have easy access to coplanar, high conductive configuration thanks to its symmetry, while the longer oligomers are poorly conductive due to increased disorder induced by the extra thiophene rings. While the behaviour observed by Capozzi *et al.* is different from the one described earlier, the difference in contact nature and extent of conjugation makes the systems not directly comparable.

Thiophene-containing molecular wires were also used to demonstrate that the degree of aromaticity decreases the conductance of a metal¦*molecule*¦metal junction.[66] In a comparison between thiophene, furan and cyclopentadiene, the conductance of the former was found to be almost an order of magnitude lower than the other two compounds. In another study, thiophene was used to demonstrate the effect of molecular symmetry on single-molecule conductance: a comparison between simple biphenyl and bithiophene molecular wire showed

a broadening of the conductance peak due to the 5-fold symmetry of the latter.[102] The effect of symmetry was further confirmed by the conductance measurement of rotationally constricted cyclopentadithiophene, which produced a conductance peak with shape similar to the biphenyl one.

1.6 Environmental Effects in Molecular Electronics

The environment surrounding the molecules during single molecule conductance measurements can have a huge impact on the values obtained. Just a few months after publishing the *STM-BJ* paper, Xiao, Xu and Tao discovered that the conductance of single-peptide molecular wires bearing amine or carboxyl side groups is linked to the pH.[103] While the study itself is not ground breaking, as it is known that presence of charges in the tunnelling barrier alters its shape and width, it is the first example of environmental dependence of conductance. A few months later the same group discovered that single molecule peptide conductance can be increased by orders of magnitude upon metal ion binding.[104] They studied four thiol-terminated peptides in *STM-BJ* experiments and found that, for the peptides with the highest number of binding sites (a side group or the deprotonated peptide bond) complexation with copper atoms increased conductance by a factor of 320.

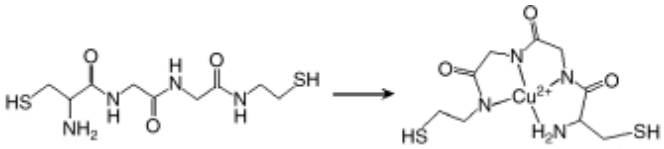

Figure 1.24: Change in peptide conformation upon complexation with a copper atom. A new, shorter conduction pathway is present, mediated by the metal ion. *Reprinted from ref. 104.*

A change in the energy levels of the peptide and in shape and width of the tunnelling barrier upon metal complexation, and the presence of a new electron tunnelling pathway through the chelate bonds and the metal atom were deemed responsible for this dramatic increase in conductance, although this can be seen as a "chemical" rather than purely environmental effect.

Conformational changes in peptides can be also triggered by pH variations, and Scullion *et al.* demonstrated that these changes can affect the conductance value[105]. The peptide Hys-(Glu-Leu)$_5$-Cys exists in a very compact α-helical state at low pH, and a conductance value of

1.7 nS was measured using STM-based techniques for Au|*peptide*|Au junctions. When the pH is raised to neutrality, the peptide adopts an extended configuration and the electron transfer is therefore very inefficient: its conductance fell below the sensitivity of the instrument used, <0.1 nS. However, pH is not the only variable that can influence charge transport across a molecular junction. Two separate research groups reported in 2011 a spread of conductance values of a single molecule when measured in different solvents. They both used the same molecule (benzene-1,4-diamine) as molecular wire and were able to relate the change in conductance to a shift in the Au contact work function induced by solvents binding to the electrode around the metal|*molecule*|metal junction.[106] Using a number of similar solvents (halogenated benzenes) Fatemi *et al.* were also able to demonstrate that the solvent-induced shift is proportional to the affinity of the solvent to Au,[107] therefore implying a degree of chemical control on the level alignment and transport properties of a molecular wire.

In a pioneering attempt to measure single-molecule electronic properties, Kasibhatla *et al.* demonstrated that formation of donor-acceptor charge transfer complex with tetracyanoethylene (TCNE) can significantly alter the *I-V* characteristic of tetramethylxylyldithiol (TMXYL), resulting in a switch from insulating to ohmic behaviour.[108] The TMXYL:TCNE complex can be broken by treating it with a solution of tetrathiafulvalene (TTF), a stronger electron donor than TMXYL. This change in behaviour was attributed to the introduction of a hybridised charge transfer (CT) complex energy level that lies near to the Fermi level of the substrate. Similarly, Del Re *et al* observed changes in molecular conductance of individual oligophenylene-vinylene molecules due to π donor-acceptor interactions with small electron-deficient conjugated aromatic molecules. In particular, changes due to interaction with nitrobenzene and dinitrobenzene were among the highest observed, making this system a good candidate as sensors for explosive compounds.[109] However, the chemical environment surrounding the molecular wire is not the only variable that can alter molecular conductance. Dulic *et al.* performed SMC measurements on a series of photochromic molecules and found that the light-induced chemical reactions open new, shorter electron transfer pathways in dithienylcyclopentenes, thus increasing conductance.[110] Similar light-sensitive (optoelectronic) molecular switches have been discussed in the literature from a theoretical point of view,[111–114] and some experimental results[115–117] are so far very

encouraging. As example, Darwish *et al.* recently demonstrated that a spiropyran molecular wire bearing –NO_2 contacts has good switching behaviour upon ring opening induced by UV light or acid-catalysed.[117] The spiropyran – merocyanine photochromic tautomerism is well known in the literature,[118,119] and its fast, reversible behaviour makes it an excellent candidate for future devices.

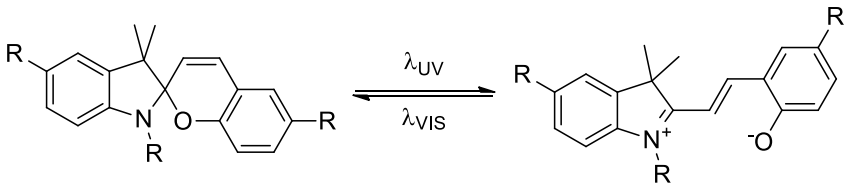

Figure 1.25: Spiropyran – merocyanine photochromic tautomerism

1.7 Thesis Outline

Much effort in making and electrically characterising metal|*molecule*|metal junctions has been devoted to the attainment of the most efficient possible charge transport over long distances, but, although it is expected that the molecular conductance is someway affected by the surrounding environment (interactions with solvents and/or other molecules), very few reports probing this problem actually exist. This issue is addressed in the present thesis, where the conductance of a class of dithiaalkyl-oligothiophene molecular wires and similar systems is measured in the presence of various environments to better understand their behaviour. In Chapter 2 the conductance decay with length of a series of terthiophene molecular wires capped with thioalkyl chains of differing length is presented, with a comparison to similar systems (dithiaalkylbenzene, dithiaalkylviologen and fully saturated alkanedithiols). Weak length dependence is found in the DTB systems, and this is attributed to the presence of the sulphur-promoted contact "gateway" state. Furthermore, the presence of H_2O (as ambient moisture) increases conductance through the terthiophene-containing molecular wire and leads to a very shallow length dependence, while measurements performed in anhydrous environment show smaller conductance and slightly stronger decay with length. Molecular wires whose conductance is not dependent on the presence of moisture show stronger length dependence, but still far from the value measured for fully saturated systems[120] (alkanedithiols), ≈ 1 $Å^{-1}$. In Chapter 3 the temperature dependence of thiopentane capped

oligothiophene molecular wires is discussed: the presence of H_2O triggers the switch from a temperature independent to a thermally activated charge transport, and the effect is stronger as the number of thiophene rings is increased. Measurements performed in air (i.e. in the presence of water) and measurements performed in UHV are presented, and an explanation is given on the basis of coherent tunnelling and thermal broadening of transmission resonance. In Chapter 4 the possibility of "doping" by charge transfer complex formation is discussed: upon complexation of a molecular wire containing appropriate electron donor moieties with a variety of electron accepting molecules a boost in conductance is seen, ranging from a 20 to a 90-fold increase depending on the nature of the donor and acceptor. DFT and transport calculation demonstrated that this boost is caused by an interference feature (a Fano resonance[121]) in the transmission curve that arises after complexation. Due to the nature of such resonances, they are very near to the Fermi level of the metallic leads when the complex is in its optimal geometry, thus increasing the transmission probability and, therefore, molecular conductance. In Chapter 5 and 6, the synthesis and characterisation of the molecular wires used in this thesis and the methodology of STM measurements and data analysis are discussed, respectively. In Chapter 7 some conclusions are drawn and possible future work is outlined.

Alkyl Chain Length Dependence

CHAPTER 2

Nature is pleased with simplicity. And nature is no dummy.

Sir Isaac Newton, 1687.

Simple tunnelling theory predicts that conductance across a nanojunction should decay exponentially with its length, following a relationship $G = Ae^{-\beta L}$, where L is the junction length and A is a pre-exponential factor dependent on junction contacts and nature of metallic leads. The nature of the molecular wire bridging the two metallic leads has a strong effect on the exponential attenuation factor β: as demonstrated by Wold *et al.* in 2002,[120] conjugated molecular wires such as oligophenylene exhibit conductance values that decay with increasing number of phenyl units to the extent of $\beta = 0.41$ Å^{-1}, while alkanedithiols units showed stronger attenuation with increasing length, with $\beta = 0.94$ Å^{-1}. Similar findings were reported in other studies,[122–125] and other conjugated systems such as oligophenyleneimine[34] and oligonaphtalenefluoreneimine[24] showed low attenuation factors of 0.3 Å^{-1} and 0.25 Å^{-1}, respectively. Extremely low values of β were found in systems such as *meso*-to-*meso* bridged oligoporphyrins[38,126,127] (0.040 ± 0.006 Å^{-1}), axially-bridged oligoporphyrins[128] (0.015 ± 0.006 Å^{-1}), oligoynes[129] (0.06 ± 0.03 Å^{-1}), carbodithioate-capped oligophenylene-ethynylene[130] (0.05 ± 0.01 Å^{-1}), and extended viologens[131] (0.006 ± 0.004 Å^{-1}). Oligothiophenes, on the other hand, showed a more complex behaviour, with unusual conductance decay with the number of thiophene rings[99–101] and water-dependent switching.[62] The effect of molecular wire structure on the value of β is still not completely understood, and simple rationalisation using back-of-the-envelope calculations is not enough to completely understand the junction behaviour: comprehensive experiments, detailed modelling and DFT transport computation are needed to take into account complex features introduced by metal | molecule contact, orbital resonances and other quantum mechanical effects that can strongly affect molecular conductance.[40,79,82,101,132,133]

2.1 Background and Scope

Incorporating a conjugated moiety between two insulating barriers is known to promote conductance across the junction by producing a notch (well) in the energy profile,[43,46,134,135] but the effect of both barrier length and nature of the conjugated well on molecular conductance and attenuation factor is still not completely understood. Dithiaalkyl-terthiophene, dithiaalkyl-phenyl and dithiaalkyl-viologen with side-chain length of varying methylene units were synthesised and their conductance in metal | *molecule* | metal junctions

has been measured and compared with published alkanedithiol results,[44,52,53,79,84,136,137] to better understand the nature of charge transport across such systems.

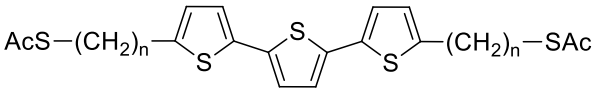

X[T3]X

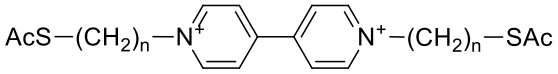

X[V]X

X[Ph]X

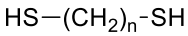

ADT

Figure 2.1: Structures and labelling of molecule classes used in single molecule conductance determination in this chapter. X is the varying sidechain length (nCH_2) and the nature of the central conjugated unit is abbreviated between brackets. Counterions on X[V]X are not shown for clarity.

Measurements were performed in air and under dry argon atmosphere, to confirm the findings of Leary *et al.* (*i.e.* conductance gating promoted by water presence in oligothiophene molecular wires) and test the effect of alkyl chain length and ambient moisture on the attenuation factor in double tunnelling barrier molecular wires.

2.2 Methods

Series of molecular wires (1[T3]1, 3[T3]3, 4[T3]4, 5[T3]5, 6[T3]6, 8[T3]8, 2[V]2, 4[V]4, 6[V]6, 9[V]9, 3[Ph]3, 4[Ph]4 and 6[Ph]6) were synthesised (see Chapter 5 for synthetic procedures) and characterised using common synthetic laboratory techniques. 1[Ph]1 (benzenedimethanethiol) was purchased from Sigma-Aldrich and used as received. All SMC measurements were performed using an STM equipped with a freshly cut Au tip on gold-on-glass slides. The *I(z)* technique has been used to obtain single molecule conductance values, with varying withdrawal rate, setpoint current and bias voltage. Molecules were deposited on flame annealed gold-on-glass substrates by immersion in 10^{-4} M MeOH/EtOH/CH_2Cl_2

(solvent chosen to maximise solubility) solutions for 90 s. The substrates were then rinsed with ethanol and blown dry with a stream of argon before being put in the STM sample holder. An environmental chamber containing a small amount of silica desiccant was used in experiments conducted under dry Ar and the atmosphere chamber was purged for 24 hours before starting the measurements in those cases. Measurement on the B conductance group for the X[Ph]X system were performed by Dr. Carly Brooke during her PhD.[138] Molecular length was calculated using Spartan® '08 (Wavefunction Inc.) molecular modelling software as distance between two gold atoms connected to the sulfur contacts in the lowest energy state. DFT molecular modelling and transport calculations have been performed by Ms. Sara Sangtarash and Prof. Colin Lambert (Lancaster University, UK). See Chapter 6 for detailed information about sample preparation, SMC experimental techniques, theory and data analysis. Experimental data in the form of histograms and 2d "density" plots are presented in Appendix A.

2.3 Results

The first measurements were performed on the X[T3]X system, with side-chain length between 1 and 8 methylene units each, in ambient atmosphere and in solvents (with no effort to exclude environmental water). Each molecule in the 1 - 8 interval showed two distinct conductance groups, as already reported in the literature and generally believed to arise from different contact geometries at the metal|molecule interface.[81,84,139,140] The conductance values decrease from 1[T3]1 to 3[T3]3 to settle on a plateau, with an apparently length-independent conductance at ≈ 0.8 nS and ≈ 0.25 nS (A and B groups respectively). When the side-chain length reaches 6 methylene units (6[T3]6) the conductance start to decrease again and the longest terthiophene-containing molecular wire that has been measured, 8[T3]8, showed two conductance groups at 0.31 ± 0.09 and 0.11 ± 0.03 nS.

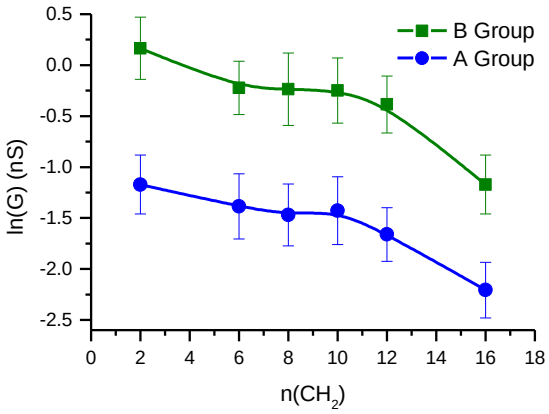

Figure 2.2: Natural logarithm of conductance for X[T3]X in ambient atmosphere *vs* total number of methylene units. Connecting line (b-spline interpolation) as guide for the eyes.

In ambient atmosphere a β value across the whole X[T3]X series of 0.07 ± 0.02 per methylene unit (0.06 ± 0.01 $Å^{-1}$), was calculated from the single molecule conductance data: this value is extremely low if compared with the literature about alkanedithiols, that showed a β of 1.07 - 0.94 per methylene unit[44,79,84] (≈ 1 $Å^{-1}$). Although remarkably low for a non-conjugated junction, values of β of the same magnitude have been reported in the literature for fully-conjugated systems.[38,126–131] The conductance of the X[T3]X molecules was then measured under dry argon atmosphere, and the behaviour observed by Leary *et al.*[62] has been reproduced: after 24 hours of purging, a new set of peaks appeared in the histograms at much lower current.

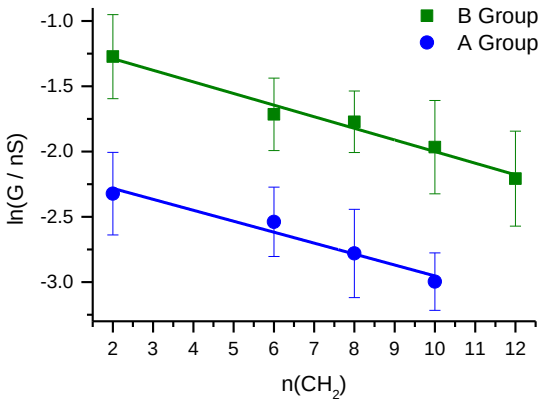

Figure 2.3: Natural logarithm of conductance for X[T3]X under dry Ar *vs* total number of methylene units.

Conductance in the absence of water decreased more consistently with molecular length, albeit still with a low β value of 0.10 ± 0.02 per methylene unit (0.08 ± 0.01 $Å^{-1}$). Measurements on the longer molecular wires in dry atmosphere resulted in a number of noisy traces with low-

current features that did not result in a peak in the histograms: (Leary *et al.* reported a conductance of ≈ 0.01 nS for 6[T3]6 after 24 hours of Ar purge).[62] Conductance values are reported in Table 2.1.

	Length (nm)	G (air) (nS)	G (Ar) (nS)	Appendix Reference
1[T3]1	1.89	1.22 ± 0.36 0.31 ± 0.09	0.28 ± 0.09 0.098 ± 0.031	A.1 / A.7
3[T3]3	2.35	0.80 ± 0.21 0.25 ± 0.08	0.18 ± 0.05 0.079 ± 0.021	A.2 / A.8
4[T3]4	2.49	0.79 ± 0.28 0.23 ± 0.07	0.17 ± 0.04 0.062 ± 0.021	A.3 / A.9
5[T3]5	2.81	0.78 ± 0.25 0.21 ± 0.08	0.14 ± 0.05 0.050 ± 0.011	A.4 / A.10
6[T3]6	2.98	0.69 ± 0.19 0.19 ± 0.05	0.11 ± 0.04 --	A.5 / A.11
8[T3]8	3.46	0.31 ± 0.09 0.11 ± 0.03	-- --	A.6

Table 2.1: Summary of length and conductance values for the X[T3]X system in air and under Ar atmosphere. See appendix A for individual single molecule conductance histograms and density plots.

To better understand the effect of the central conjugated unit and the unusually low β value the dialkylterthiophene system was compared to systems with a different conjugated central unit, namely a single phenyl ring or a viologen (4,4'-bipyridinium), and a varying number of methylene units in the side chains. When the number of methylene units in the side chains is low (2 - 8), the presence of a phenyl ring or a viologen resulted in higher conductance than the corresponding terthiophene-containing molecular wire: as example, measurements on 4[T3]4 resulted in a B group conductance of 0.79 ± 0.28 nS, while 4[Ph]4 and 4[V]4 showed conductance of 1.21 ± 0.19 and 4.41 ± 1.66, respectively. As the number of methylene units in the side chains grows, however, the situation changes, as 6[Ph]6 exhibited a B conductance of 0.82 ± 0.18 nS, very similar (within experimental error) to the value found for 6[T3]6 (0.69 ± 0.19 nS), while 6[V]6 showed much lower conductance, at 0.46 ± 0.12 nS.

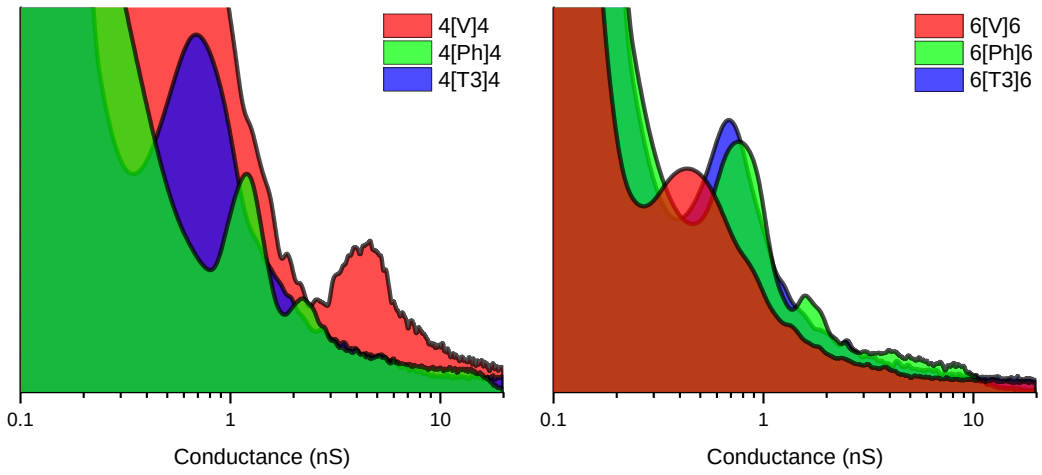

Figure 2.4: Comparison of conductance histograms for the B contact group of 4[X]4 (left) and 6[X]6 (right). A group conductance showed the same trend. Histogram are normalised to the total number of *I(z)* scans. See Appendix A for individual linear histograms and 2d "density" plots.

As result, X[Ph]X showed a higher attenuation factor than X[T3]X, with β = 0.17 ± 0.03 per methylene unit (0.14 ± 0.02 $Å^{-1}$), and measurements on X[V]X resulted in an even higher β of 0.52 ± 0.01 per methylene unit (0.39 ± 0.01 $Å^{-1}$). The dithiaalkyl-viologen system has been the object of theoretical[141] and experimental[43,142] studies, and the published β value is slightly higher, at 0.66 - 0.76 per methylene unit. It must be noted, however, that these published values were obtained using the limited length interval from 5[V]5 to 8[V]8, measured with the *STM-BJ* technique, while the data presented in this thesis spans a significantly larger interval, from 2[V]2 to 9[V]9.

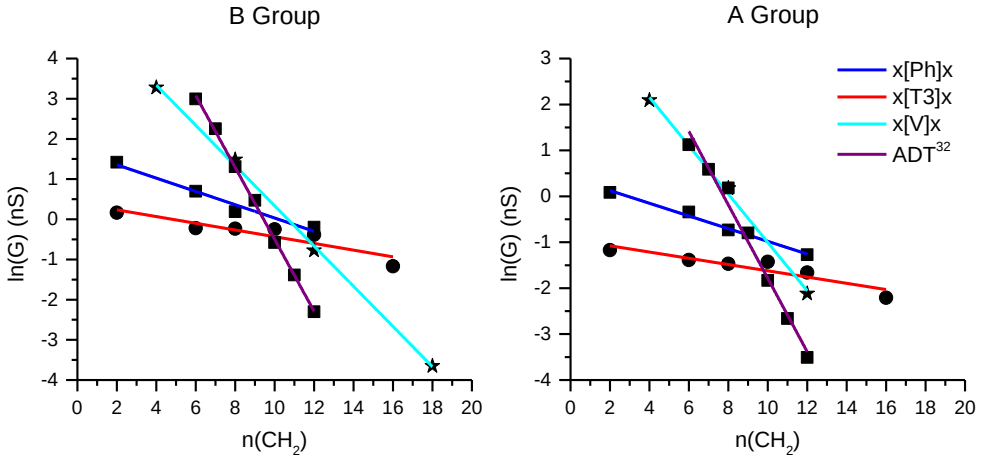

Figure 2.5: Natural logarithm of contact group B (left) and A (right) conductances vs the total number of methylene units for the systems presented in this chapter, in air. Conductances of alkanedithiols as comparison are taken from ref. 32. Error bars are omitted for clarity, and values can be found in Table 2.2.

	Length (nm)	G (air) (nS)	Appendix Reference
1[Ph]1[a]	1.19	4.14 ± 0.58 1.09 ± 0.27	A.12
3[Ph]3[a]	1.67	2.01 ± 0.32 0.71 ± 0.23	A.13
4[Ph]4[a]	1.86	1.21 ± 0.19 0.48 ± 0.15	A.14
6[Ph]6[a]	2.37	0.82 ± 0.18 0.28 ± 0.09	A.15
2[V]2	1.69	26.5 ± 6.3 8.10 ± 1.96	A.16
4[V]4	2.21	4.41 ± 1.66 1.19 ± 0.39	A.17
6[V]6	2.72	0.46 ± 0.12 0.12 ± 0.03	A.18
9[V]9	3.52	0.026 ± 0.008 --	A.19

Table 2.2: Summary of length and conductance values for the X[Ph]X and X[V]X system. See appendix A for individual single molecule conductance histograms and density plots. a) B group measured by Dr. Carly Brooke.[138]

Apart from discrepancies in the numbers, the fact that an indentation in the tunnelling barrier promotes conductance in long molecular wires and reduces attenuation with length is clear, and the nature of the potential well plays a strong role in both. From a simplistic point of view, the more extensive the conjugation, the weaker the conductance decay with length, as terthiophene is the most conjugated moiety and the viologen, in its dication state, has a break in conjugation due to inter-ring torsion.[143] The low attenuation factor could suggest that the electron transfer is non-coherent, similar to a 2-step tunnelling process with the charge residing for a finite amount on time on the potential well,[39] but coherent tunnelling systems with very low β values (< 0.1 $Å^{-1}$) have been reported in the literature for a variety of systems.[38,126–131] Detailed modelling and transport calculation are needed to better understand the mechanism of charge transport in these molecular wires. In order to apply DFT based transport computations the molecules should be short enough so that coherent tunnelling dominates transport.

2.4 Theoretical Calculations

Charge transport across the molecular junctions presented in this chapter was modelled using DFT-NEGF calculations to understand the reasons underlying the observed variation in the tunnelling decay factor. The optimal geometry and ground state Hamiltonian was obtained using the SIESTA[144] code and the phase-coherent, elastic scattering properties of molecular junctions were calculated using the GOLLUM[145] code. Each system consists of a left (source) and right (drain) gold lead, and the scattering region (molecular wire). The transmission coefficient *T(E)* for electrons of energy *E* passing from the source to the drain through the scattering region is calculated *via* the relation:

$$T(E) = Trace(\Gamma_R(E)\, G^R(E) \Gamma_L(E)\, G^{R\dagger}(E)) \qquad \textit{Equation 2.1}$$

In this expression $\Gamma_{L,R}(E) = i\left(\sum_{L,R}(E) - \sum_{L,R}{}^{\dagger}(E)\right)$ describes the level broadening due to the coupling between left (L) and right (R) electrodes and the central scattering region, $\sum_{L,R}(E)$ are the retarded self-energies associated with this coupling and $G^R = (ES - H - \sum_L - \sum_R)^{-1}$ is the retarded Green's function, where *H* is the Hamiltonian and *S* is overlap matrix. The obtained transmission coefficient *T(E)* was used to calculate the conductance *G* = *I*/*V* at finite voltage V, where

$$I = \frac{2e}{h} \int dE\; T(E)\,(f_L(E) - f_R(E)) \qquad \textit{Equation 2.2}$$

for a range of values of E_f, where $f(E) = 1/(1 \pm \exp\frac{E-E_F}{k_B T})$ is the Fermi function of the left (L) or right (R) electrode. Results are shown in Figure 2.6.

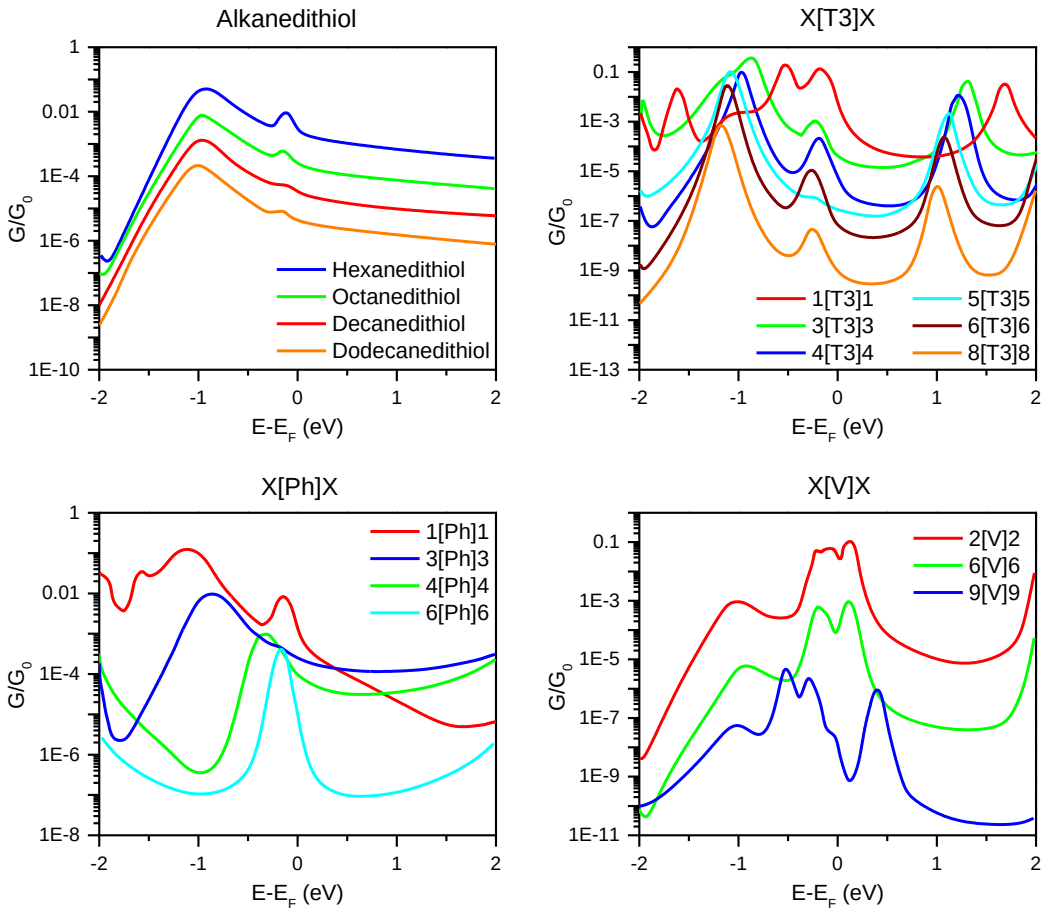

Figure 2.6: Calculated finite-bias conductance *vs* energy plots for the three sets of molecular wires studied in this chapter and alkanedithiols as comparison. Plots calculated at room temperature, with predicted DFT-gap from Kohn-Sham mean field Hamiltonian.

As can be seen in the conductance *vs* energy plots, a small resonance is always present near the Fermi level, but this is not related to any molecular orbital. It is the result of the strong interaction between the sulfur contacts and the gold electrodes, and it has been described in the literature as a "gateway state" or "contact resonance".[82–84] As discussed in the introduction of this thesis, this is an intermediary state, coupling the metallic lead to the molecular backbone through the sulfur orbitals,[83] and it accounts for the higher transmission probability of covalent S-Au contacts. This phenomenon is not limited to thiol contacts, and it has been observed, for example, in junctions with covalent C-Au bonds.[146] In the absence of an indentation in the tunnelling barrier, (*i.e.* alkanedithiols), as the saturated chain increases in length, the gateway state is less pronounced due to contact decoupling from the backbone, as can be seen in the top-left panel of Figure 2.6. When an indentation is present (*i.e.* the DTB systems presented in this chapter), however, coupling between the conjugated central unit and

the two sulfur contacts results in an enhanced contact resonance, and the conductance decay is therefore attenuated. The structure of the molecular wire plays a strong role in the decay factor β because the nature of the central conjugated unit controls the magnitude of the coupling with the sulfur contacts, and its extent of conjugation might be a dominating parameter.

Using the theoretical conductance at the Fermi level, a β value can be calculated. This resulted to be in good agreement with the experimental data, as the same trend, β(ADT) > β(X[V]X) > β(X[Ph]X) > β(X[T3]X), was obtained.

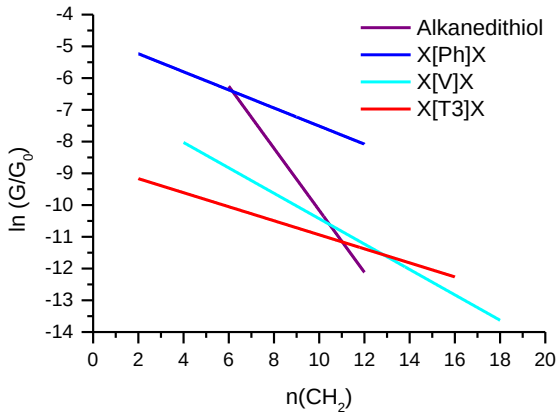

Figure 2.7: Natural logarithm of calculated finite-bias conductance vs total number of methylene units for the systems presented in this chapter, with values calculated for alkanedithiols as comparison. Conductance values obtained from the curves presented in Figure 2.6 at $E - E_F = 0$.

2.5 Conclusions and future work

In this chapter the properties of molecular wires consisting of a conjugated central unit sandwiched between two insulating chains were presented. As described by Leary *et al.*, when then central unit is a terthiophene moiety a water "gating" effect can be seen, with conductance decreasing when ambient atmosphere is replaced with a dry, inert gas. In both cases a shallow decay of conductance with the length of the saturated chains was observed and a comparison with similar systems, namely phenyl- and viologen-containing dithiaalkyl molecular wires, showed a definite trend in the conductance decay, with the terthiophene showing the shallowest and viologen the strongest, approaching the value found for alkanedithiols. DFT and NEGF transport calculations demonstrated that this shallow length dependence is linked to the generation of a gateway state upon Au-S contact in the

transmission curves. Coupling between the sulfur orbitals and the conjugated central unit enhances this gateway state, resulting in the observed reduced conductance attenuation with length. Theoretical calculations are in good agreement with empirical data, as the predicted trend, β(ADT) > β(X[V]X) > β(X[Ph]X) > β(X[T3]X) is the same as the experimentally measured.

Measurements on similar molecular junctions, differing only in the contact nature, will help to shed more light on this particular issue. The use of thioether contacts, which bind to gold through the lone pair on the sulfur atom, should not generate a gateway state in the transmission curves, and as a result the β factor is predicted to be higher. A set of molecular wires consisting of a phenyl ring sandwiched between two alkyl chains with methyl thioether contacts is currently being synthesised, and measurement on this system will be performed to assess the validity of the theory presented in this chapter.

Temperature Dependence

CHAPTER 3

Although nature commences with reason and ends in experience it is necessary for us to do the opposite, that is to commence as I said before with experience and from this to proceed to investigate the reason.

Leonardo da Vinci, ca. 1510.

Measurement of molecular wires conductance performed over a range of temperatures can give useful insights about the mechanism of charge transfer. A thermally activated mechanism, with conductance increasing in inverse proportion to $e^{1/T}$ is generally considered a signature of incoherent hopping, while temperature independent behaviour is associated with coherent tunnelling[32]. This general rule, however, has its exceptions, particularly when a transport resonance lies close to the E_F: the thermal broadening of Fermi function can induce increases in the transmission coefficient[37] and, therefore, in conductance. Furthermore, subsequent incoherent tunnelling mechanisms, as proposed by Kuznetsov and Ulstrup, rely on charge localisation on the redox bridge site during charge transport followed by vibrational relaxation, and have strong temperature dependence.[39] In many cases, experiments alone have been unable to distinguish between mechanisms, and only theoretical modelling and transport calculations can help to discriminate.

Portions of the following chapter have been published in Physical Review B[147] and a journal article on the major findings is currently being written. The results were also presented as a poster[1] at Faraday Discussion 174 (University of Strathclyde, Glasgow, 8 - 10th September 2014).

3.1 Background and Scope

Leary *et al.* demonstrated in 2008 that the conductance of oligothiophene molecular wires decreases upon removal of ambient moisture to an extent dependent upon conjugation length.[62] Furthermore, in the presence of ambient air the conductance of such molecular wires *increases* as the degree of conjugation (the number of thiophene rings) increased[99], which does not accord with a simple tunnelling mechanism of charge transport. Leary *et al.* found that after purging the apparatus with dry argon the conductances fell exponentially as a function of increasing number of thiophene rings, as expected for charge transport *via* a tunnelling or super-exchange mechanism. DFT combined with non-equilibrium Green's function (NEGF) based transport calculations suggested that a weak dipolar interaction of water with the π-

[1]Available online at http://dx.doi.org/10.13140/2.1.3095.2008

bonding thiophene orbitals causes a shift of the LUMO resonance towards the E_F of the Au leads, thus increasing conductance. The shift of transport resonance is more pronounced for the longer molecules, sufficient to offset the decay of conductance with length.

Conductance values of set of bis(pentane-1-thioacetate)oligothiophene molecular wires (Figure 3.1) have been determined in air, argon and UHV[148] and at different temperatures, to investigate whether this conductance boost is due to a change of mechanism of charge transport (from tunnelling to something more akin to hopping) or not. Conductance values for 1,10-decanedithiol (DDT) were determined under the same experimental conditions. Transport through alkanedithiols is generally believed to be *via* a direct tunnelling mechanism, and the large HOMO-LUMO bandgap should result in a temperature independent behaviour, hence serving as a useful control experiment.

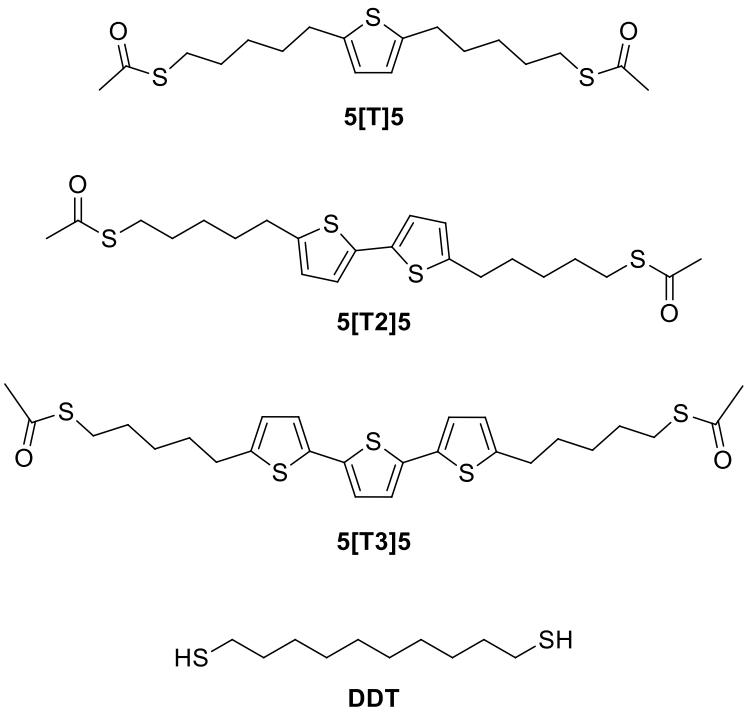

Figure 3.1: Structures and labelling of molecules used in single molecule conductance measurements in the present chapter.

3.2 Methods

5[T]5, 5[T2]5 and 5[T3]5 were prepared and characterised using common synthetic laboratory techniques (see chapter 5 for details about the synthesis). DDT was purchased (Alfa Aesar, USA) and used as received. All the experiments in air or in dry argon atmosphere were

performed using an STM equipped with a freshly cut Au tip. The *I(z)* technique has been used to obtain single molecule conductance values for the bis(pentane-1-thioacetate)oligothiophene system (4 nm withdrawal at 40 nm s^{-1}). Molecules were deposited on flame annealed gold-on-glass substrates by immersion in 10^{-4} M CH_2Cl_2 solutions for 90 s. The substrates were then rinsed with ethanol and blown dry with a stream of argon. A setpoint current (I_0) of 7 nA and a tip bias voltage (V_{BIAS}) of 0.3 V were used throughout all the experiments described in this chapter, giving an initial tip-to-substrate distance z_0 of 0.9 nm as determined by distance calibration. An environmental chamber containing a small amount of silica desiccant was used for the experiments under dry Ar and it was purged for 24 hours before starting the measurements. Variable temperature measurements in air were performed using a Lakeshore 332 temperature controller and a high temperature sample plate equipped with a resistance and a thermocouple control circuit operating in the range 295-523K. Gold samples were mounted on the heated metal plate and left there for 1 hour before starting the measurements to allow the temperature to stabilise. Chapter 6 gives detailed information about sample preparation, SMC experimental techniques, theory and data analysis. Experimental data in the form of histograms and 2d "density" plots are presented in Appendix A. Ultra-High Vacuum (UHV) variable temperature measurements were performed by Dr. Ellis Pires[148] and Dr. Martin Elliott at Cardiff University. The *I(z)* technique was used (I_0 = 0.5 nA, V_{BIAS} = 0.2 – 1.6 V) and single molecule conductance values were determined at 298K and 390K.

Molecular length was calculated using Spartan® '08 (Wavefunction Inc.) molecular modelling software as distance between two gold atoms connected to the sulfur contacts in the lowest energy state. DFT molecular modelling and transport calculations have been performed by Dr. Iain Grace and Prof. Colin Lambert (Lancaster University, UK).

3.3 Results

The bis(pentane-1-thioacetate)oligothiophene set behaved in the same manner observed by Leary *et al.* in bis(hexane-1-thioacetate)oligothiophenes, thus confirming that the potential well is responsible for the unusual behaviour. Conductance in the presence of ambient moisture increases with the number of thiophene rings, with β = -0.03 $Å^{-1}$, while under argon

and UHV it decays exponentially with the length, with $\beta = 0.19$ Å^{-1} and 0.16 Å^{-1}, respectively. Using the *I(z)* technique two distinct contact groups were observed in air and under dry argon (A and B), but only group A (low conductance) could be observed under UHV. See Appendix A for individual SMC plots.

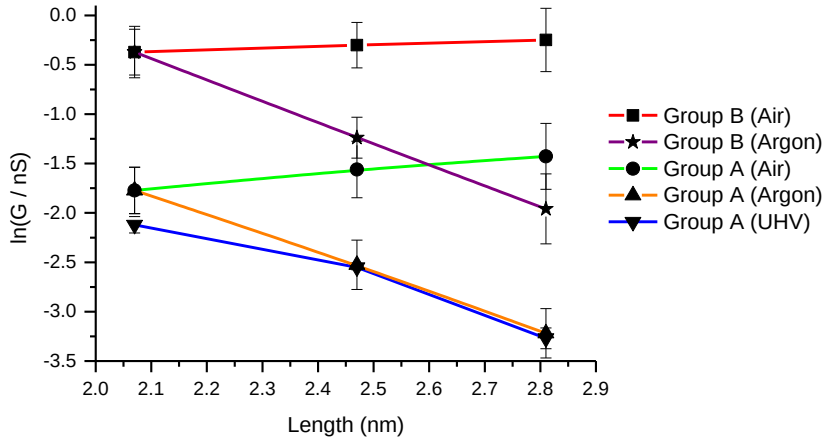

Figure 3.2: Plot of ln(G) vs molecular length for medium and low conductance groups of the three DTB oligothiophene molecular wires in three different environments.

	Length (nm)	G (air) (nS)	G (Ar) (nS)	G (UHV) (nS)	Appendix Reference
5[T]5	2.07	0.69 ± 0.16 (B) 0.17 ± 0.04 (A)	0.69 ± 0.18 (B) 0.17 ± 0.04 (A)	0.12 ± 0.08 (A)	A.20 / A.23
5[T2]5	2.47	0.74 ± 0.17 (B) 0.21 ± 0.06 (A)	0.29 ± 0.06 (B) 0.08 ± 0.02 (A)	0.078 ± 0.002 (A)	A.21 / A.24
5[T3]5	2.81	0.78 ± 0.25 (B) 0.24 ± 0.08 (A)	0.14 ± 0.05 (B) 0.04 ± 0.01 (A)	0.038 ± 0.004 (A)	A.4 / A.10

Table 3.1: Summary of length and conductance values for the DTB oligothiophene system in the investigated environments at room temperature (295 ± 1 K).

Measurements over a range of temperatures performed in air (*i.e.* with water present) led to the observation of a thermally-activated behaviour in 5[T2]5 and 5[T3]5, but 5[T]5 showed activationless charge transport.

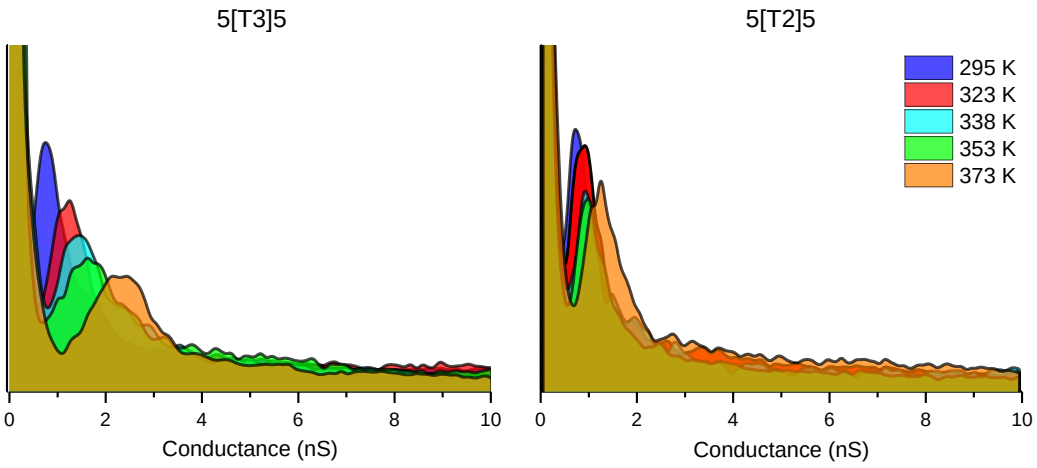

Figure 3.3: Conductance histograms obtained over a range of temperatures (295 – 373 K) for 5[T3]5 (left) and 5[T2]5 (right). Histograms are normalised to the number of *I(z)* scans. See Appendix A for individual histograms and 2d "density" plots.

Temp. (K)	5[T]5 (A) (nS)	5[T]5 (B) (nS)	5[T2]5 (A) (nS)	5[T2]5 (B) (nS)	5[T3]5 (A) (nS)	5[T3]5 (B) (nS)
295	0.17 ± 0.04	0.69 ± 0.14	0.21 ± 0.05	0.74 ± 0.17	0.24 ± 0.08	0.78 ± 0.25
323	0.16 ± 0.04	0.67 ± 0.15	0.26 ± 0.07	0.93 ± 0.21	0.33 ± 0.10	1.29 ± 0.38
338	0.16 ± 0.04	0.69 ± 0.14	0.30 ± 0.06	1.01 ± 0.26	0.38 ± 0.09	1.49 ± 0.39
353	0.17 ± 0.05	0.67 ± 0.15	0.32 ± 0.07	1.05 ± 0.27	0.49 ± 0.14	1.75 ± 0.59
373	0.17 ± 0.04	0.70 ± 0.2	0.38 ± 0.09	1.33 ± 0.31	0.59 ± 0.15	2.34 ± 0.65
Appendix Reference	A.24		A.25		A.26	

Table 3.2: Summary of conductance values for the bis(pentane-1-thioacetate)oligothiophene system measured over a range of temperatures (295 – 373 K) in air.

The temperature-dependent data was plotted in the form of an Arrhenius plot (Figure 3.4) to obtain activation energy values (E_a) of 0.08 eV for 5[T2]5 and 0.13 eV for 5[T3]5. These values are the same for both the conductance groups of each molecule, thus ruling out the possibility of contact contribution to the thermal activation. Furthermore, similar variable temperature measurements performed on DDT showed no temperature dependence, as expected from a molecule known to conduct *via* direct tunnelling through a single potential barrier (see Appendix A, paragraph A.27 for conductance data).

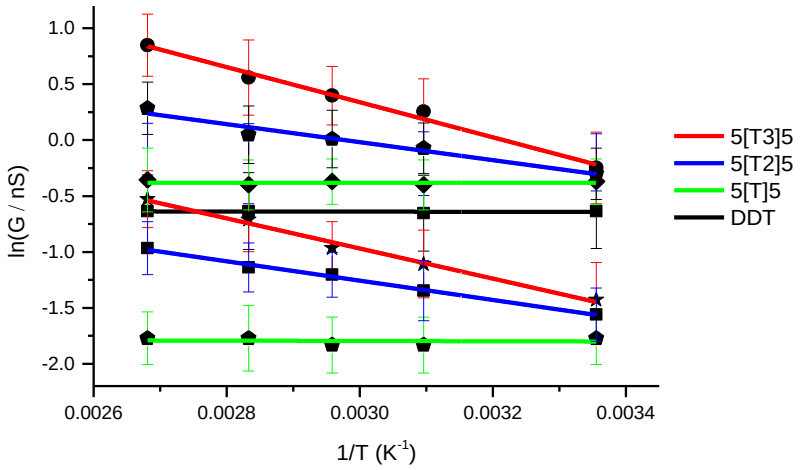

Figure 3.4: Arrhenius plot for the bis(pentane-1-thioacetate)oligothiophene molecular wires set expressed as ln(G) vs T^{-1}. Activationless DDT as control experiment is included in the plot (black line).

No measurements at different temperature could be performed under dry argon atmosphere because the variable temperature sample plate could not be fitted inside the environmental chamber. High temperature measurements performed in Cardiff under UHV (*i.e.* no water present) showed no thermal activation in any oligothiophene molecule.[148]

An increase in conductance upon exposure to ambient moisture and transition from activationless to thermally activated charge transport might suggest that the presence of water "gates" the conductance mechanism to a more efficient incoherent hopping or sequential multistep tunnelling pathway, perhaps by solvating the charged oligothiophene intermediate. However, as discussed earlier, the broadening of transport resonances can explain the temperature dependence consistent within a coherent tunnelling mechanism,[37,38] given that these resonances lie close to E_F. Detailed molecular modelling and transport calculations are therefore required to further examine this issue.

3.4 Theoretical Calculations

Phase-coherent tunnelling should be the dominant mechanism of charge transport for molecular wires shorter than ≈ 4 nm, as suggested by experimental conductance measurements. Therefore a simple explanation such as switching of charge conductance mechanism to thermally-activated incoherent hopping is unlikely, and a set of calculations on the series of molecular wires presented in this chapter was performed using the GOLLUM[145]

transport code and the DFT SIESTA[144] code. Using an extended molecule approach the electron transmission coefficient was computed both in vacuum and water for the three different length molecules. As discussed in the previous chapters, a number of molecular orbital resonances appear in these curves as sharp peaks. As example, in Figure 3.6, left panel, the HOMO resonance can be seen at negative values of $E - E_F$, and the LUMO resonance at positive values. To introduce water into the junction environment a 'solvation shell' of water molecules was placed around the central unit of the molecule, with 2 water molecules per thiophene.

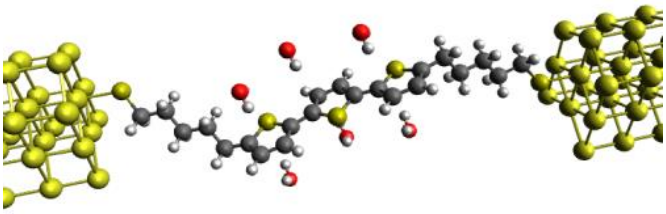

Figure 3.5: Water solvation shell around 5[T3]5 contacted between two gold electrodes.

The zero temperature transmission coefficient *T(E)* was evaluated for each oligothiophene molecule in the series 5[T]5 – 5[T3]5, both in vacuum and in water. In 5[T]5, the shortest oligomer, the presence of water causes a shifting of the HOMO resonance away from the Fermi energy (0 eV) due to the gating effect of the water solvation shell, but the conductance remains essentially unchanged. As the transport resonances broaden with increasing temperature, the temperature dependence can be evaluated using the formula

$$G(E_F) = \frac{2e^2}{h}\int_{-\infty}^{\infty} dE\, T(E)\left(-\frac{df(E,E_F)}{dE}\right) \qquad \textit{Equation 3.1}$$

Where *f* is the Fermi Dirac distribution function and *–df/dE* is the thermal broadening function. Transmission curves at temperatures in the interval 295 – 370 K were calculated, and no temperature dependence was predicted in both environments. The calculated transmission coefficient *T(E)* (probability for a single electron to go through the potential barrier) is plotted *vs* the energy in transmission curves.

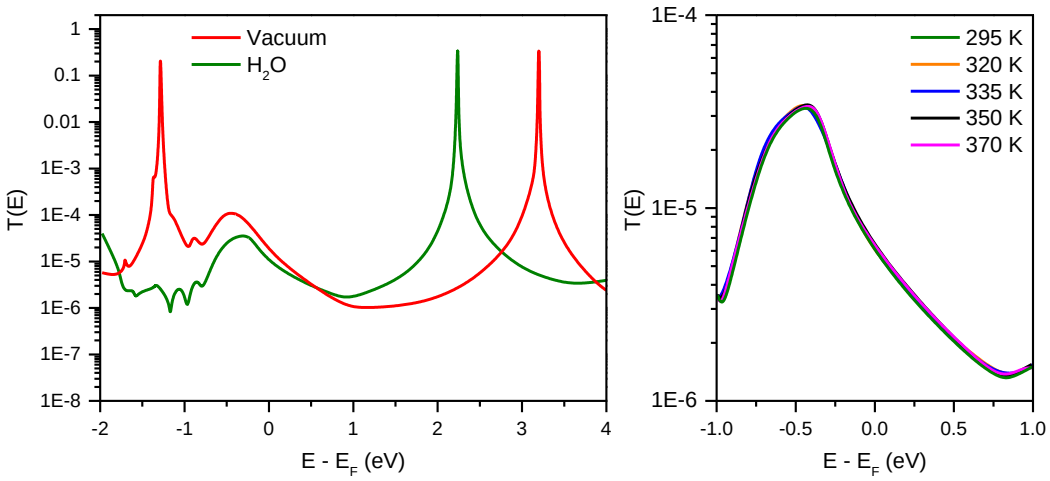

Figure 3.6: Transmission curves at 0 K (left) for 5[T]5 in vacuum and with a water solvation shell. Closeup of the -1 – 1 eV region (right), with transmission curves calculated in the presence of a water solvation shell, over a range of temperatures.

The same procedure was repeated for 5[T2]5 and 5[T3]5, and in these cases the presence of a water shell surrounding the terthiophene central unit shifts the LUMO resonance close to the Fermi level, leading to an increase of the conductance, and the presence of more water molecules produces a larger gating effect. As can be seen in Figure 3.7 for 5[T3]5, now a transport resonance is close to the Fermi level and its thermal broadening causes an increase in the transmission function at 0 eV. As a result, temperature dependence is predicted in the presence of water for 5[T2]5 and 5[T3]5, in agreement with the experimental results.

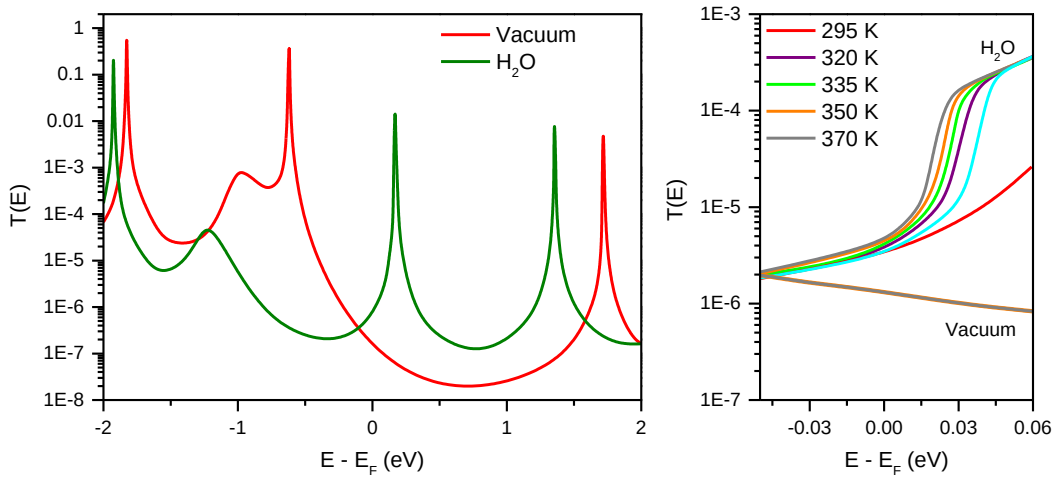

Figure 3.7: Transmission curves at 0 K (left) for 5[T3]5 in vacuum and with a water solvation shell. Closeup of the -0.05 – 0.06 eV region (right), with transmission curves calculated in the presence of a water solvation shell and in vacuum, over a range of temperatures.

3.5 Control Experiment: Temperature dependence of 6[Ph]6

As additional control experiment, the conductance of 6[Ph]6, another double tunnelling barrier molecular wire, has been measured over a range of temperatures. This is more similar to the dipentyl-oligothiophene system than 1,10-decanedithiol as it has an indentation in the tunnelling barrier (a phenyl ring), but showed no conductance change upon removal of ambient moisture.[149] No transport resonances are close enough to the Fermi level for their thermal broadening to have any effect.

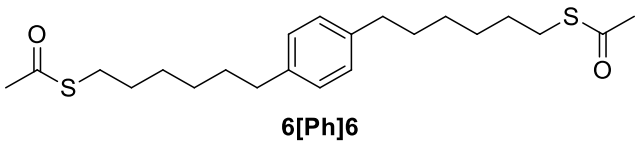

6[Ph]6

Figure 3.8: Structure of 6[Ph]6

Measurements performed over a range of temperatures in air showed no temperature dependence, as expected for coherent charge transport such as direct tunnelling or superexchange.

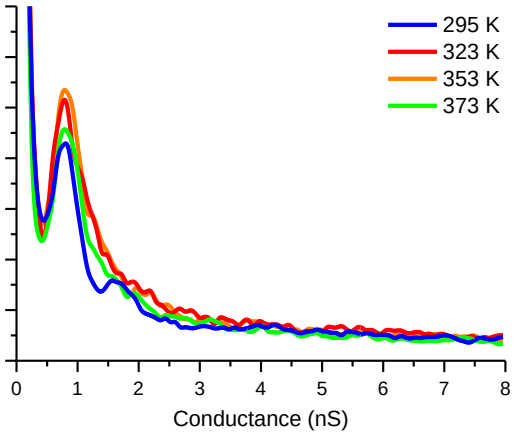

Figure 3.9: Comparison of histograms obtained at different temperatures for the 6[Ph]6 molecular wire.

3.6 Conclusions

In this chapter the effect of water and temperature on a series of oligothiophene molecular wires, with a number of thiophene rings between 1 and 3, was presented. Single-molecule conductance experiments are generally performed without rigorous exclusion of ambient

moisture in the STM chamber or in the solvent used in the STM cell. The solvent or the presence of water can however have a dramatic effect both on the conductance of molecular junctions and on their T-dependence. The molecular wires with more than one thiophene ring in their structure showed conductance several times lower when water was removed from the system and thermally-activated charge transport. Measurements in UHV confirmed the conductance values and showed activationless charge transport in the absence of H_2O. Theoretical calculations within a phase-coherent tunnelling theory explained the observed behaviour: the presence of a water solvating shell surrounding the central oligothiophene systems triggers a shift of the transport resonances to lower energies. In 5[T]5, with a single thiophene ring that can be solvated, the shift is less pronounced and it does not lead to an increase in conductance. Resonances in 5[T2]5 and 5[T3]5, on the other hand, exhibit bigger shifts upon water solvation, and this results in a conductance increase as the LUMO resonance is moved close to the Fermi level. This same effect is responsible for the observed thermally-activated charge transport. Thermal broadening of transport resonances increase the transmission coefficient at E_F, and the conductance increases following the relationship

$$lnG \propto T^{-1} \qquad \textit{Equation 3.2}$$

In vacuum the three molecular junctions have no resonance close enough to E_F to produce observable temperature dependence. However, in the presence of a solvating shell significant temperature dependence is apparent in 5[T2]5 and 5[T3]5, with activation energy proportional to the number of thiophene rings.

Charge Transfer Complexation

CHAPTER 4

Science is simply common sense at its best, that is, rigidly accurate in observation, and merciless to fallacy in logic.

Thomas Henry Huxley, *ca.* 1880

In the early 1950s the discovery at Bell Laboratories that treatment of polycyclic aromatic compounds (asphaltenes) with halogens forms surprisingly conductive organic materials initiated the systematic study of the electrical properties of these charge transfer (CT) complexes. In particular, the treatment of perylene with bromine resulted in the formation of a highly conductive (≈ 1 S m^{-1}) black crystals,[150] and treatment with iodine resulted in even more conductive (≈ 12 S m^{-1}) brown material.[151] The development of stronger molecular acceptors, such as tetracyanoquinodimethane[152] (TCNQ) and tetracyanoethylene[153] (TCNE), and of donors such as tetrathiafulvalene[154] (TTF), permitted important discoveries, such as the first molecular metal[155] (the charge transfer salt TTF:TCNQ) and the first molecular low-temperature superconductor or Bechgaard salt[156] ($[TMTSF]_2:PF_6$; TMTSF = tetramethyltetraselenofulvalene).

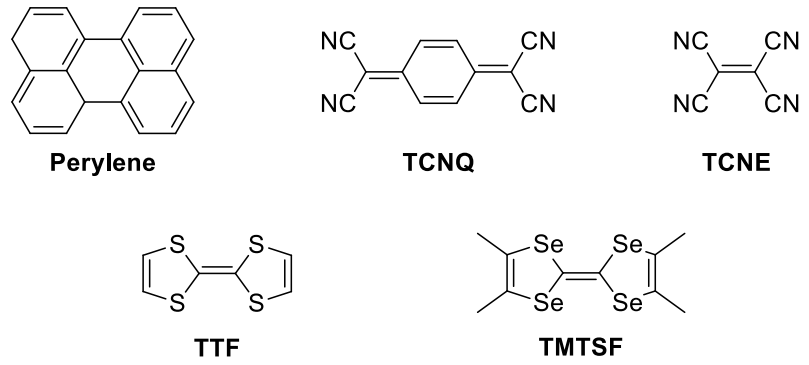

Figure 4.1: Structure of important donors and acceptors

Given the impressive properties of charge transfer complexes in the crystalline solid state, it is of great interest to study and comprehend the effect of CT complexation on *single* molecules, and following the research originally performed by Kasibhatla *et al.*, an effect on conductance of molecular junctions is expected.[108]

4.1 Properties of Charge Transfer Complexes

A charge transfer complex is defined in the IUPAC Gold Book as "*An electron-donor/electron-acceptor complex, characterised by electronic transition(s) to an excited state in which there is a partial transfer of electronic charge from the donor to the acceptor moiety*".[157] Therefore, in such a complex, a fraction of electronic charge is transferred between the molecular entities and the resulting electrostatic attraction provides a stabilising force. There is no stable chemical bond

between the donor-acceptor pair and the interaction is much weaker than covalent or ionic interactions. Transition into excited electronic states usually occurs in the visible region of the electromagnetic spectrum and these complexes are often intensely coloured. These optical absorption bands are usually referred to as CT (charge transfer) bands.

The absorption wavelength of CT bands is characteristic of the specific type of donor and acceptor entities, and it is directly related to the overall energy balance ΔE, that is the energy gained upon spontaneous charge transfer. It is defined as:

$$\Delta E = E_A - E_I + J \qquad \textit{Equation 4.1}$$

Where E_A is the electron affinity of the acceptor, E_I is the ionisation potential of the donor and J is the resulting electrostatic attraction between the two molecular entities.[158]

Since charge transfer complexes are formed by weak association of molecules, the association occurs in a chemical equilibrium with the independent donor (D) and acceptor (A)

$$D + A \rightleftharpoons DA \qquad \textit{Equation 4.2}$$

The intensity of charge transfer bands in the absorbance spectrum is strongly dependent on the equilibrium constant of this association reaction, and several methods have been developed to determine its value from spectroscopic data. The first and still more used procedure is called the Benesi-Hildebrand method, and it requires the measurement of absorption intensity of CT bands as a function of the concentration of donor and acceptor components in solution.[159]

For a 1:1 donor-acceptor complex, K_{DA} is

$$K = \frac{[DA]}{([A] - [DA])([D] - [DA])} \qquad \textit{Equation 4.3}$$

Where [DA] is the concentration of the complex, [A] is the concentration of free acceptor and [D] is the concentration of free donor. ε (extinction coefficient of the complex), according to Beer-Lambert-Bouger law is

$$\varepsilon = \frac{A}{[DA]l} \qquad \textit{Equation 4.4}$$

Where A is the absorbance of the charge transfer complex and l is the optical pathlength in cm. Equation 1.4 can be reformulated as

$$[DA] = \frac{A}{\varepsilon l} \qquad \textit{Equation 4.5}$$

Assuming a pathlength of 1 cm, substitution of [DA] in equation 4.3 with equation 4.5 leads to an expression relating the association constant to the absorbance of the complex

$$\frac{[A][D]}{A} = \frac{1}{K_{DA}\varepsilon} + \frac{[D]}{\varepsilon} \qquad \textit{Equation 4.6}$$

Therefore, by measuring the absorbance of the complex over a range of donor concentrations, a plot of [A][D]/A vs [D] should yield a straight line of slope 1/ε and intercept $1/K_{DA}\varepsilon$.[160] This procedure is only an approximation and is only valid where the CT band of the complex is in a spectral region where none of the other components of the mixture absorbs.[161]

4.2 Background and Scope

It has been discussed in Chapter 2 and 3 that oligothiophene-containing molecular wires conductance is strongly dependent on the environment. DFT calculations showed that the weak dipolar interaction between water and the thiophene π-bonding orbital causes a shift of the LUMO transmission resonances towards E_F of the metallic leads, thus increasing conductance and offsetting the decay of conductance with length. Charge transfer complexation of such molecular wires with appropriate electron acceptors could conceivably have an even stronger effect. Simple oligothiophenes (α-bithiophene, α-terthiophene, α-quaterthiophene) readily form charge transfer complexes with a wide array of acceptors, such as TCNE,[162] TCNQ,[163] I_2,[164] and treatment of poly(3-hexylthiophene) with F_4TCNQ formed a stacked CT system with an increase in conductivity of up to 5 orders of magnitude.[165] Interactions with electron acceptor are also found in benzene and its substituted analogues,[159] and a pioneering STM study on *single* complexes demonstrated an effect on the electrical properties upon interaction with TCNE.[108]

A series of molecular wires (Fig 4.1) has been therefore synthesised and their conductance values have been measured in the presence of a variety of electron acceptors (see Figure 4.2) using a variety of complementary techniques (*I(z)*, *I(t)* and *STM-BJ*) to investigate whether charge transfer complexation has an effect on junction conductance. A control experiment using 1,10-decanedithiol (DDT) in the presence of TCNE has been performed to rule out

interaction of the electron acceptor with the gold leads or the sulfur contacts (there is no electron-donating site in such a molecule).

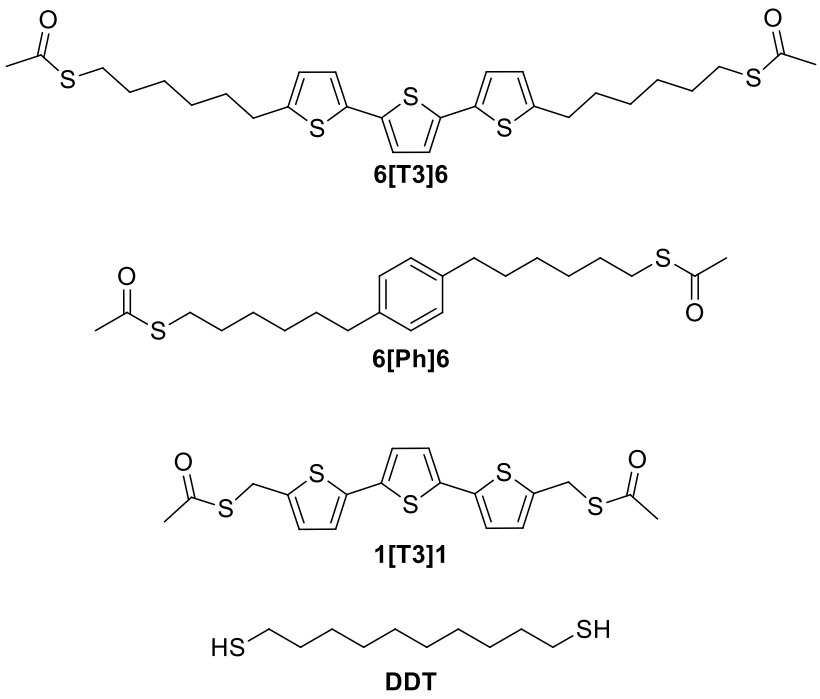

Figure 4.2: Structure and labelling of molecular wires used in SMC measurements in the present chapter.

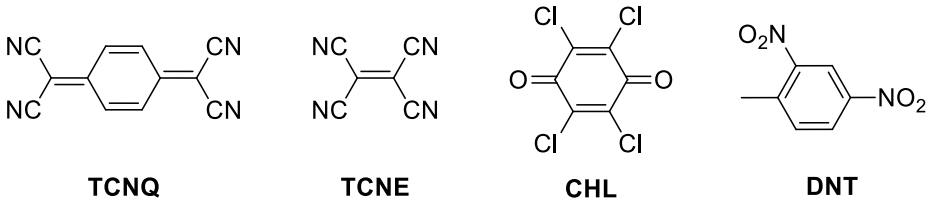

Figure 4.3: Structure and labelling of electron accepting compounds used to form charge transfer complexes with the molecular wires. CHL = Chloranil or tetrachloro-*p*-benzoquinone – DNT = 2,4-dinitrotoluene

4.3 Methods

6[T3]6, 1[T3]1 and 6[Ph]6 were prepared and characterised using common synthetic laboratory techniques (*see* chapter 5 for synthetic methodology and characterisation). DDT was purchased (Alfa Aesar, USA) and used as received. 1,2,4-trichlorobenzene (TCB), TCNE, TCNQ, I_2, chloranil and DNT were purchased from Sigma-Aldrich and purified according to literature[166] prior to use.

UV-Vis spectra were recorded in CH_2Cl_2 on a double beam Perkin Elmer Lambda25 spectrophotometer, operating in the region 50000 - 9000 cm^{-1} using a 1 cm quartz cell at room temperature. 1,4-diethylbenzene has been used as surrogate for 6[Ph]6 in the Benesi-Hildebrant procedure.

All SMC measurements were performed using an STM equipped with a freshly cut Au tip on gold-on-glass slides.

A variety of techniques (*STM*-BJ, *I(z)* and *I(t)*) has been used to obtain single molecule conductance values for the isolated molecules and their charge transfer complexes: see chapter 6 for details about sample preparation, SMC experimental techniques and data processing. Conductance of CT complexes has been measured either in solution (1 mM dopant in TCB) or in air. The iodine complex with 6[T3]6 had to be measured in air as free iodine etches gold surfaces,[167,168] thus making the STM too unstable to perform any measurement. The complex was therefore formed in solution (10^{-4} 6[T3]6, 10^{-3} I_2 in CH_2Cl_2) and deposited on gold by immersion (90 s). A control experiment using the 6[T3]6:TCNE complex under the same conditions has been performed to assess the possibility of measuring such complexes in air.

Molecular length was calculated using Wavefun Spartan® '08 molecular modelling software as distance between two gold atoms connected to the sulphur contacts in the lowest energy state.

DFT molecular modelling and transport calculations have been performed by Dr. Iain Grace and Prof. Colin Lambert (Lancaster University, UK).

4.4 Experimental Results

4.4.1 TCNE Charge Transfer Complexation of 6[T3]6 and 6[Ph]6

To assess the effect of CT complexation, a first experiment using 6[T3]6 as "donor" molecular wire and TCNE as "acceptor" dopant has been performed. Conductance of 6[T3]6 in pure 1,2,4-trichlorobenzene (TCB) has been measured using the *STM-BJ* technique using a bias voltage of 0.1 V. The experiment has then been repeated introducing 1 mM TCNE in the solvent, collecting the same amount (500) of scans showing molecular bridge formation (i.e.

discarding only scans showing plain snap-back and current exponential decay) without any further data selection. Results are shown in Figure 4.4.

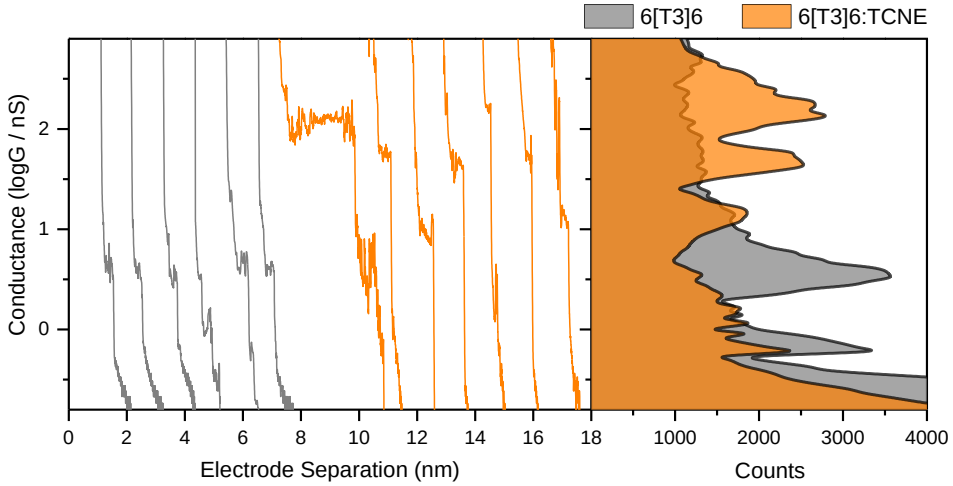

Figure 4.4: Representative *I(z)* traces (left) and logarithmic conductance histogram (right, binsize = 0.03 log G) for 6[T3]6 in pure TCB (grey) and in 1 mM TCNE in TCB (orange). Each histogram is obtained from 500 scans. *STM-BJ* technique, 0.1 V tip bias.

The histogram for 6[T3]6 alone shows only 2 peaks, of conductance 0.63 ± 0.21 and 3.46 ± 0.89 nS, and the noise level for the experimental conditions is between 0.2 and 0.3 nS. As previously discussed, molecular wires with thiol contacts usually show three sets of conductance values arising from different Au-S coordination, and using the less noisy *I(z)* technique, a third, lower conductance value (0.19 ± 0.05 nS) has been measured (see Table 4.1). Upon exposure to 1 mM TCNE, three new high conductance features appear in the histogram, and these have been attributed to charge transport through the 6[T3]6:TCNE CT complex. Each contact group (A, B and C), for both the isolated molecule and the complex (in solution and in air) with TCNE has been also individually characterised using different techniques, and the results are reported respectively in Table 4.1 and Table 4.2.

	6[T3]6 in Air[a] (nS)	6[T3]6 in TCB[a] (nS)	6[T3]6 in TCB[b] (nS)
G_A	0.19 ± 0.05	0.20 ± 0.05	--
G_B	0.69 ± 0.19	0.69 ± 0.16	0.63 ± 0.21
G_C	3.18 ± 0.79	3.38 ± 0.88	3.46 ± 0.89
Data Reference	A.5	A.29	Figure 4.4

Table 4.1: Summary of conductance values for 6[T3]6 in various environments. a) measured in TCB as isolated contact groups with different techniques (see Appendix A for SMC data). b) measured in TCB with the *STM-BJ* technique without data selection.

	6[T3]6 1 mM TCNE in TCB[a] (nS)	6[T3]6 1mM TCNE in TCB[b] (nS)	6[T3]6:TCNE in Air[a] (nS)
G_A	12.7 ± 3.5	13.8 ± 3.6	11.9 ± 2.9
G_B	43.9 ± 10.7	45.7 ± 12.1	44.2 ± 11.8
G_C	143 ± 22	138 ± 28	151 ± 36
Data Reference	A.30	Figure 4.4	A.31

Table 4.2: Summary of conductance values for the 6[T3]6:TCNE complex in various environments. a) measured as isolated contact groups with different techniques (see Appendix A for SMC data). b) measured in TCB with the *STM-BJ* technique without data selection.

On average, a 60-fold enhancement in molecular conductance is promoted by CT complexation of 6[T3]6 with TCNE. To rule out the possibility that interaction of TCNE with other parts of the molecular junction (Au-S contacts, Au leads, etc.) contribute to this conductance boost, a series of control experiments has been performed. First, *STM-BJ* and *I(z)* measurements were performed on a bare gold slide in the presence of 1 mM TCNE in TCB, but no plateaux could be seen in the current-distance traces, as evidence that, although having potential contact groups (-CN), TCNE is unable to form stable junctions. Second, the conductance of 1,10-decanedithiol has been measured in the presence of 1 mM TCNE in TCB, without evidence of conductance boost (i.e. new features at high G values did not appear in the current-distance traces and conductance histograms). Finally, *I(t)* measurements confirmed the conductance boost through the spontaneous formation of highly conductive molecular junctions, with results consistent with the previous measurements. The complex has also been characterised using UV-Vis spectroscopy, and the results are shown in Figure

4.5: treatment of 2 mM 6[T3]6 with 2 equivalents of TCNE in CH_2Cl_2 resulted in the formation of a band in the visible spectrum at 850 nm. This is at a lower energy than for the TCNE complex of 5,5'-dimethyl-2-2'-bithiophene (650 nm)[164] or α-terthiophene (765 nm)[163] as expected since 6[T3]6 is more conjugated than the bithiophene derivative and more electron rich than unfunctionalised terthiophene.

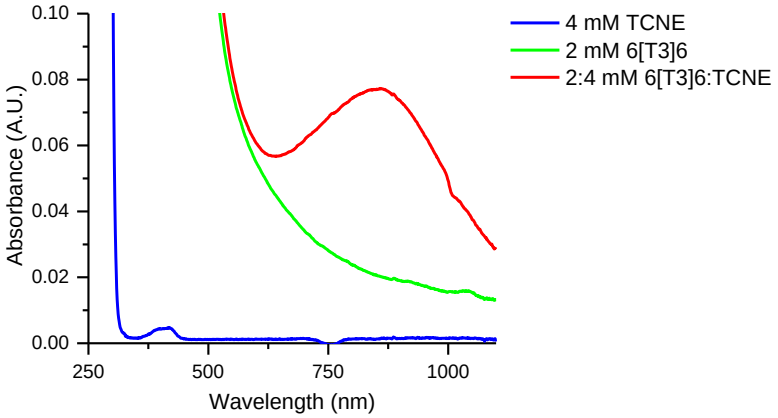

Figure 4.5: UV-Vis spectrum of 6[T3]6:TCNE compared with spectra of its components.

Benzene and its derivatives are known to form CT complexes with appropriate acceptors, and a set of experiments aimed at assessment of the electrical and optical properties of a dialkylbenzene molecular wire, 6[Ph]6, has been performed. Conductance of 6[Ph]6 alone and in the presence of TCNE has been measured under the same conditions employed in the characterisation of Au|6[T3]6|Au junctions (*STM-BJ* technique, 0.1 V tip bias) and the resulting histograms are shown in Fig 4.6. As seen in the 6[T3]6:TCNE system, upon treatment with 1 mM TCNE in TCB, three new peaks appear in the conductance histogram of 6[Ph]6, and these feature have been attributed to the effect of charge transfer complexation. The logarithmic histogram for 6[Ph]6 alone shows only two peaks, relative to the group B and C conductance: group A conductance is lost in the instrumental noise and has therefore been measured using the less noisy *I(z)* technique.

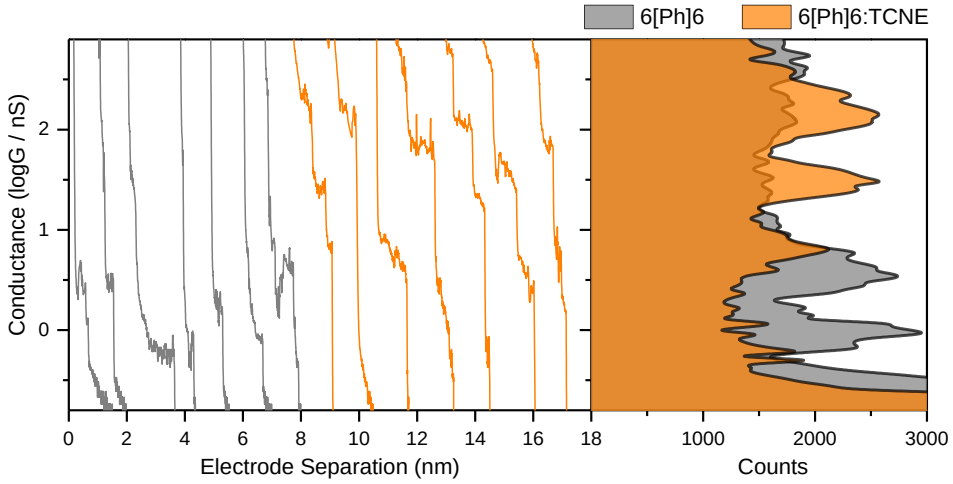

Figure 4.6: Representative I(z) traces (left) and logarithmic conductance histogram (right, binsize = 0.03 log G) for 6[Ph]6 in pure TCB (grey) and in 1 mM TCNE in TCB (orange). Each histogram is obtained from 500 scans. *STM-BJ* technique, 0.1 V tip bias.

As can be inferred from the histograms, CT complexation promotes an average 25-fold conductance boost across the three contact groups.

	6[Ph]6 TCB[a] (nS)	6[Ph]6 TCB[b] (nS)	6[Ph]6 1 mM TCNE in TCB[a] (nS)	6[Ph]6 1mM TCNE in TCB[b] (nS)
G_A	0.28 ± 0.09	--	--	6.41± 1.98
G_B	0.82 ± 0.18	0.89 ± 0.18	18.3 ± 5.1	22.6 ± 7.4
G_C	3.32 ± 0.88	3.46± 0.90	93 ± 27	112 ± 24
Data Reference	A.36	Figure 4.6	A.37	Figure 4.6

Table 4.3: Summary of conductance values for the 6[Ph]6 and its TCNE complex. a) measured as isolated contact groups with different techniques (see Appendix A for SMC data). b) measured in TCB with the *STM-BJ* technique without data selection.

The complex has also been characterised *via* UV-Vis spectroscopy, and a full Benesi-Hildebrand analysis could be performed. 1,4-Diethylbenzene (DEB) has been used as surrogate because these analyses require large amounts of electron-donor compound that proved difficult to synthesise. On adding TCNE to a solution of DEB in CH_2Cl_2, an orange colour was seen due to charge transfer complex formation. UV-Visible spectra were acquired of mixtures of DEB and TCNE as a function of concentrations of the components, to enable the equilibrium constant for complexation (K_C) and the molar extinction coefficient (ε), of

the CT peak to be determined by extrapolation. Two bands, a main peak at 420 nm and a shoulder at 490 nm, were responsible for the orange colour, and analysis of the main peak absorbance as a function of donor and acceptor concentrations (see paragraph 4.1) gave K_{DA} = 2.7 and ε_{CT} = 500 dm^3 mol^{-1} cm^{-1}.

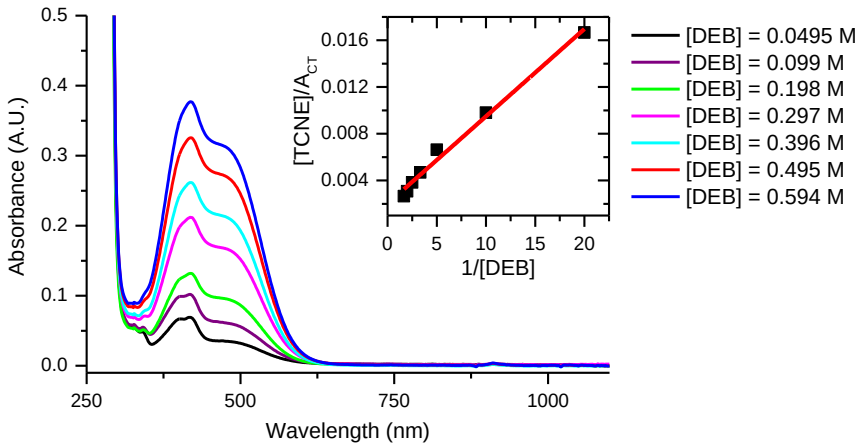

Figure 4.7: Spectral changes attendant upon the incremental addition of DEB to TCNE, with Benesi-Hildebrand plot displayed as inset. [TCNE] is constant in all spectra, 1.01 mM.

It should be noted that the Benesi-Hildebrand method is only an approximation and is only valid where the minority species (in this case, TCNE) is largely complexed. Therefore, by discarding the two points where [DEB] is lowest (and hence the first criterion is least likely to be met) the extrapolated K_{DA} = 0.5 and ε_{CT} = 1500 dm^3 mol^{-1} cm^{-1}. This procedure could not be used to determine K_{DA} and ε_{CT} for 6[T3]6:TCNE since, as can be seen in Figure 4.5, the CT absorption partly overlaps with the low-energy side of the terthiophene π-π^* absorption.

4.4.2 Effect of Other Dopants on 6[T3]6 Molecular Conductance

Several other π- and σ-acceptor molecules have been tested to check whether a conductance boost could be observed on 6[T3]6, and the results are reported in Table 4.3 (TCNE effect discussed earlier as comparison).

	6[T3]6[a] (nS)	Iodine[b] (nS)	CHL[c] (nS)	DNT[c] (nS)	TCNE[c] (nS)	TCNQ[c] (nS)
G_A	0.20 ± 0.05	7.49 ± 1.71	8.31 ± 1.85	9.59 ± 2.61	12.7 ± 3.5	18.1 ± 4.5
G_B	0.69 ± 0.16	27.6 ±7.8	33.9 ± 8.0	35.7 ± 9.5	43.9 ± 10.7	56.7 ± 14.6
G_C	3.38 ± 0.88	89.8 ±15.4	110 ± 19.2	112 ± 28	143 ± 22	225 ± 54
Boost	--	≈ 35x	≈ 40x	≈ 45x	≈ 60x	≈ 85x
Data Reference	A.29	A.35	A.33	A.32	A.30	A.34

Table 4.4: Summary of conductance values for the 6[T3]6 charge transfer complexes measured as isolated contact groups using the *I(z)* and *STM-BJ* technique. a) measured in TCB b) measured in Air c) measured in TCB with 1 mM concentration. Conductance boosts are expressed as average across the three conductance groups, rounded to the nearest multiple of 5. See Appendix A for SMC data.

Complexes prepared using 6[T3]6 and chloranil (CHL), TCNE or TCNQ showed conductance boost (upon complexation) proportional to the electron affinity of the acceptor, that is, respectively, 2.55 ± 0.10[169], 2.77 ± 0.09 and 2.84 ± 0.10 eV[170,171]. The electron affinity can be seen as a measurement of the accepting power of the electron-deficient partner in a charge transfer complex and, therefore, the stronger the interaction between the electron-rich molecular wire and the acceptor, the higher the conductance boost. Iodine, on the other hand, is a σ-acceptor, as it has no accessible π orbitals to accept electrons. Despite its electron affinity of 2.48 ± 0.05 eV[170], the charge transfer interaction is weaker as the overlap between π orbital from the electron rich molecular wire and the σ orbital of iodine is less efficient, and the conductance boost is lower too (≈ 35x). The behaviour of the complex with 2,4-dinitrotoluene (DNT) is more difficult to rationalise. It has the lowest electron affinity of all the dopants tested (1.17 ± 0.21[170] or 1.60 ± 0.05 eV[172], depending on the method used), but it promoted an average conductance boost of *circa* 45x, compared with the uncomplexed molecular wire. However, the presence of both a π system delocalised on the phenyl ring and strong electron withdrawing pendant moieties (the 2 nitro groups) can help to understand its "odd" behaviour. The charge transfer interaction may not be as straightforward as observed in complexes with the other electron acceptors employed, but a mix of π-π and π-σ electron transfer.

These back-of-the-envelope calculations can be useful to rationalise the differences in conductance boost, but more detailed DFT computations and electron transport simulations are required to fully understand the observed behaviour.

4.4.3 TCNE conductance boost on 1[T3]1

The effect of charge-transfer complexation on a shorter terthiophene molecular wire, 1[T3]1, has been tested. Having only one methylene unit between the sulfur contact and the conjugated terthiophene moiety, 1[T3]1 has a frontier orbital, the HOMO, extending to the two sulfur leads, and cannot be therefore regarded as a proper double tunnelling barrier system. It has been used as an initial system to evaluate whether the increase in conductance observed in 6[T3]6 and 6[Ph]6 is limited to systems where the complexation site is decoupled from the contacts or not.

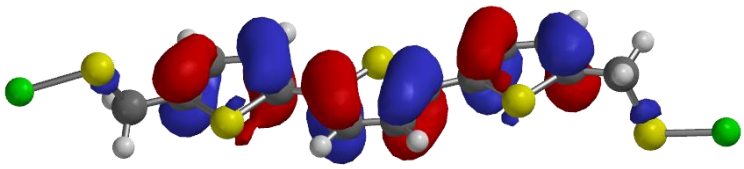

Figure 4.8: 1[T3]1 HOMO orbital calculated by DFT – B3LYP hybrid exchange correlation function with 6-31G* basis set.

Conductance of 1[T3]1 was measured in TCB and then in the presence of 1 mM TCNE in TCB, with the same procedure used for the longer molecules. Again, three distinct conductance values were found, both for the isolated molecule and the charge transfer complex with TCNE, the latter being roughly 90 times more conductive than the former.

	1[T3]1 TCB (nS)	1[T3]1 1 mM TCNE in TCB (nS)
G_A	0.33 ± 0.12	24.3 ± 5.4
G_B	1.18 ± 0.32	108 ± 27
G_C	4.93 ± 0.34	403 ± 95
Data Reference	A.38	A.39

Table 4.5: Summary of conductance values for the 1[T3]1 and its TCNE complex, measured as isolated contact groups with different techniques (see Appendix A for SMC data).

Therefore, the conductance increase upon charge-transfer complexation does not require complete decoupling from the sulfur leads, and it might be a general occurring phenomenon, where an appropriate binding site is present in the molecular wire.

4.5 Theoretical Calculations

To probe the reason for the substantial enhancement of junction conductance upon TCNE charge transfer complexation of the examined molecular wires, DFT and NEGF transport calculations were performed. The theory used to describe the conductance enhancement is based on phase-coherent tunnelling, as experimental conductance measurements indicate that this is the dominant mechanism for molecular junctions up to 4 nm wide.[24,34] The SMEAGOL[173] code was used to compute the transmission coefficient *T(E)* for electrons of energy E passing through the molecular junction from one electrode to the other, for the isolated molecular wire and the various CT complexes. Upon CT complexation, an additional resonance appears in the *T(E) vs E* plot, at around $E - E_F^0 = 0.1$ eV in the optimal configuration, very close to the Fermi level of the metallic electrodes. This is a Fano resonance, consisting of both an anti-resonance and a nearby resonance.

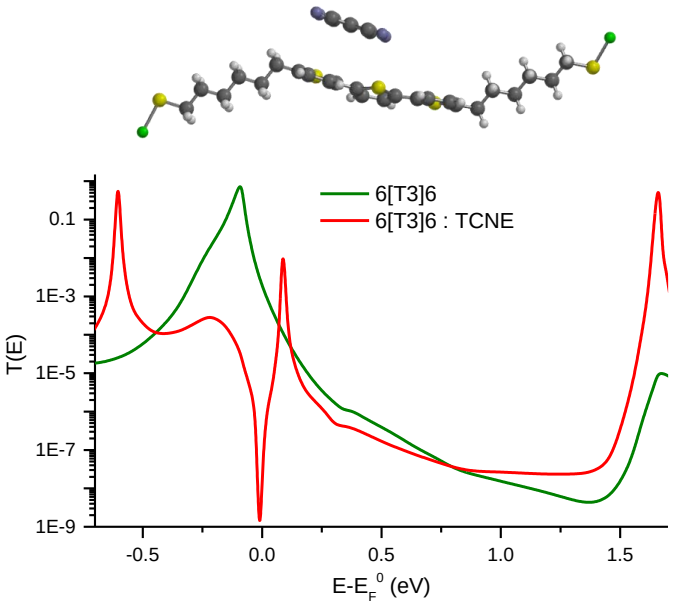

Figure 4.9: Optimal geometry of 6[T3]6:TCNE complex (top) and calculated transmission curves at 0 K (bottom).

In a room temperature experiment, however, the electron accepting molecule is likely to sample a range of positions and orientations relative to the electron-rich backbone, with minimal changes in binding energy. Transmission curves were therefore calculated for 500 different conformations of the CT complexes: the Fano resonance is always present, but its location shifts with conformation, leading to smeared "bumps" in the thermally-averaged transmission curves. Finite-bias conductance at 298 K was calculated for both the free molecular wire and its CT complexes using the equations described in the previous chapters.

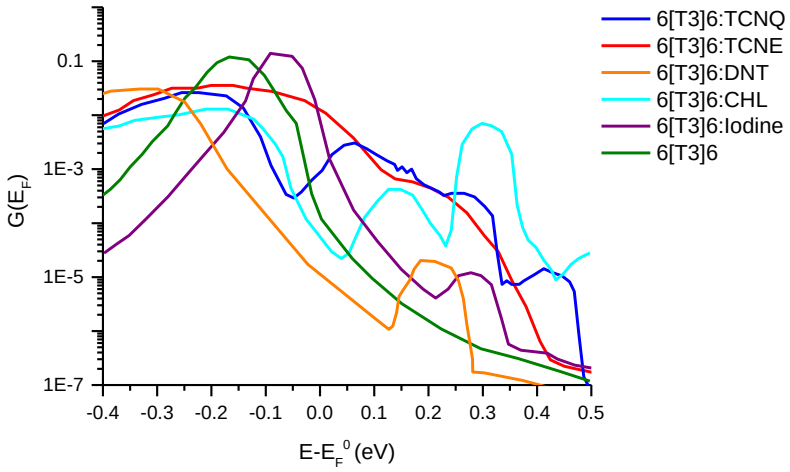

Figure 4.10: Finite-bias thermally averaged conductance plot vs energy for 6[T3]6 and its CT complex with various acceptors.

The calculated conductance enhancement at $E_F = E_F^0 + 0.1$ eV (within DFT error) is approximately 100 for TCNQ, 55 for TCNE, 23 for DNT (at 0.2 eV), 40 for CHL, and 9 for Iodine. The binding constant for these CT complexes was calculated at 0.87 eV for TCNQ, 0.65 eV for TCNE, 0.61 eV for DNT, 0.59 eV for CHL and 0.1 eV for Iodine. It is clear that binding constant and conductance enhancement are correlated, and the theoretical predictions follow the pattern of the experimental data, with the only exception being DNT. The change in the increase of conductance can be therefore attributed to the shifting position of the Fano resonance with respect to the Fermi energy in the different configurations of the CT complex: a weaker binding energy and coupling strength leads to larger shift in position, which results in greater smearing out of the resonance and lower conductance enhancement.

4.6 Conclusions and future work

In this chapter the effect on molecular conductance of electron-deficient moieties, which can form charge transfer complexes with electron-rich molecular wires, has been described from an experimental and theoretical point of view. Conductance of molecular wires with a charge transfer binding site was measured in the presence of appropriate electron acceptors, and an increase in conductance of up to two orders of magnitude upon complexation was found. Theoretical calculations within a phase-coherent tunnelling theory are in good agreement with the empirical results, and the conductance enhancement is attributed to the generation of a Fano resonance in the transmission function near the contact Fermi energy. While this conductance enhancement appears to be a general phenomenon, its magnitude is linked to the strength of the donor-acceptor interaction: higher CT complex binding constant resulted in higher conductance.

A number of experiments on fully-conjugated molecular wires is required to assess the generality of the observed behaviour, as the molecular wires used in this chapter have no *molecular* resonance in the transmission curves near to the Fermi level, where the Fano resonance appears upon CT complexation, and the HOMO-LUMO gap is large. Published results on interactions of fully-conjugated molecular wires with DNT and other electron-deficient molecules[109] suggest that their conductance might actually *decrease* upon complexation. The destructive interference part of the Fano resonance observed in the calculations presented in this chapter may be responsible of this, and further investigations, both theoretical and experimental, are therefore needed.

Synthesis

CHAPTER 5

Organic chemistry just now is enough to drive one mad. It gives me the impression of a primeval forest full of the most remarkable things, a monstrous and boundless thicket, with no way of escape, into which one may well dread to enter.

Friedrich Wöhler, 1835.

The molecular wires used in this thesis project were synthesised using common preparative chemistry techniques. All reactions that are air or moisture sensitive were performed in degassed or dry solvents, in oven dried glassware, under Ar. All reagents were purchased from Sigma-Aldrich Chemical Company except where otherwise stated and used as received except the following:

- THF and Et_2O where used after distillation over sodium benzophenone ketyl when needed anhydrous.
- Toluene and $CDCl_3$ were dried over $MgSO_4$ and stored under activated 3 Å molecular sieves (20% m/v) when needed anhydrous.[174]
- NBS was recrystallised from boiling H_2O and dried overnight under vacuum in the presence of silica gel before use.
- 2-Bromothiophene was distilled prior to use in a quick-path apparatus under reduced pressure.
- PPh_3, DPPP and DPPE were recrystallised from boiling 95% ethanol, dried in vacuum and stored under Ar.
- Mg turnings were oven dried before being used in Grignard reactions.
- Alkyllithium compounds were titrated against benzylbenzamide to a blue endpoint before use.
- Copper bronze was activated by the method of Vogel[175] before Ullmann coupling

Thin layer chromatography was performed on Merck Silica Gel 60 F-254 plates. Flash column chromatography was performed using Sigma-Aldrich technical grade silica (230-400 mesh, pore size 60 Å) using compressed air.

Proton and ^{13}C NMR spectra were recorder using a Bruker Avance 400 Ultrashield spectrometer and referenced to internal TMS. Mass spectra were recorded using a Carlo Erba 8000 Trio-1000 quadrupole spectrometer in CI positive ion mode (NH_3). High resolution mass spectra were recorded using an Agilent Q-TOF 7200 GC/MS or a Waters Micromass LCT TOF spectrometer.

5.1 Synthesis of 1[T3]1

The shortest double alkyl tunnelling barrier terthiophene molecule was synthesised *via* substitution of the hydroxyl function of [2,2':5',2"-terthiophene]5,5"-dimethanol with a chloride and nucleophilic displacement of the halogen with a thioacetate group.

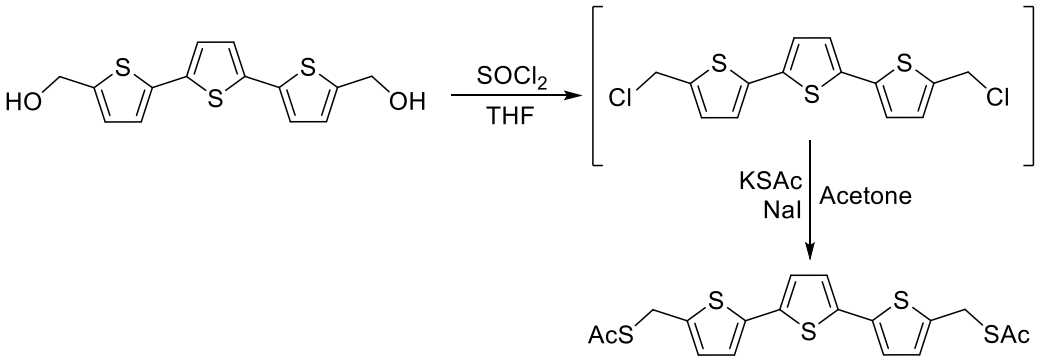

Figure 5.1: Synthesis of 1[T3]1

2,2':5',2"-Terthiophene was synthesised *via* Kumada coupling as reported in many literature sources[176,177] using [$NiCl_2$(dppe)] as catalyst in THF. Double Vilsmeier-Haack formylation of 2,2':5',2"-terthiophene using $POCl_3$ in DMF afforded the dicarbaldehyde[178,179] that was subsequently reduced with $NaBH_4$ in MeOH to [2,2':5',2"-terthiophene]5,5"-dimethanol as in the procedure developed by Lin *et al.*[180]

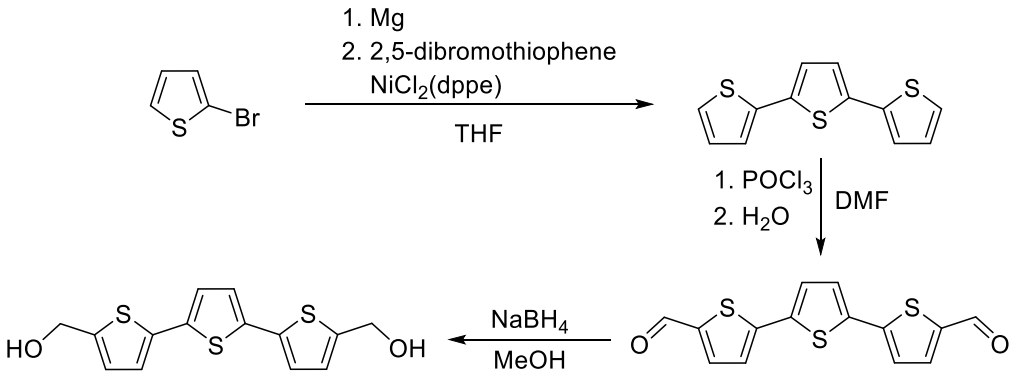

Figure 5.2: Synthesis of [2,2':5',2"-terthiophene]5,5"-dimethanol

The 2-step dithioacetate preparation had to be performed under Ar, in the same reaction vessel, without workup or purification of the dichloro intermediate: the compound decomposed to black tar-like material after about 30 minutes of exposure to air in previous synthetic attempts.

1[T3]1 was synthesised by Harry O'Brien during his MChem 4th year project.

5.1.1 1[T3]1

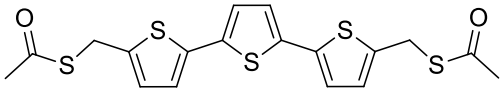

IUPAC: S,S'-([2,2':5',2''-terthiophene]-5,5''-diylbis(methylene)) diethanethioate. $SOCl_2$ (0.24 mL, 3.31 mmol) was added to a solution of [2,2':5',2"-terthiophene]5,5"-dimethanol (103 mg, 0.34 mmol) in dry THF at 0 °C and stirred at RT under Ar for 1 h. Ar was then flushed through the reaction flask until all the solvent and remaining $SOCl_2$ had been stripped away. KSAc (150 mg, 1.31 mmol) in dry degassed acetone (40 mL) was added *via* syringe and the resulting suspension was refluxed for 16 h under Ar. The solvent was then removed *in vacuo,* CH_2Cl_2 was added, the resulting suspension filtered and the crude product was purified by flash chromatography on silica (CH_2Cl_2 as eluant) to give the title compound as a yellow solid (119 mg, 83 %). Found: C = 49.79, H = 3.71, S = 37.75 %. $C_{22}H_{30}O_2S_4$ requires C = 50.91, H = 3.80, S = 37.76 %. ^{1}H NMR (400 MHz, $CDCl_3$): δ = 6.98 (s, 2H, Th), 6.93 (d, 2H, J = 3.8, Th), 6.86 (d, 2H, J = 3.4, Th) 4.28 (s, 4H, CH_2), 2.37 (s, 6H, CH_3), 2.05 (p, 4H, J = 7.3, CH_2) ppm. ^{13}C NMR (100 MHz, $CDCl_3$): 194.8, 139.5, 136.9, 136.0, 127.5, 124.2, 123.2, 30.4, 28.3 ppm. *m/z* (HRMS, CI, CH_4) 424.9748 $[M+H]^+$. $C_{18}H_{17}O_2S_5$ calc. 424.9832. No impurities were detected in the proton or ^{13}C NMR, thus the low C figure in the elemental analysis was attributed to incomplete combustion.

5.2 Synthesis of N[TX]N (N = 3-6; X = 1-3)

The double tunnelling oligothiophene molecules were synthesised adapting the procedure developed by Leary *et al.* for the synthesis of α,ω-dithiaalkane molecular wires[46]. Dichlorobis(acetonitrile)palladium(II) $[PdCl_2(MeCN)_2]$ was synthesised according to the procedure reported by Ito and Ozawa.[181] Bromination of 2,2':5',2"-terthiophene (prepared as discussed earlier) and 2,2'-bithiophene were performed using NBS in DMF according to the procedure developed by Bäuerle *et al.*[182]

The synthetic steps were Sonogashira cross-coupling of the appropriate dibromooligothiophene with a α,ω-chloroalkyne, H_2/Pd reduction of the alkynyl function and treatment with KSAc to afford the corresponding thioacetic acid esters.

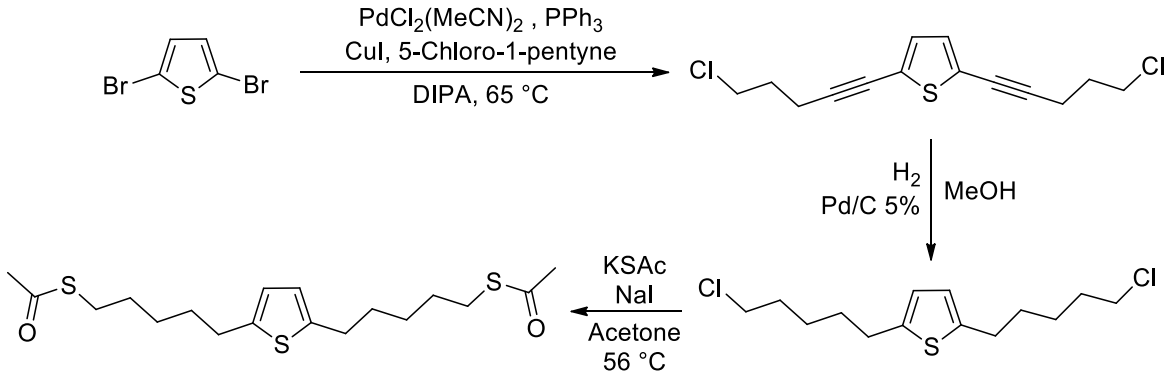

Figure 5.3: Synthetic example: preparation of 5[T1]5.

6[T3]6 was synthesised by Dr. Carly Brooke during her Ph.D.

A modified procedure had to be adopted for the preparation of 3[T3]3 and 4[T3]4 as 4-chlorobutyne is not commercially available and propargyl chloride is known to react with the Pd pre-catalyst to form a π-allenyl complex with loss of the halogen moiety.

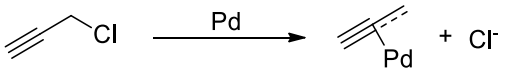

Figure 5.4: Formation of a π-allenyl complex from propargyl chloride

The Sonogashira coupling therefore employed terminal alkynes with alcohol moieties on the opposite terminus: H_2/Pd reduction to alkane, modified Appel procedure (using DPPE and 1,2-dibromotetrachloroethane - DBTCE) to substitute the alcoholic function with a bromide and final treatment with KSAc afforded the desired compound as thioacetic acid ester.[46]

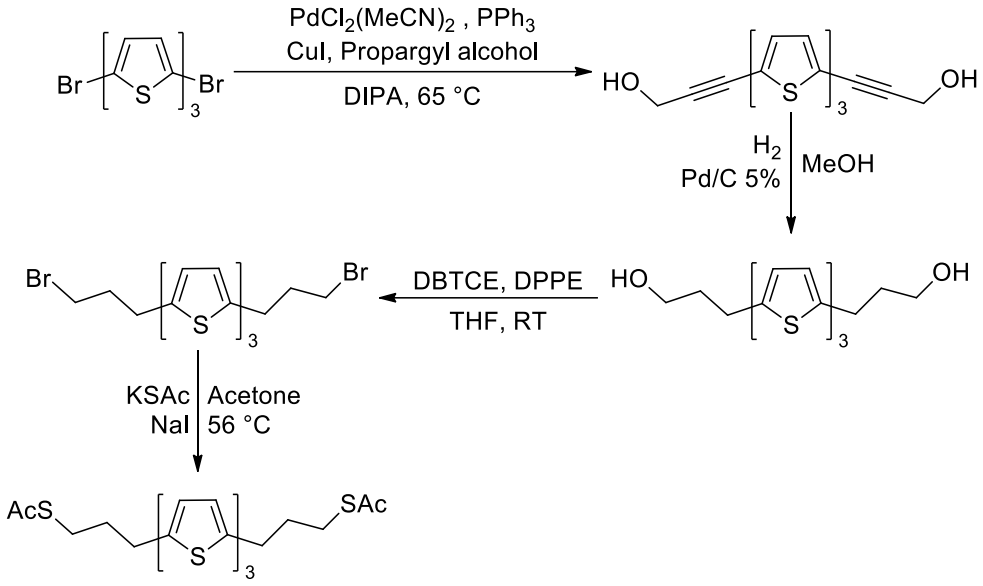

Figure 5.5: Synthetic example: preparation of 3[T3]3.

5.2.1 2,5-Bis-(5-chloropent-1-yn-1-yl)thiophene

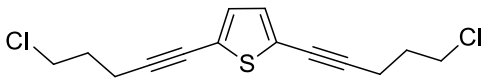

DIPA:THF (1:1, 40mL) was degassed by bubbling Ar through for 30 minutes prior to the addition of 2,5 dibromothiophene (1 g, 4,13 mmol), [$PdCl_2(MeCN)_2$] (55 mg, 0.2 mmol), PPh_3 (160 mg, 0.6 mmol) and CuI (23 mg ,0.12 mmol). After flushing with Ar for an additional 10 minutes, 5-chloro-1-pentyne (1.3g, 13.4mmol) was added and the reaction was heated to 65 °C under Ar and stirred for 16 hours. The resulting suspension was then allowed to cool down to room temperature, filtered, the residue washed with CH_2Cl_2 and the combined filtrates were concentrated *in vacuo* to a brown oil. The crude product was purified by flash chromatography on silica (10 % CH_2Cl_2 in hexanes as eluant) to give the title compound as a clear pale yellow oil (1.02 g, 87 %). ^{1}H NMR (400 MHz, $CDCl_3$): δ = 6.94 (s, 2H, Th), 3.69 (t, 4H, J = 6.4, CH_2), 2.62 (t, 4H, J = 7.5, CH_2), 2.05 (m, 4H, CH_2) ppm. ^{13}C NMR (100 MHz, $CDCl_3$): 131.4, 124.5, 93.2, 74.7, 44.2, 31.6, 17.6 ppm. *m/z* (HRMS, CI, CH_4) 285.0268 $[M+H]^+$, $C_{14}H_{15}Cl_2S$ calc. 285.0271.

5.2.2 2,5-Bis-(5-chloropentyl)thiophene

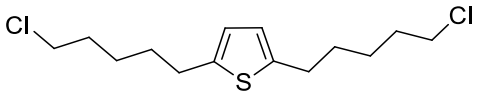

2,5-Bis-(5-chloropent-1-yn-1-yl)thiophene (740 mg, 2.59 mmol) was subjected to catalytic hydrogenation (50 mL MeOH, 30 mg Pd/C 10%, H_2 atmosphere, 24 h, room temperature). The resulting solution was filtered through a bed of celite and the solvent removed *in vacuo* to give a brown oil. The crude product was purified by flash chromatography on silica (20 % CH_2Cl_2 in hexanes as eluant) to give the title compound as a clear yellow oil (624 mg, 82 %). ^{1}H NMR (400 MHz, $CDCl_3$): δ = 6.56 (s, 2H, Th), 3.53 (t, 4H, J = 6.7, CH_2), 2.76 (t, 4H, J = 7.5, CH_2), 1.81 (m, 4H, CH_2), 1.67 (m, 4H, CH_2), 1.50 (m, 4H, CH_2) ppm. ^{13}C NMR (100 MHz, $CDCl_3$): 143.2, 123.9, 45.4, 32.8, 31.3, 30.4, 26.8 ppm. *m/z* (HRMS, CI, CH_4) 293.0813 $[M+H]^+$, $C_{14}H_{23}Cl_2S$ calc. 293.0897.

5.2.3 5[T1]5

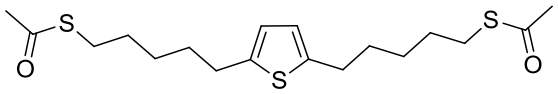

IUPAC: S,S'-(Thiophene-2,5-diylbis(pentane-5,1-diyl)) diethanethioate. A solution of 2,5-bis-(5-chloropentyl)thiophene (424 mg, 1,44 mmol), sodium iodide (108 mg, 0.72 mmol) and KSAc (574 mg, 5.04 mmol) in acetone (35 mL) was refluxed under Ar atmosphere for 18 hours. The resulting orange suspension was filtered, the residue washed with cold acetone and the combined filtrates were concentrated *in vacuo*. The obtained crude oil was purified by flash chromatography on silica (CH_2Cl_2 as eluant) to give the title compound as a brown oil (255 mg, 47 %). Found: C = 57.91, H = 7.40, S = 25.82 %. $C_{18}H_{28}O_2S_3$ requires C = 58.02, H = 7.57, S = 25.82 %. ^{1}H NMR (400 MHz, $CDCl_3$): δ = 6.55 (s, 2H, Th), 2.86 (t, 4H, J = 7.6, CH_2), 2.74 (t, 4H, J = 7.6, CH_2), 2.32 (s, 6H, CH_3), 1.70-1.54 (m, 8H, CH_2), 1.43 (m, 4H, CH_2) ppm. ^{13}C NMR (100 MHz, $CDCl_3$): 196.5, 143.3, 123.8, 31.6, 31.1, 30.4, 29.7, 29.4, 28.7 ppm. *m/z* (HRMS, CI, CH_4) 373.1327 $[M+H]^+$, $C_{18}H_{29}O_2S_3$ calc. 373.1330.

5.2.4 5,5'-Bis(5-chloropent-1-yn-1-yl)-2,2'-bithiophen

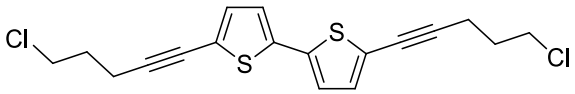

DIPA:THF (1:1, 40 mL) was degassed by bubbling Ar through for 30 minutes prior to the addition of 5,5'-dibromo-2,2'-bithiophene (2 g, 6.21 mmol), $PdCl_2(MeCN)_2$ (80 mg, 0.3 mmol), PPh_3 (242 mg, 0.6 mmol) and CuI (45 mg ,0.23 mmol). After flushing with Ar for additional 10 minutes, 5-chloro-1-pentyne (1.9 g, 18.51 mmol) was added and the reaction was heated to 65 °C under Ar and stirred for 16 hours. The resulting suspension was then allowed to cool down to room temperature and filtered. The residue was washed with 3x20mL CH_2Cl_2 and the solvent was then removed *in vacuo*. The crude product was purified by flash chromatography on silica (10 % CH_2Cl_2 in hexanes as eluant) to give the title compound as a pale yellow powder (1.97 g, 86 %). ^{1}H NMR (400 MHz, $CDCl_3$): δ = 6.99 (dd, 4H, J = 11.6, 3.8, Th), 3.69, (t, 4H, J = 6.4, CH_2), 2.64 (t, 4H, J = 6.8, CH_2), 2.06 (m, 4H, CH_2). ^{13}C NMR (100 MHz, $CDCl_3$): 137.5, 132.6, 123.9, 123.2, 94.1, 74.8, 44.1, 31.6, 17.6. *m/z* (HRMS, CI, CH_4) 367.0144 $[M+H]^+$, $C_{18}H_{17}Cl_2S_2$ calc. 367.0149.

5.2.5 5,5'-Bis(5-chloropentyl)-2,2'-bithiophene

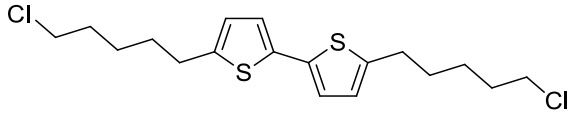

5,5'-Bis(5-chloropent-1-yn-1-yl)-2,2'-bithiophene (1.665 g, 4.53 mmol) was subjected to catalytic hydrogenation (60 mL MeOH, 50 mg Pd/C 10%, H_2 atmosphere, 48 h, room temperature). The resulting solution was filtered through a bed of celite and the solvent removed *in vacuo* to a brown oil. The crude product was purified by flash chromatography on silica (10 % CH_2Cl_2 in hexanes as eluant) to obtain an impure yellow oil. The title compound was obtained in higher purity as a pale yellow powder by recrystallisation from boiling EtOH (1.612 mg, 97 %). ^{1}H NMR (400 MHz, $CDCl_3$): δ = 6.89 (d, 2H, J = 3.5, Th), 6.65 (d, 2H, J = 3.8, Th), 3.54 (t, 4H, J = 6.7, CH_2), 2.79 (t, 4H, J = 7.5, CH_2), 1.81 (m, 4H, CH_2), 1.71 (m, 4H, CH_2), 1.52 (m, 4H, CH_2). ^{13}C NMR (100 MHz, $CDCl_3$): 144.4, 135.8, 125.2,

123.1, 45.3, 32.8, 31.3, 30.4, 26.7. *m/z* (HRMS, CI, CH_4) 375.0754 $[M+H]^+$, $C_{18}H_{25}Cl_2S_2$ calc. 375.0775.

5.2.6 5[T2]5

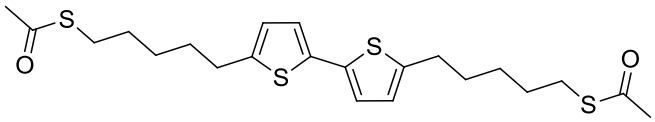

IUPAC: S,S'-([2,2'-bithiophene]-5,5'-diylbis(pentane-5,1-diyl)) diethanethioate. A solution of 5,5'-bis(5-chloropentyl)-2,2'-bithiophene (1.5 g, 4 mmol), sodium iodide (300 mg, 2 mmol) and KSAc (1.48 g, 13 mmol) in acetone (40 mL) was refluxed under Ar atmosphere for 18 hours. The resulting orange suspension was filtered, the residue washed with cold acetone and the combined filtrates were concentrated *in vacuo*. The obtained crude product was purified by flash chromatography on silica (CH_2Cl_2 as eluant) and recrystallised from boiling EtOH to give the title compound as a pale yellow powder (1.49 g, 79 %). Found: C = 58.01, H = 6.45, S = 28.97 %. $C_{22}H_{30}O_2S_4$ requires C = 58.11, H = 6.65, S = 28.21 %. ^{1}H NMR (400 MHz, $CDCl_3$): δ = 6.98 (d, 2H, J = 3.6, Th), 6.64 (d, 2H, J = 3.6, Th), 2.87 (t, 4H, J = 7.2, CH_2), 2.78 (t, 4H, J = 7.7, CH_2), 2.31 (s, 6H, CH_3), 1.73 – 1.56 (m, 8H, CH_2), 1.44 (m, 4H, CH_2). ^{13}C NMR (100 MHz, $CDCl_3$): 196.1, 144.2, 132.3, 124.8, 122.7, 31.0, 30.7, 29.9, 29.3, 28.9, 28.1. *m/z* (HRMS, CI, CH_4) 455.1204 $[M+H]^+$, $C_{22}H_{31}O_2S_4$ calc. 455.1207.

5.2.7 3,3'-([2,2':5',2''-Terthiophene]-5,5''-diyl)bis(prop-2-yn-1-ol)

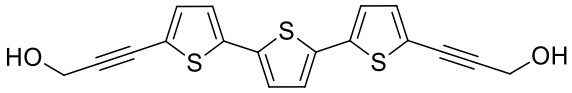

DIPA (40 ml) was degassed by bubbling Ar through for 20 minutes prior to the addition of 5,5''–dibromo–2,2':5',2''–terthiophene (570 mg, 1.4 mmol), $[PdCl_2(MeCN)_2]$ (15 mg, 0.06 mmol), triphenylphosphine (48 mg, 0.18 mmol) and CuI (7 mg, 0.03 mmol). After flushing with Ar for additional 10 minutes, propargyl alcohol (0.2 ml, 3.5 mmol) was added and the reaction was heated to 60°C under Ar and stirred for 16 hours. The resulting suspension was then allowed to cool down to room temperature, the orange solids were filtered, washed with hexanes and water and dried *in vacuo* (279 mg, 56 %). ^{1}H NMR (400 MHz, $CDCl_3$) δ: 7.03

(d, 2H. J = 3.4, Th), 7.01 (d, 2H, J = 3.8, Th), 6.98 (s, 2H, Th), 4.50 (s, 4H, CH_2). ^{13}C NMR (100 MHz, $CDCl_3$) δ: 144.5, 135.6, 134.9, 126.8, 126.3, 123.2, 90.1, 88.7, 45.2. *m/z* (HRMS, CI, CH_4) 357.0072 $[M+H]^+$, $C_{18}H_{13}O_2S_3$ calc. 357.0078

5.2.8 3,3'-([2,2':5',2''-Terthiophene]-5,5''-diyl)bis(propan-1-ol)

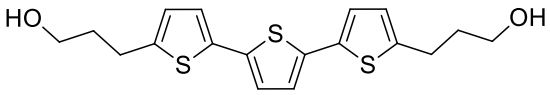

3,3'-([2,2':5',2''-Terthiophene]-5,5''-diyl)bis(prop-2-yn-1-ol) (250 mg, 0.70 mmol) was subjected to catalytic hydrogenation (50 ml MeOH, 20 mg Pd/C 10%, H_2 atmosphere, 24 h, room temperature). The resulting suspension was filtered through a bed of celite and the solvent removed *in vacuo* to give the title compound as an orange solid (249 mg, 98 %). ^1H NMR (400 MHz, $CDCl_3$) δ: 6.97 (s, 2H, Th), 6.96 (d, 2H, Th), 6.67 (d, 2H, J = 3.4, Th) 3.68 (t, J = 6.4Hz, 4H, CH_2) 2.68 (t, J = 7.7Hz, 4H, CH_2), 1.93-1.84 (m, 4H, CH_2). *m/z* (HRMS, CI, CH_4) 365.0699 $[M+H]^+$, $C_{18}H_{21}O_2S_3$ calc. 365.0703.

5.2.9 5,5''–Bis(3-bromopropyl)–2,2':5',2''–terthiophene

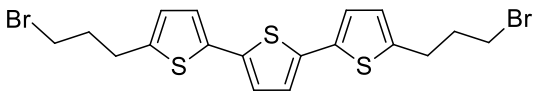

To a solution of DPPE (220 mg, 0.55 mmol) in THF (20 ml) under Ar was added 1,2-dibromotetrachloroethane (360 mg, 1.11 mmol). To the resulting white suspension was added dropwise 3,3'-([2,2':5',2''-terthiophene]-5,5''-diyl)bis(propan-1-ol) (200 mg, 0,55 mmol) in THF (10 mL) while cooling on a ice bath. After a short time the solid dissolved and the solution was allowed to stir overnight (16 h), after which time a greyish solid had precipitated. The suspension was filtered, the solvent removed *in vacuo* and the crude product was purified by flash chromatography on silica (0 - 20 % CH_2Cl_2 in hexanes as eluant) to give the title compound as a yellow solid (198 mg, 74 %). ^1H NMR (400 MHz, $CDCl_3$) δ: 6.97 (s, 2H, Th), 6.96 (d, 2H, Th), 6.67 (d, 2H, J = 3.4 Hz, Th) 3.42 (t, 4H, J = 6.8 Hz, CH_2) 2.61 (t, 4H, J = 7.3 Hz, CH_2), 1.94-1.86 (m, 4H, CH_2). *m/z* (HRMS, CI, NH_3) 488.9023 $[M+H]^+$, $C_{18}H_{19}Br_2S_3$ calc. 488.9016.

5.2.10 3[T3]3

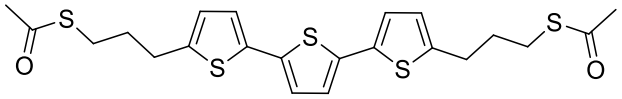

IUPAC: S,S'-([2,2':5',2''-terthiophene]-5,5''-diylbis(propane-3,1-diyl)) diethanethioate. A solution of 5,5''–bis(3-bromopropyl)–2,2':5',2''–terthiophene (120 mg, 0.25 mmol), sodium iodide (20 mg, 0,13 mmol) and potassium thioacetate (100 mg, 0.87 mmol) in acetone (25 ml) was refluxed under Ar atmosphere for 24 hours. The solvent was then removed *in vacuo* and the crude product was purified by flash chromatography on silica (CH_2Cl_2 as eluant) to give the title compound as a yellow solid (54 mg, 46 %). Found: C = 54.90, H = 5.09, S = 33.29 %. $C_{22}H_{24}O_2S_5$ requires C = 54.96, H = 5.03, S = 33.35 %. ^{1}H NMR (400 MHz, $CDCl_3$) δ: 6.96 (s, 2H, Th), 6.94 (d, 2H, Th), 6.66 (d, 2H, J=3.4, Th), 2.96 (t, 4H, J=7.1 Hz, CH_2), 2.88 (m, 4H, CH_2), 2.34 (s, 6H, CH_3), 1.98-1.89 (m, 4H, CH_2). ^{13}C NMR (100 MHz, $CDCl_3$): δ: 200.6, 145.4, 136.5, 135.1, 125.9, 124.1, 123.6, 31.7, 31.0, 29.8, 28.6. MS (CI+ (NH_3)) *m/z* 498.1 ($[M+NH_4]^+$, 28 %) 481.0 ($[M+H]^+$, 100 %). *m/z* (HRMS, CI, CH_4) 481.0448 $[M+H]^+$, $C_{22}H_{25}O_2S_5$ calc. 481.0458.

5.2.11 4,4'-([2,2':5',2''-Terthiophene]-5,5''-diyl)bis(but-3-yn-1-ol)

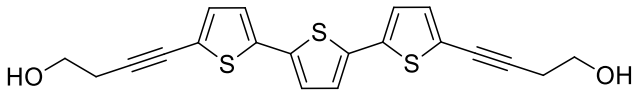

DIPA (40 ml) was degassed by bubbling Ar through for 20 minutes prior to the addition of 5,5''–dibromo–2,2':5',2''–terthiophene (550 mg, 1.37 mmol), $[PdCl_2(MeCN)_2]$ (15 mg, 0.06 mmol), PPh_3 (48 mg, 0.18 mmol) and CuI (7 mg, 0.03 mmol). After flushing with Ar for additional 10 minutes, 3-butyn-1-ol (240 mg, 3.4 mmol) was added and the reaction was heated to 60 °C under Ar and stirred for 16 hours. The resulting suspension was then allowed to cool down to room temperature, the orange solids were filtered, washed with water and hexanes and recrystallised from boiling THF to afford a bright orange powder (336 mg, 64% yield). ^{1}H NMR (400 MHz, THF-d8) δ: 7.09 (m, 6H. J = 3.9, Th), 4.02 (s, 2H, Th), 3.65 (4H, dd, J = 6.0, 6.3 Hz, CH_2) 2.61 (t, 4H, J = 6.2 Hz, CH_2). ^{13}C NMR (100 MHz, THF-d8): δ: 136.2, 132.5, 129.2, 125.1, 123.9, 123.5, 100.21, 93.7, 73.9, 60.7. *m/z* (HRMS, CI, CH_4) 385.0389 $[M+H]^+$, $C_{20}H_{17}O_2S_3$ calc. 385.0391.

5.2.12 4,4'-([2,2':5',2''-Terthiophene]-5,5''-diyl)bis(butan-1-ol)

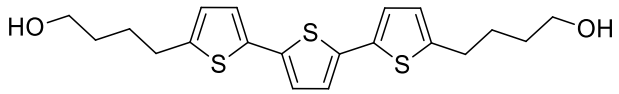

4,4'-([2,2':5',2''-Terthiophene]-5,5''-diyl)bis(but-3-yn-1-ol) (325 mg, 0.85 mmol) was subjected to catalytic hydrogenation (50 ml MeOH, 30 mg Pd/C 10%, H_2 atmosphere, 24 h, room temperature). The resulting suspension was filtered through a bed of celite and the solvent removed *in vacuo* to give the title compound as an orange solid (323 mg, 97 %). ^{1}H NMR (400 MHz, $CDCl_3$) δ: 6.97 (m, 2H, Th), 6.96 (s, 2H, Th), 6.69 (d, 2H, J = 3.4, Th), 3.69 (t, 4H, J = 5.9 Hz, CH_2), 2.84 (t, 4H, J = 7.4 Hz, CH_2) 1.80-1.63 (m, 8H, CH_2), ^{13}C NMR (100 MHz, $CDCl_3$) δ: 145.1, 136.3, 135.2, 125.5, 123.9, 123.6, 62.8, 32.5, 30.3, 28.2. *m/z* (HRMS, CI, CH_4) 393.1020 $[M+H]^+$, $C_{20}H_{25}O_2S_3$ calc. 393.1017.

5.2.13 5,5''-Bis(4-bromobutyl)-2,2':5',2''-terthiophene

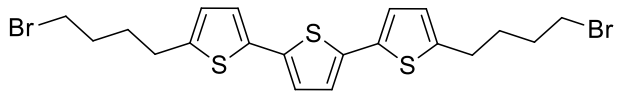

To a solution of DPPE (318 mg, 0.8 mmol) in THF (20 ml) under Ar was added 1,2-dibromotetrachloroethane (521 mg, 1,6 mmol). To the resulting white suspension was added dropwise 4,4'-([2,2':5',2''-terthiophene]-5,5''-diyl)bis(butan-1-ol) (300 mg, 0,77 mmol) in THF (10 mL) while cooling on a ice bath. After a short time the solid dissolved and the solution was allowed to stir overnight (16 h), after which time a grayish solid had precipitated. The suspension was filtered, the solvent removed *in vacuo* and the crude product was purified by flash chromatography on silica (0 - 20 % CH_2Cl_2 in hexanes as eluant) to give the title compound as a yellow solid (307 mg, 78 %). ^{1}H NMR (400 MHz, $CDCl_3$) δ: 6.97 (m, 4H, Th), 6.69 (d, 2H, J = 3.6, Th), 3.44 (t, 4H, J = 6.4 Hz, CH_2), 2.83 (t, 4H, J = 8.6 Hz, CH_2) 1.98-1.90 (m, 4H, CH_2) 1.89-1.81 (m, 4H, CH_2). *m/z* (HRMS, CI, NH_3) 516.9322 $[M+H]^+$, $C_{20}H_{23}Br_2S_3$ calc. 516.9328.

5.2.14 4[T3]4

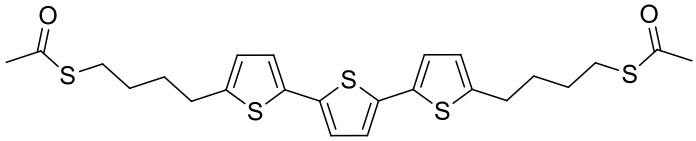

IUPAC: S,S'-([2,2':5',2''-terthiophene]-5,5''-diylbis(butane-4,1-diyl)) diethanethioate. A solution of 5,5''-bis(4-bromobutyl)-2,2':5',2''-terthiophene (300 mg, 0.58 mmol), sodium iodide (43 mg, 0,29 mmol) and potassium thioacetate (231 mg, 2 mmol) in acetone (35 ml) was refluxed under Ar atmosphere for 24 hours. The solvent was then removed *in vacuo* and the crude product was purified by flash chromatography on silica (CH_2Cl_2 as eluant) to give the title compound as a yellow solid (154 mg, 52 %). Found: C = 56.55, H = 5.54, S = 31.43 %. $C_{24}H_{28}O_2S_5$ requires C = 56.65, H = 5.55, S = 31.51 %. ^{1}H NMR (400 MHz, $CDCl_3$) δ: 6.96 (s, 2H, Th), 6.95 (d, 2H, Th), 6.65 (d, 2H, J = 3.4, Th) 2.89 (t, 4H, J = 6.9 Hz, CH_2), 2.58 (t, 4H, J = 7.3 Hz, CH_2), 2.32 (s, 6H, CH_3), 1.74-1.58 (m, 8H, CH_2). ^{13}C NMR (100 MHz, $CDCl_3$): δ: 195.9, 144.4, 136.5, 135.9, 125.9, 123.3, 122.9, 33.6, 31.4, 30.5, 29.8, 28.8. *m/z* (HRMS, CI, CH_4) 509.0738 $[M+H]^+$, $C_{24}H_{29}O_2S_5$ calc. 509.0771.

5.2.15 5,5''-Bis(5-chloropent-1-yn-1-yl)-2,2':5',2''-terthiophene

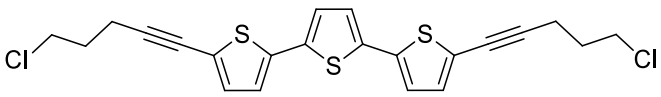

DIPA:THF (1:1, 40 mL) was degassed by bubbling Ar through for 30 minutes prior to the addition of 5,5''–dibromo–2,2':5',2''–terthiophene (0.5 g, 1.23 mmol), $[PdCl_2(MeCN)_2]$ (16 mg, 0.06 mmol), PPh_3 (48 mg, 0.18 mmol) and CuI (7 mg, 0.04 mmol). After flushing with Ar for additional 10 minutes, 5-chloro-1-pentyne (378 mg, 3.69 mmol) was added and the reaction was heated to 60 °C under Ar and stirred for 16 hours. The resulting suspension was then allowed to cool down to room temperature and filtered. The residue was washed with 3x20 mL CH_2Cl_2 and the combined filtrates were then concentrated *in vacuo*. The crude product was purified by flash chromatography on silica (20 % CH_2Cl_2 in hexanes as eluant) to give the title compound as a bright yellow powder (0.449 g, 88 %). ^{1}H NMR (400 MHz, $CDCl_3$): δ = 7.05 (s, 2H, Th), 7.01 (dd, 4H, J = 9.78, 4.05, Th), 3.71, (t, 4H, J = 6.8, CH_2), 2.65 (t, 4H, J = 7.4, CH_2), 2.07 (m, 4H, CH_2). ^{13}C NMR (100 MHz, $CDCl_3$): 137.3, 135.9,

132.2, 124.7, 123.4, 122.6, 93.7, 74.5, 43.7, 31.2, 17.3. *m/z* (HRMS, CI, CH_4) 449.0018 $[M+H]^+$, $C_{22}H_{19}Cl_2S_3$ calc. 449.0025.

5.2.16 5,5''-Bis(5-chloropentyl)-2,2':5',2''-terthiophene

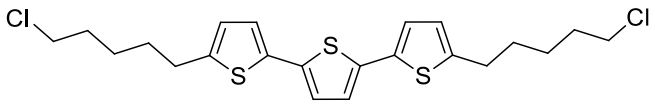

5,5''-Bis(5-chloropent-1-yn-1-yl)-2,2':5',2''-terthiophene (0.431 g, 0.96 mmol) was subjected to catalytic hydrogenation (50 mL EtOAc, 50 mg Pd/C 10 %, H_2 atmosphere, 36 h, room temperature). The resulting solution was filtered through a bed of celite and the solvent removed *in vacuo* to give a yellow solid. The crude product was purified by flash chromatography on silica (10 % CH_2Cl_2 in hexanes as eluant) to obtain the title compound as yellow powder (0.424 g, 95 %). ^{1}H NMR (400 MHz, $CDCl_3$): δ = 6.97 (s, 2H, Th), 6.95 (d, 2H, J = 1.7, Th), 6.68 (d, 2H, J = 1.7, Th) 3.54 (t, 4H, J = 7.32, CH_2), 2.80 (t, 4H, J = 7.5, CH_2), 1.81 (m, 4H, CH_2), 1.71 (m, 4H, CH_2), 1.52 (m, 4H, CH_2). ^{13}C NMR (100 MHz, $CDCl_3$): 144.6, 136.1, 134.8, 125.0, 123.6, 123.2, 44.9, 32.3, 30.9, 30.0, 26.3. *m/z* (HRMS, CI, CH_4) 457.0662 $[M+H]^+$, $C_{22}H_{27}Cl_2S_3$ calc. 457.0652.

5.2.17 5[T3]5

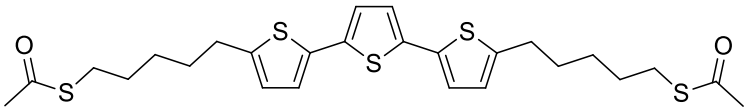

IUPAC: S,S'-([2,2':5',2''-terthiophene]-5,5''-diylbis(pentane-5,1-diyl)) diethanethioate. A solution of 5,5''-bis(5-chloropentyl)-2,2':5',2''-terthiophene (0.397 g, 0.87 mmol), sodium iodide (70 mg, 0.4 mmol) and KSAc (0.375 g, 3.2 mmol) in acetone (30mL) was refluxed under Ar atmosphere for 16 hours. The resulting brown suspension was filtered, the residue washed with cold acetone and the combined filtrates were concentrated *in vacuo*. The obtained crude product was purified by flash chromatography on silica (CH_2Cl_2 as eluant) to give the title compound as a yellow powder (0.279 g, 60 %). Found: C = 58.11, H = 6.00, S = 29.65 %. $C_{26}H_{32}O_2S_5$ requires C = 58.17, H = 6.01, S = 29.86 %. ^{1}H NMR (400 MHz, $CDCl_3$) δ: 6.96 (s, 2H, Th), 6.95 (d, 2H, J = 3.4, Th), 6.65 (d, 2H, J=3.4, Th), 2.90 (t, 4H, J = 7.0 Hz, CH_2), 2.79 (t, 4H, j = 7.4, CH_2), 2.33 (s, 6H, CH_3), 1.71 (m, 4H, CH_2), 1.66 – 1.42 (m,

8H, CH_2). ^{13}C NMR (100 MHz, $CDCl_3$): δ: 196.4, 145.2, 136.5, 135.2, 125.4, 123.9, 123.1, 31.4, 31.1, 30.4, 29.7, 29.4, 28.5. (HRMS, CI, CH_4) 537.1090 $[M+H]^+$, $C_{26}H_{33}O_2S_5$ calc. 537.1084.

5.2.18 5,5″-Bis(6-chlorohex-1-ynyl)-2,2′:5′,2″-terthiophene.

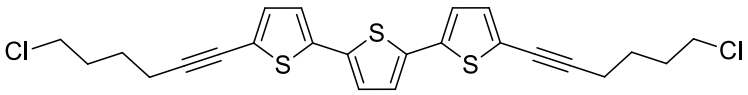

Di*iso*propylamine (50 mL) was degassed for 40 minutes by Ar bubbling prior to the addition of 5,5''-dibromo-2,2':5',2''-terthiophene (1.50 g, 3.69 mmol), $[PdCl_2(MeCN)_2]$ (48 mg, 0.18 mmol), PPh_3 (97 mg, 0.37 mmol) and CuI (21 mg, 0.1 mmol). After flushing with Ar for an additional 10 minutes, 6-chloro-hex-1-yne (1.155 g, 1.21 mL, 2.7 eq.) was added and the mixture was heated to 80°C under Ar and stirred for 16 hours. The resulting suspension was then allowed to cool down to room temperature and was filtered. The orange residue was triturated with hexanes, filtered again, washed with water and dried *in vacuo* to yield the title compound as bright yellow solid (1.12 g, 64 %). Found: C = 60.03, H = 4.60 %. $C_{24}H_{22}Cl_2S_3$ requires C = 60.37, H = 4.64 %. ^1H NMR (400 MHz, $CDCl_3$) δ = 7.03 (s, 2H, Th), 6.98-7.01 (AB, 4H, J = 3.8, Th), 3.60 (t, 4H, J = 6.5, CH_2), 2.50 (t, 4H, J = 7.0, CH_2), 1.78-1.94 (m, 8H, CH_2). ^{13}C NMR (100 MHz, $CDCl_3$) δ = 137.2, 136.0, 132.0, 124.6, 123.4, 123.0, 94.9, 74.3, 44.5, 31.7, 25.7, 19.1. MS: *m/z* 477 $[M^+]$. *m/z* (HRMS, CI, CH_4) 477.0340 $[M+H]^+$, $C_{24}H_{23}Cl_2S_3$ calc. 477.0339.

5.2.19 5,5″-Bis(6-chlorohexyl)-2,2′:5′,2″-terthiophene

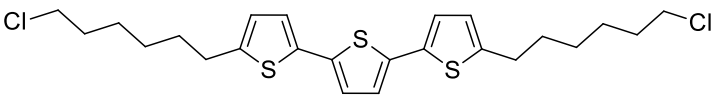

5,5''-Bis(6-chlorohex-1-ynyl)-2,2':5',2''-terthiophene (0.630 g, 1.32 mmol) was subjected to catalytic hydrogenation (0.18 g Pd/C 10 %, H_2 atmosphere, 24 h, room temperature) in 50 mL of EtOAc. The catalyst was then filtered off through a bed of Celite and the solvent was removed *in vacuo*. The crude yellow solid was purified by flash column chromatography on silica (5 % EtOAc in hexanes as eluant) to yield the title compound as a bright yellow solid (0.43 g, 67 %). Found: C = 59.66, H = 6.10 %. $C_{24}H_{30}Cl_2S_3$ requires C = 59.36, H = 6.23

%. ^{1}H NMR (400 MHz, $CDCl_3$) δ = 6.97 (s, 2H, Th), 6.96 (d, 2H, J = 3.1, Th), 6.67 (d, 2H, J = 3.4, Th), 3.53 (t, 4H, J = 6.7, CH_2), 2.80 (t, 4H, J = 7.6, CH_2), 1.70-1.79 (m, 8H, CH_2), 1.37-1.52 (m, 8H, CH_2). ^{13}C NMR (100 MHz, $CDCl_3$) δ = 143.8, 136.6, 125.3, 123.9, 123.6, 99.9, 45.4, 32.9, 31.8, 30.4, 28.6, 26.9. MS: m/z 485 [M^+]. *m/z* (HRMS, CI, CH_4) 485.0959 [M+H]$^+$, $C_{24}H_{31}Cl_2S_3$ calc. 485.0965.

5.2.20 6[T3]6

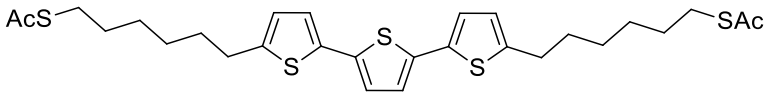

IUPAC: S,S'-([2,2':5',2''-terthiophene]-5,5''-diylbis(hexane-5,1-diyl)) diethanethioate. A solution of 5,5”-bis(6-chlorohexyl)-2,2’:5’,2”-terthiophene (0.363 g, 0.748 mmol), KSAc (0.263 g, 2.3 mmol) and NaI (0.011 g, 10 mol %) in acetone (50 mL) was refluxed under Ar atmosphere for 16 hours. The resulting brown suspension was filtered, the residue washed with cold acetone and the combined filtrates were concentrated *in vacuo*. The obtained crude product was purified by flash column chromatography on silica (CH_2Cl_2) and recrystallised from 30:70 CH_2Cl_2:hexanes to give the title compound as a dull yellow solid (0.120 g, 28 %). Found: C = 59.32, H = 6.59 %. $C_{28}H_{36}O_2S_5$ requires C = 59.53, H = 6.42 %. ^{1}H NMR (400 MHz, $CDCl_3$) δ = 6.97 (s, 2H, Th), 6.66-6.95 (AB, 4H, J = 3.5, Th), 2.87 (t, 4H, J = 6.5, CH_2), 2.78 (t, 4H, J = 7.4, CH_2), 2.32 (s, 6H, CH_3), 1.58-1.67 (m, 8H, CH_2), 1.39 (m, 8H, CH_2). ^{13}C NMR (100 MHz, $CDCl_3$) δ = 196.2, 145.1, 136.1, 134.7, 124.9, 123.5, 123.2, 31.4, 30.7, 30.1, 29.4, 29.1, 28.6, 28.5. MS: m/z 582 [M+NH_4]$^+$, 565 [M+H]$^+$. *m/z* (HRMS, ES+, MeOH) 587.1220 [M+Na]$^+$, $C_{28}H_{36}O_2NaS_5$ calc. 587.1217.

5.3 Synthesis of 8[T3]8

The longer alkyl chain terthiophene compound has been more of a challenge to synthesise than the shorter chain analogues. Heck coupling using 5,5”-dibromo-2,2’:5’,2”-terthiophene and 8-chloro-oct-1-ene gave a mixture of regioisomers that proved impossible to purify, and in modest yield (22%). Sonogashira coupling between 5,5”-dibromo-2,2’:5’,2”-terthiophene and 8-chloro-oct-1-yne or 7-octyn-1-ol failed, leading to recovery of starting material and

homocoupled alkyne due to competing Glaser coupling. Similarly, Kumada coupling between 5,5''-dibromo-2,2':5',2''-terthiophene and 8-bromo-1-octanol failed, even when the alcoholic function was protected as benzyl or THP ether and using a variety of ligands for the Nickel catalyst. Kumada coupling between 5,5''-dibromo-2,2':5',2''-terthiophene and 1-(8-Bromooctyloxy)-4-methoxybenzene (the 4-methoxybenzene ether can be converted to halogen following the procedure developed by Bäuerle *et al.*[183]) gave the product in low yield (12% from crude NMR), but it was impossible to purify it either by column chromatography or recrystallisation. Failed coupling are summarised in Table 5.1.

Coupling Reaction	Coupling Reagent	Reaction Outcome
Sonogashira[a]	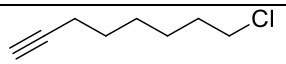	Failed; Glaser coupling product recovered
Sonogashira[a]	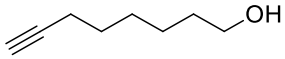	Failed; Glaser coupling product recovered
Heck[b]	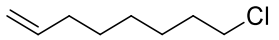	22% (after chromatography); mixture of regioisomers
Kumada[c]	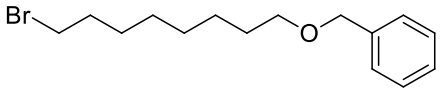	Failed; no characterisable product recovered
Kumada[c]	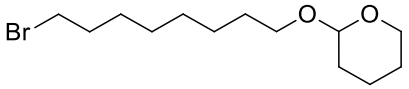	Failed; no characterisable product recovered
Kumada[c]	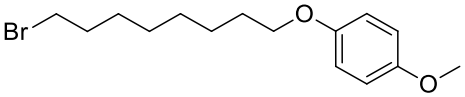	12% (NMR); impossible to purify

Table 5.1: Summary of attempted 8[T3]8 synthesis *via* organometallic coupling of 5,5''-dibromo-2,2':5',2''-terthiophene. a) Sonogashira conditions: $[PdCl_2(MeCN)_2]$ 5%, PPh_3 15%, CuI 3% or $[Pd(PPh_3)_4]$ 5%, CuI 3%. Reaction run in DIPA:THF 1:1 at 60° C. b) Heck conditions: $[Pd(PPh_3)_4]$ 10% in NEt_3 at 40° C. c) Kumada conditions: $[NiCl_2(dppe)]$ or $[NiCl_2(dppp)]$ 1% in THF or Et_2O at 50° C. Grignard reagent freshly prepared using Mg shavings in THF with I_2 or dibromoethane and heat as initiator. All reactions were run under Argon and solvents were thoroughly degassed before use.

In a desperate attempt, 5,5''-bis(8-bromooctyl)-2,2':5',2''-terthiophene was prepared in very low yield (5%) by adding 5,5''-dilithio-2,2':5',2''-terthiophene (freshly prepared by lithiation of 2,2':5',2''-terthiophene with *n*-BuLi) in THF to a concentrated solution of 1,8-dibromooctane in THF kept at -78 °C. Nucleophilic displacement of the halogen with KSAc afforded 8[T3]8.

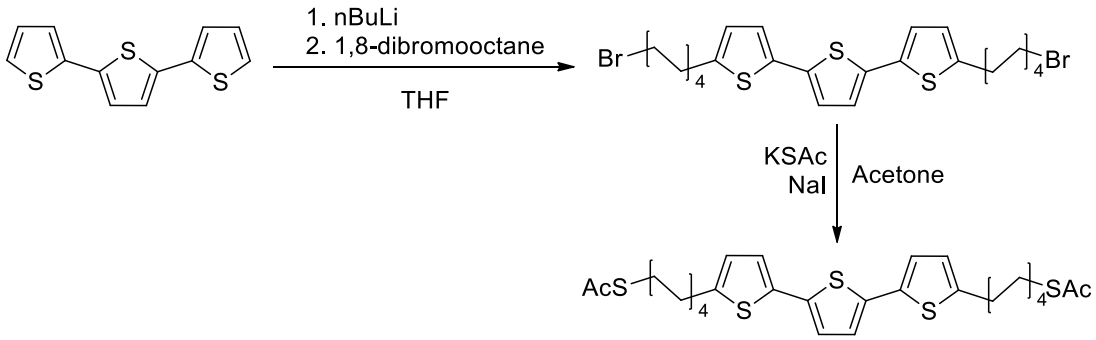

Figure 5.6: Synthesis of 8[T3]8

5.3.1 5,5''-bis(8-bromooctyl)-2,2':5',2''-terthiophene

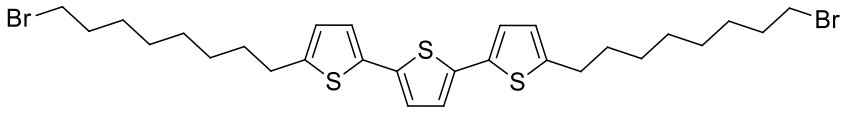

To an argon-purged flask was added 2,2':5',2''-terthiophene (0.5 g, 2.01 mmol) and 15 mL of dry THF. The solution was cooled to -78 °C and *n*-BuLi (caution! 1.58 M in hexane, 2.6 mL, 4.10 mmol) was added dropwise. The resulting yellow suspension was allowed to stir at -78 °C for one hour, warmed to room temperature and then transferred drop wise *via* wide bore needle syringe to a separate argon-purged flask containing 1,8-dibromooctane (2.2 g, 8.05 mmol) in 15 mL of THF at -78 °C. The reaction was allowed to warm to room temperature overnight and then poured into ice water, extracted with CH_2Cl_2 (4 x 35 mL), the combined organics washed with water and brine, dried over $MgSO_4$, filtered, and concentrated *in vacuo*. The crude product was purified by flash column chromatography on silica (10 % CH_2Cl_2 in hexanes as eluant) to give the title compound as a yellow solid (64 mg, 5 %). Found: C = 53.47, H = 5.95, S = 15.73 %. $C_{24}H_{22}Cl_2S_3$ requires C = 53.33, H = 6.07, S = 15.25 %. ^{1}H NMR (400 MHz, $CDCl_3$) δ = 6.97 (s, 2H, Th), 6.96 (d, 2H, J = 3.7, Th), 6.67 (d, 2H J = 3.6, Th), 3.40 (t, 4H, J = 6.9, CH_2), 2.78 (t,4H, J = 7.8, CH_2), 1.85 (m, 4H, CH_2), 1.68 (m, 4H, J = 7.5, CH_2), 1.24-1.48 (m, 16H, CH_2). ^{13}C NMR (100 MHz, $CDCl_3$) δ = 145.3, 136.1, 133.8, 124.9, 123.5, 123.2, 34.1, 32.7, 31.5, 30.1, 29.2, 28.9, 28.6, 28.1.

5.3.2 8[T3]8

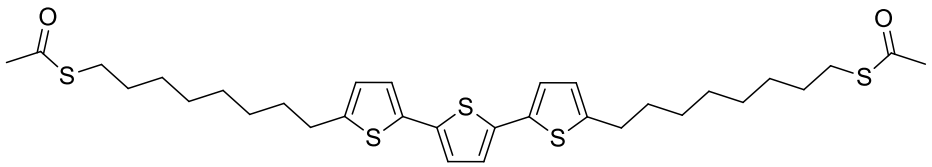

IUPAC: S,S'-([2,2':5',2''-terthiophene]-5,5''-diylbis(octane-8,1-diyl)) diethanethioate. A solution of 5,5''-bis(8-bromooctyl)-2,2':5',2''-terthiophene (60 mg, 0.095 mmol), KSAc (40 mg, 0.33 mmol) and NaI (7 mg, 0.05 mmol) in acetone (15 mL) was refluxed under Ar atmosphere for 16 hours. The resulting brown suspension was filtered, the residue washed with cold acetone and the combined filtrates were concentrated *in vacuo*. The obtained crude product was purified by flash column chromatography on silica (CH_2Cl_2 as eluant) to give the title compound as a yellow solid (34 mg, 55 %). Found: C = 61.78, H = 7.15, S = 25.75 %. $C_{32}H_{44}O_2S_5$ requires C = 61.89, H = 7.14, S = 25.82 %. ^{1}H NMR (400 MHz, $CDCl_3$) δ = 6.97 (s, 2H, Th), 6.95 (d, 2H, J = 3.5, Th), 6.67 (d, 2H, J = 3.2, Th), 2.86 (t, 4H, J = 7.5 Hz, CH_2), 2.78 (t, 4H, j = 7.9, CH_2), 2.32 (s, 6H, CH_3), 1.67 (m, 4H, CH_2), 1,56 (m, 4H, CH_2), 1.45 – 1.28 (m, 16H, CH_2). ^{13}C NMR (100 MHz, $CDCl_3$) δ = 190.1, 145.3, 136.1, 134.7, 124.8, 123.5, 123.2, 31.5, 30.6, 30.1, 29.5, 29.2, 29.1, 29.0, 28.9, 28.7. (HRMS, CI, CH_4) 621.2019 $[M+H]^+$, $C_{32}H_{45}O_2S_5$ calc. 621.2023.

5.4 Synthesis of X[V]X

The viologen containing molecules were prepared by quaternisation of 4,4'-bipyridyl, using the corresponding 1-acetylthio-ω-bromoalkane in acetonitrile or DMF, as bromide salt.

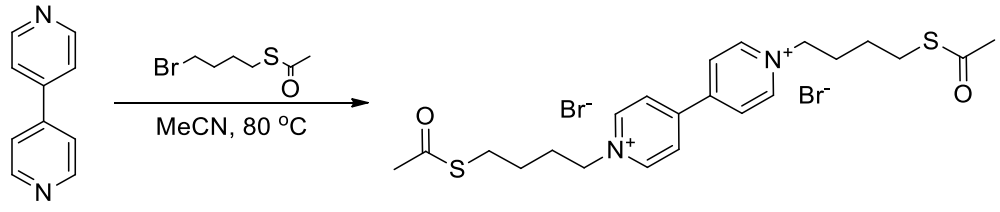

Figure 5.7: Synthetic example: preparation of 4[V]4 as bromide salt

The 4[V]4 dibromide salt resulted to be very hygroscopic, to the point of deliquescence: it was therefore dissolved in H_2O and then treated with excess NH_4PF_6 to precipitate the hexafluorophosphate salt. 1-Acetylthio-4-bromobutane was prepared according to literature

procedure.[184] The syntheses of 6[V]6 and 9[V]9 have been performed following literature procedure[185] by Horst Höbenreich. 2[V]2 [186] was synthesised by Dr. Laurent Bouffier.

5.4.2 4[V]4

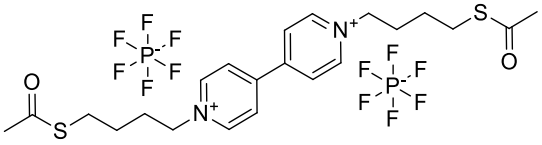

IUPAC: 1,1'-bis(4-(acetylthio)butyl)-[4,4'-bipyridine]-1,1'-diium hexafluorophosphate(V). A solution of 1-acetylthio-4-bromobutane (2.42 g, 11.45 mmol) and 4,4'-bipyridyl (0.447 g, 2.86 mmol) in MeCN (10 mL) was refluxed for 36 hours. The mixture was allowed to cool down to RT, sonicated, filtered and the precipitate was washed with cold EtOH (20 mL) and diethyl ether (20 mL), to afford the crude product as >90 % pure (NMR) deliquescent dibromide salt (*circa* 1.4 g, 85 %). A portion of the crude solid was transferred to a Schlenk flask and dried overnight *in vacuo* before weighing (0.44 g, 0.76 mmol). It was then dissolved in H_2O (25 mL) and excess NH_4PF_6 (0.51 g, 3 mmol) was added to precipitate the corresponding hexafluorophosphate salt. The resulting white suspension was stirred for 10 minutes, sonicated, filtered off, washed with cold water (25 mL) and dried overnight *in vacuo* to afford the product as a dirty white solid (0.491g, 91 %). The hexafluorophosphate salt showed no sign of hygroscopicity. Found: C = 37.26, H = 4.15, N = 3.94 %. $C_{22}H_{30}F_{12}N_2O_2P_2S_2$ requires C = 37.19, H = 4.17, N = 3.95 %. ^{1}H NMR (400 MHz, Acetone-d_6) δ = 9.46 (d, 4H, J = 7.0, Py), 8.85 (d, 4H, J = 7.1, Py), 5.09 (t, 4H, J=7.3, CH_2), 2.95 (t, 4H, J = 7.2, CH_2), 2.31 (s, 6H, CH_3), 2.82 (*obs* m, 4H, CH_2), 1.75 (m, 4H, CH_2). ^{13}C NMR (100 MHz, Acetone-d_6) δ = 219.3, 194.9, 150.2, 146.1, 61.6, 30.2, 29.7, 27.6, 26.2. MS: m/z 563 $[M\text{-}PF_6]^+$, 731 $[M+Na]^+$. *m/z* (HRMS, ES+, MeOH) 731.0928 $[M+Na]^+$. $C_{22}H_{30}F_{12}N_2O_2NaP_2S_2$ calc. 731.0930.

5.5 Synthesis of Ph[T]Ph

The conjugated molecular wire was synthesised by Pd/Cu catalysed Sonogashira coupling between 2,5-diethynylthiophene and S-(4-iodophenyl)ethanethioate in THF:DIPA 5:1.[187]

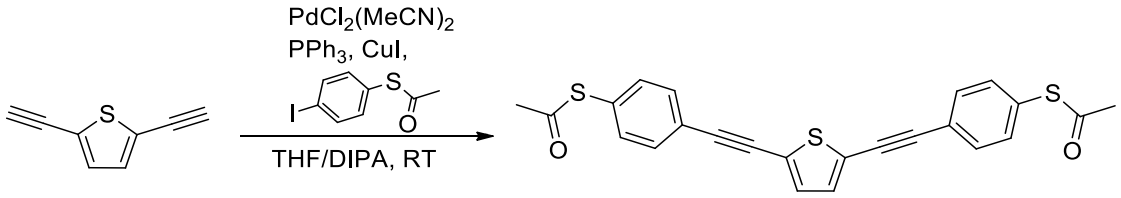

Figure 5.8: Synthesis of Ph[T]Ph.

2,5-Diethynylthiophene was prepared following the procedure developed by Neenan and Whitesides,[188] involving Pd/Cu catalysed Sonogashira coupling of 2,5-dibromothiophene with TMS-acetylene in DIPA and subsequent removal of the TMS protecting group by treatment with K_2CO_3 in MeOH:CH_2Cl_2 1:1.

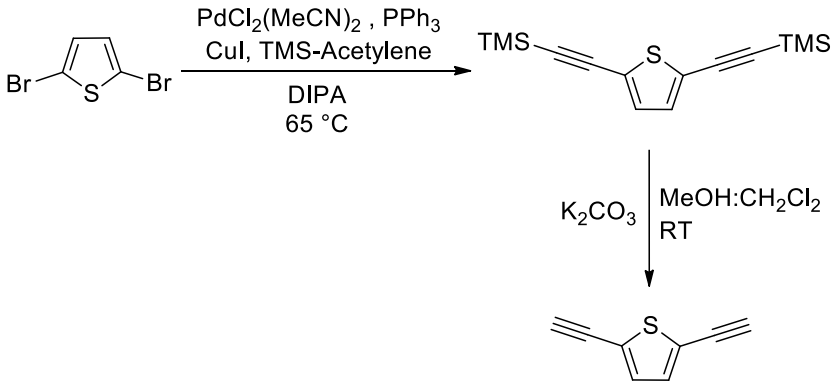

Figure 5.9: Synthesis of 2,5-diethynylthiophene

S-(4-Iodophenyl)ethanethioate is not commercially available and has been synthesised in 42% yield by Cu-catalysed coupling of 1,4-diiodobenzene with potassium thioacetate, modifying the procedure developed by Soria-Castro and Penenory.[189]

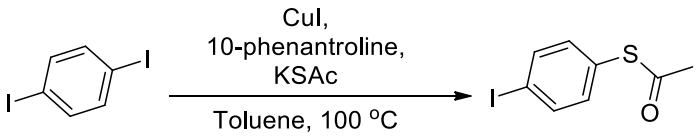

Figure 5.10: Synthesis of S-(4-iodophenyl)ethanethioate.

5.5.1 S-(4-Iodophenyl)ethanethioate

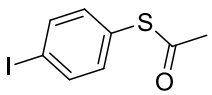

A solution of 1,4-diiodobenzene (1,65 g, 5 mmol) in dry toluene (40 mL) was degassed by bubbling Ar through for 30 minutes in a Schlenk flask. CuI (95 mg, 0.5 mmol), KSAc (0.685 g, 6 mmol) and 1,10-phenantroline (180 mg, 0.1 mmol) were added while keeping the flask

in a gentle stream of dry argon and the resulting suspension was stirred for 24 h at 100 °C, after which time the colour changed to deep brown. Upon cooling, 50 mL of H_2O were added and the organic layer was separated. The aqueous layer was extracted with CH_2Cl_2 (2 x 25 mL), the combined organics washed with brine and dried over $MgSO_4$. The solvent was removed to yield a red crude product that was purified by flash column chromatography on silica (20 % CH_2Cl_2 in hexanes as eluant) to give the title compound as a pale yellow solid (0.581 g, 42 %). ^{1}H NMR (400 MHz, $CDCl_3$) δ = 7.65 (d, J = 8.3 Hz, 2H, Ph), 7.03 (d, J = 8.5 Hz, 2H, Ph), 2.32 (s, 3H, CH_3). ^{13}C NMR (100 MHz, $CDCl_3$) δ = 193.2, 138.3, 135.9, 127.6, 95.9, 30.3. *m/z* (HRMS, CI, NH_3) 295.9609 $[M+NH_4]^+$, $C_8H_{11}NIOS$ calc. 284.9606.

5.5.2 Ph[T]Ph

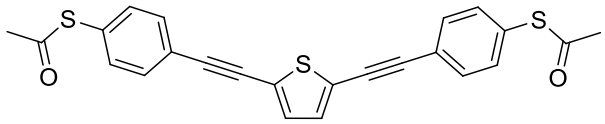

IUPAC: S,S'-((thiophene-2,5-diylbis(ethyne-2,1-diyl))bis(4,1-phenylene)) diethanethioate. THF:DIPA (5:1, 30mL) was degassed by bubbling Ar through for 30 minutes prior to the addition of S-(4-iodophenyl)ethanethioate (0.45 g, 1.62 mmol), $PdCl_2(MeCN)_2$ (25 mg, 0.09 mmol), PPh_3 (75 mg, 0.28 mmol) and CuI (18 mg, 0.09 mmol). After flushing with Ar for additional 10 minutes, 2,5-diethynylthiophene (0.126 g, 0.95 mmol) was added and the reaction stirred for 16 hours at room temperature under Ar. Water (30 mL) was added to the resulting orange suspension and the product was extracted with CH_2Cl_2 (3 x 25 mL). The combined organic portions were dried over $MgSO_4$ and the solvent was removed *in vacuo* to give a red crude product. Purification by flash column chromatography on silica (5 % EtOAc in hexanes as eluant) afforded the title compound as yellow solid (0.085 g, 25 %). Found: C = 66.61, H = 3.82, S = 2.18 %. $C_{24}H_{16}O_2S_3$ requires C = 66.64, H = 3.73, S = 22.24 %. ^{1}H NMR (400 MHz, $CDCl_3$) δ = 7.54 (d, J = 8.5 Hz, 4H, Ph), 7.40 (d, J = 8.5 Hz, 4H, Ph), 7.18 (s, 2H, Th), 2.44 (s, 6H, CH_3). ^{13}C NMR (100 MHz, $CDCl_3$) δ = 193.2, 134.2, 132.2, 131.9, 128.7, 124.7, 93.5, 83.8, 30.3. *m/z* (HRMS, CI, CH_4) 433.0384 $[M+H]^+$, $C_{24}H_{17}O_2S_3$ calc. 432.0391.

STM Measurements

CHAPTER 6

By the means of Telescopes, there is nothing so far distant but may be represented to our view; and by the help of Microscopes, there is nothing so small as to escape our inquiry; hence there is a new visible World discovered to the understanding.

Robert Hooke, 1665.

In the last 20 years a number of methods to measure single molecule conductance has been developed and consolidated. In this thesis three STM-based techniques (*I(z)*, *I(t)* and *STM-BJ*) have been employed for the conductance measurements and further electrical characterisation has been achieved by measuring I-V curves, either on self-assembled monolayers, or at the single molecule level using single point STS or an implementation of the *I(v,z)* technique. In this chapter the experimental procedure are described for the preparation of STM samples, the measurement conditions employed and details of the statistical data analysis used to obtain conductance values.

6.1 Gold on Glass Sample Preparation

The commercial polycrystalline gold slides used (11x 11 mm gold-on-glass, Arrandee® GmbH, DE – 250 nm Au | 2.5 nm Cr | 0.7 mm borosilicate glass) have high RMS roughness and cannot be successfully employed in STM measurements as they are shipped: they require flame annealing with a Bunsen burner or a butane torch. The annealing process involves heating the sample held at ~45° in the flame until it glows red and then keeping it glowing for 10 s by moving it in and out of the flame. It is important to avoid overheating of the substrate as this will result in bent samples that can cause frequent tip crashes while undertaking STM measurements. The sample is then allowed to cool down for 30 s and the process is repeated three times. This procedure leads to the formation of atomically flat Au terraces, as can be seen in Figure 6.1, which shows triangular (111) morphology and one-atom-deep step-like features (image rendered using Nanotech WsXM software[190]). The sample is allowed to spontaneously reach room temperature before use.

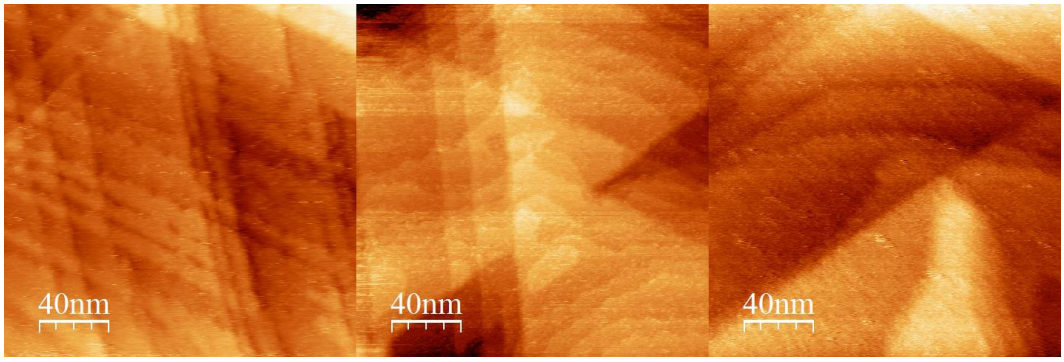

Figure 6.1: STM images (200x200 nm) of gold on glass samples after flame annealing

6.2 SMC Experimental Techniques

In all the experiment performed in this thesis, an STM (former Molecular Imaging PicoSPM I, now Agilent 4500 SPM, Agilent Technologies Inc., USA or an Agilent 5500 SPM, Agilent Technologies Inc., USA) equipped with a freshly cut gold tip (Goodfellow Cambridge Ltd., UK - 99.99+%, 0.25mm), is used to form metal|molecule|metal junctions.

In the *I(z)* method,[43] molecules are adsorbed on the surface by dipping flame-annealed gold-on-glass samples in a 10^{-4} M solution of the appropriate molecular wire and the tip is held above the surface at a desired setpoint current and bias voltage. The feedback loop is disabled and the tip is withdrawn along the vertical axis at constant speed (10 – 40 nm s^{-1}) while maintaining a constant *x-y* position. During the withdrawal a current-distance (*I-z*) curve is collected. If a molecule bridges the gap between the tip and the surface, a characteristic shape is observed in *I(z)* curves: the current (*I*) decreases with distance (*z*) to settle at a plateau, typical of conductance across the Au|molecule|Au junction, and then it abruptly decays to zero when the junction is broken. Step-like features are common in these current-distance scans and point to multiple molecules bridging the contacts (i.e. more than one molecule sitting in the tip-substrate gap): they occur at integer multiples of a single value. Multiple steps in a single retraction trace may also result from different distinct binding configurations.

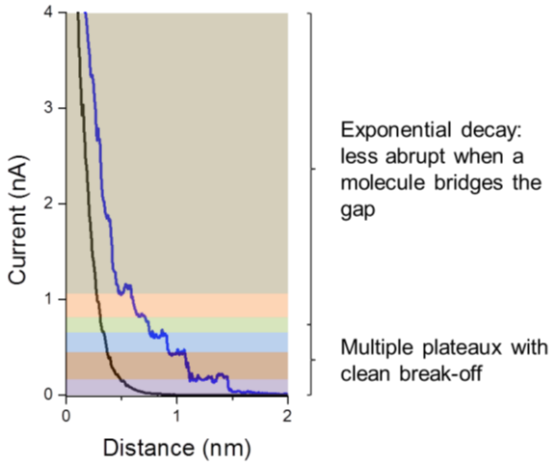

Figure 6.2: Current decay *I(z)* scans: control curve for a clean Au surface (black) and the response for a dithiol compound bridging the gap (blue). Evidence of multiple bridging at integer multiples of a single value (color-coded as guide to the eye) can be seen.

The experimental break-off distance must be reasonably consistent with the length of the molecules (contact-to-contact) to provide confirmation that we are dealing with molecular

events and that the conductance pathway is from a sulfur end to the other, with the molecule in a fully-extended configuration. Many *I(z)* traces are recorded, and only those that show discernible plateaux (300-800 per experiment) are collected together in histogram plots to determine conductance values. The occurrence of plateaux in *I(z)* curves results in peaks in the conductance histograms. The same *I(z)* traces are used to compose 2-dimensional density plots, accounting for the experimentally determined tip-sample separation (z_0) before tip withdrawal. These 2D "density" plots are used to check the break-off values for the junctions, i.e. that the measured value represents conductance across the entire molecule in its extended configuration, ruling out the possibility of alternative pathways (different conformers, gold-thiophene contact, etc.).

In the *STM-BJ* technique,[51] the tip is deliberately pushed into the surface before withdrawal in the presence of either a sub-monolayer or a dilute solution of the appropriate molecular wire, while keeping a constant bias voltage across the junction. As the tip is withdrawn after crashing into the surface, the current decreases in quantised G_0 steps until a single gold atom bridges the junction, and the conductance is equal to G_0, 77.4 nS. After the Au-Au monoatomic contact is broken, the two separated gold electrodes "snap back" and a nanogap of ≈ 0.5 - 0.7 nm is created.[191] The snap-back of the two leads results in an abrupt decay in conductance of several orders of magnitude. When a molecule present in solution bridges the Au-Au gap, conductance through its backbone results in plateaux similar to those seen in the *I(z)* technique. The STMs used throughout this thesis are equipped with current follower with an upper limit of 100 nA, and it is not possible to observe G_0 steps during *STM-BJ* experiments at the bias voltage applied. Nevertheless, the occurrence of abrupt decay in current typical of snap-back of the gold electrodes is a signature of the break-off of a clean Au-Au contact and traces that did not show a clear snap-back were discarded and not included in the data analysis.

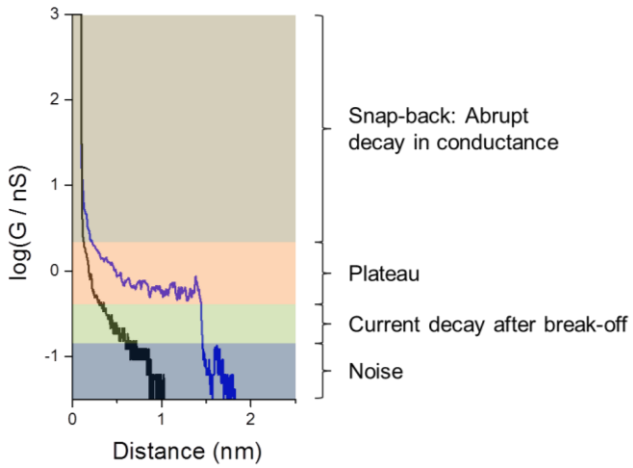

Figure 6.3: Current decay *I(z)* scans: baseline for a clean Au surface (black) and response a dithiol compound bridging the gap (blue). Evidence of snap-back of the leads and molecular bridging leading to plateau and break-off (color-coded as guide to the eye) can be seen.

The *I(z)* technique mainly differs from the *STM-BJ* technique originally developed by Xu and Tao[51] in that no physical contact between gold tip and gold substrate occurs prior to the formation the molecular junctions. The geometry of the STM tip is essentially unchanged for the entire duration of experiments, increasing stability and reproducibility of single molecular junctions and reducing noise. The *STM-BJ* technique usually has a noise threshold of 0.7 – 0.07 nS (10^{-5} – 10^{-6} G_0),[191] while the *I(z)* technique allows the measurement of rather poorly conductive molecular wires, with a noise level of 5-0.5 pS (10^{-7} – 10^{-8} G_0). Moreover, as the tip is maintained sharp, it is possible periodically to monitor the gold surface with imaging at high resolution.

The *I(t)* technique[52] is different from the aforementioned ones as the tip is not moved along the *z* axis; the current is monitored as a function of time, while the x-y position of the tip is fixed and the feedback loop is disabled. During an *I(t)* experiment, lasting between 200 ms and 1 s, characteristic jumps can be observed in the tunnelling current as molecular junctions are stochastically formed and broken. The tunnelling parameters (setpoint current and bias voltage) are chosen to have a tip-substrate gap shorter than the length of the molecule.

6.3 Distance (z_0) Calibration

Current-distance traces were aligned for display as 2D "density" plots using extrapolation routines. During the *I(z)* experiments, a number of exponential decay scans showing no trace

of molecular bridging were plotted as ln(*I*) *vs* distance (*z*), and linear regression was used to determine the slope of the linear part of these plots. These were then extrapolated back to the metal-to-metal point contact conductance (G_0, 77.4 μS) and Equation 6.1 was used to calculate the initial tip-sample separation.

$$z_0 = \frac{\ln\left(G_0 \, {}^{V_{BIAS}}/_{I_0}\right)}{{}^{dlnI}/_{dz}} \qquad \textit{Equation 6.19}$$

The same approach was used to align traces in the *STM-BJ* experiments. It has been demonstrated that after about 20 cycles of repeated indentation the two metallic electrodes are shaped into tips of reproducible structure and shape.[192] This is referred to as "mechanical annealing". The distance between the two metallic leads at the start of the push-pull has therefore been calculated using the aforementioned extrapolation routine after mechanical annealing of the 2 electrodes (tip and surface). The calculated initial tip-sample separation was then added to the individual scans that are displayed statistically in the form of 2D "density" plots (*vide infra*).

6.4 Current *vs* Distance Trace Selection

In the *I(z)* and *STM-BJ* techniques, the hit-rate (percentage of scans showing molecular bridging) is usually below 30%, and curves that did not show evidence of junction formation, but just a monotonic current decay, were discarded and not included in the statistical analysis. As discussed in Chapter 1, thiolate moieties can bind to gold in two different geometries: at a step site, with higher conductance (H) and on defect-free flat regions, with lower conductance (L). This gives rise to three different contact groups, High (or C, HH configuration), Medium (or B, HL) and Low (or A, LL).

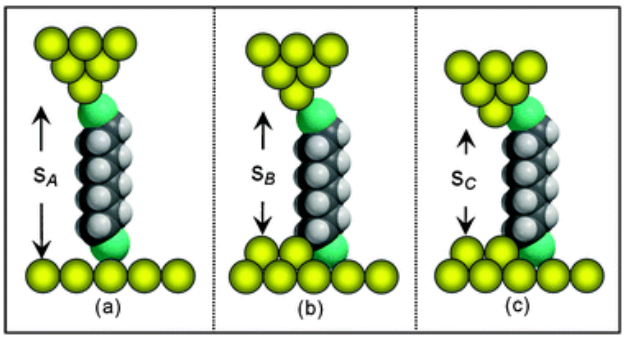

Figure 6.4: Three possible configuration of a dithiol molecular bridge between Au contacts: (a) shows both sulfur atoms in a low conducting geometry, bound to single gold atoms or terrace sites; (b) shows the bottom thiolate contact in high conducting geometry, adsorbed on a step site; (c) shows both sulfur contacts adsorbed in high conducting sites. *Reprinted from ref. 79.*

Multiple bridging, noise and stochastic switching of molecular conductance can smear the conductance groups in a single broad peak in the histograms, and this effect is particularly strong for poorly conducting molecules due to electrical and mechanical noise. Using different techniques and exploiting the properties of these contact groups is a way to select traces belonging to one group from the others with a good degree of confidence. Contact groups have different distribution across the *I(z)* and the *STM-BJ* technique, and depending on the roughness of the gold surface[81]: on very flat surfaces, the *I(z)* technique at relatively low setpoint current (1-10 nA) promotes the formation of low conductance junctions, involving low-coordinate contact groups, while only the *STM-BJ* technique efficiently promotes the formation of high conductance junctions, involving more highly coordinated contact groups, for instance at step edges.

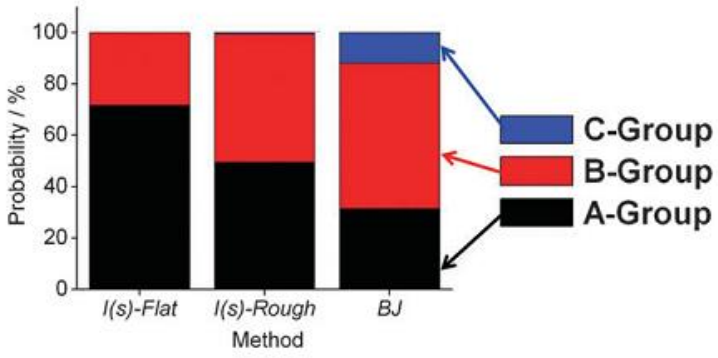

Figure 6.5: Distribution of conductance groups across two different techniques on substrate of variable roughness (bottom panel). *Reprinted from ref. 81.*

Therefore, the low-setpoint *I(z)* technique has been used on very flat Au (111) regions of the gold sample (showing triangular reconstruction by STM imaging) to find and isolate the

lowest value of conductance, and switching to the *STM-BJ* technique facilitated observation of the highest contact group. The remaining group, that could be seen using both techniques (*STM-BJ* and *I(z)* at higher setpoint) has been attributed to the medium conductance value.

6.5 *I-V* Curves (current-voltage characteristics)

As discussed in Chapter 1, *I-V* curves are a representation of the relationship between the electric current through a material and the corresponding potential difference across it. Such curves can be used as a tool to determine and understand the basic parameters of a component or device and mathematically model its behaviour within an electronic circuit.

Since the *I-V* characteristic is a convolution of the electronic structure of the junction, it is critically affected by the shape and density of states of the two electrodes. Therefore, atomically sharp tips used for STM imaging, that have a non-uniform electronic structure, produce unreliable spectroscopy, while blunt tips with poor spatial resolution are more likely to be successfully used to obtain reproducible current-voltage curves. At the same time the optimal STS tip should have a symmetric geometry to avoid artefacts. For these reasons, Au tips used to obtain *I-V* curves have been mechanically annealed with a cycle of 50 repeated indentations into the Au substrate prior use: this is known to produce well-defined, symmetric tips[192], although with poor imaging resolution.

Substrates for STS were prepared by flame annealing of gold-on-glass slides and molecular adsorption from solution as discussed previously for SMC measurements. After mechanical annealing of the tip, the tunnelling parameters (setpoint current and voltage bias) are chosen to have a tip-substrate gap shorter than the length of the molecule and the feedback loop is disabled. The voltage is then swept between two values (usually -1 and 1 V) while recording the current. Two different types of *I-V* curves are usually seen: a linear, "metallic" behaviour when the tip-substrate gap is empty (metal-to-metal tunnelling) and semiconductor-type behaviour when a molecule bridges the gap. The occurrence of junctions with different contact geometries results in different slopes of the linear region of the *I-V* characteristics. A large number (50-100) of such curves is collected and the spurious data (arising from contamination or noise, or containing clear artefacts or molecular bridge destruction) is

discarded. An implementation of the *I(V,z)* technique[53] has also been used when it was difficult to select data belonging to different contact groups. In this technique, the tip is held over the surface at high setpoint (>60 nA) and then retracted in small increments (≈ 0.1 nm) by subsequently decreasing the setpoint current: *I-V* curves are taken at each step by sweeping the potential between two values. This produces a series of curves as a function of distance from the surface. When there is no molecule in the junction, the set of *I-V* curves has metallic, linear behaviour with decreasing slope. If a molecule bridges the tip-substrate gap the curve set tends to converge towards groups of semiconductor-type behaviour, characteristics of the different contact groups of the molecule.

6.6 Statistical Analysis in *I(z)* and *STM-BJ* Experiments

As previously discussed, electrical and mechanical noise, multiple bridging and occurrence of various molecular conformers cause oscillation in the current during SMC measurement, and the data needs statistical analysis to obtain an average zero-bias conductance value. Throughout this thesis, data has been analysed and presented in the form of 1D histograms and 2D "density" plots. The raw current data is first converted to conductance using Equation 6.2:

$$\sigma = \frac{I}{V_{BIAS}} \qquad \textit{Equation 6.20}$$

where σ is the conductance (expressed in nanosiemens, nS), *i* is the current from the raw data (expressed in nanoamperes, nA), and V_{BIAS} is the voltage applied across the tip-substrate gap. All the so-obtained conductance-distance scans are combined and plotted as frequency histograms, using appropriate bin sizes according to the molecular conductance. The occurrence of plateaux in the current-distance curves results in peaks in the histograms: the absolute conductance value and standard deviation is calculated from the histogram peak using descriptive statistics algorithms (OriginPro9®, OriginLab Corp., USA).

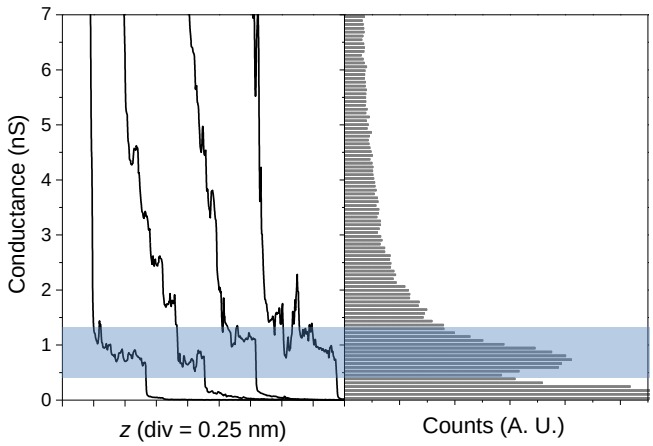

Figure 6.6: Examples of I(z) scans (left) for 5[T3]5 in air at 298 K and conductance histogram (right) obtained from 500 such scans (0.07 nS bin size). Area of plateau occurrence and histogram peak are highlighted as guide to the eye. σ = 0.78 ± 0.25 nS

The same conductance-distance scans are used to obtain 2D "density" plots using 2D frequency count and binning algorithms (OriginPro9®, OriginLab Corp., USA). A matrix of 100 x 100 bins is calculated using such algorithms and it is used to obtain a colour fill (blue to red) contour plot. In such 2D "density" plots, the occurrence of plateaux in the current-distance scans results in high density (red) areas, at the same conductance values observed in the 1D histograms, that usually extend in the *x* axis to match the length of the Au|*molecule*|Au junction.

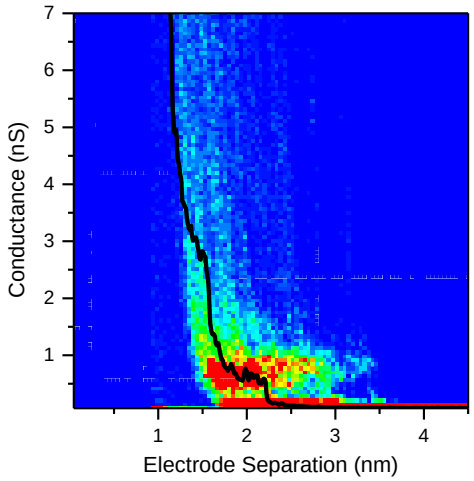

Figure 6.7: 5[T3]5 2D "density" plot (0.045 nm *x* bin size, 0.07 nS *y* bin size) built from 500 scans with a single *I(z)* trace superimposed. The Au|5[T3]5|Au junction is 2.81 nm wide (contact-to-contact) and the high density (red) feature at 0.78 nS extends to ≈ 2.7 nm, thus confirming the conductance value for the molecule in a fully extended geometry. The plot has been calibrated accounting for s_0 (initial electrode distance) that, at 7 nA setpoint and 0.3 V tip bias is 0.9 nm.

Conclusions

CHAPTER 7

That's all, folks!

Porky Pig, 1938.

The major focus of this thesis has been to investigate the effect of the environment surrounding a molecular junction on its conductance, measured using STM techniques. Molecules containing an oligothiophene core were chosen as a primary focus as they presented several known properties both as environmental-dependent molecular wires, such as water[62] and electrochemical[99] gating, and as bulk materials, such as the possibility of doping[94] to achieve higher conductivity. At the beginning of the research project, it was decided to sandwich the oligothiophene core between two insulating chains, to have molecular systems similar to those measured by Leary *et al.*,[62] and to provide the molecules with thiol contacts, as they were considered a robust choice in terms of reliability of measurements and their vast use in the literature[38,43,79,82,84,126,127,136,193]. Several molecular wires with a terthiophene conjugated core and thiaalkanes of varying length as side chains, were synthesised using common organic laboratory techniques, and some unusual properties were discovered during the measurement of their conductance.

First, the length of the two side-chains showed to have little effect on the conductance of molecular junction prepared with terthiophene-containing molecular wires, with a very low attenuation factor of only 0.07 per methylene units in ambient conditions. When water was removed from the environment, their conductance decreased and the attenuation factor increased slightly, to 0.1 per methylene. This unusually shallow decay with length prompted a series of experiments on similar molecular wires having a different conjugated core, which were synthesised to have their conductance measured. The nature of the conjugated central unit was found to have a very strong effect on the conductance attenuation with length, and this was attributed, after a series of theoretical calculations, to the gateway state generated by the coupling of the molecular backbone to the sulfur-Au contacts, within a coherent tunnelling mechanism.

During the measurements performed using 5[T3]5 (having a terthiophene core and two pentyl chain) as molecular wire, it was discovered that its conductance increased with temperature. A new set of molecular wires, this time with a conjugated core of varying number of thiophene rings and constant number of methylene in the side chains, were synthesised, and their conductance measured as a function of temperature. 5[T]5, having only one thiophene ring as tunnelling indentation, showed no temperature dependence, and 5[T2]5,

with a bithiophene core, had a thermally-activated behaviour, albeit with activation energy lower than its terthiophene counterpart. The synthesised molecular wires were sent to Cardiff, to have their properties investigated under UHV (*i.e.* in absence of ambient moisture), as it was reasoned that the observed water gating effect could have an effect on the thermal activation. Surprisingly, this turned out to be true, as no thermal activation was found for the three molecular wires under UHV. Theoretical calculations were able to explain the observed behaviour within a coherent tunnelling mechanism, as the presence of water triggers a shift of transport resonance towards the Fermi level, thus increasing conductance, and thermal broadening of such resonances accounts for the temperature dependence of conductance.

Water therefore has a strong effect on both the molecular conductance and its behaviour with temperature, and it was postulated that many other compounds could form complexes with the terthiophene moiety. Supramolecular interactions such as charge-transfer complexes were chosen as there is ample literature on the subject, and oligothiophenes readily forms such complexes with strong electron acceptors such as TCNE.[164] Furthermore, experiments performed by Kasibhatla *et al.* showed that TCNE complexation of molecules assembled in a monolayer on a gold surface caused a significant change in the conductance spectra. Terthiophene- and phenyl-containing molecular wires were therefore treated with a variety of electron deficient molecules, and the resulting CT complex had conductance enhanced by a factor ranging from 20 to 100 times. DFT and transport calculations suggested that the generation of an interference in the transmission curves is responsible for the experimental behaviour, and the conductance enhancement is dependent on the binding constant of the complex.

In summary, this thesis has shown that both the molecular structure and the surrounding environment of a molecular junction have a strong effect on its electrical conductance and its thermal behaviour. Thiol contacts, among the first used in molecular electronics as a mean of connecting a molecular backbone to metallic electrodes, showed to have still a number of undisclosed properties, and they might be an ideal candidate for charge transport across long molecular wires thanks to the observed low attenuation with length. At the same time, the presence of a moiety that can coordinate to water or electron-deficient molecules provides the opportunity to tune the conductance across the junction by forming supramolecular

complexes. A number of further experiments are required to fully characterise the phenomena presented in this thesis, and it is hoped that this work will provide background and inspiration for such future studies.

Single Molecule Conductance Data

APPENDIX A

Data! Data! Data! I can't make bricks without clay!

Sir Arthur Conan Doyle, 1892.

Data obtained from STM measurements are presented as histograms (100 bins) and 2d "density plots" (100 x 100 matrix), each of them obtained from 300 - 800 individual *I(z)* or *STM-BJ* scans. Conductance values presented in this thesis were calculated from the raw data histogram using a descriptive statistical algorithm (OriginPro9®, OriginLab Corp., USA). Technique and experimental conditions are reported for each plot in the caption. See Chapter 6 for details about the techniques, data selection criteria and statistical analysis.

A.1 1[T3]1 in Air, 295K

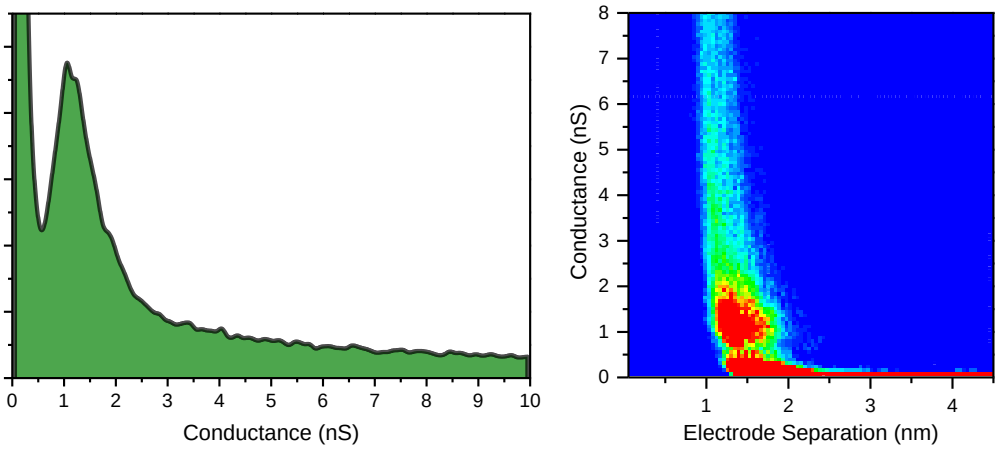

Figure A1: SMC data for 1[T3]1 contact group B in air.
I(z) technique, 20 nA setpoint, 0.3 V tip bias.

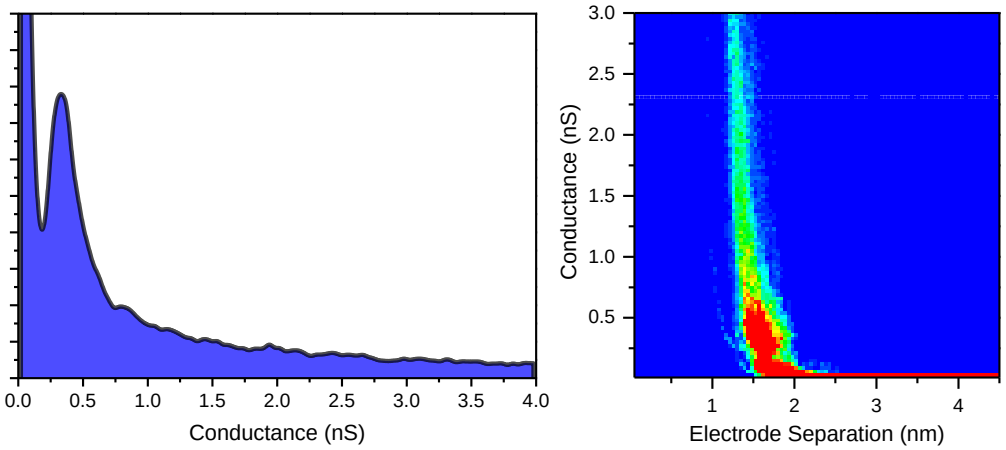

Figure A2: SMC data for 1[T3]1 contact group A in air.
I(z) technique, 9 nA setpoint, 0.3 V tip bias.

A.2 3[T3]3 in Air, 295K

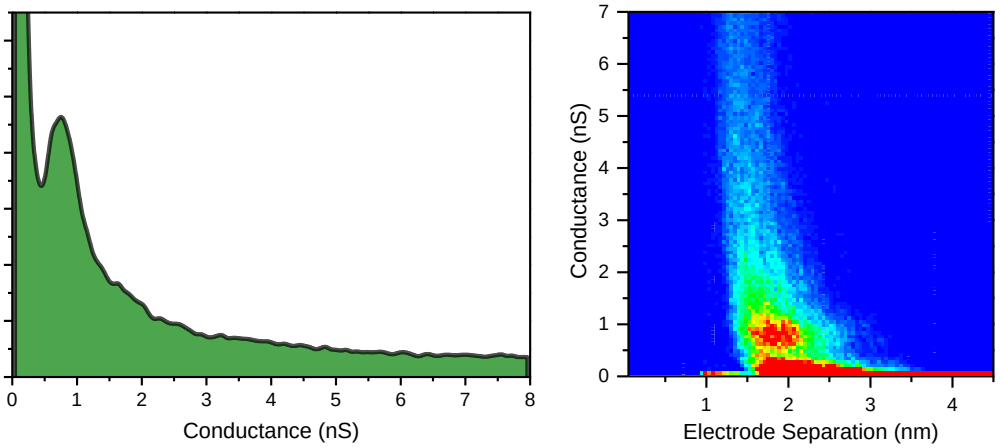

Figure A3: SMC data for 3[T3]3 contact group B in air.
I(z) technique, 7 nA setpoint, 0.3 V tip bias.

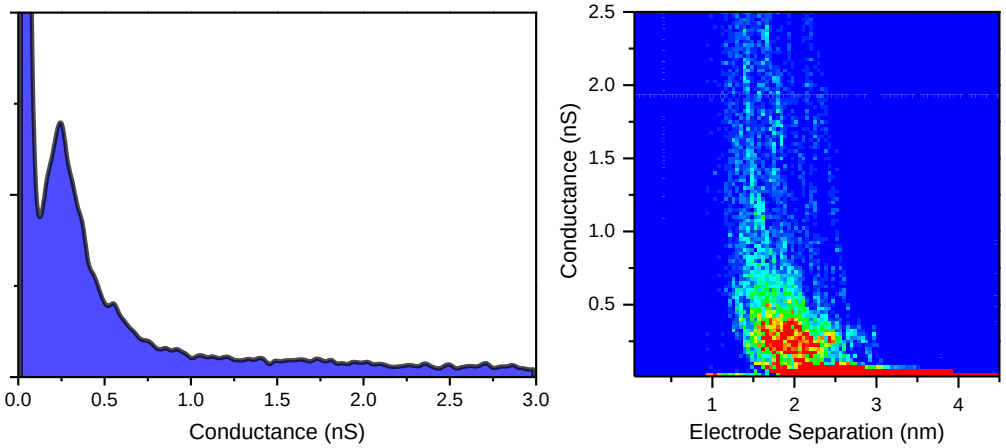

Figure A4: SMC data for 3[T3]3 contact group A in air.
I(z) technique, 7 nA setpoint, 0.3 V tip bias.

A.3 4[T3]4 in Air, 295K

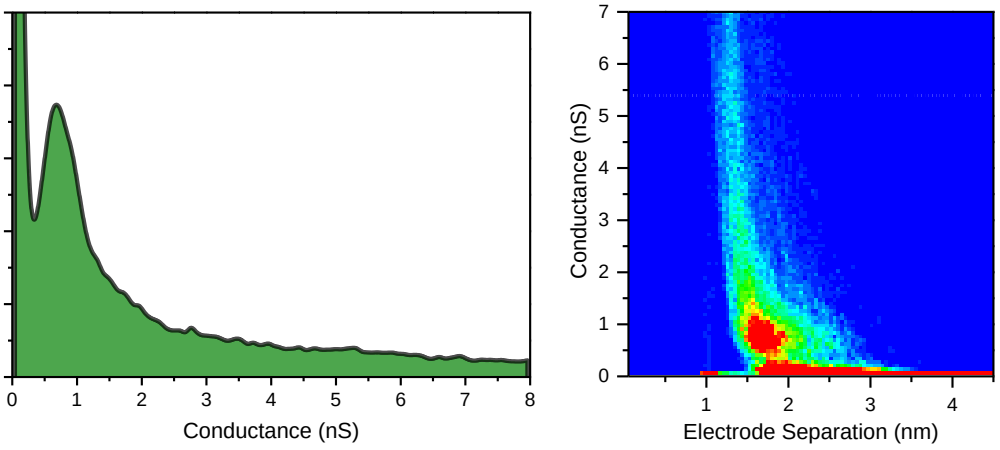

Figure A5: SMC data for 4[T3]4 contact group B in air.
I(z) technique, 7 nA setpoint, 0.3 V tip bias.

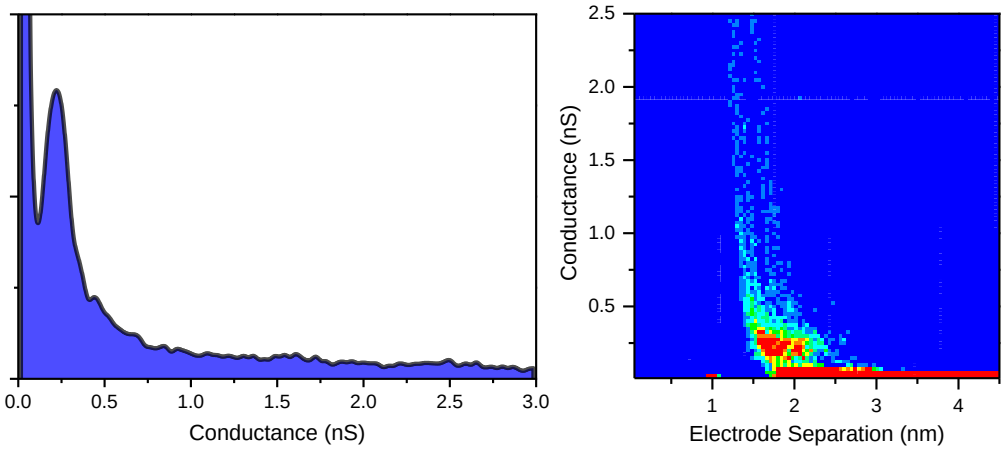

Figure A6: SMC data for 4[T3]4 contact group A in air.
I(z) technique, 7 nA setpoint, 0.3 V tip bias.

A.4 5[T3]5 in Air, 295K

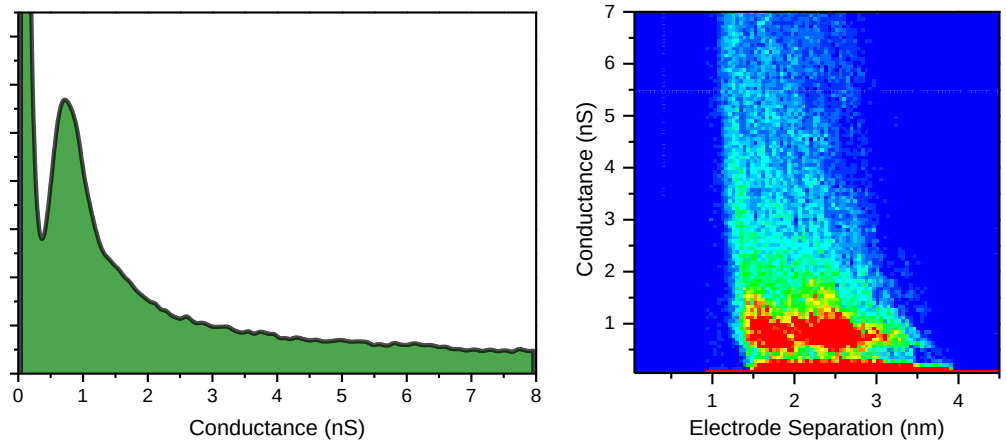

Figure A7: SMC data for 5[T3]5 contact group B in air.
I(z) technique, 7 nA setpoint, 0.3 V tip bias.

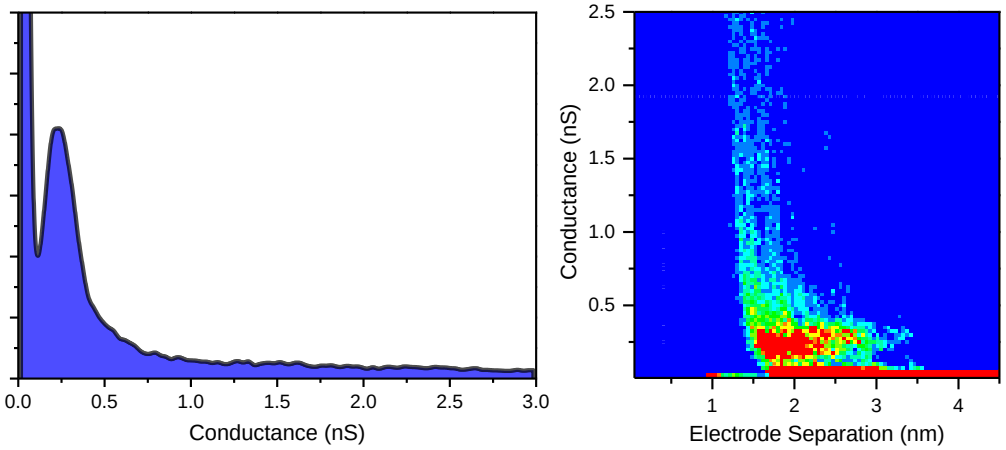

Figure A8: SMC data for 5[T3]5 contact group A in air.
I(z) technique, 7 nA setpoint, 0.3 V tip bias.

A.5 6[T3]6 in Air, 295K

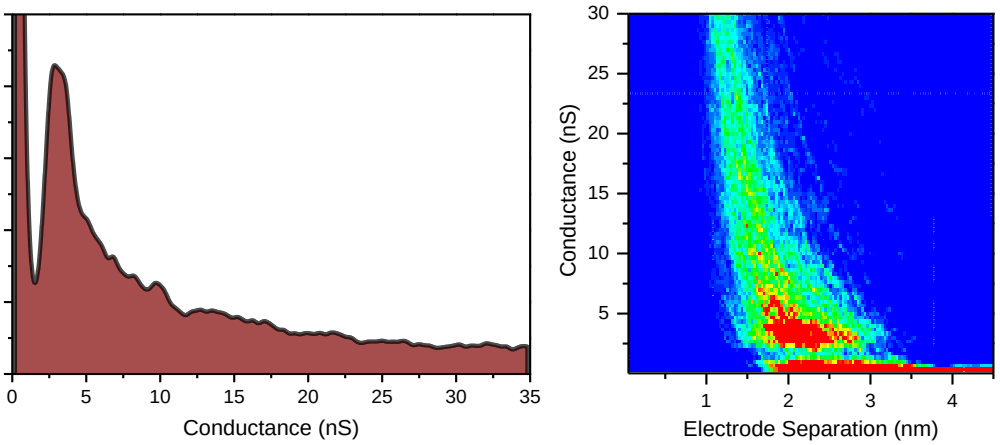

Figure A9: SMC data for 6[T3]6 contact group C in air.
STM-BJ technique, 0.3 V tip bias.

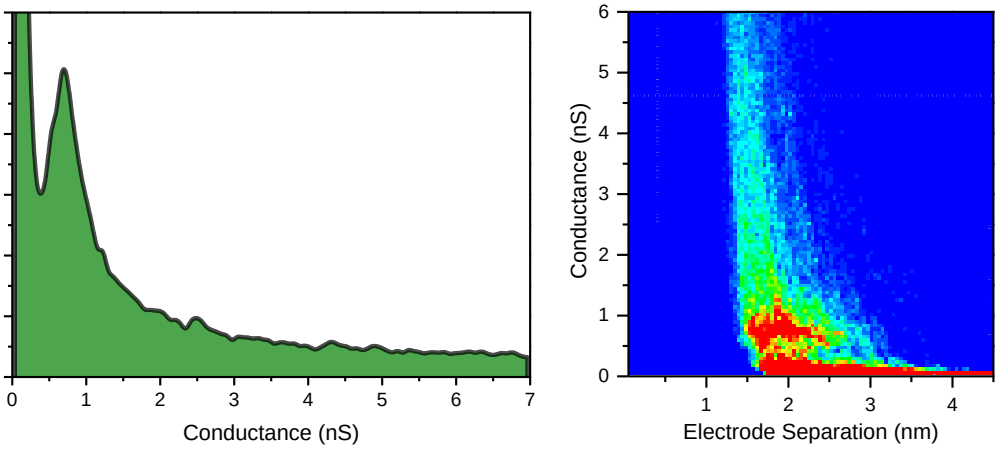

Figure A10: SMC data for 6[T3]6 contact group B in air.
I(z) technique, 7 nA setpoint, 0.3 V tip bias.

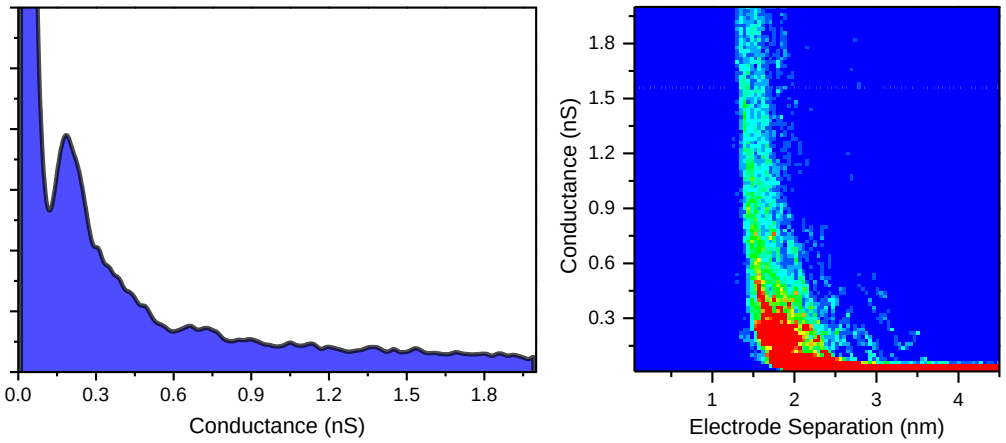

Figure A11: SMC data for 6[T3]6 contact group A in air.
I(z) technique, 7 nA setpoint, 0.3 V tip bias.

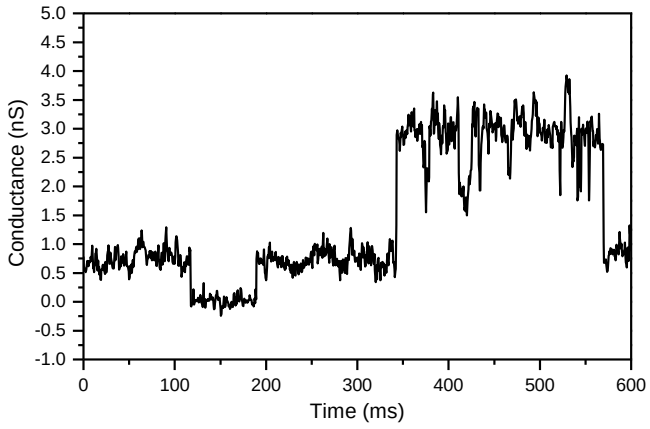

Figure A12: *I(t)* scan for 6[T3]6 in air. Current jumps corresponding to the B (≈ 0.7 nS) and C (≈ 3 nS) contact groups conductance can be seen.
I(t) technique, 1 nA setpoint, 0.3 V tip bias.

A.6 8[T3]8 in Air, 295K

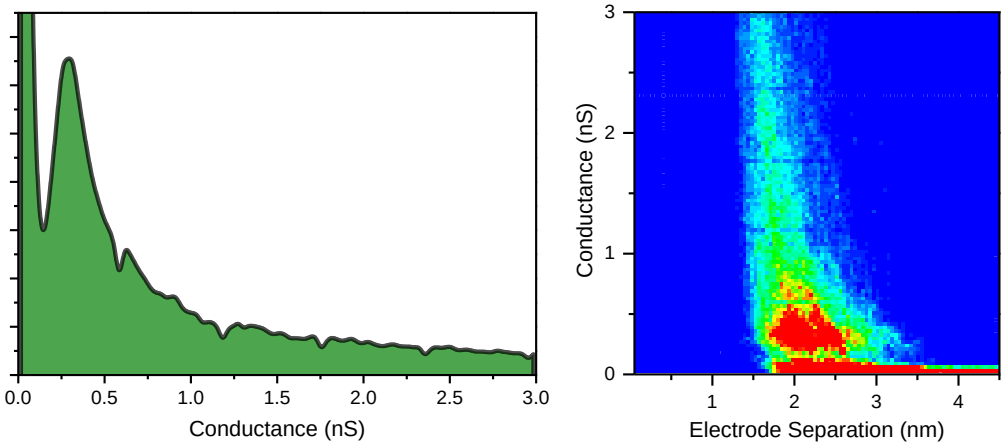

Figure A13: SMC data for 8[T3]8 contact group B in air.
I(z) technique, 6 nA setpoint, 0.3 V tip bias.

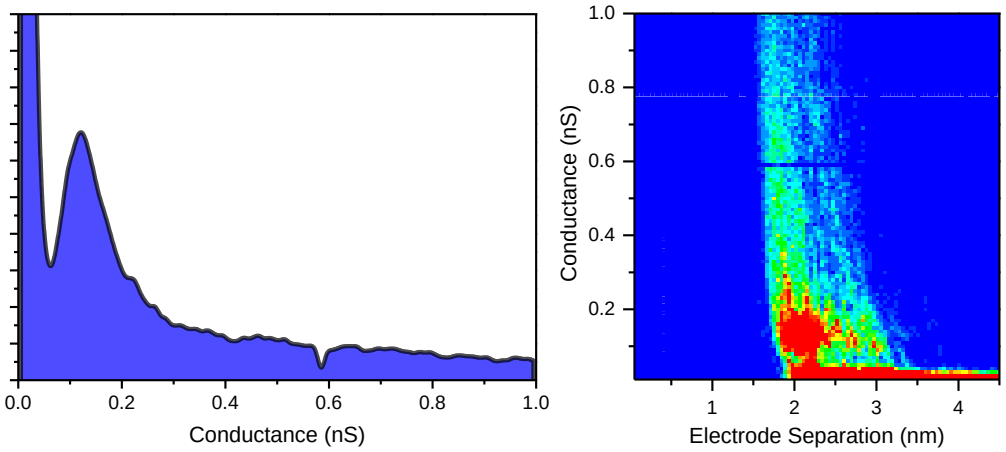

Figure A14: SMC data for 8[T3]8 contact group A in air.
I(z) technique, 4 nA setpoint, 0.3 V tip bias.

A.7 1[T3]1 in Argon, 295 K

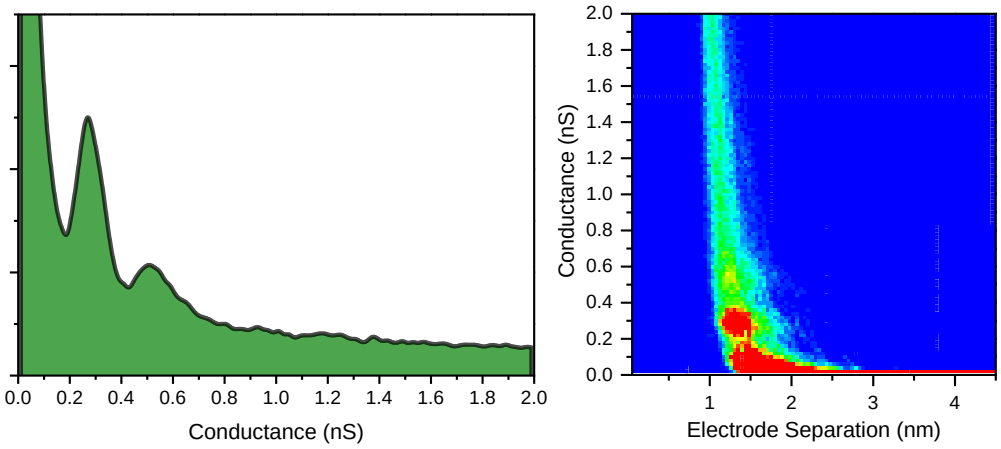

Figure A15: SMC data for 1[T3]1 contact group B under dry Ar.
I(z) technique, 10 nA setpoint, 0.3 V tip bias.

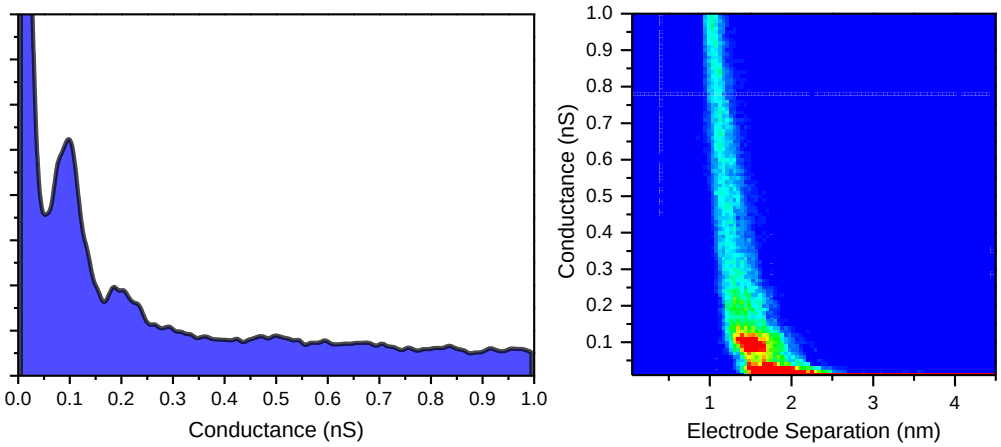

Figure A16: SMC data for 1[T3]1 contact group A under dry Ar.
I(z) technique, 7 nA setpoint, 0.3 V tip bias.

A.8 3[T3]3 in Argon, 295 K

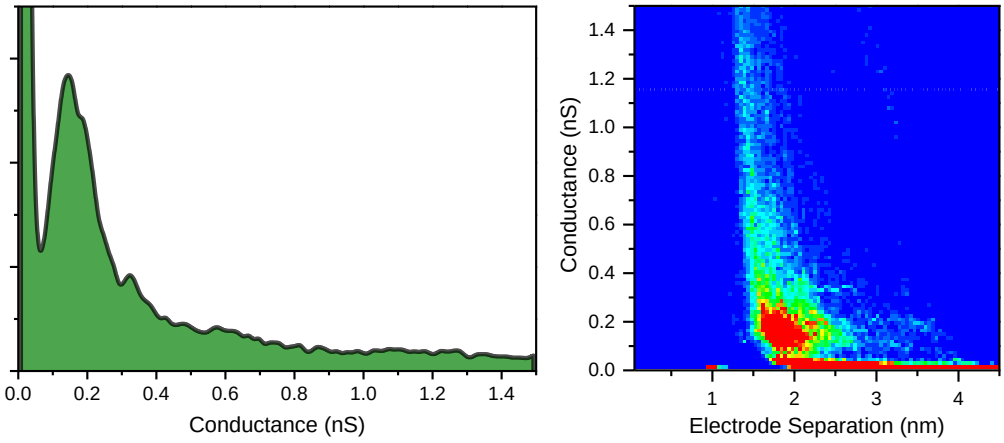

Figure A17: SMC data for 3[T3]3 contact group B under dry Ar.
I(z) technique, 7 nA setpoint, 0.3 V tip bias.

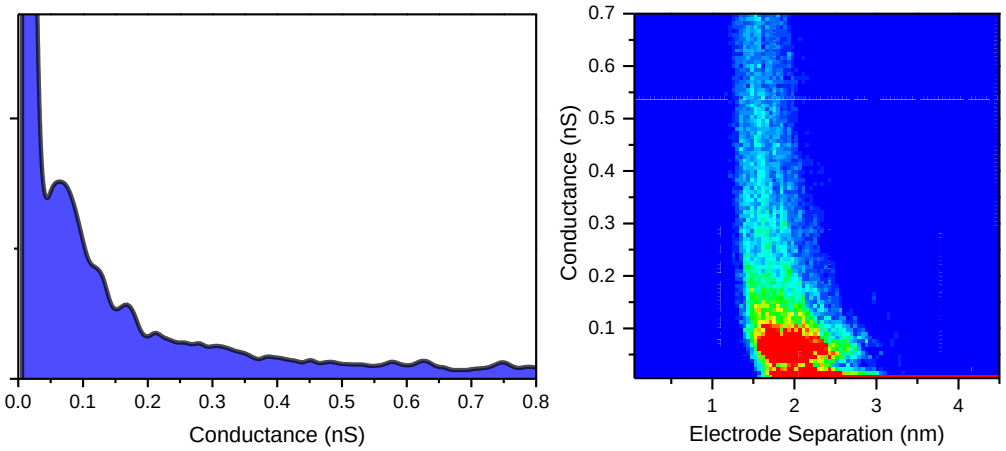

Figure A18: SMC data for 3[T3]3 contact group A under dry Ar.
I(z) technique, 7 nA setpoint, 0.3 V tip bias.

A.9 4[T3]4 in Argon, 295K

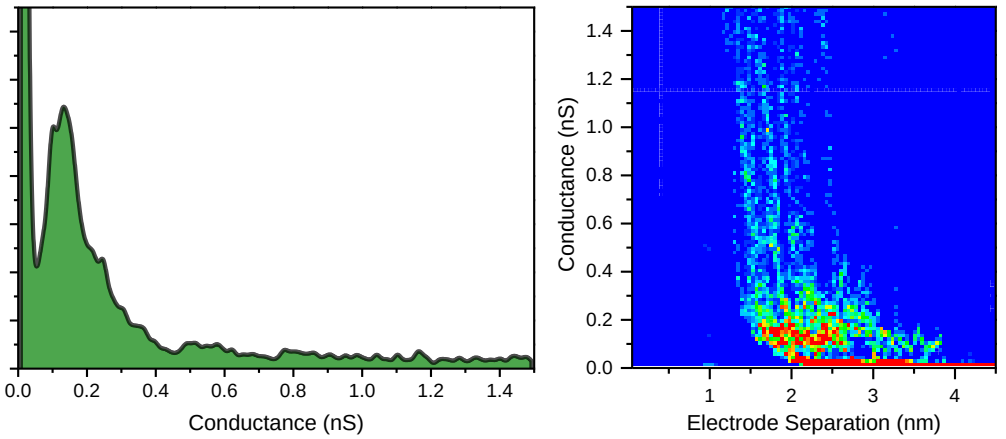

Figure A19: SMC data for 4[T3]4 contact group B under dry Ar.
I(z) technique, 7 nA setpoint, 0.3 V tip bias.

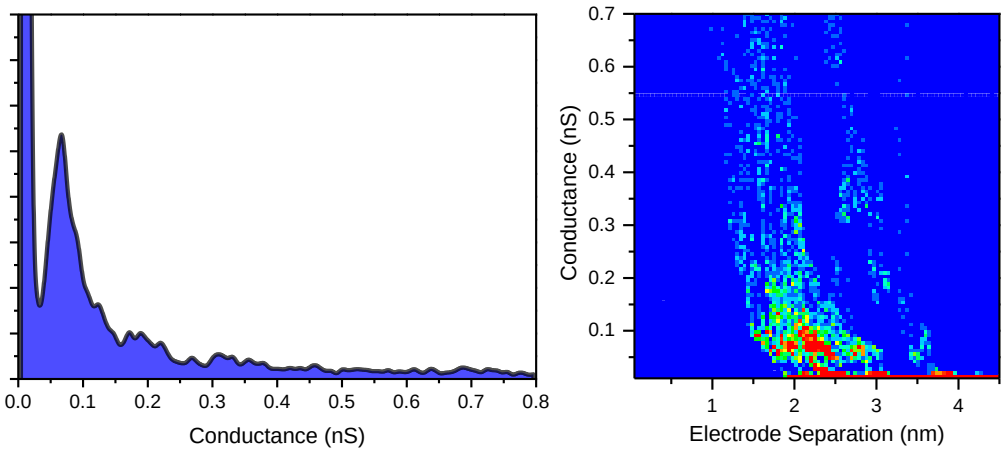

Figure A20: SMC data for 4[T3]4 contact group A under dry Ar.
I(z) technique, 7 nA setpoint, 0.3 V tip bias.

A.10 5[T3]5 in Argon, 295K

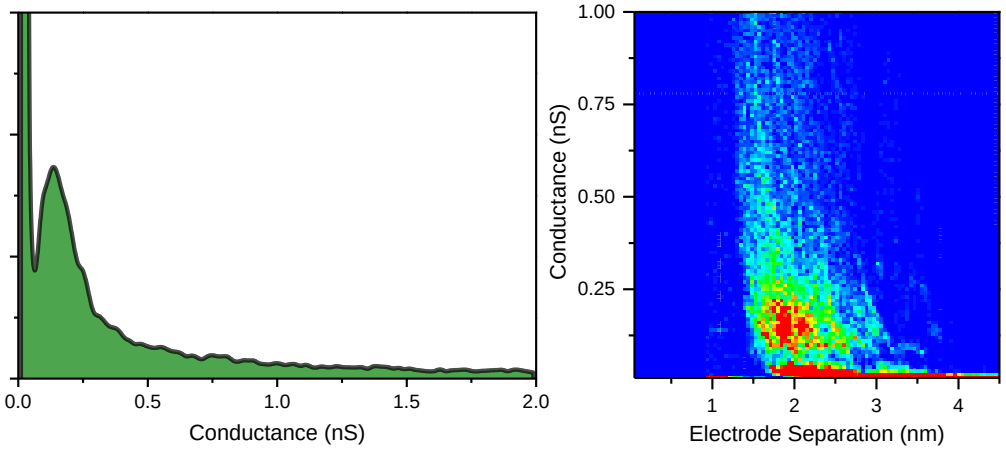

Figure A21: SMC data for 5[T3]5 contact group B under dry Ar.
I(z) technique, 7 nA setpoint, 0.3 V tip bias.

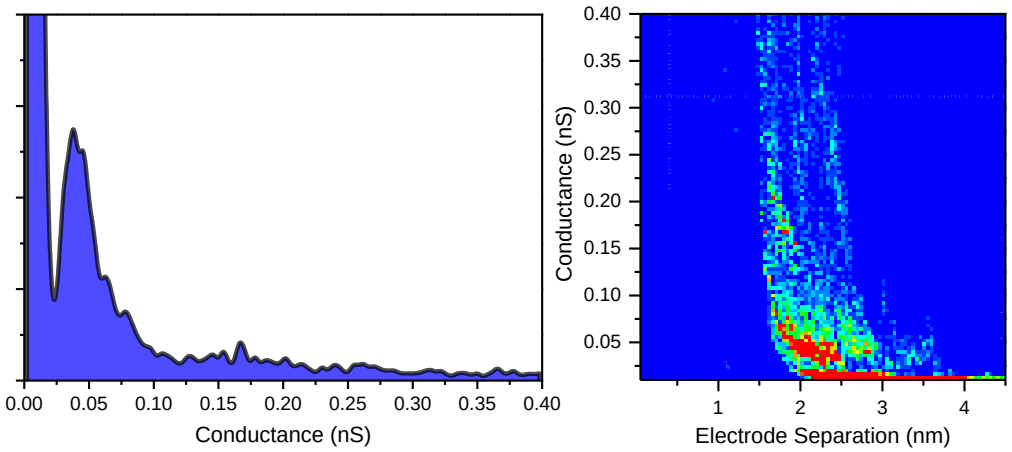

Figure A22: SMC data for 5[T3]5 contact group A under dry Ar.
I(z) technique, 7 nA setpoint, 0.3 V tip bias.

A.11 6[T3]6 in Argon, 295K

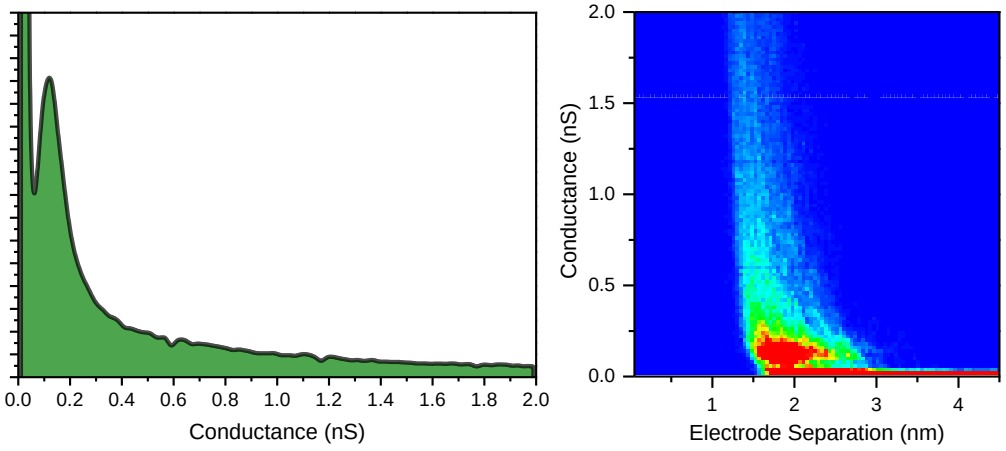

Figure A23: SMC data for 6[T3]6 contact group B under dry Ar.
I(z) technique, 7 nA setpoint, 0.3 V tip bias.

A.12 1[Ph]1 in Air, 295K

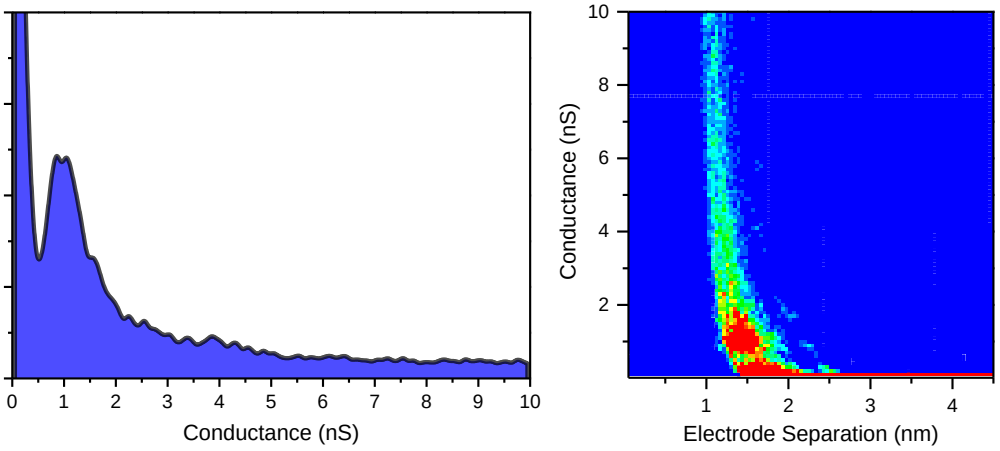

Figure A24: SMC data for 1[Ph]1 contact group A in air.
I(z) technique, 10 nA setpoint, 0.3 V tip bias.

A.13 3[Ph]3 in Air, 295K

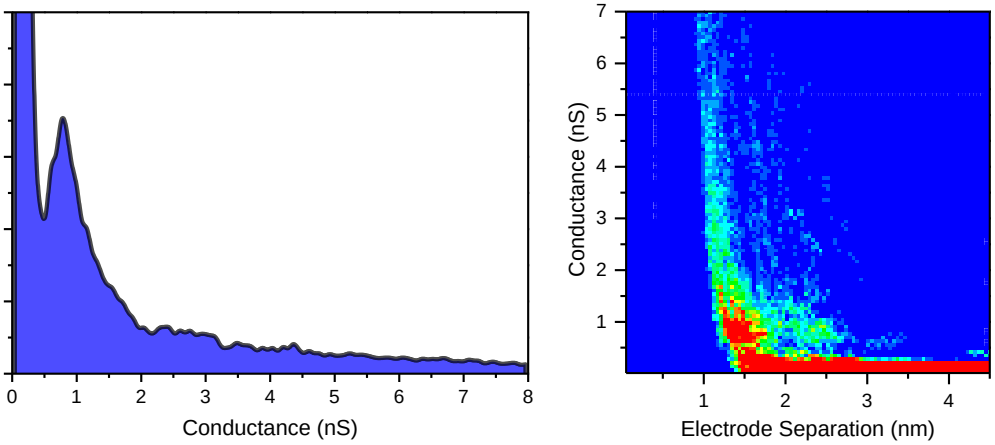

Figure A25: SMC data for 3[Ph]3 contact group A in air.
I(z) technique, 7 nA setpoint, 0.3 V tip bias.

A.14 4[Ph]4 in Air, 295K

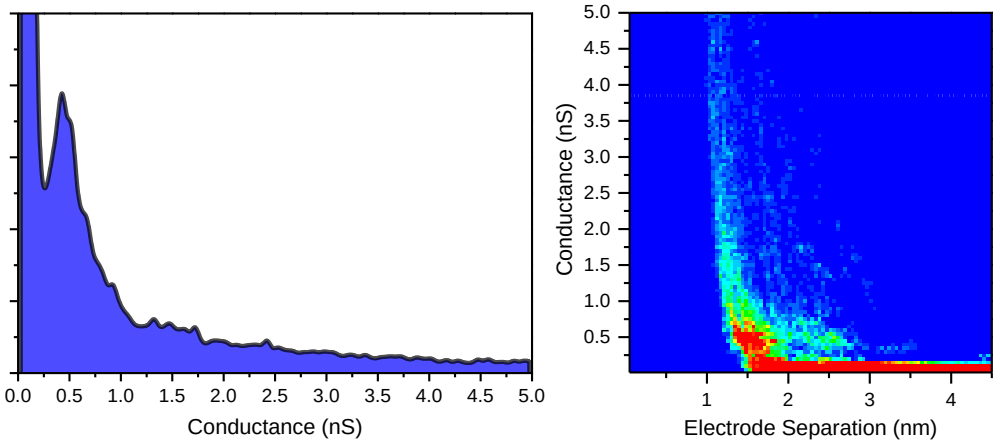

Figure A26: SMC data for 4[Ph]4 contact group A in air.
I(z) technique, 7 nA setpoint, 0.3 V tip bias.

A.15 6[Ph]6 in Air, 295K

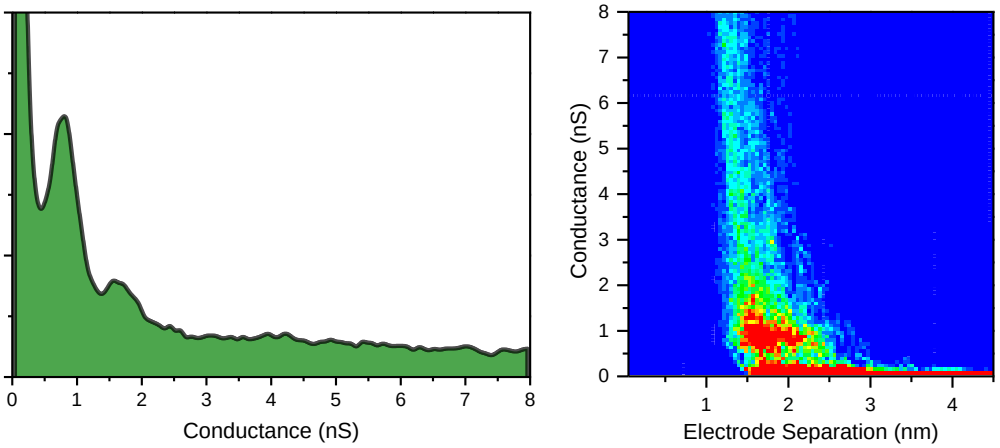

Figure A27: SMC data for 6[Ph]6 contact group B in air.
I(z) technique, 7 nA setpoint, 0.3 V tip bias.

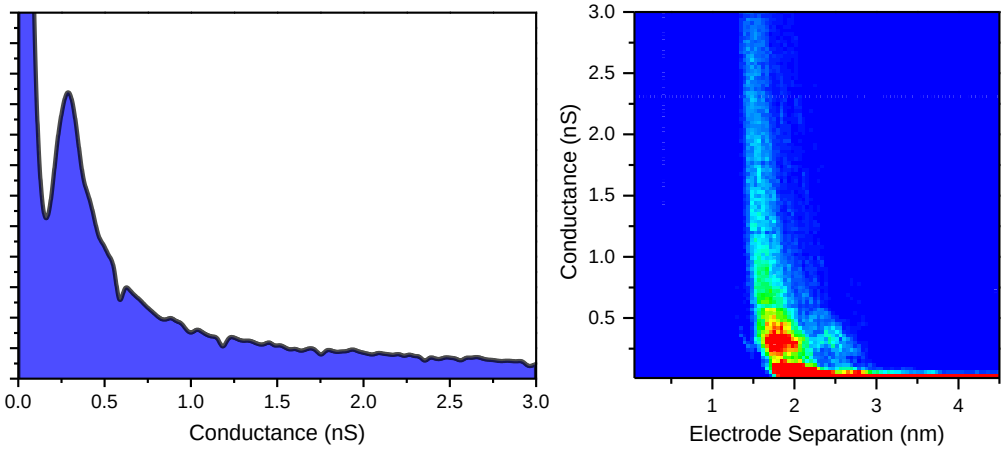

Figure A28: SMC data for 6[Ph]6 contact group A in air.
I(z) technique, 7 nA setpoint, 0.3 V tip bias.

A.16 2[V]2 in Air, 295K

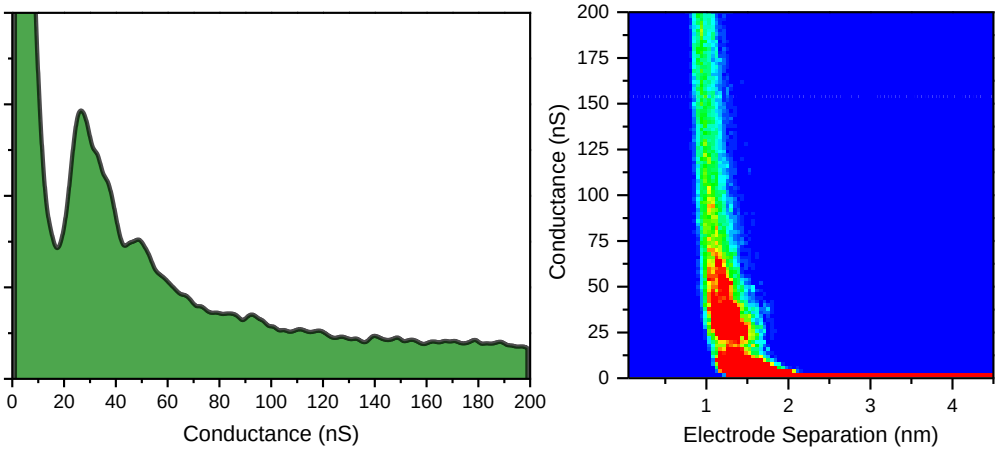

Figure A29: SMC data for 2[V]2 contact group B in air.
I(z) technique, 60 nA setpoint, 0.3 V tip bias.

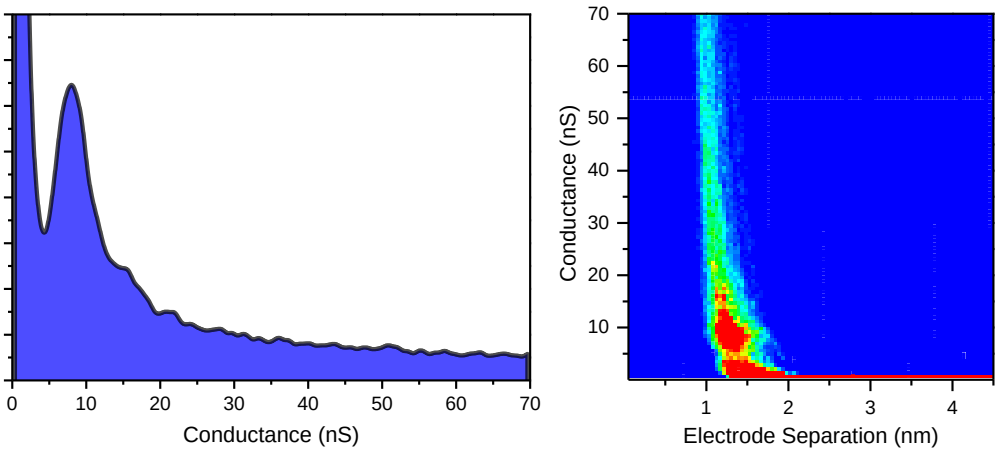

Figure A30: SMC data for 2[V]2 contact group A in air.
I(z) technique, 20 nA setpoint, 0.3 V tip bias.

A.17 4[V]4 in Air, 295K

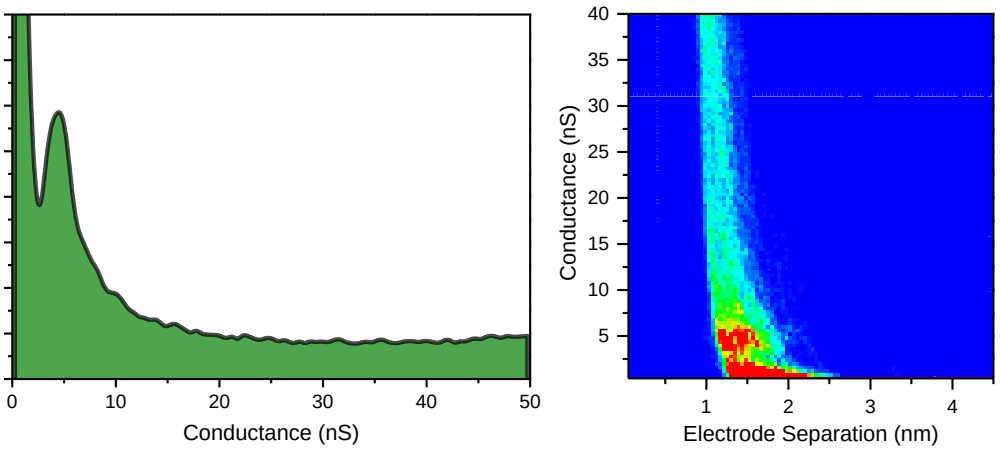

Figure A31: SMC data for 4[V]4 contact group B in air.
I(z) technique, 20 nA setpoint, 0.3 V tip bias.

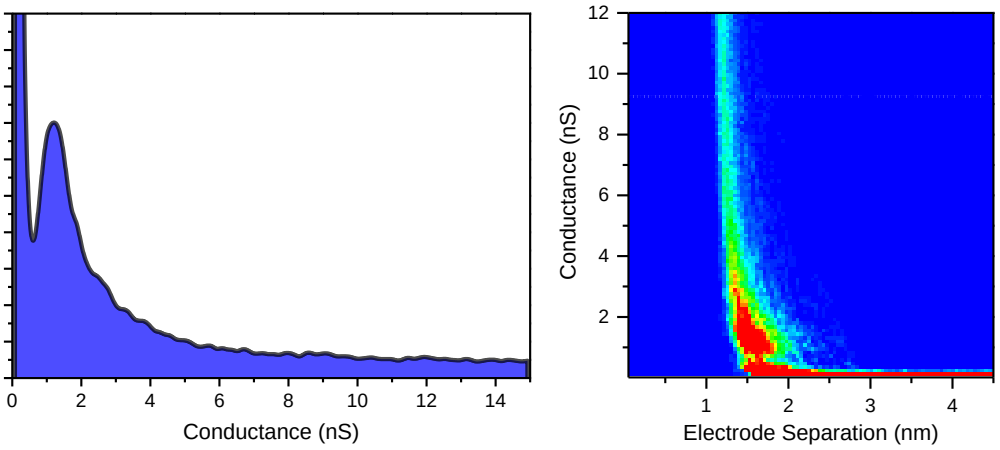

Figure A32: SMC data for 4[V]4 contact group A in air.
I(z) technique, 10 nA setpoint, 0.3 V tip bias.

A.18 6[V]6 in Air, 295K

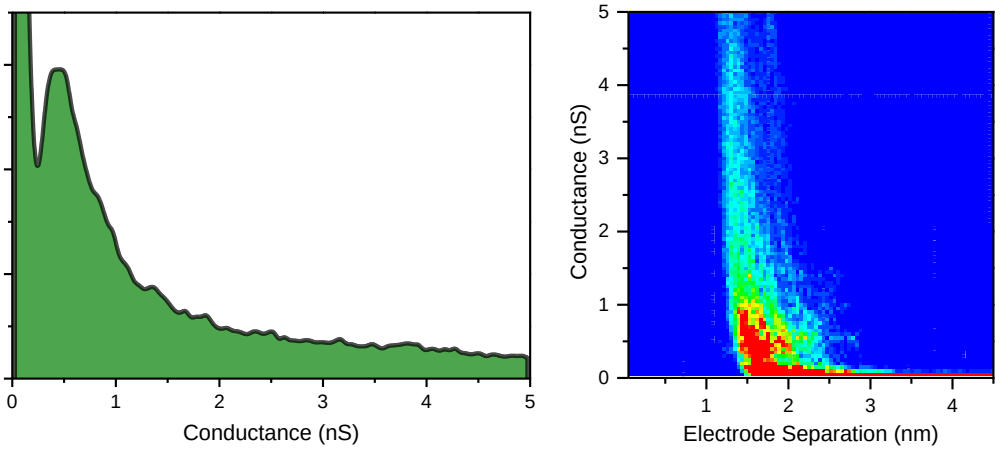

Figure A33: SMC data for 6[V]6 contact group B in air.
I(z) technique, 8 nA setpoint, 0.3 V tip bias.

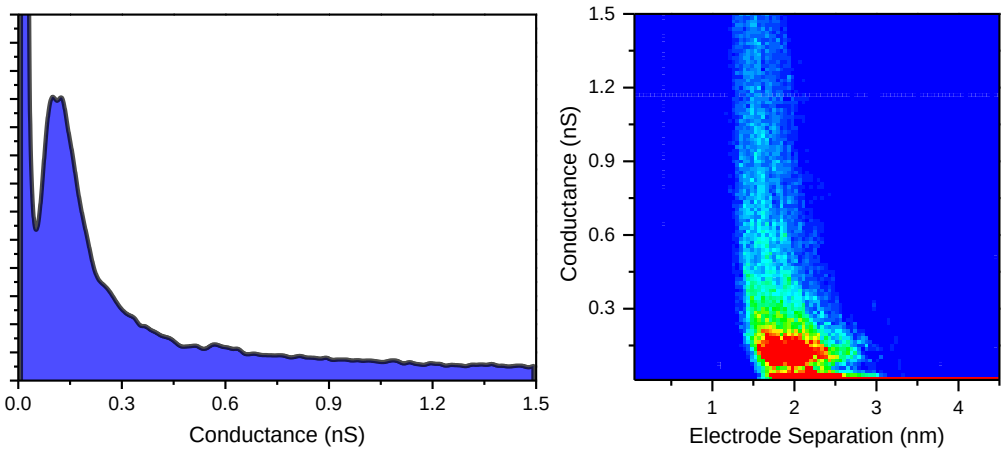

Figure A34: SMC data for 6[V]6 contact group A in air.
I(z) technique, 8 nA setpoint, 0.3 V tip bias.

A.19 9[V]9 in Air, 295K

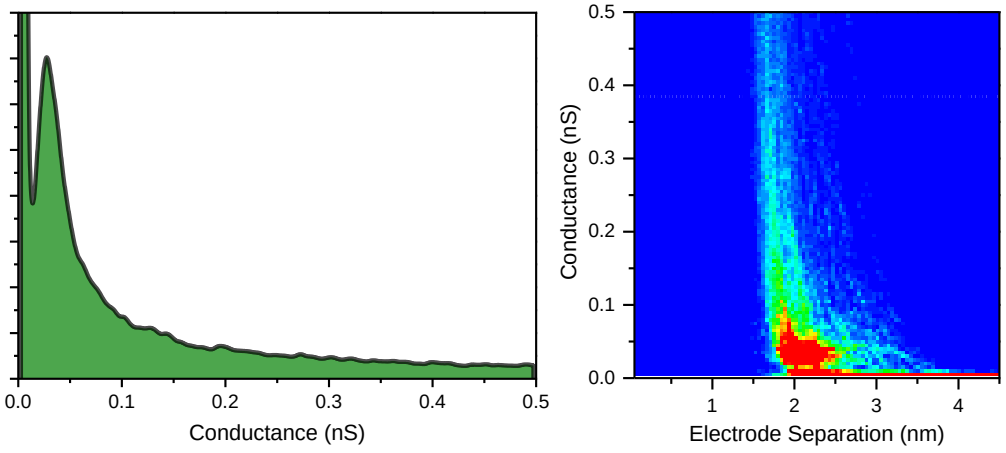

Figure A35: SMC data for 9[V]9 contact group B in air.
I(z) technique, 5 nA setpoint, 0.3 V tip bias.

A.20 5[T]5 in Air, 295K

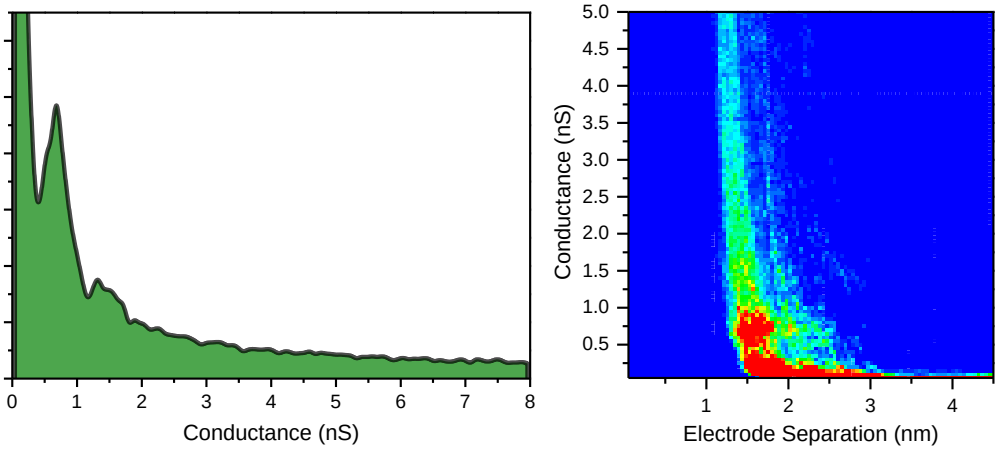

Figure A36: SMC data for 5[T]5 contact group B in air at 295K.
I(z) technique, 7 nA setpoint, 0.3 V tip bias.

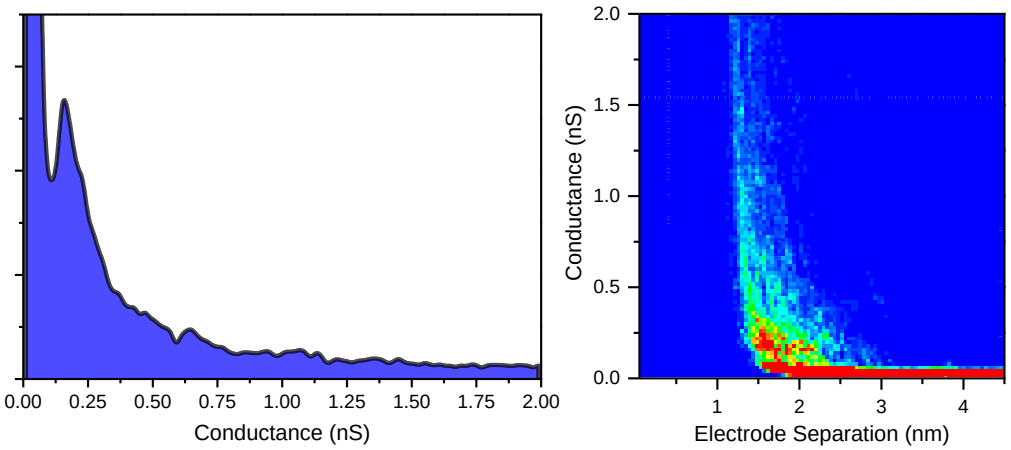

Figure A37: SMC data for 5[T]5 contact group A in air at 295K.
I(z) technique, 7 nA setpoint, 0.3 V tip bias.

A.21 5[T2]5 in Air, 295K

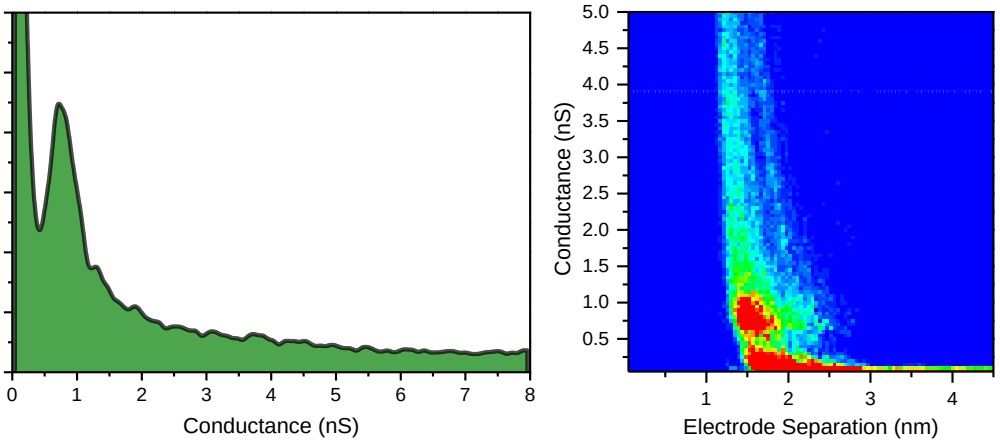

Figure A38: SMC data for 5[T2]5 contact group B in air at 295K.
I(z) technique, 7 nA setpoint, 0.3 V tip bias.

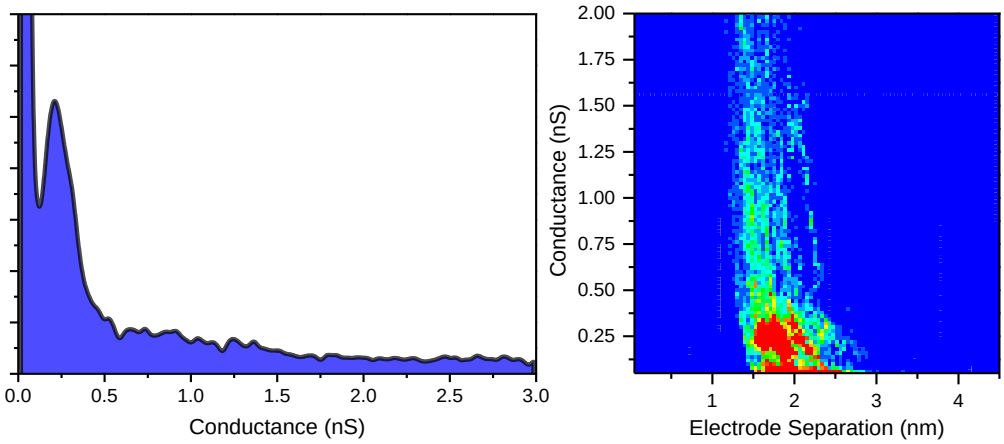

Figure A39: SMC data for 5[T2]5 contact group A in air at 295K.
I(z) technique, 7 nA setpoint, 0.3 V tip bias.

A.22 5[T]5 in Argon, 295K

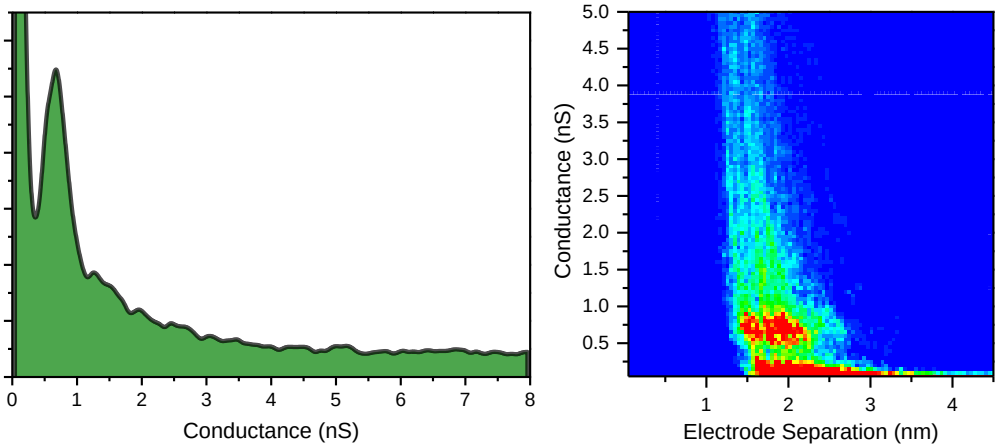

Figure A40: SMC data for 5[T]5 contact group B under dry Ar at 295K.
I(z) technique, 7 nA setpoint, 0.3 V tip bias.

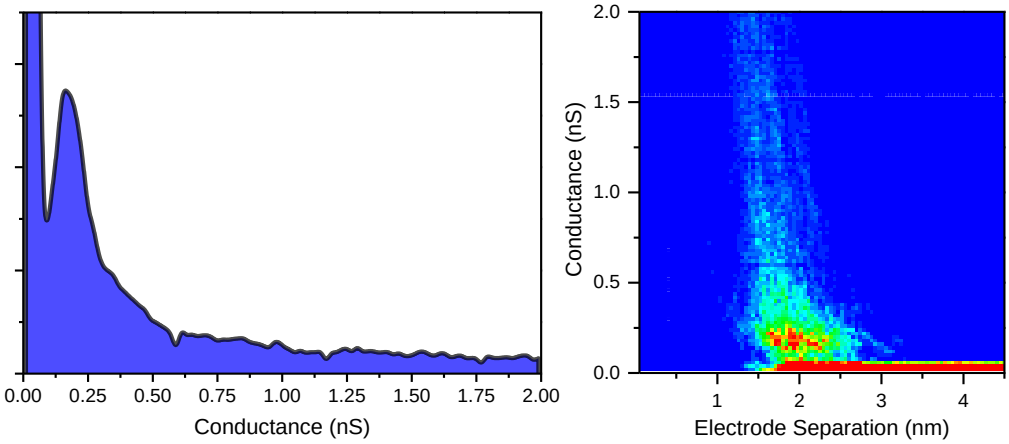

Figure A41: SMC data for 5[T]5 contact group A under dry Ar at 295K.
I(z) technique, 7 nA setpoint, 0.3 V tip bias.

A.23 5[T2]5 in Argon, 295K

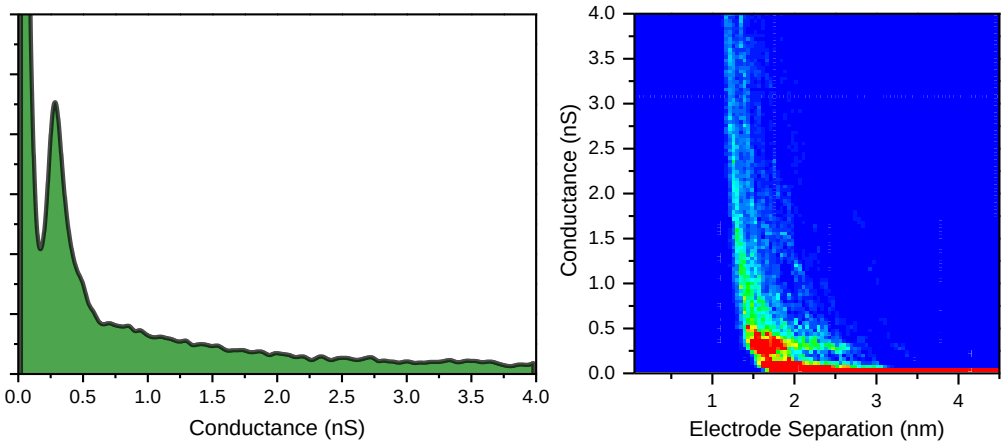

Figure A42: SMC data for 5[T2]5 contact group B under dry Ar at 295K. *I(z)* technique, 7 nA setpoint, 0.3 V tip bias.

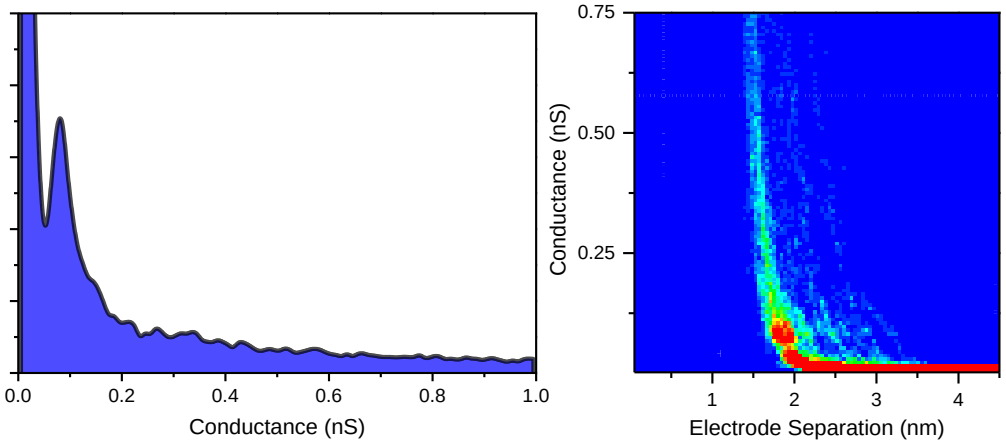

Figure A43: SMC data for 5[T2]5 contact group A under dry Ar at 295K. *I(z)* technique, 7 nA setpoint, 0.3 V tip bias.

A.24 5[T]5 in Air, Variable Temperature

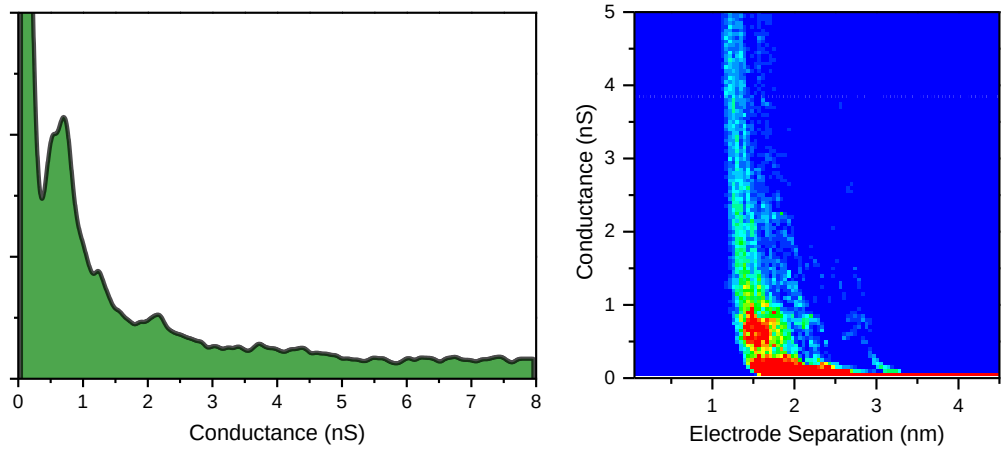

Figure A44: SMC data for 5[T]5 contact group B in air at 323K. *I(z)* technique, 7 nA setpoint, 0.3 V tip bias.

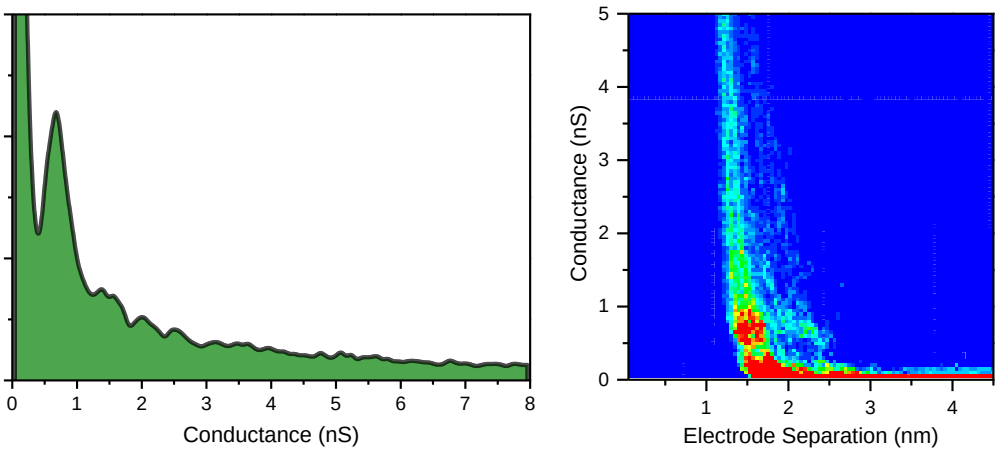

Figure A45: SMC data for 5[T]5 contact group B in air at 338K.
I(z) technique, 7 nA setpoint, 0.3 V tip bias.

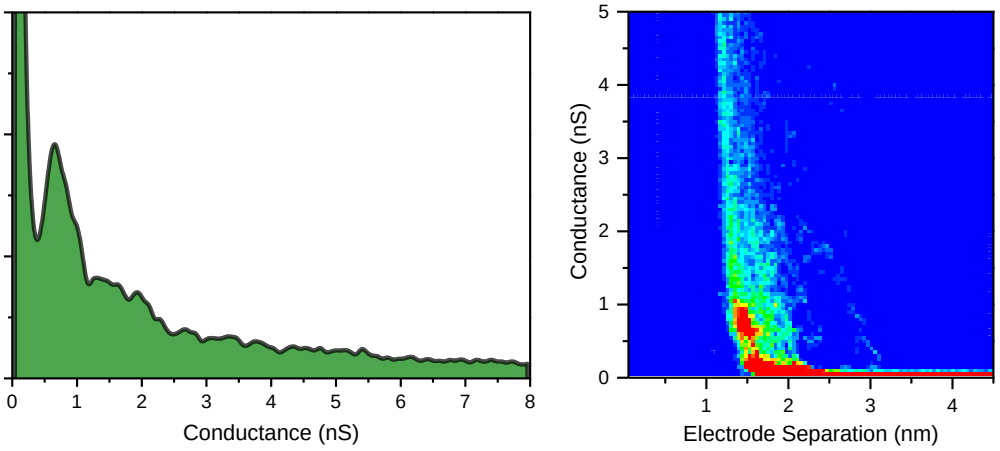

Figure A46: SMC data for 5[T]5 contact group B in air at 353K.
I(z) technique, 7 nA setpoint, 0.3 V tip bias.

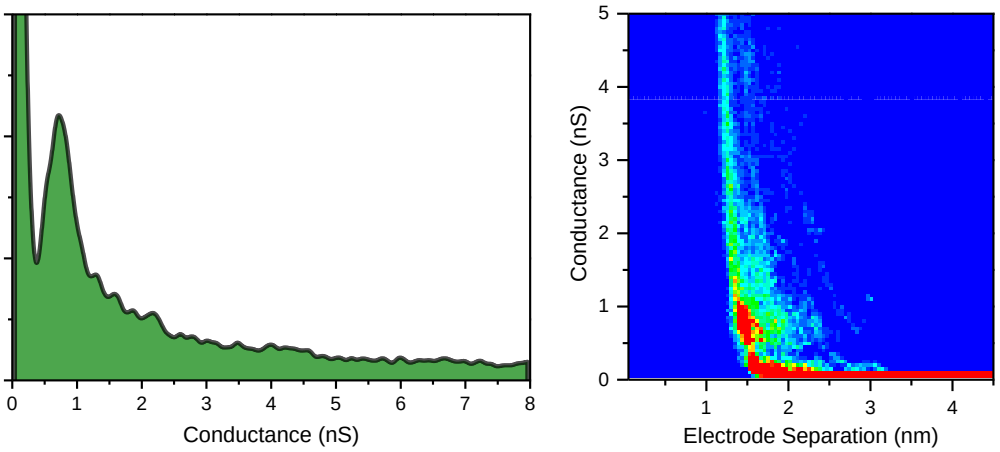

Figure A47: SMC data for 5[T]5 contact group B in air at 373K.
I(z) technique, 7 nA setpoint, 0.3 V tip bias.

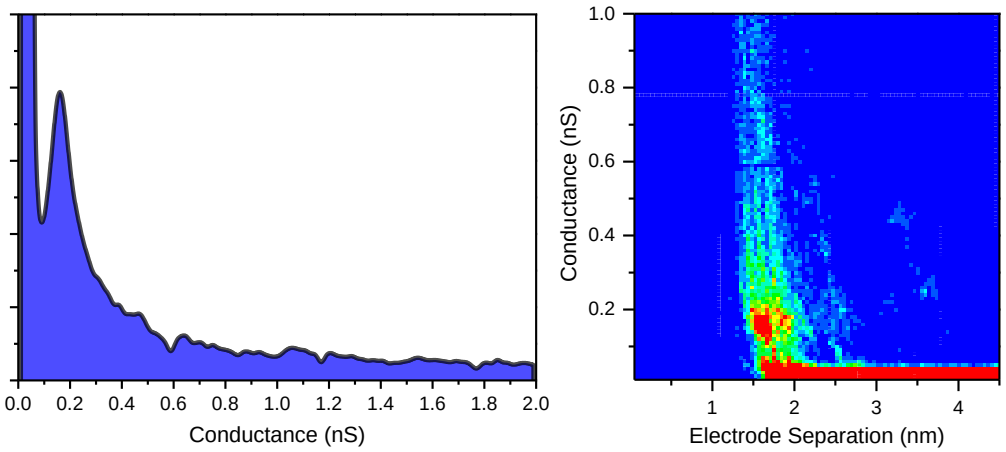

Figure A48: SMC data for 5[T]5 contact group A in air at 323K.
I(z) technique, 7 nA setpoint, 0.3 V tip bias.

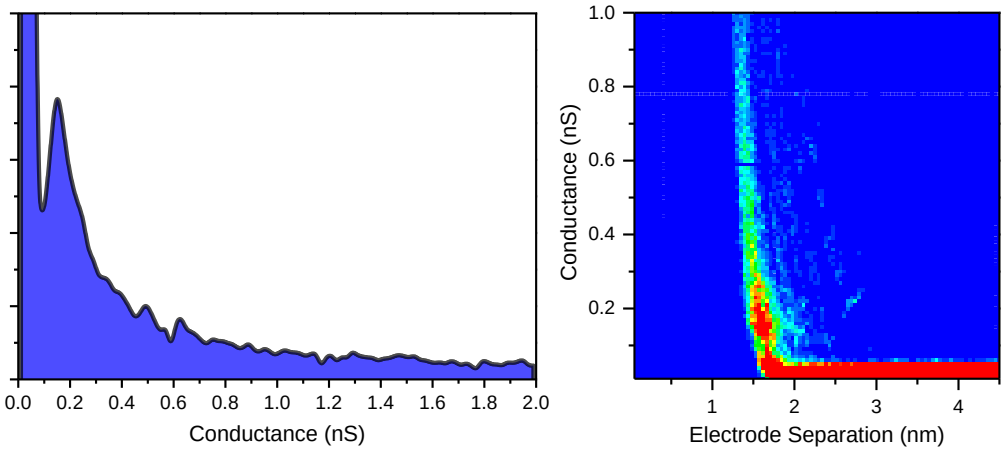

Figure A49: SMC data for 5[T]5 contact group A in air at 338K.
I(z) technique, 7 nA setpoint, 0.3 V tip bias.

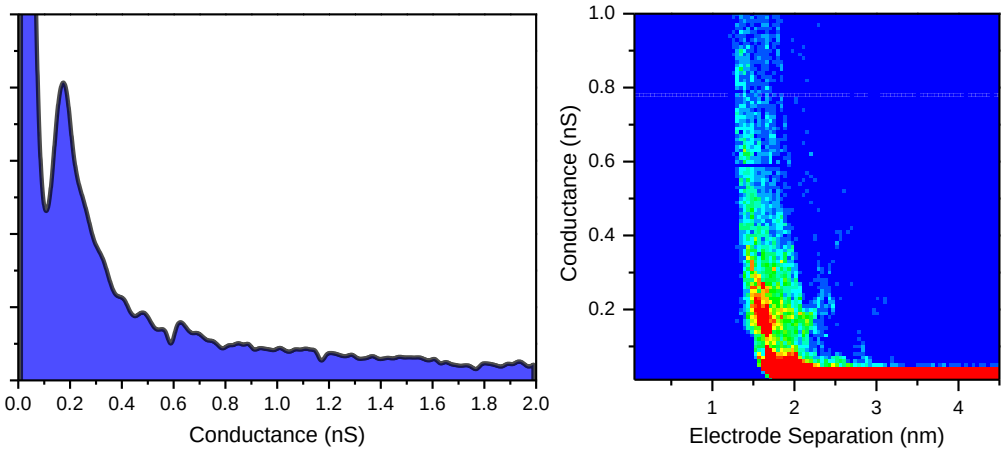

Figure A50: SMC data for 5[T]5 contact group A in air at 353K.
I(z) technique, 7 nA setpoint, 0.3 V tip bias.

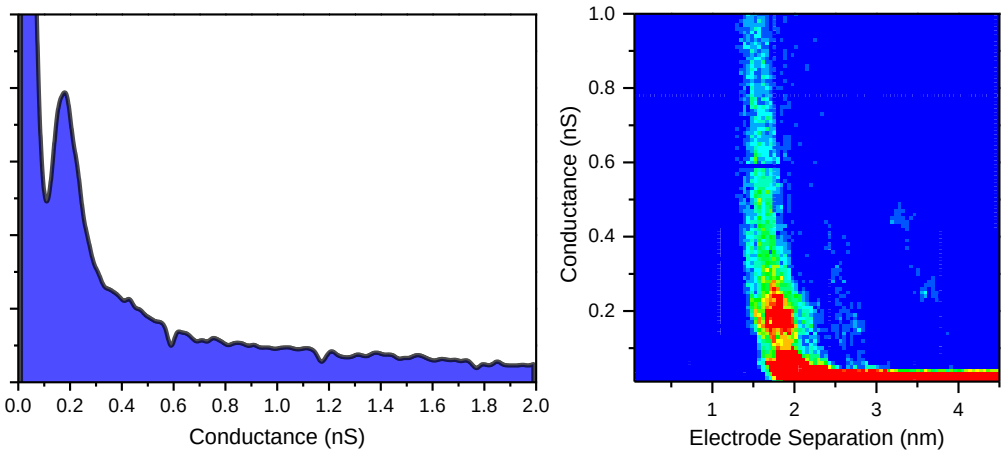

Figure A51: SMC data for 5[T]5 contact group A in air at 373K.
I(z) technique, 7 nA setpoint, 0.3 V tip bias.

A.25 5[T2]5 in Air, Variable Temperature

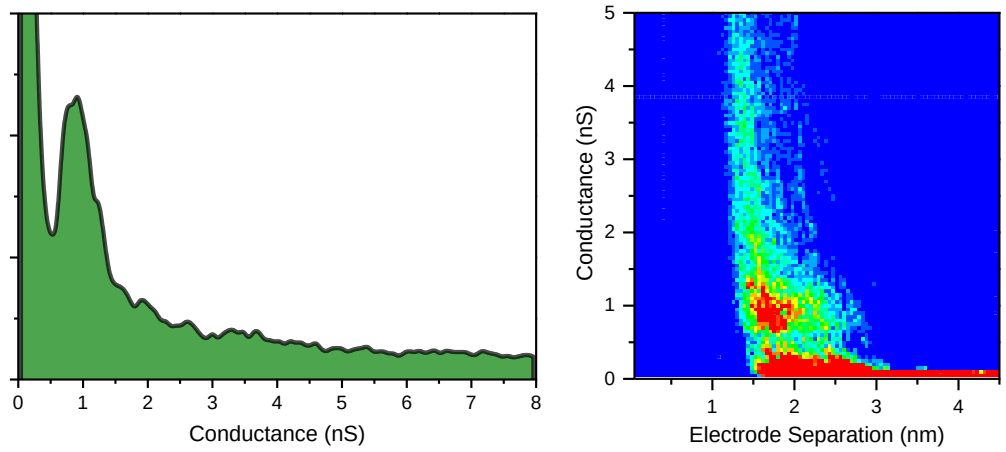

Figure A52: SMC data for 5[T2]5 contact group B in air at 323K.
I(z) technique, 7 nA setpoint, 0.3 V tip bias.

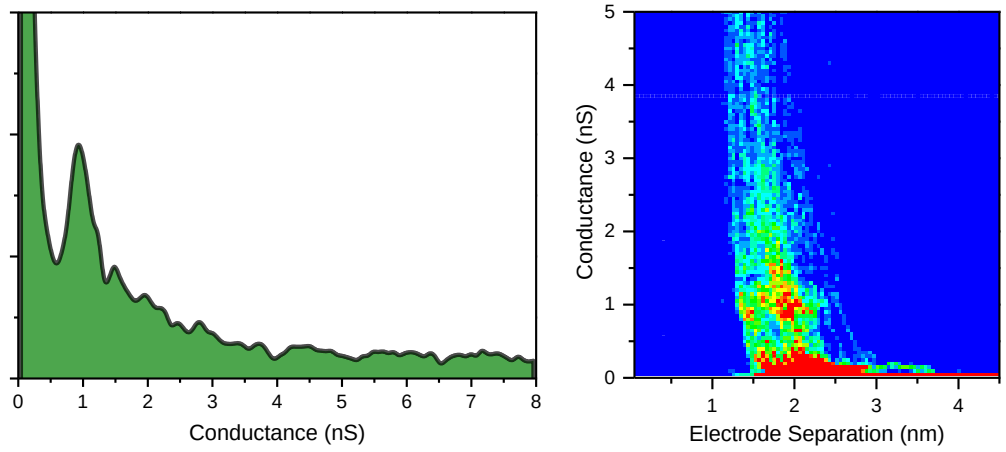

Figure A53: SMC data for 5[T2]5 contact group B in air at 338K.
I(z) technique, 7 nA setpoint, 0.3 V tip bias.

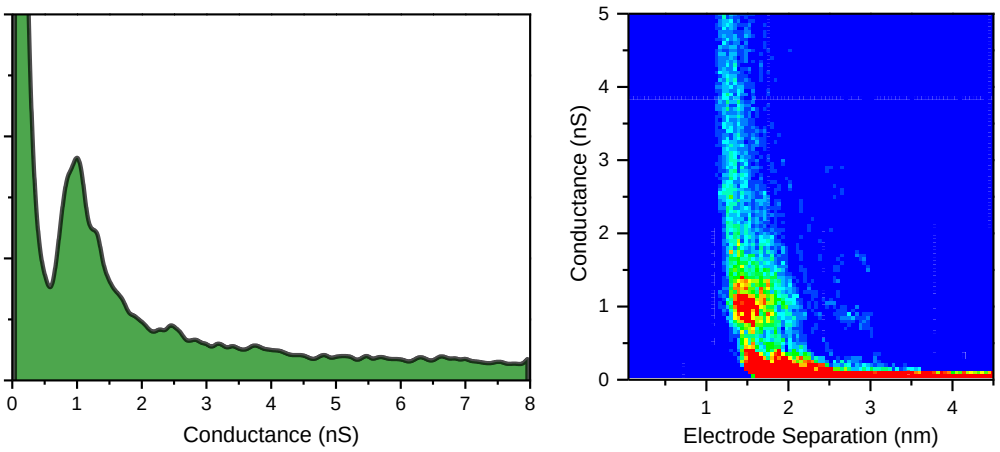

Figure A54: SMC data for 5[T2]5 contact group B in air at 353K.
I(z) technique, 7 nA setpoint, 0.3 V tip bias.

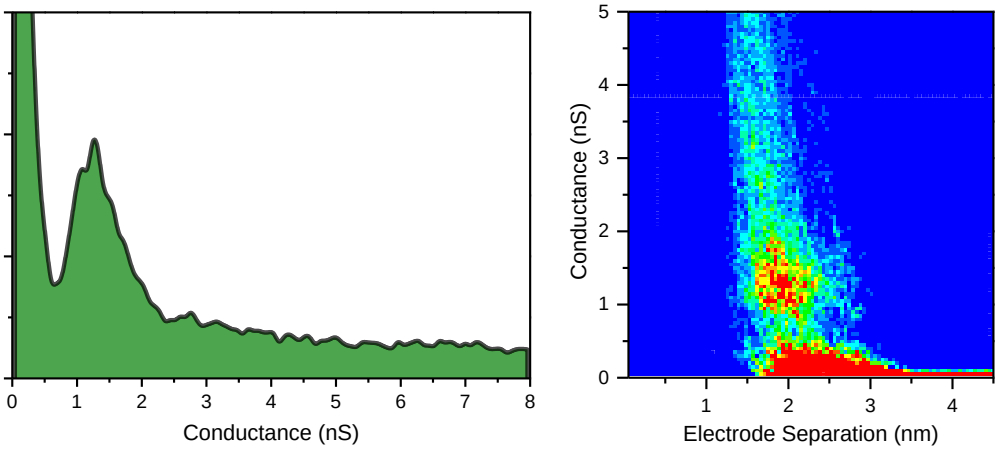

Figure A55: SMC data for 5[T2]5 contact group B in air at 373K.
I(z) technique, 7 nA setpoint, 0.3 V tip bias.

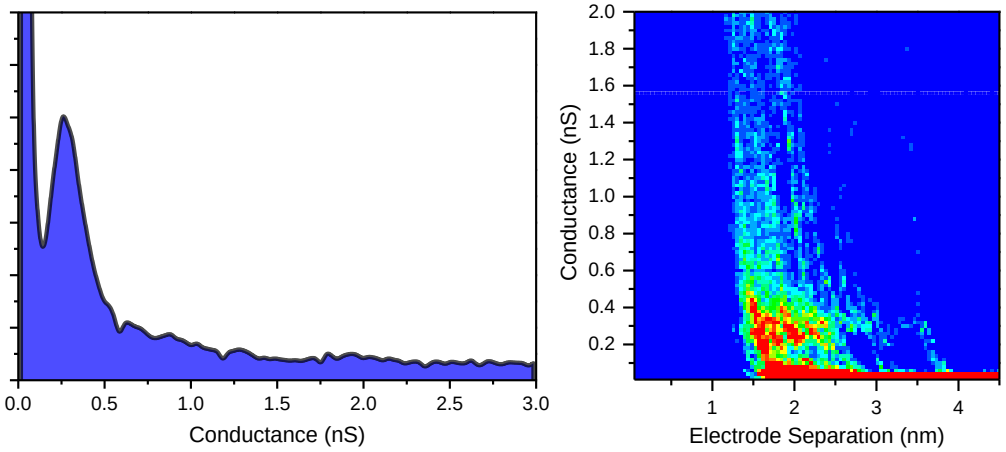

Figure A56: SMC data for 5[T2]5 contact group A in air at 323K.
I(z) technique, 7 nA setpoint, 0.3 V tip bias.

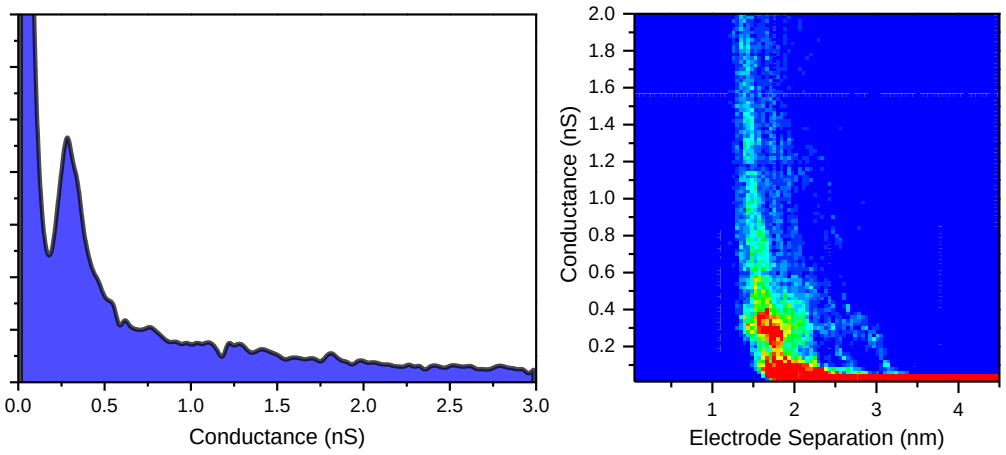

Figure A57: SMC data for 5[T2]5 contact group A in air at 338K.
I(z) technique, 7 nA setpoint, 0.3 V tip bias.

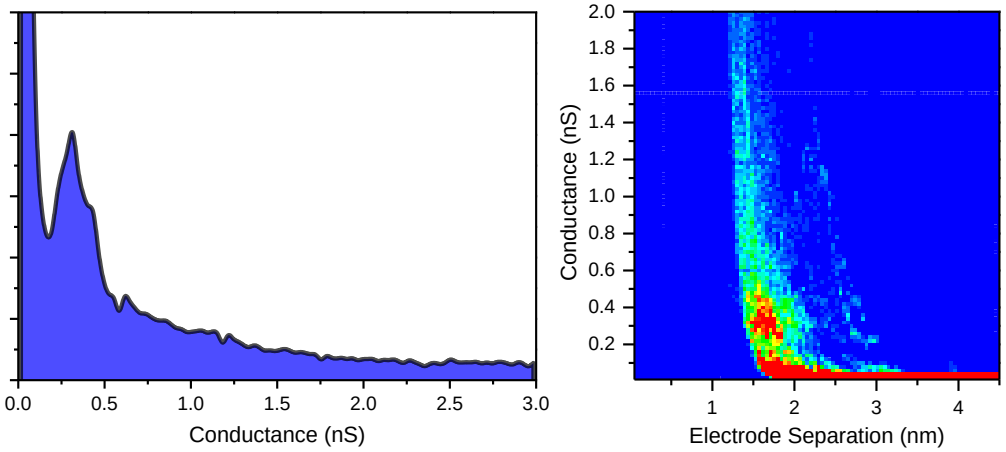

Figure A58: SMC data for 5[T2]5 contact group A in air at 353K.
I(z) technique, 7 nA setpoint, 0.3 V tip bias.

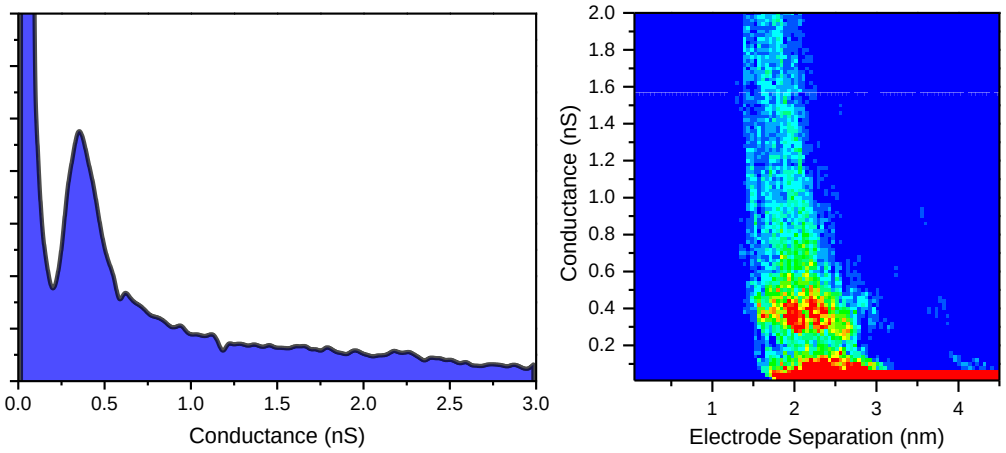

Figure A59: SMC data for 5[T2]5 contact group A in air at 373K.
I(z) technique, 7 nA setpoint, 0.3 V tip bias.

A.26 5[T3]5 in Air, Variable Temperature

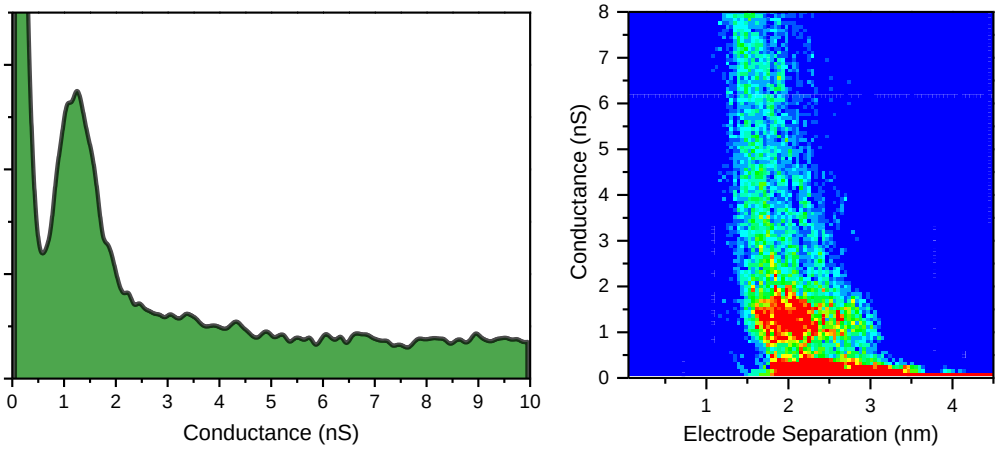

Figure A60: SMC data for 5[T3]5 contact group B in air at 323K.
I(z) technique, 7 nA setpoint, 0.3 V tip bias.

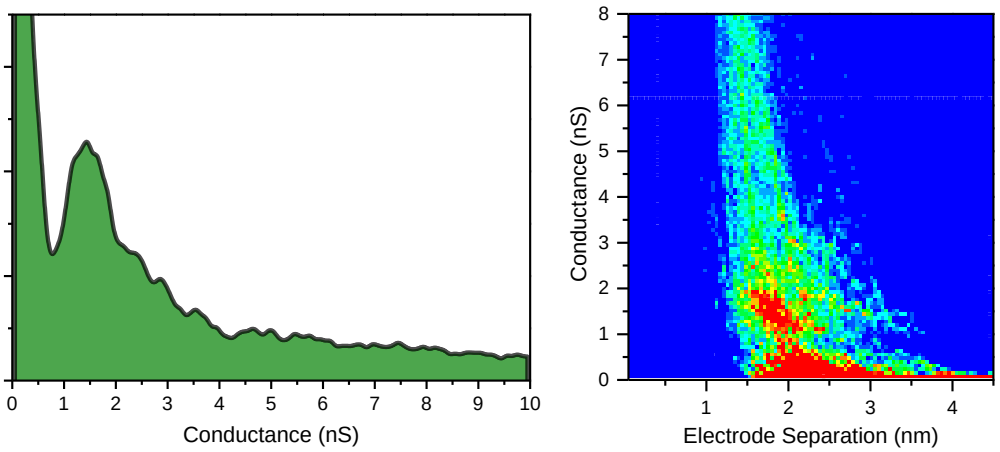

Figure A61: SMC data for 5[T3]5 contact group B in air at 338K.
I(z) technique, 7 nA setpoint, 0.3 V tip bias.

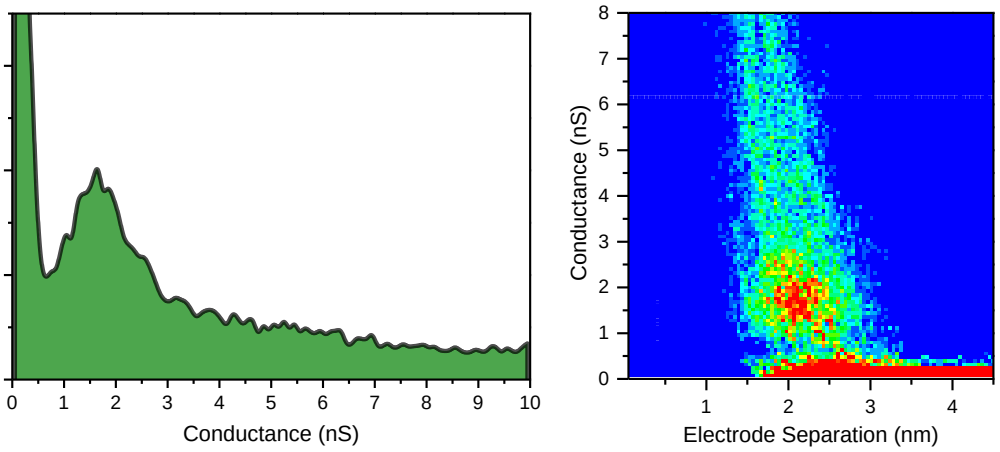

Figure A62: SMC data for 5[T3]5 contact group B in air at 353K.
I(z) technique, 7 nA setpoint, 0.3 V tip bias.

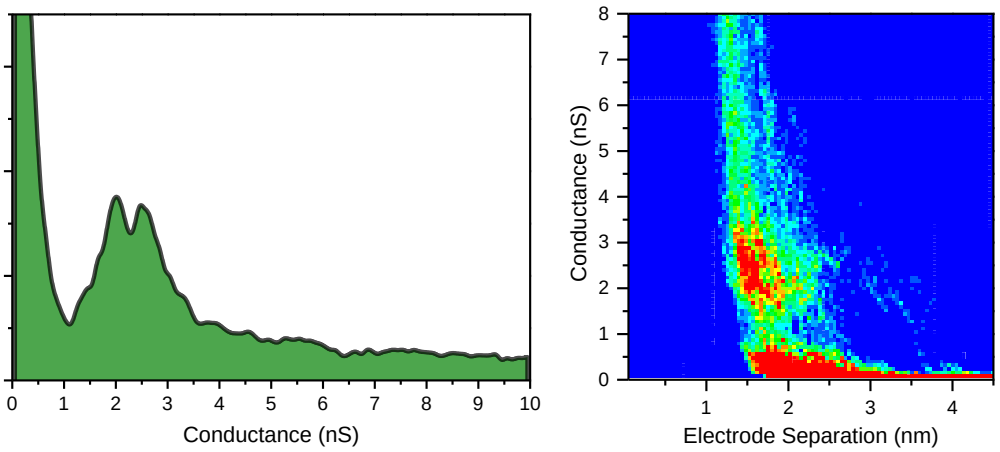

Figure A63: SMC data for 5[T3]5 contact group B in air at 373K.
I(z) technique, 7 nA setpoint, 0.3 V tip bias.

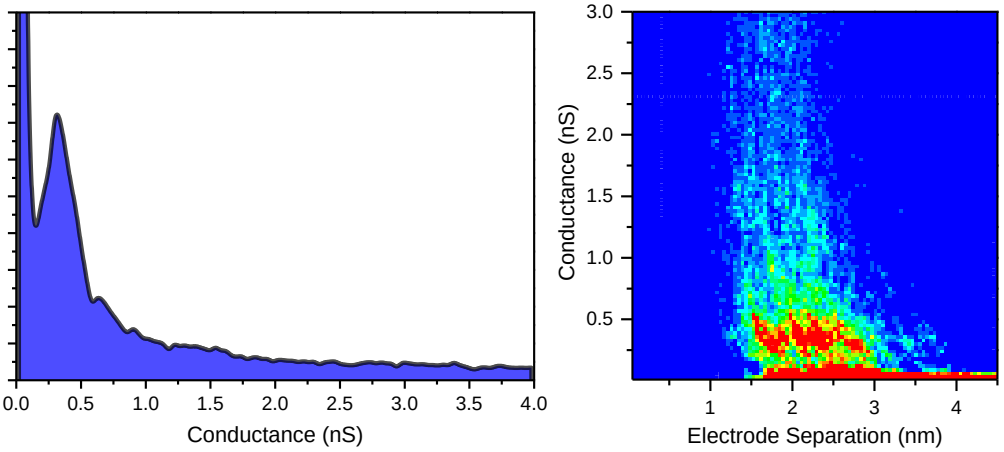

Figure A64: SMC data for 5[T3]5 contact group A in air at 323K.
I(z) technique, 7 nA setpoint, 0.3 V tip bias.

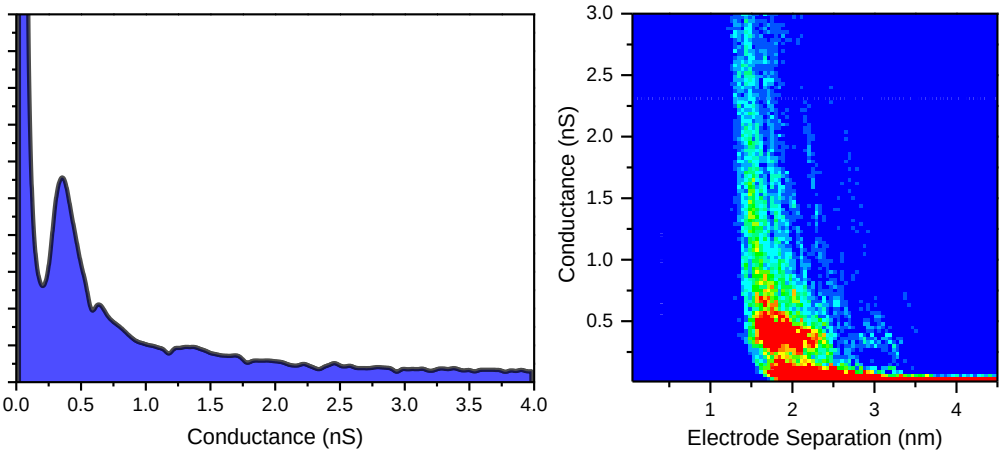

Figure A65: SMC data for 5[T3]5 contact group A in air at 338K.
I(z) technique, 7 nA setpoint, 0.3 V tip bias.

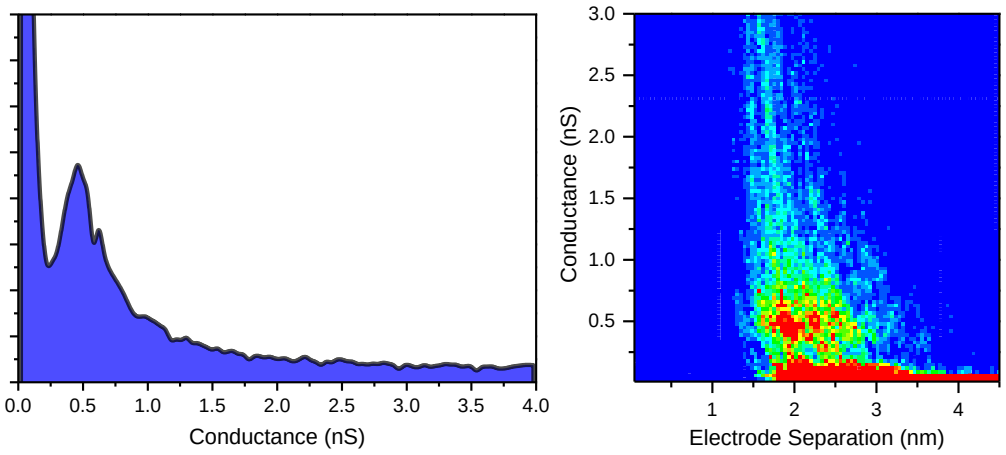

Figure A66: SMC data for 5[T3]5 contact group A in air at 353K.
I(z) technique, 7 nA setpoint, 0.3 V tip bias.

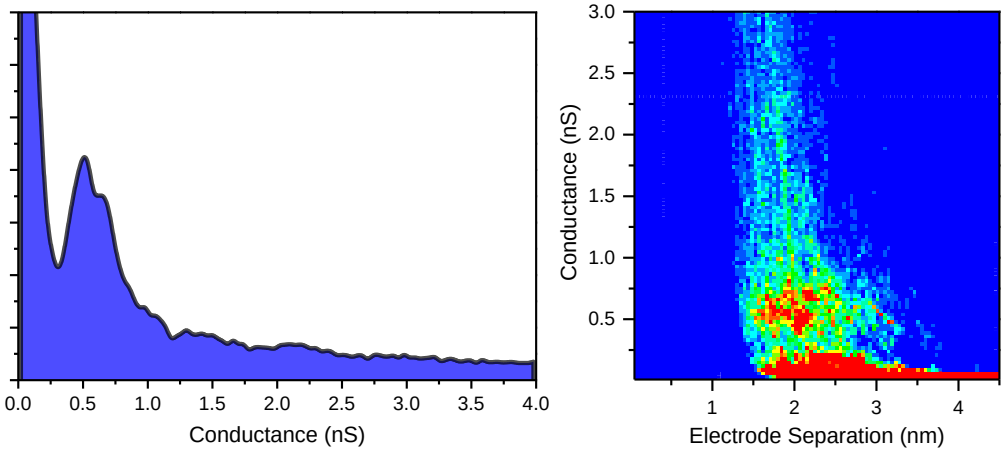

Figure A67: SMC data for 5[T3]5 contact group A in air at 373K.
I(z) technique, 7 nA setpoint, 0.3 V tip bias.

A.27 Decanedithiol in Air, Variable Temperature

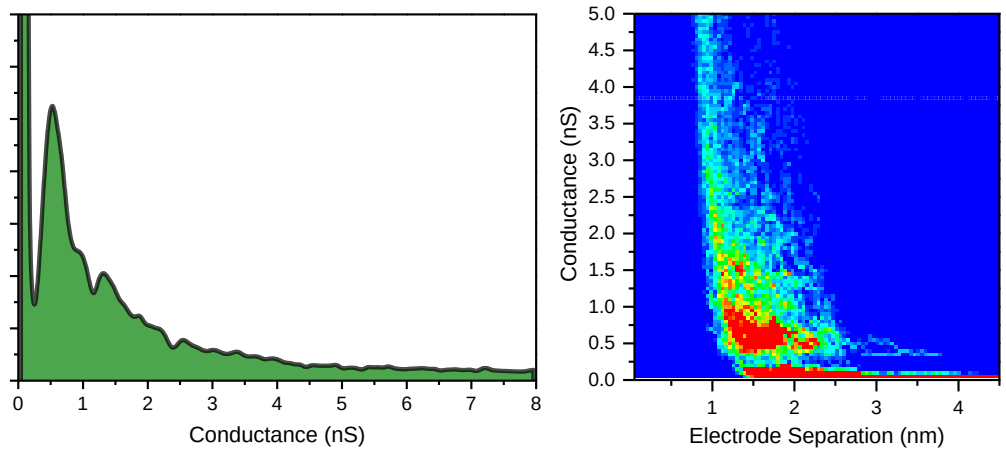

Figure A68: SMC data for DDT contact group B in air at 295K.
I(z) technique, 7 nA setpoint, 0.3 V tip bias.

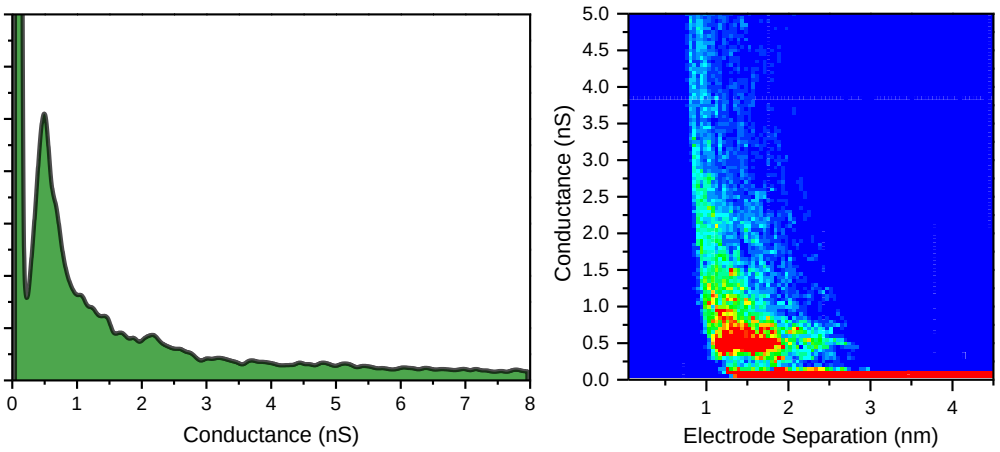

Figure A69: SMC data for DDT contact group B in air at 323K.
I(z) technique, 7 nA setpoint, 0.3 V tip bias.

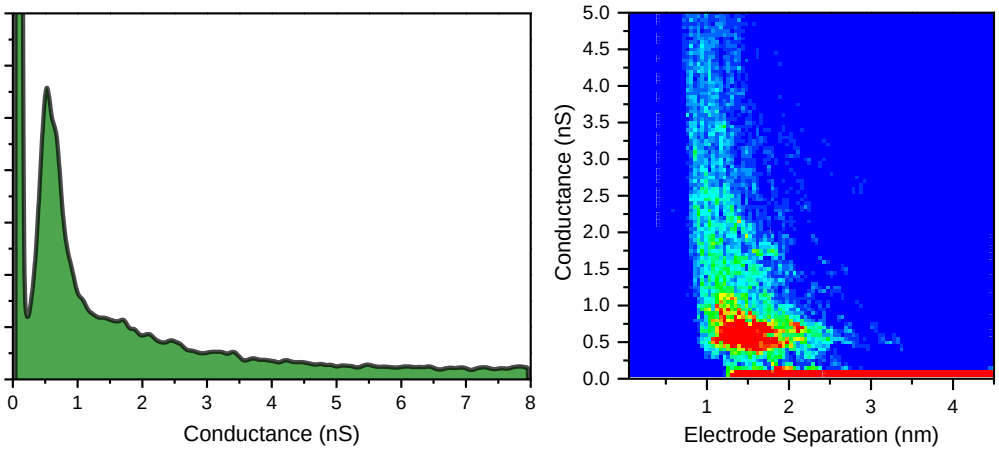

Figure A70: SMC data for DDT contact group B in air at 353K.
I(z) technique, 7 nA setpoint, 0.3 V tip bias.

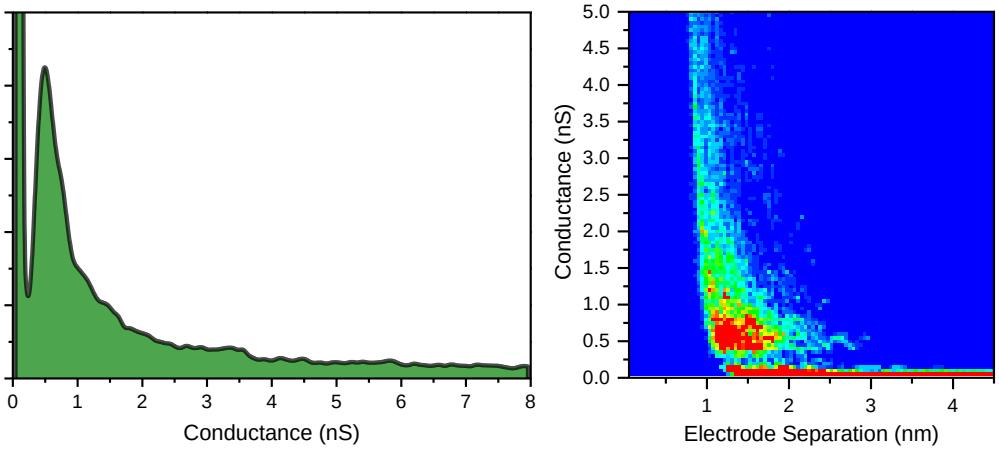

Figure A71: SMC data for DDT contact group B in air at 373K.
I(z) technique, 7 nA setpoint, 0.3 V tip bias.

A.28 6[Ph]6 in Air, Variable Temperature

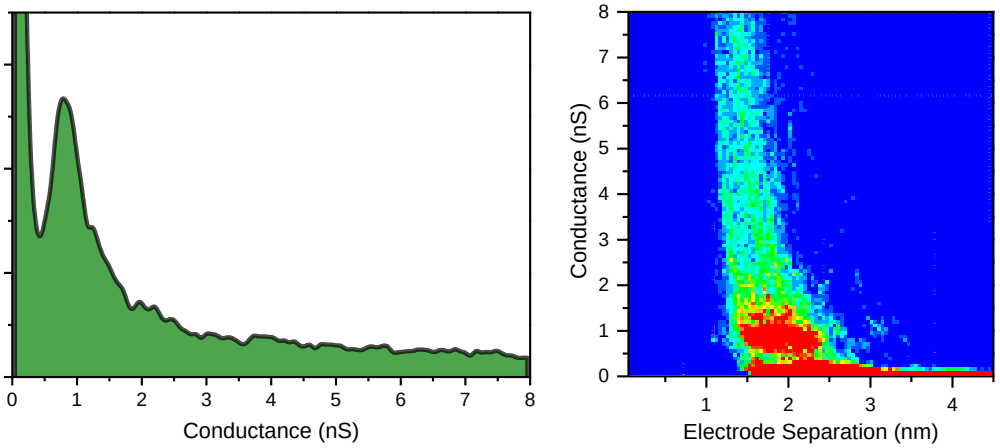

Figure A72: SMC data for 6[Ph]6 contact group B at 323 K.
I(z) technique, 7 nA setpoint, 0.3 V tip bias.

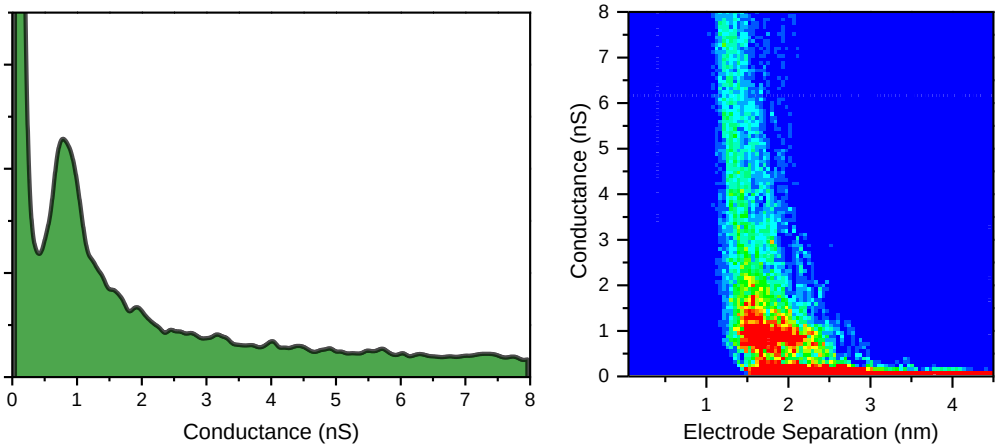

Figure A73: SMC data for 6[Ph]6 contact group B at 353 K.
I(z) technique, 7 nA setpoint, 0.3 V tip bias.

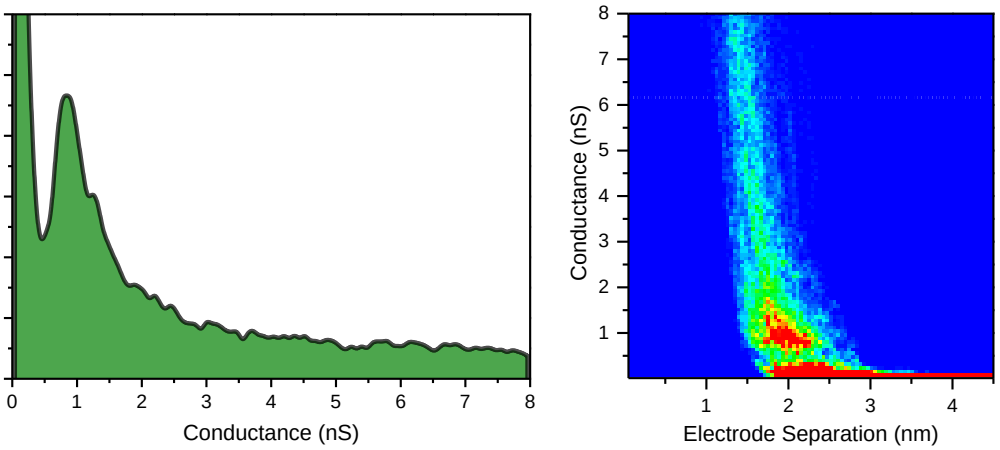

Figure A74: SMC data for 6[Ph]6 contact group B at 373 K.
I(z) technique, 7 nA setpoint, 0.3 V tip bias.

A.29 6[T3]6 in TCB, 295K

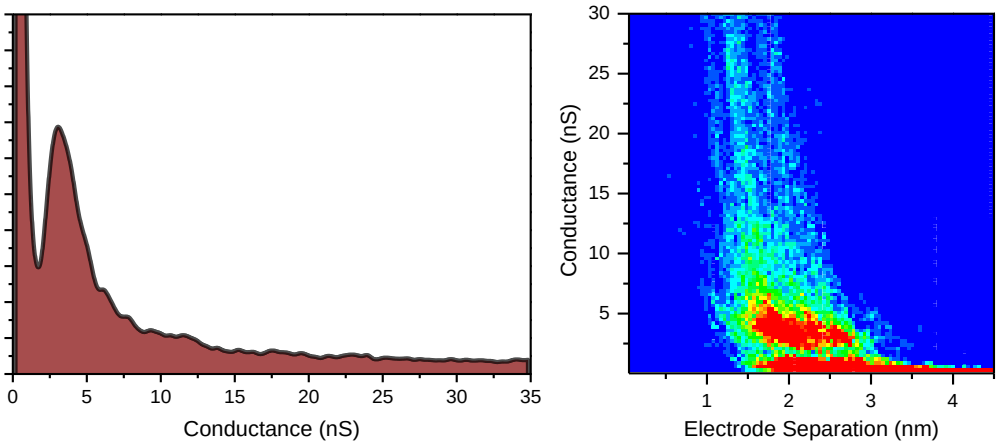

Figure A75: SMC data for 6[T3]6 contact group C in TCB.
STM-BJ technique, 0.3 V tip bias.

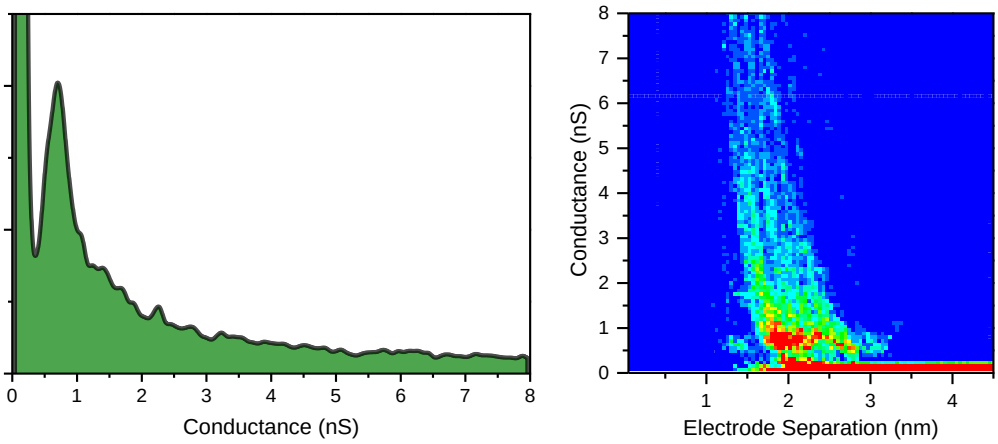

Figure A76: SMC data for 6[T3]6 contact group B in TCB.
I(z) technique, 10 nA setpoint, 0.3 V tip bias.

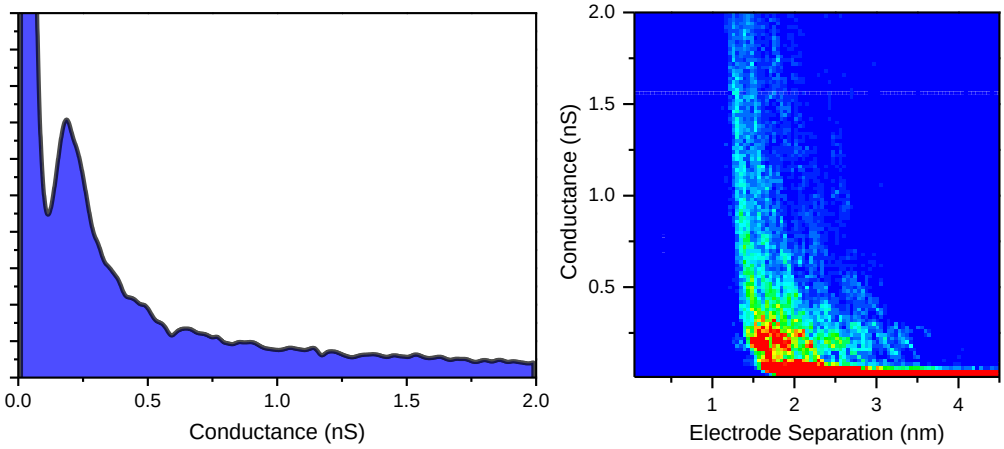

Figure A77: SMC data for 6[T3]6 contact group A in TCB.
I(z) technique, 7 nA setpoint, 0.3 V tip bias.

A.30 6[T3]6 in TCNE 1mM in TCB, 295K

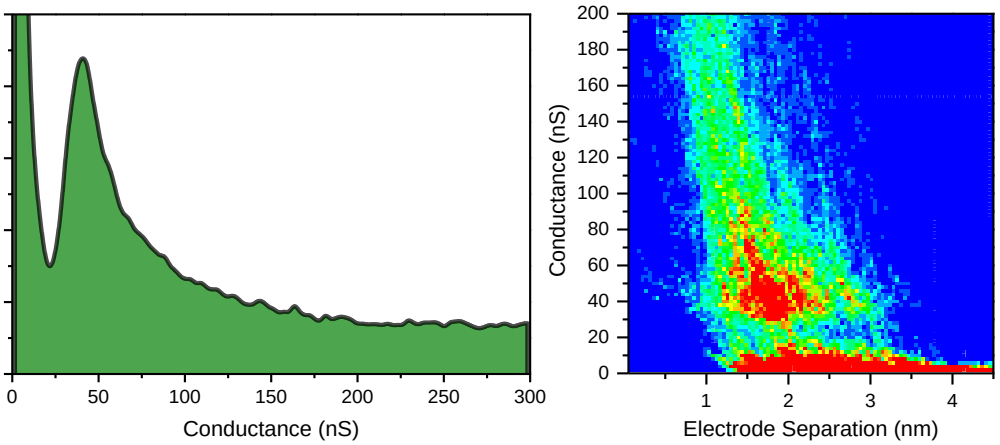

Figure A78: SMC data for 6[T3]6 contact group B in TCNE 1mM in TCB.
STM-BJ technique, 0.1 V tip bias.

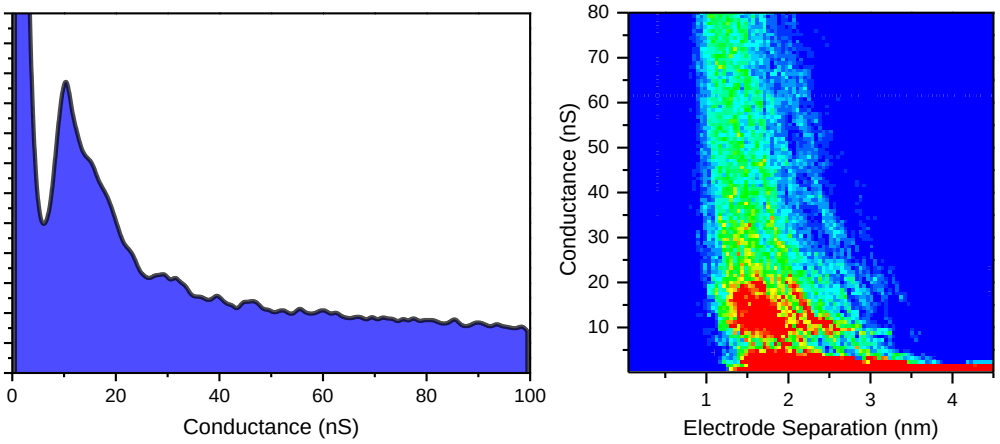

Figure A79: SMC data for 6[T3]6 contact group A in TCNE 1 mM in TCB.
I(z) technique, 60 nA setpoint, 0.3 V tip bias.

A.31 6[T3]6:TCNE in Air, 295K

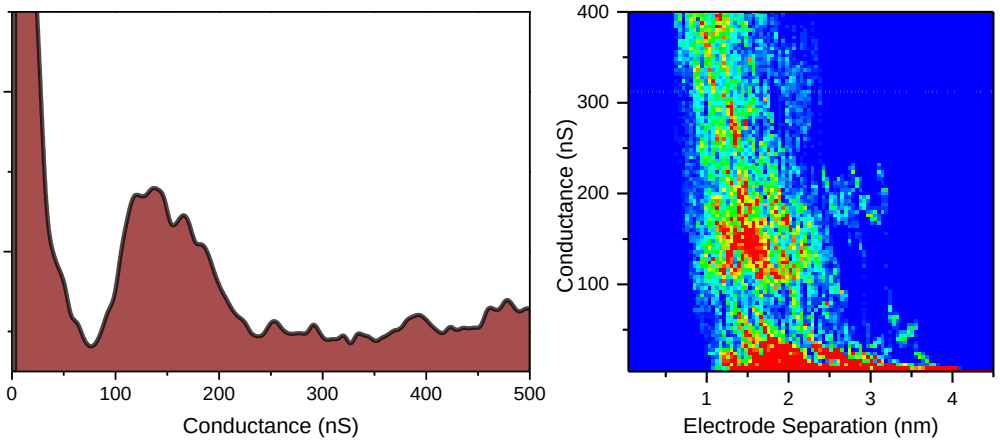

Figure A80: SMC data for 6[T3]6:TCNE contact group C in air.
STM-BJ technique, 0.1 V tip bias.

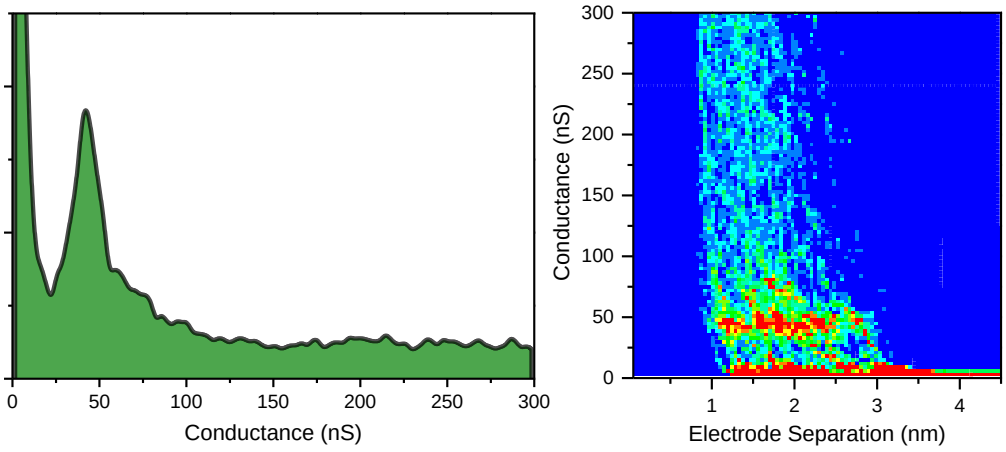

Figure A81: SMC data for 6[T3]6:TCNE contact group B in air.
STM-BJ technique, 0.3 V tip bias.

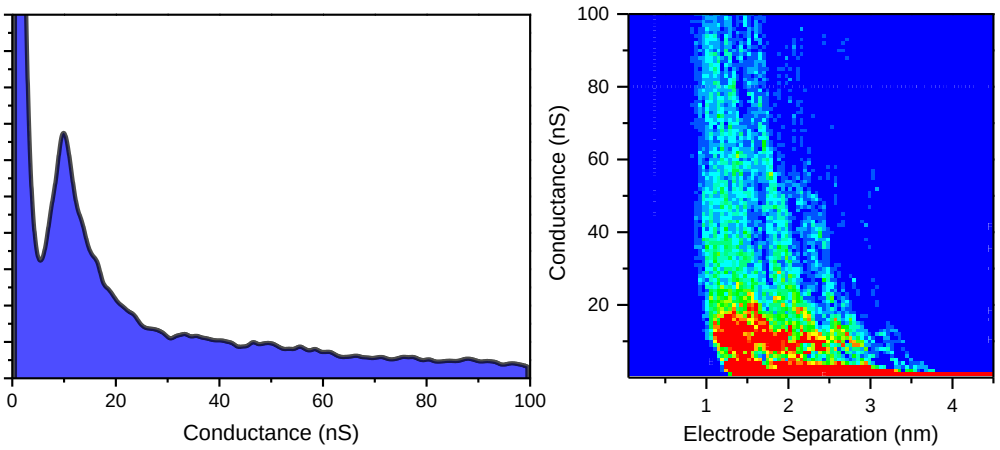

Figure A82: SMC data for 6[T3]6:TCNE contact group A in air.
I(z) technique, 60 nA setpoint, 0.3 V tip bias.

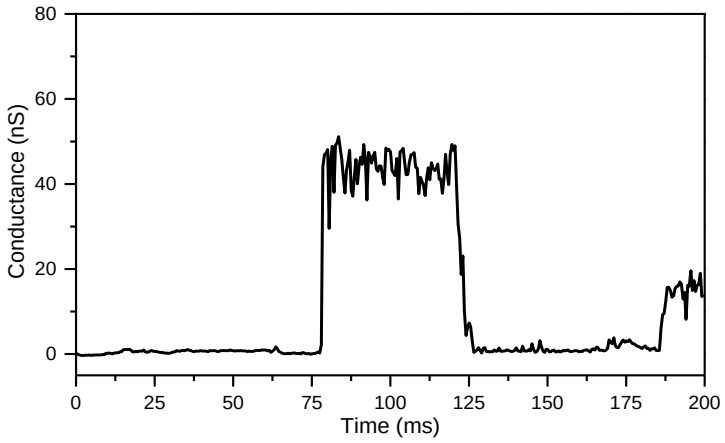

Figure A83: *I(t)* scan for 6[T3]6:TCNE in air. Current jumps corresponding to the A (≈ 15 nS) and B (≈ 45 nS) contact groups conductance can be seen.
I(t) technique, 1 nA setpoint, 0.1 V tip bias.

A.32 6[T3]6 in DNT 1mM in TCB, 295K

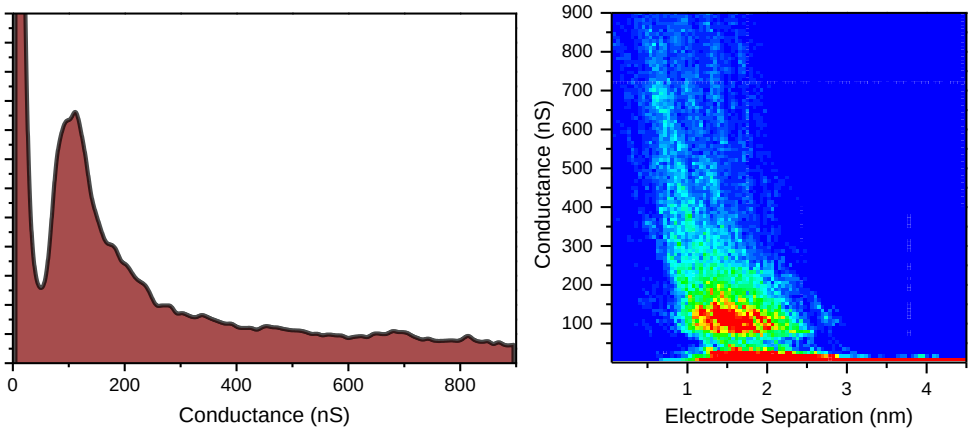

Figure A84: SMC data for 6[T3]6 contact group C in DNT 1 mM in TCB. *STM-BJ* technique, 0.1 V tip bias.

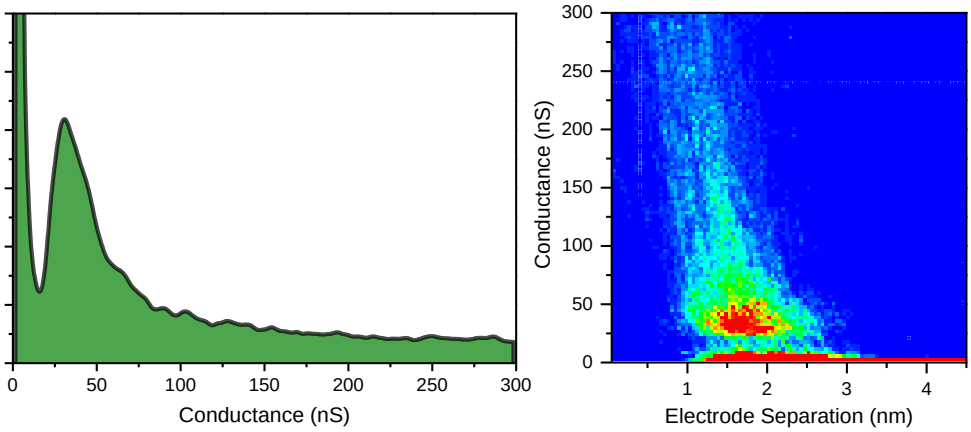

Figure A85: SMC data for 6[T3]6 contact group B in DNT 1 mM in TCB. *STM-BJ* technique, 0.3 V tip bias.

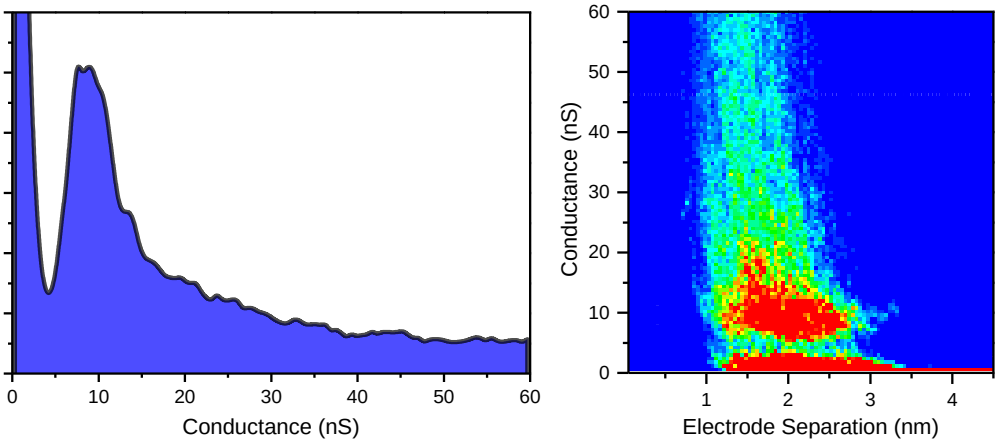

Figure A86: SMC data for 6[T3]6 contact group A in DNT 1 mM in TCB. *I(z)* technique, 60 nA setpoint, 0.3 V tip bias.

A.33 6[T3]6 in CHL 1mM in TCB, 295K

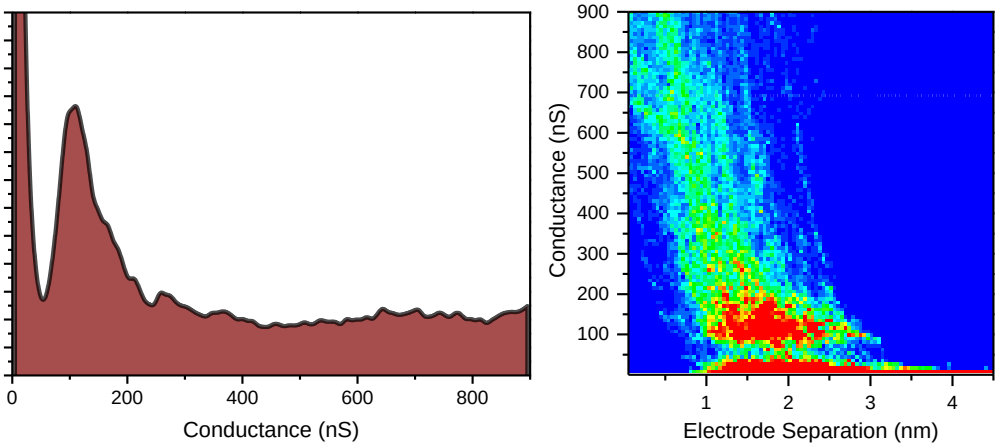

Figure A87: SMC data for 6[T3]6 contact group C in CHL 1 mM in TCB. *STM-BJ* technique, 0.1 V tip bias.

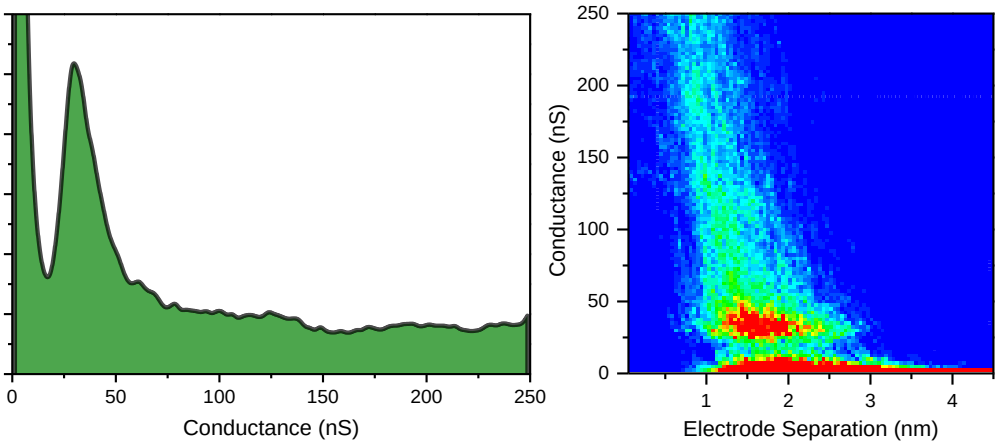

Figure A88: SMC data for 6[T3]6 contact group B in CHL 1 mM in TCB. *STM-BJ* technique, 0.3 V tip bias.

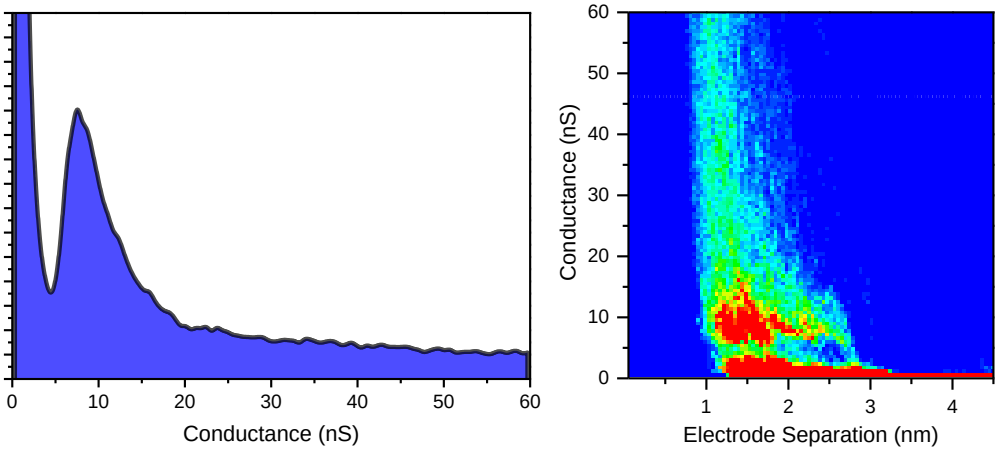

Figure A89: SMC data for 6[T3]6 contact group A in CHL 1 mM in TCB. *I(z)* technique, 60 nA setpoint, 0.3 V tip bias.

A.34 6[T3]6 in TCNQ 1mM in TCB, 295K

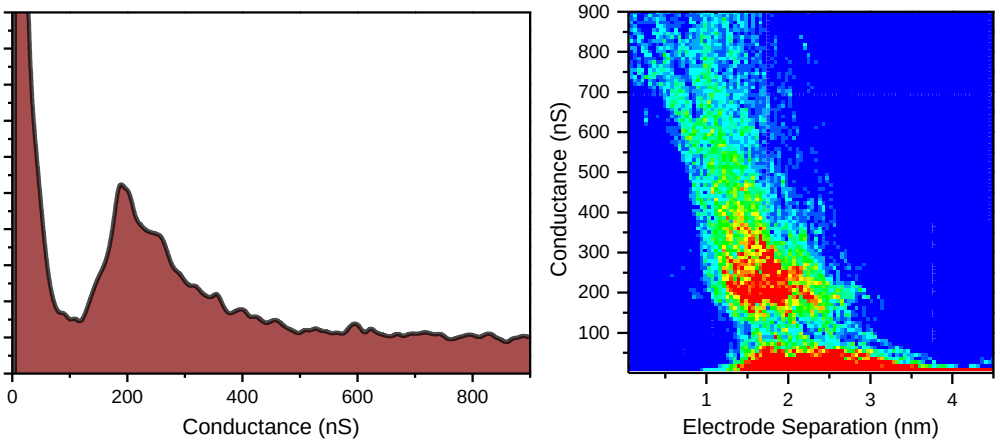

Figure A90: SMC data for 6[T3]6 contact group C in TCNQ 1 mM in TCB. *STM-BJ* technique, 0.1 V tip bias.

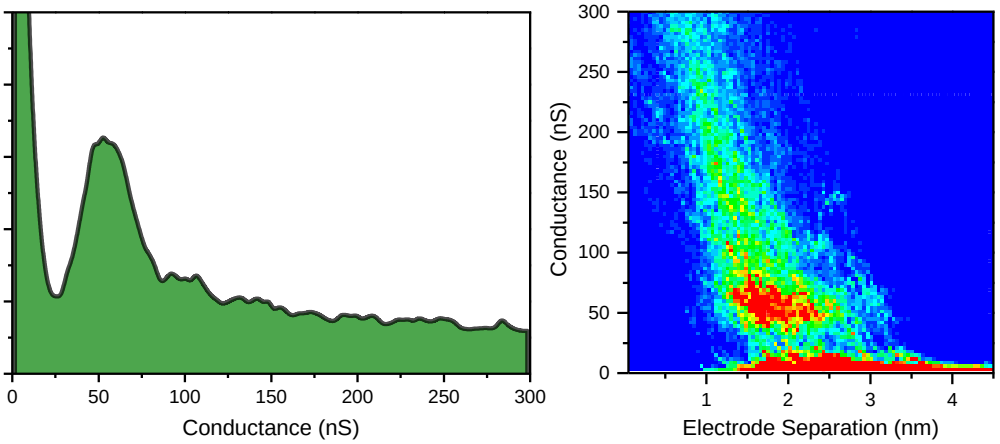

Figure A91: SMC data for 6[T3]6 contact group B in TCNQ 1 mM in TCB. *STM-BJ* technique, 0.3 V tip bias.

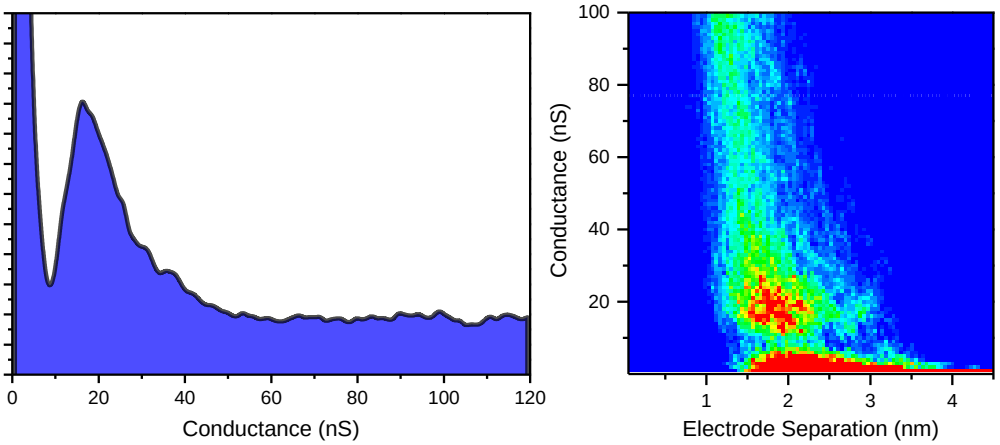

Figure A92: SMC data for 6[T3]6 contact group A in TCNQ 1 mM in TCB. *I(z)* technique, 60 nA setpoint, 0.3 V tip bias.

A.35 6[T3]6:I_2 in Air, 295K

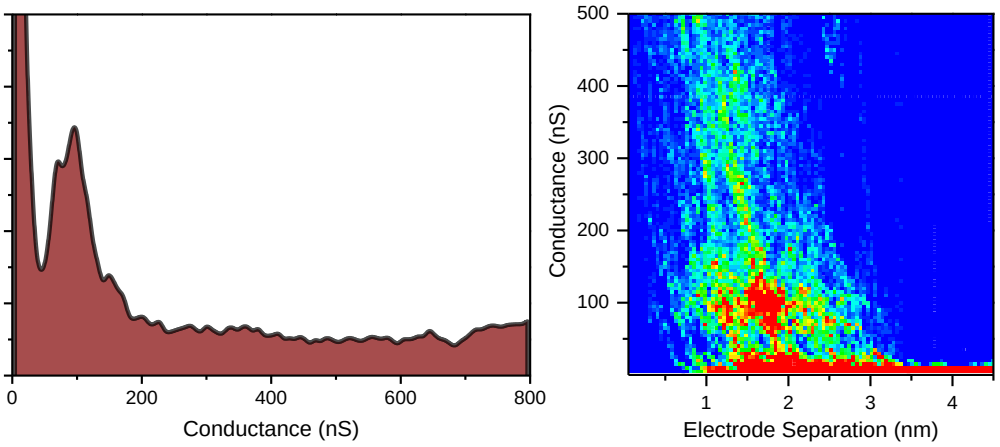

Figure A93: SMC data for 6[T3]6:I_2 contact group C in air.
STM-BJ technique, 0.1 V tip bias.

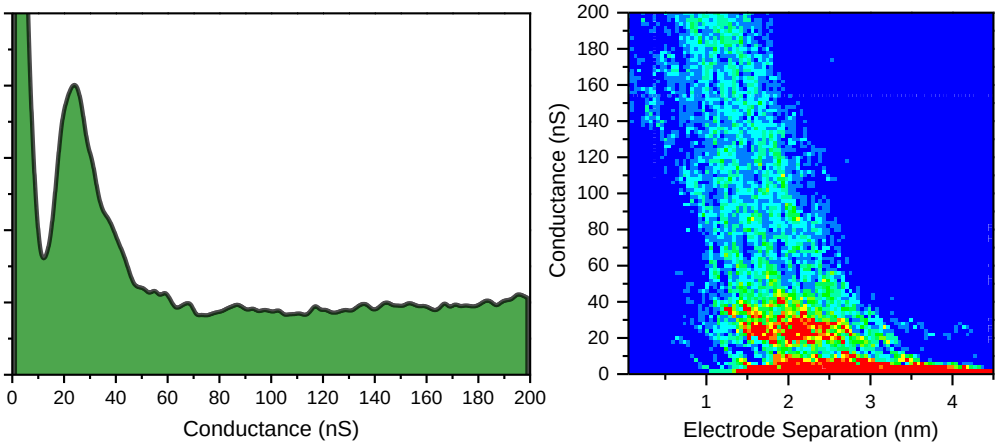

Figure A94: SMC data for 6[T3]6:I_2 contact group B in air.
STM-BJ technique, 0.3 V tip bias.

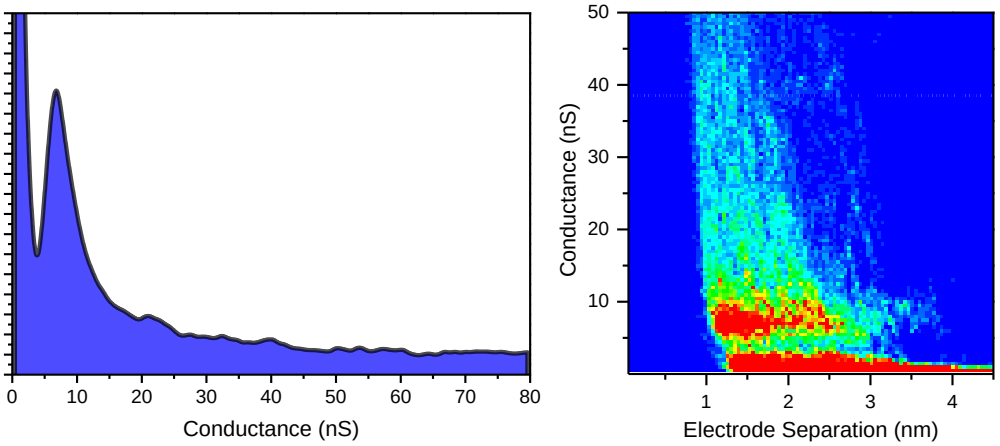

Figure A95: SMC data for 6[T3]6:I_2 contact group A in air.
I(z) technique, 60 nA setpoint, 0.3 V tip bias.

A.36 6[Ph]6 in TCB, 295K

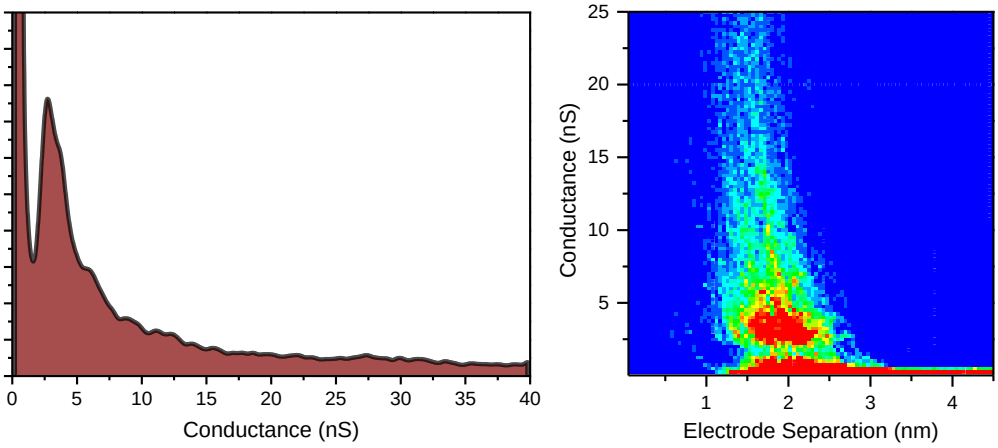

Figure A96: SMC data for 6[Ph]6 contact group C in TCB.
STM-BJ technique, 0.3 V tip bias.

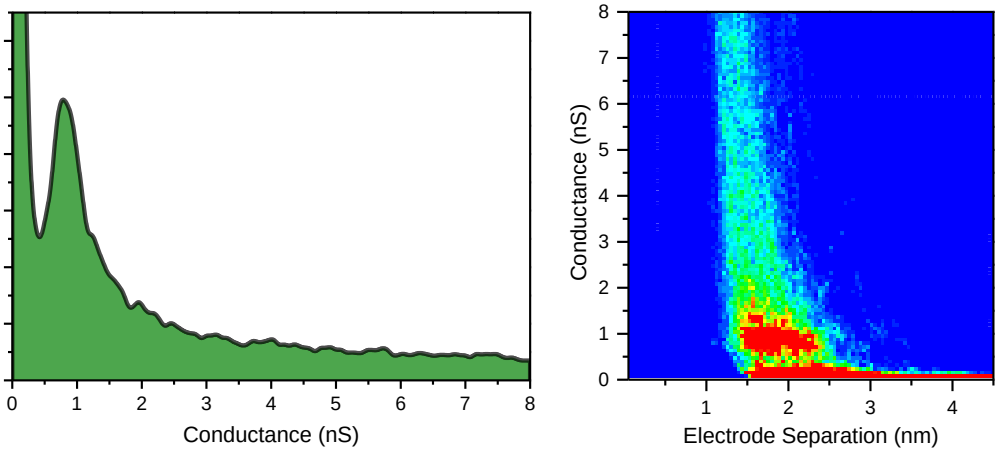

Figure A97: SMC data for 6[Ph]6 contact group B in TCB.
I(z) technique, 10 nA setpoint, 0.3 V tip bias.

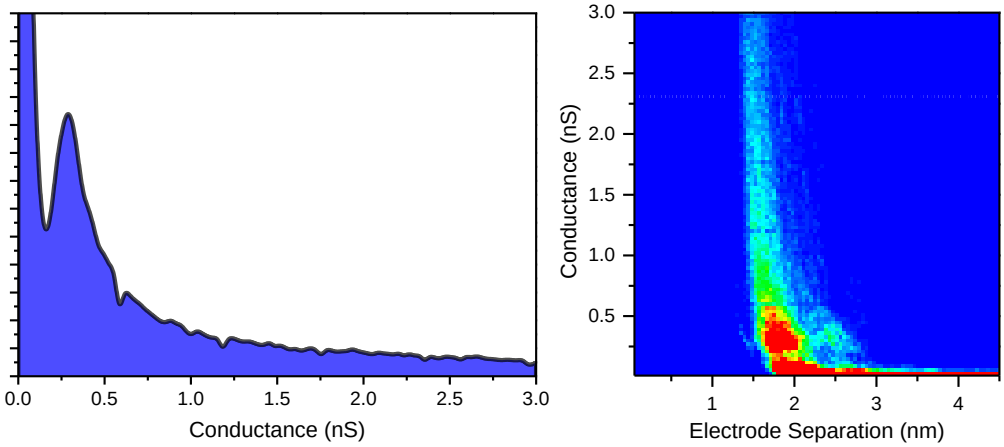

Figure A98: SMC data for 6[Ph]6 contact group A in TCB.
I(z) technique, 6 nA setpoint, 0.3 V tip bias.

A.37 6[Ph]6 in TCNE 1 mM in TCB, 295K

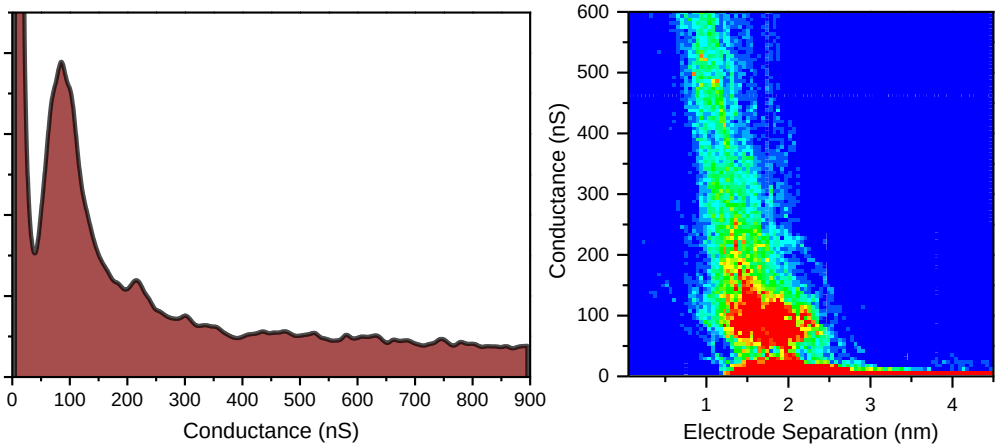

Figure A99: SMC data for 6[Ph]6 contact group C in TCNE 1 mM in TCB.
STM-BJ technique, 0.1 V tip bias.

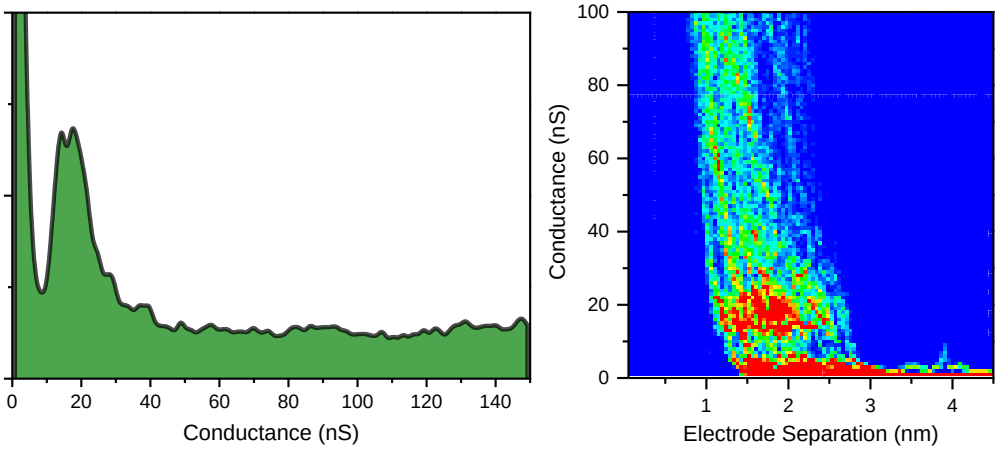

Figure A100: SMC data for 6[Ph]6 contact group B in TCNE 1 mM in TCB.
I(z) technique, 60 nA setpoint, 0.3 V tip bias.

A.38 1[T3]1 in TCB, 295K

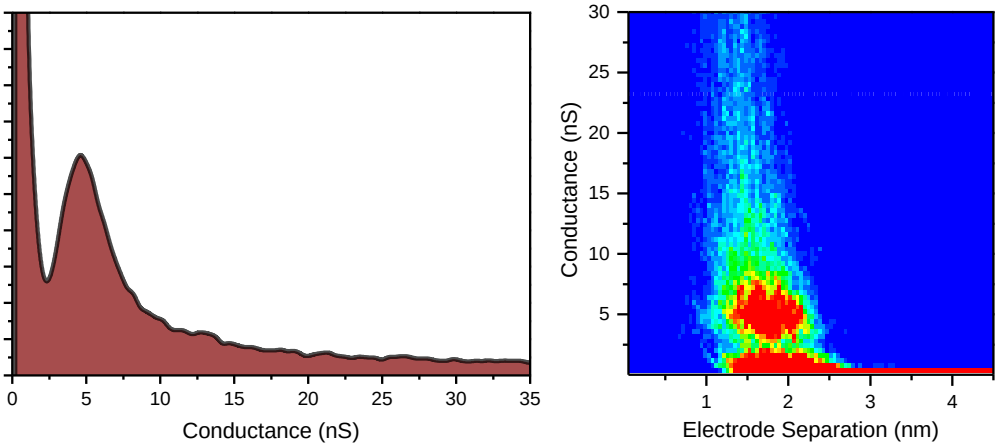

Figure A101: SMC data for 1[T3]1 contact group C in TCB.
STM-BJ technique, 0.3 V tip bias.

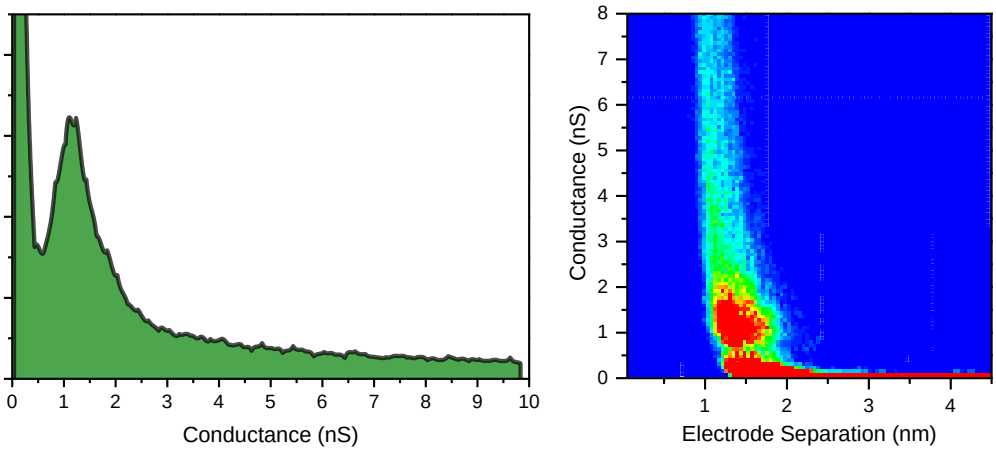

Figure A102: SMC data for 1[T3]1 contact group B in TCB.
I(z) technique, 20 nA setpoint, 0.3 V tip bias.

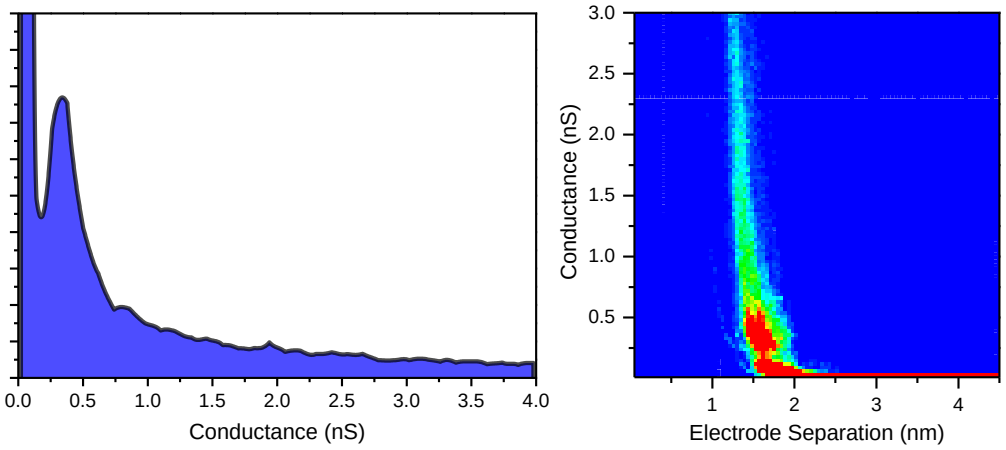

Figure A103: SMC data for 1[T3]1 contact group A in TCB.
I(z) technique, 9 nA setpoint, 0.3 V tip bias.

A.39 1[T3]1 in TCNE 1 mM in TCB, 295K

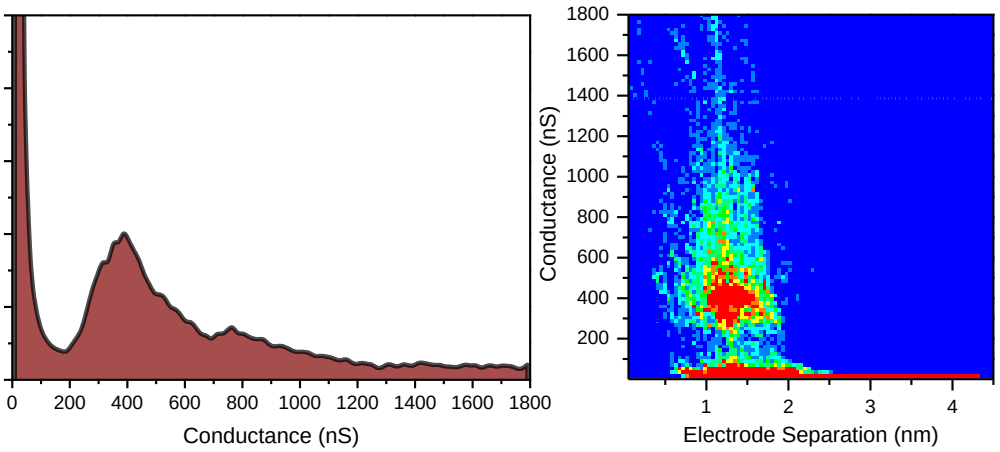

Figure A104: SMC data for 1[T1]6 contact group C in TCNE 1 mM in TCB.
STM-BJ technique, 0.05 V tip bias.

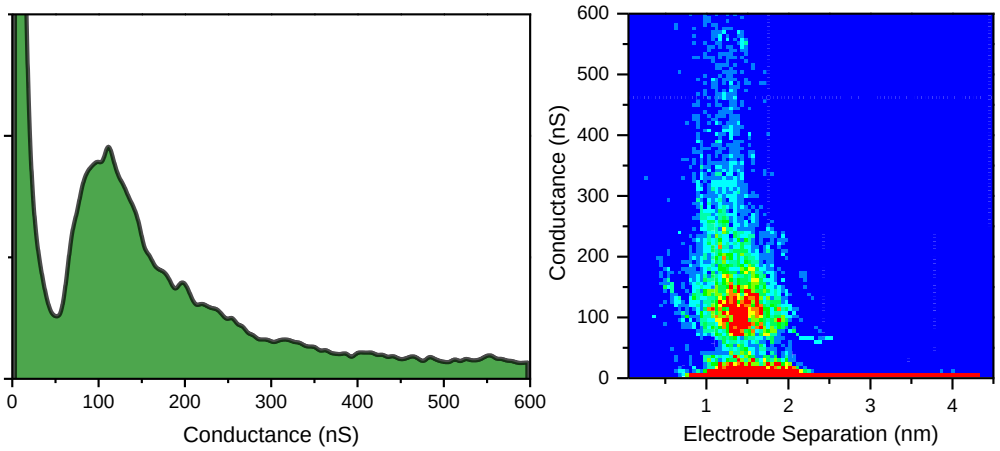

Figure A105: SMC data for 1[T1]6 contact group B in TCNE 1 mM in TCB. *STM-BJ* technique, 0.1 V tip bias.

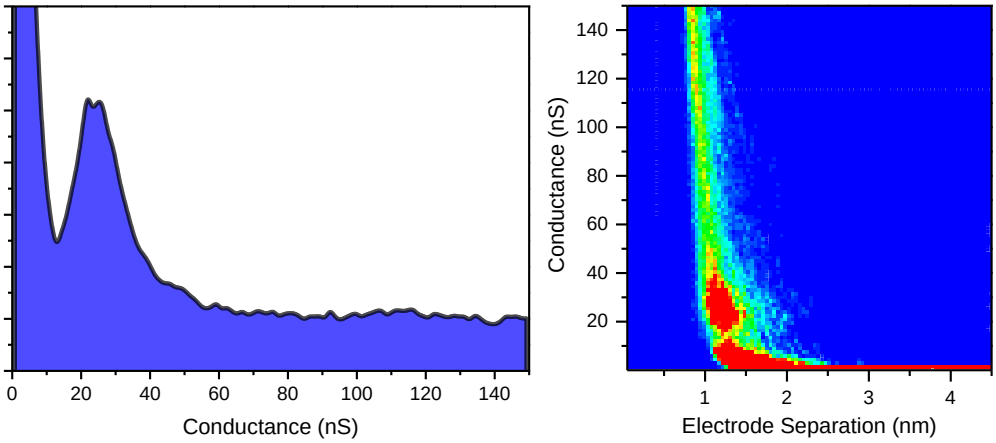

Figure A106: SMC data for 1[T1]6 contact group A in TCNE 1 mM in TCB. *I(z)* technique, 60 nA setpoint, 0.3 V tip bias.

A.40 Conductance Values

	Length (nm)	G in air (nS)	G in TCB (nS)	G under Ar (nS)	Temperatue Dependent?	G in TCNE/TCB (nS)	G in TCNQ/TCB (nS)	G in DNT/TCB (nS)	G in CHL/TCB (nS)	G as I_2 complex (nS)
1[T3]1	1.89	1.22 ± 0.36 0.31 ± 0.09		0.28 ± 0.09 0.098 ± 0.031						
3[T3]3	2.35	0.80 ± 0.21 0.25 ± 0.08		0.18 ± 0.05 0.079 ± 0.021						
4[T3]4	2.49	0.79 ± 0.28 0.23 ± 0.07		0.17 ± 0.04 0.062 ± 0.021						
5[T]5	2.07	0.69 ± 0.16 0.17 ± 0.04		0.69 ± 0.18 0.17 ± 0.04	×					
5[T2]5	2.47	0.74 ± 0.17 0.21 ± 0.06		0.29 ± 0.06 0.08 ± 0.02	✓					
5[T3]5	2.81	0.78 ± 0.25 0.21 ± 0.08		0.14 ± 0.05 0.040 ± 0.011	✓					
6[T3]6	2.98	3.18 ± 0.79 0.69 ± 0.19 0.19 ± 0.05	3.38 ± 0.88 0.69 ± 0.16 0.20 ± 0.05	-- 0.10 ± 0.04 --		143 ± 22 43.9 ± 10.7 12.7 ± 3.5	225 ± 54 56.7 ± 14.6 18.1 ± 4.5	112 ± 28 35.7 ± 9.5 9.59 ± 2.61	110 ± 19.2 33.9 ± 8.0 8.31 ± 1.85	89.8 ± 15.4 27.6 ± 7.8 7.49 ± 1.71
8[T3]8	3.46	0.31 ± 0.09 0.11 ± 0.03								
1[Ph]1	1.19	4.14 ± 0.58 1.09 ± 0.27								
3[Ph]3	1.67	2.01 ± 0.32 0.71 ± 0.23								
4[Ph]4	1.86	1.21 ± 0.19 0.48 ± 0.15								
6[Ph]6	2.37	-- 0.82 ± 0.18 0.28 ± 0.10	3.32 ± 0.88 0.82 ± 0.18 0.28 ± 0.09		×	112 ± 24 22.6 ± 7.4 6.41 ± 1.98				
2[V]2	1.69	26.5 ± 6.3 8.10 ± 1.96								
4[V]4	2.21	4.41 ± 1.66 1.19 ± 0.39								
6[V]6	2.72	0.46 ± 0.12 0.12 ± 0.03								
9[V]9	3.52	0.026 ± 0.008 --								

Table A1: Conductance values for the molecular wires presented in this thesis.

6[T3]6:TCNE without Data Selection

APPENDIX B

If you torture the data enough, nature will always confess.

Ronald Harry Coase, 1981.

Experiments using an SPM to measure conductance of single molecule junctions usually results in a number of current-distance traces that are noisy, unstable, or show no sign of molecular bridging. In this thesis, only the traces bearing signs of proper molecular bridging, with clear exponential decay of current with distance, settling on a plateau for more than 0.05 nm and clear break-off, were manually selected during the experiments. By selecting data using a consistent procedure across all dataset, traces where no proper junction was formed were excluded, which is important to retain information about the contact geometry. However, manually selecting data always carry the risk of experimenter's bias, and experiments without data selection are useful to understand whether the selection criteria are appropriate or not.

B.1 6[T3]6 and its TCNE complex

An experiment on 6[T3]6 and its CT complex with TCNE in 1,2,4-trichlorobenzene was performed using the *STM-BJ* technique, using a logarithmic current follower. 5000 scans were acquired for each target with no further data selection, thus including ill-formed junctions, traces with no molecule bridging the Au-Au gap, and noisy ones. Using this logarithmic current follower it is possible to resolve the G_0 peak, characteristic of the last Au-Au contact before opening of the nanogap, and the following data is plotted as $\log(G / G_0)$, where G_0 (≈ 77.48 μS) is the conductance through a *single* Au channel. Measurements on 6[T3]6 (as 1 mM in TCB) resulted in a broad shoulder spanning 2 orders of magnitude, from 10^{-4} G_0 to the noise level, at 10^{-6} G_0. When TCNE was introduced in the system (at 10 mM concentration), a broad peak centred at 10^{-3} G_0 appeared, thus confirming the conductance enhancement upon CT complexation.

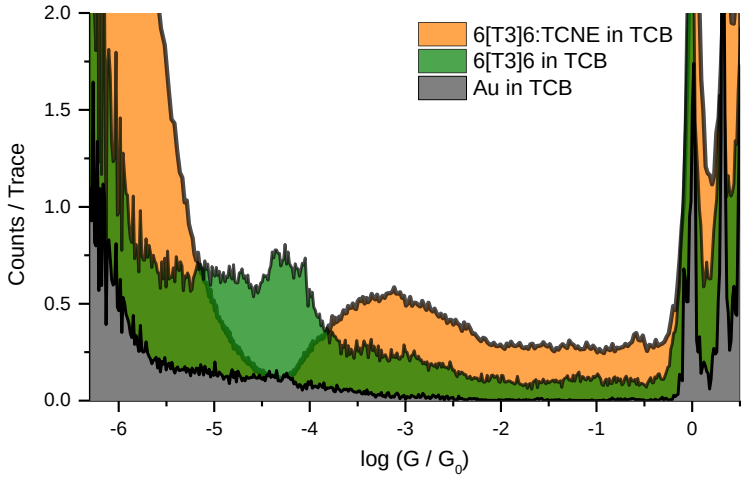

Figure B1: Logarithmic conductance histograms obtained without data selection on 6[T3]6 and its complex with TCNE, with bare gold in TCB shown as comparison. Each histogram consists of 5000 scans, obtained with a logarithmic current follower, using 1 mM concentration of molecular wire and 10 mM concentration of TCNE in TCB at 0.3 V tip bias. A retraction rate of 5 nm s-1 was used in these experiments. Plots are normalised to counts / trace.

Data obtained without trace selection were compared to the histograms presented in Chapter 4. It is clear that when no selection is applied to the dataset, contact information is lost and the three conductance groups envelope into a single, broad feature in the histograms.

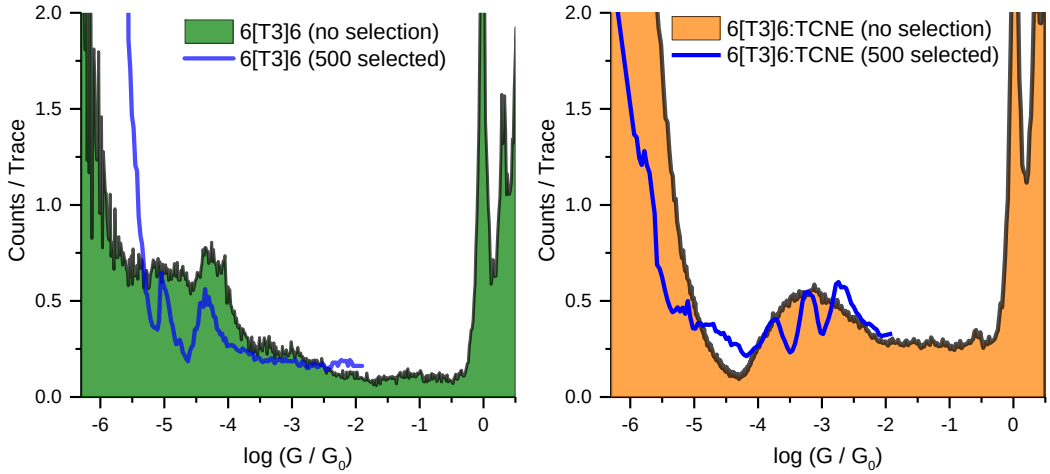

Figure B2: Comparison of dataset with (solid) and without (line) trace selection for 6[T3]6 (left) and its complex with TCNE (right). Selected data is the same presented in Figure 4.4. Plots are normalised to counts / trace.

A control experiment using only TCNE 10 mM in TCB as environment, with no molecular wire present, was performed, and the high noise level observed in the histograms presented in Figures B1-B2 was attributed to Faradaic current due to the presence of TCNE, acting like an electrolyte.

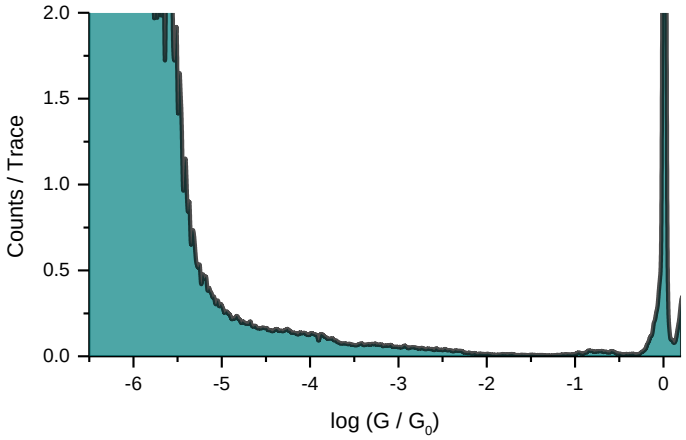

Figure B3: Logarithmic conductance histogram of TCNE 10 mM in TCB. Leakage at 10^{-5} G_0 is attributed to Faradaic current due to the high concentration of TCNE. Tip bias 0.3 V. A retraction rate of 5 nm s-1 was used. Plot is normalised to counts / trace.

Bibliography

1. Moore, G. E. Cramming more components onto integrated circuits. *Electronics* **38,** 33–35 (1965).

2. Schaller, R. R. Moore's Law: Past, Present and Future. *IEEE Spectr.* **34,** 52–59 (1997).

3. Chien, A. A. & Karamcheti, V. Moore's Law: The First Ending and a New Beginning. *Computer (Long. Beach. Calif).* **46,** 48–53 (2013).

4. Mann, B. Tunneling through Fatty Acid Salt Monolayers. *J. Appl. Phys.* **42,** 4398 (1971).

5. Miles, J. L. & McMahon, H. O. Use of Monomolecular Layers in Evaporated-Film Tunneling Devices. *J. Appl. Phys.* **32,** 1176 (1961).

6. Buchwald, C. E., Gallagher, D. M., Haskins, C. P., Thatcher, E. M. & Zahl, P. A. Measurements of Resistance and Capacity of Monofilms of Barium Stearate. *Proc. Natl. Acad. Sci.* **24,** 204–208 (1938).

7. Race, H. H. & Reynolds, S. I. Electrical Properties of Multimolecular Films. *J. Am. Chem. Soc.* **61,** 1425 (1939).

8. Aviram, A. & Ratner, M. A. Molecular rectifiers. *Chem. Phys. Lett.* **29,** 277–283 (1974).

9. Binnig, G. & Rohrer, H. Scanning Tunnelling Microscopy. *Surf. Sci.* **126,** 236–244 (1983).

10. Aviram, A., Joachim, C. & Pomerantz, M. Evidence of switching and rectification by a single molecule effected with a scanning tunneling microscope. *Chem. Phys. Lett.* **146,** 490–495 (1988).

11. Reed, M. A., Zhou, C., Muller, C. J., Burgin, T. P. & Tour, J. M. Conductance of a Molecular Junction. *Science (80-.).* **278,** 252–254 (1997).

12. Ratner, M. A. A brief history of molecular electronics. *Nat. Nanotechnol.* **8,** 378–81 (2013).

13. Young, R., Ward, J. & Scire, F. The topografiner: an instrument for measuring surface microtopography. *Rev. Sci. Instrum.* **43,** 999–1011 (1972).

14. Binnig, G., Rohrer, H., Gerber, C. & Weibel, E. Surface Studies by Scanning Tunnelling Microscopy. *Phys. Rev. Lett.* **49,** 57–61 (1982).

15. Binnig, G. & Rohrer, H. 7x7 reconstruction on Si (111) resolved in real space. *Phys. Rev. Lett.* **50,** 120–123 (1983).

16. Kim, Y., McCarley, R. & Bard, A. Scanning tunneling microscopy studies of gold (111) derivatized with organothiols. *J. Phys. Chem.* **96,** 7416–7421 (1992).

17. Schardt, B. C., Yau, S.-L. & Rinaldi, F. Atomic resolution imaging of adsorbates on metal surfaces in air: iodine adsorption on pt(111). *Science (80-.).* **243,** 1050–3 (1989).

18. De Oteyza, D. G. *et al.* Direct imaging of covalent bond structure in single-molecule chemical reactions. *Science (80-.).* **340,** 1434–7 (2013).

19. Zhao, A. *et al.* STM tip-assisted single molecule chemistry. *Phys. Chem. Chem. Phys.* **15,** 12428–41 (2013).

20. Atkins, P. & de Paula, J. *Physical Chemistry.* (Oxford University Press, 2009).

21. Sze, S. M. & Ng, K. K. *Physics of Semiconductor Devices.* (2007).

22. Hines, T. *et al.* Transition from Tunneling to Hopping in Single Molecular. *J. Am. Chem. Soc.* **115,** 11658–11664 (2010).

23. Li, X. *et al.* Thermally activated electron transport in single redox molecules. *J. Am. Chem. Soc.* **129,** 11535–42 (2007).

24. Choi, S. H. *et al.* Transition from tunneling to hopping transport in long, conjugated oligo-imine wires connected to metals. *J. Am. Chem. Soc.* **132,** 4358–68 (2010).

25. Luo, L. *et al.* Length and Temperature Dependent Conduction of Ruthenium-Containing Redox-Active Molecular Wires. *J. Phys. Chem. C* **115,** 19955–19961 (2011).

26. Wang, W., Lee, T. & Reed, M. A. in *Nano Mol. Electron. Handb.* 1–12 (CRC Press, 2007).

27. Weiss, E. A., Kriebel, J. K., Rampi, M.-A. & Whitesides, G. M. The study of charge transport through organic thin films: mechanism, tools and applications. *Philos. Trans. A. Math. Phys. Eng. Sci.* **365,** 1509–37 (2007).

28. Bohm, D. *Quantum Theory.* (Prentice-Hall, 1951).

29. Luryi, S. Coherent versus Incoherend Resonant Tunnelling and Implications for Fast Devices. *Superlattices Microstruct.* **5,** 375–382 (1989).

30. Piela, L. *Ideas of Quantum Chemistry.* (Elsevier, 2013).

31. Sollner, T. C. L. G., Goodhue, W. D., Tannenwald, P. E., Parker, C. D. & Peck, D. D. Resonant tunneling through quantum wells at frequencies up to 2.5 THz. *Appl. Phys. Lett.* **43,** 588–590 (1983).

32. Cuevas, J. C. & Scheer, E. *Molecular Electronics: an Introduction to Theory and Experiment.* (World Scientific, 2010).

33. Luo, L., Choi, S. H. & Frisbie, C. D. Probing Hopping Conduction in Conjugated Molecular Wires Connected to Metal Electrodes. *Chem. Mater.* **23,** 631–645 (2011).

34. Ho Choi, S., Kim, B. & Frisbie, C. D. Electrical resistance of long conjugated molecular wires. *Science* **320,** 1482–6 (2008).

35. Luo, L. & Frisbie, C. D. Length-dependent conductance of conjugated molecular wires synthesized by stepwise 'click' chemistry. *J. Am. Chem. Soc.* **132,** 8854–5 (2010).

36. Lu, Q. *et al.* From Tunneling to Hopping : A Comprehensive Investigation of Charge Transport Mechanism in Molecular Junctions Based on Oligo(p-phenylene ethynylene)s. *ACS Nano* **3,** 3861–3868 (2009).

37. Poot, M. *et al.* Temperature Dependence of Three-Terminal Molecular Junctions with Sulfur End-Functionalized Tercyclohexylidenes. *Nano Lett.* **6,** 1031–1035 (2006).

38. Sedghi, G. *et al.* Long-range electron tunnelling in oligo-porphyrin molecular wires. *Nat. Nanotechnol.* **6,** 517–23 (2011).

39. Kuznetsov, A. M. & Ulstrup, J. Mechanisms of in Situ Scanning Tunnelling Microscopy of Organized Redox Molecular Assemblies. *J. Phys. Chem. A* **104,** 11531–11540 (2000).

40. Perrin, M. L. *et al.* Large negative differential conductance in single-molecule break junctions. *Nat. Nanotechnol.* **9,** (2014).

41. Majima, Y. *et al.* Negative differential resistance by molecular resonant tunneling between neutral tribenzosubporphine anchored to a Au(111) surface and tribenzosubporphine cation adsorbed on to a tungsten tip. *J. Am. Chem. Soc.* **135,** 14159–66 (2013).

42. Gaudioso, J., Lauhon, L. J. & Ho, W. Vibrationally Mediated Negative Differential Resistance in a Single Molecule. *Phys. Rev. Lett.* **85,** 1918–1921 (2000).

43. Haiss, W. *et al.* Redox state dependence of single molecule conductivity. *J. Am. Chem. Soc.* **125,** 15294–5 (2003).

44. Haiss, W. *et al.* Anomalous length and voltage dependence of single molecule conductance. *Phys. Chem. Chem. Phys.* **11,** 10831–8 (2009).

45. Pobelov, I. V., Li, Z. & Wandlowski, T. Electrolyte Gating in Redox-Active Tunneling Junctions: An Electrochemical STM Approach. *J. Am. Chem. Soc.* **130,** 16045–16054 (2008).

46. Leary, E., Higgins, S. J., van Zalinge, H., Haiss, W. & Nichols, R. J. Chemical control of double barrier tunnelling in alpha,omega-dithiaalkane molecular wires. *Chem. Commun. (Camb).* 3939–41 (2007). doi:10.1039/b709576g

47. Datta, S. *Quantum Transport: Atom to Transistor.* (Cambridge University Press, 2005).

48. Park, H. *et al.* Nanomechanical oscillations in a single-C60 transistor. *Nature* **407,** 57–60 (2000).

49. Cui, X. D. *et al.* Reproducible measurement of single-molecule conductivity. *Science (80-.).* **294,** 571–4 (2001).

50. Cui, X. D. *et al.* Changes in the Electronic Properties of a Molecule When It Is Wired into a Circuit. *J. Phys. Chem. B* **106,** 8609–8614 (2002).

51. Xu, B. & Tao, N. J. Measurement of single-molecule resistance by repeated formation of molecular junctions. *Science* **301,** 1221–3 (2003).

52. Haiss, W. *et al.* Measurement of Single Molecule Conductivity Using the Spontaneous Formation of Molecular Wires. *Phys. Chem. Chem. Phys.* **6,** 4330–4337 (2004).

53. Pires, E., Macdonald, J. E. & Elliott, M. Chain length and temperature dependence of alkanedithiol molecular conductance under ultra high vacuum. *Nanoscale* **5,** 9397–403 (2013).

54. Feenstra, R. M., Thompson, W. A. & Fein, A. P. Real Space Observation of Pi-Bonded Chains and Surface Disorder on Si(111)2x1. *Phys. Rev. Lett.* **56,** 608–611 (1986).

55. Frisenda, R., Perrin, M. L., Valkenier, H., Hummelen, J. C. & van der Zant, H. S. J. Statistical analysis of single-molecule breaking traces. *Phys. Status Solidi* **250,** 2431–2436 (2013).

56. Reichert, J. *et al.* Driving Current through Single Organic Molecules. *Phys. Rev. Lett.* **88,** 176804 (2002).

57. Catarelli, S. R. *et al.* Ionic Liquid Based Approach for Single-Molecule Electronics with Cobalt Contacts. *Langmuir* (2014). doi:10.1021/la503077c

58. Brooke, R. J. *et al.* A single-molecule electrochemical transistor utilizing a nickel-pyridyl spinterface. *Nano Lett.* (2014). doi:10.1021/nl503518q

59. Kim, T., Vázquez, H., Hybertsen, M. S. & Venkataraman, L. Conductance of molecular junctions formed with silver electrodes. *Nano Lett.* **13,** 3358–64 (2013).

60. Kiguchi, M. *et al.* Conductance of Single 1,4-Benzenediamine Molecule Bridging between Au and Pt Electrodes. *J. Phys. Chem. C* **112,** 13349–13352 (2008).

61. Zhao, Y. *et al.* Combined effect of polar substituents on the electronic flows in the carotenoid molecular wires. *Chemistry* **19,** 10832–5 (2013).

62. Leary, E. *et al.* Single-Molecule Solvation-Shell Sensing. *Phys. Rev. Lett.* **102,** 086801 (2009).

63. Arroyo, C. R. *et al.* Signatures of quantum interference effects on charge transport through a single benzene ring. *Angew. Chem. Int. Ed. Engl.* **52,** 3152–5 (2013).

64. Gao, D. *et al.* Fabrication of asymmetric molecular junctions by the oriented assembly of dithiocarbamate rectifiers. *J. Am. Chem. Soc.* **133,** 5921–30 (2011).

65. Hong, W. *et al.* Single molecular conductance of tolanes: experimental and theoretical study on the junction evolution dependent on the anchoring group. *J. Am. Chem. Soc.* **134,** 2292–304 (2012).

66. Chen, W. *et al.* Aromaticity decreases single-molecule junction conductance. *J. Am. Chem. Soc.* **136,** 918–20 (2014).

67. Martin, C. a *et al.* Fullerene-based anchoring groups for molecular electronics. *J. Am. Chem. Soc.* **130,** 13198–9 (2008).

68. Yasuda, S. *et al.* Bond fluctuation of S/Se anchoring observed in single-molecule conductance measurements using the point contact method with scanning tunneling microscopy. *J. Am. Chem. Soc.* **128,** 7746–7 (2006).

69. Parameswaran, R. *et al.* Reliable Formation of Single Molecule Junctions with Air-Stable Diphenylphosphine Linkers. *J. Phys. Chem. Lett.* **1,** 2114–2119 (2010).

70. Zhou, X.-S., Liang, J.-H., Chen, Z.-B. & Mao, B.-W. An electrochemical jump-to-contact STM-break junction approach to construct single molecular junctions with different metallic electrodes. *Electrochem. commun.* **13,** 407–410 (2011).

71. Marqués-González, S. *et al.* Simplifying the conductance profiles of molecular junctions: the use of the trimethylsilylethynyl moiety as a molecule-gold contact. *Dalton Trans.* **42,** 338–41 (2013).

72. Moreno-García, P. *et al.* Single-molecule conductance of functionalized oligoynes: length dependence and junction evolution. *J. Am. Chem. Soc.* **135,** 12228–40 (2013).

73. Schneebeli, S. T. *et al.* Single-Molecule Conductance through Multiple π - π - Stacked Benzene Rings Determined with Direct Electrode-to-Benzene Ring Connections. *J. Chem. Soc. Chem. Commun.* **133,** 2136–2139 (2011).

74. Hines, T. *et al.* Controlling formation of single-molecule junctions by electrochemical reduction of diazonium terminal groups. *J. Am. Chem. Soc.* **135,** 3319–22 (2013).

75. Hong, W. *et al.* Trimethylsilyl-Terminated Oligo (phenylene ethynylene) s: An Approach to Single-Molecule Junctions with Covalent Au–C σ-Bonds. *J. Am. Chem. Soc.* **134,** 19425–19431 (2012).

76. Chen, W. *et al.* Highly Conducting π -Conjugated Molecular Junctions Covalently Bonded to Gold Electrodes. *J. Am. Chem. Soc.* **133,** 17160–17163 (2011).

77. Landauer, R. Spatial Variation of Currents and Fields Due to Localized Scatterers in Metallic Conduction. *IBM J. Res. Dev.* **1/2,** 251–259 (2000).

78. Karthauser, S. Control of molecule-based transport for future molecular devices. *J. Phys. Condens. Matter* **23,** 013001 (2011).

79. Li, X. *et al.* Conductance of Single Alkanedithiols : Conduction Mechanism and Effect of Molecule - Electrode Contacts. *J. Am. Chem. Soc.* **128,** 2135–2141 (2006).

80. Haiss, W. *et al.* Impact of junction formation method and surface roughness on single molecule conductance. *J. Phys. Chem. C* **113,** 5823–5833 (2009).

81. Nichols, R. J. *et al.* The experimental determination of the conductance of single molecules. *Phys. Chem. Chem. Phys.* **12,** 2801–15 (2010).

82. Chang, W. B. *et al.* Controlling the Thermoelectric Properties of Thiophene-derived Single Molecule Junctions. *Chem. Mater.* 141122123742007 (2014). doi:10.1021/cm504254n

83. Malen, J. a., Yee, S. K., Majumdar, A. & Segalman, R. a. Fundamentals of energy transport, energy conversion, and thermal properties in organic–inorganic heterojunctions. *Chem. Phys. Lett.* **491,** 109–122 (2010).

84. Li, C. *et al.* Charge transport in single Au / alkanedithiol / Au junctions: coordination geometries and conformational degrees of freedom. *J. Am. Chem. Soc.* **130,** 318–26 (2008).

85. Hartough, H. D. *The chemistry of heterocyclic compounds, Volume 3: Thiophene and its Derivatives.* (John Wiley and Sons, 2009).

86. Swanston, J. in *Ullman's Encycl. Ind. Chem.* (ed. Wiley-VCH) (2006).

87. Gronovitz, S. & Hornfeldt, A. B. *Thiophenes.* (Elsevier, 2004).

88. Lednicer, D. & Mitscher, L. A. *The Organic Chemistry of Drug Synthesis, Volume 6.* (John Wiley and Sons, 1998).

89. Ciofalo, M. & Ponterini, G. Generation of singlet oxygen by 2,2′:5′,2″-terthiophene and some of its derivatives. *J. Photochem. Photobiol. A Chem.* **83,** 1–6 (1994).

90. Parthasarathy, A. & Goswami, S. Photophysics and light-activated biocidal activity of visible-light-absorbing conjugated oligomers. *ACS Appl. Mater. Interfaces* **5,** 4516–4520 (2013).

91. Liu, Y., Ye, M., Guo, H. Z., Zhao, Y. Y. & Guo, D. A. New Thiophenes from Echinops Grijsii. *J. As. Nat. Prod. Res.* **4,** 175–178 (2002).

92. Roncali, J. Conjugated Poly(thiophenes): Synthesis, Functionalizatlon, and Applications. *Chem. Rev.* **92,** 711–738 (1992).

93. Assadi, A., Svensson, C., Willander, M. & Inganäs, O. Field-effect mobility of poly(3-hexylthiophene). *Appl. Phys. Lett.* **53,** 195 (1988).

94. Zaumseil, J. P3HT and Other Polythiophene Field-Effect Transistors. *Adv. Polym. Sci.* **265,** 107–137 (2014).

95. Sirringhaus, H. Integrated Optoelectronic Devices Based on Conjugated Polymers. *Science (80-.).* **280,** 1741–1744 (1998).

96. Cho, J. H. *et al.* Printable ion-gel gate dielectrics for low-voltage polymer thin-film transistors on plastic. *Nat. Mater.* **7,** 900–6 (2008).

97. Chandekar, A. & Whitten, J. E. Ultraviolet photoemission and electron loss spectroscopy of oligothiophene films. *Synth. Met.* **150,** 259–264 (2005).

98. Kobayashi, M. *et al.* Synthesis and Properties of Chemically Coupled Polythiophene. *Synth. Met.* **9,** 77–86 (1984).

99. Xu, B. Q., Li, X. L., Xiao, X. Y., Sakaguchi, H. & Tao, N. J. Electromechanical and conductance switching properties of single oligothiophene molecules. *Nano Lett.* **5,** 1491–5 (2005).

100. Yamada, R., Kumazawa, H., Noutoshi, T., Tanaka, S. & Tada, H. Electrical conductance of oligothiophene molecular wires. *Nano Lett.* **8,** 1237–40 (2008).

101. Capozzi, B. *et al.* Length-dependent conductance of oligothiophenes. *J. Am. Chem. Soc.* **136,** 10486–92 (2014).

102. Dell, E. J. *et al.* Impact of molecular symmetry on single-molecule conductance. *J. Am. Chem. Soc.* **135,** 11724–7 (2013).

103. Xiao, X., Xu, B. & Tao, N. Conductance titration of single-peptide molecules. *J. Am. Chem. Soc.* **126,** 5370–1 (2004).

104. Xiao, X., Xu, B. & Tao, N. Changes in the conductance of single peptide molecules upon metal-ion binding. *Angew. Chem. Int. Ed. Engl.* **43,** 6148–52 (2004).

105. Scullion, L. *et al.* Large Conductance Changes in Peptide Single Molecule Junctions Controlled by pH. *J. Phys. Chem. C* **115,** 8361–8368 (2011).

106. Nakashima, S., Takahashi, Y. & Kiguchi, M. Effect of the environment on the electrical conductance of the single benzene-1,4-diamine molecule junction. *Beilstein J. Nanotechnol.* **2,** 755–9 (2011).

107. Fatemi, V., Kamenetska, M., Neaton, J. B. & Venkataraman, L. Environmental control of single-molecule junction transport. *Nano Lett.* **11,** 1988–92 (2011).

108. Kasibhatla, B. S. T. *et al.* Reversibly Altering Electronic Conduction through a Single Molecule by a Chemical Binding Event. *J. Phys. Chem. B* **107,** 12378–12382 (2003).

109. Del Re, J., Moore, M. H., Ratna, B. R. & Blum, A. S. Molecular sensing: modulating molecular conduction through intermolecular interactions. *Phys. Chem. Chem. Phys.* **15,** 8318–23 (2013).

110. Dulić, D. *et al.* One-Way Optoelectronic Switching of Photochromic Molecules on Gold. *Phys. Rev. Lett.* **91,** 207402 (2003).

111. Löfås, H. *et al.* New Class of Molecular Conductance Switches Based on the [1,3]-Silyl Migration from Silanes to Silenes. *J. Phys. Chem. C* **117,** 10909–10918 (2013).

112. Löfås, H. *et al.* A computational study of potential molecular switches that exploit Baird's rule on excited-state aromaticity and antiaromaticity. *Faraday Discuss.* **174,** 105–124 (2014).

113. Choi, B.-Y. *et al.* Conformational Molecular Switch of the Azobenzene Molecule: A Scanning Tunneling Microscopy Study. *Phys. Rev. Lett.* **96,** 156106 (2006).

114. Hsu, L.-Y. & Rabitz, H. Single-Molecule Phenyl-Acetylene-Macrocycle-Based Optoelectronic Switch Functioning as a Quantum-Interference-Effect Transistor. *Phys. Rev. Lett.* **109,** 186801 (2012).

115. Mativetsky, J. M. *et al.* Azobenzenes as light-controlled molecular electronic switches in nanoscale metal-molecule-metal junctions. *J. Am. Chem. Soc.* **130,** 9192–3 (2008).

116. Battacharyya, S. *et al.* Optical modulation of molecular conductance. *Nano Lett.* **11,** 2709–14 (2011).

117. Darwish, N. A., Aragones, A. C., Darwish, T. A., Ciampi, S. & Díez-Pérez, I. Multi-Responsive Photo- and Chemo-Electrical Single-Molecule Switches. *Nano Lett.* (2014). doi:10.1021/nl5034599

118. Negri, R. M. & Prypsztejn, H. E. An Experiment on Photochromism and Kinetics for the Undergraduate Laboratory. *J. Chem. Educ.* **78,** 645 (2001).

119. Dvornikov, A. S., Malkin, J. & Rentzepis, P. M. Spectroscopy and Kinetics of Photochromic Materials for 3D Optical Memory Devices. *J. Phys. Chem.* **98,** 6746–6752 (1994).

120. Wold, D. J., Haag, R., Rampi, M. A. & Frisbie, C. D. Distance Dependence of Electron Tunneling through Self-Assembled Monolayers Measured by Conducting Probe Atomic Force Microscopy: Unsaturated versus Saturated Molecular Junctions. *J. Phys. Chem. B* **106,** 2813–2816 (2002).

121. Miroshnichenko, A. E., Flach, S. & Kivshar, Y. S. Fano resonances in nanoscale structures. *Rev. Mod. Phys.* **82,** 2257–2298 (2010).

122. Holmlin, R. E. *et al.* Electron Transport through Thin Organic Films in Metal–Insulator–Metal Junctions Based on Self-Assembled Monolayers. *J. Am. Chem. Soc.* **123,** 5075–5085 (2001).

123. Creager, S. *et al.* Electron Transfer at Electrodes through Conjugated 'Molecular Wire' Bridges. *J. Am. Chem. Soc.* **121,** 1059–1064 (1999).

124. Haag, R., Rampi, M. A., Holmlin, R. E. & Whitesides, G. M. Electrical Breakdown of Aliphatic and Aromatic Self-Assembled Monolayers Used as Nanometer-Thick Organic Dielectrics. *J. Am. Chem. Soc.* **121,** 7895–7906 (1999).

125. Baghbanzadeh, M. *et al.* Odd-Even Effects in Charge Transport across n-Alkanethiolate-Based SAMs. *J. Am. Chem. Soc.* (2014). doi:10.1021/ja509436k

126. Sedghi, G. *et al.* Single molecule conductance of porphyrin wires with ultralow attenuation. *J. Am. Chem. Soc.* **130,** 8582–3 (2008).

127. Li, Z., Park, T., Rawson, J., Therien, M. J. & Borguet, E. Quasi-ohmic single molecule charge transport through highly conjugated meso-to-meso ethyne-bridged porphyrin wires. *Nano Lett.* **12,** 2722–7 (2012).

128. Ferreira, Q., Bragança, A. M., Alcácer, L. & Morgado, J. Conductance of Well-Defined Porphyrin Self-Assembled Molecular Wires up to 14 nm in Length. *J. Phys. Chem. C* **118,** 7229–7234 (2014).

129. Wang, C. *et al.* Oligoyne single molecule wires. *J. Am. Chem. Soc.* **131,** 15647–54 (2009).

130. Xing, Y. *et al.* Optimizing single-molecule conductivity of conjugated organic oligomers with carbodithioate linkers. *J. Am. Chem. Soc.* **132,** 7946–56 (2010).

131. Kolivoška, V. *et al.* Single-Molecule Conductance in a Series of Extended Viologen Molecules. *J. Phys. Chem. Lett.* **4,** 589–595 (2013).

132. Dubi, Y. Transport through Self-Assembled Monolayer Molecular Junctions: Role of In-Plane Dephasing. *J. Phys. Chem. C* **118,** 21119–21127 (2014).

133. Selzer, Y., Cabassi, M. A., Mayer, T. S. & Allara, D. L. Thermally activated conduction in molecular junctions. *J. Am. Chem. Soc.* **126,** 4052–3 (2004).

134. Leary, E. *et al.* A molecular wire incorporating a robust hexanuclear platinum cluster. *Phys. Chem. Chem. Phys.* **11,** 5198–202 (2009).

135. Leary, E. *et al.* Structure-property relationships in redox-gated single molecule junctions--a comparison of pyrrolo-tetrathiafulvalene and viologen redox groups. *J. Am. Chem. Soc.* **130,** 12204–5 (2008).

136. Haiss, W. *et al.* Thermal gating of the single molecule conductance of alkanedithiols. *Faraday Discuss.* **131,** 253 (2006).

137. Park, Y. S. *et al.* Contact chemistry and single-molecule conductance: a comparison of phosphines, methyl sulfides, and amines. *J. Am. Chem. Soc.* **129,** 15768–9 (2007).

138. Brooke, C. Synthesis, characterisation and single molecule conductance measurements of organic molecules. (2012). at <http://repository.liv.ac.uk/9397/4/BrookeCar_Nov2012_9397.pdf>

139. Wang, K., Hamill, J. M., Zhou, J. & Xu, B. Mapping the details of contact effect of modulated Au-octanedithiol-Au break junction by force-conductance cross-correlation. *J. Am. Chem. Soc.* 8–11 (2014). doi:10.1021/ja510738y

140. Guo, S., Hihath, J., Díez-Pérez, I. & Tao, N. Measurement and statistical analysis of single-molecule current-voltage characteristics, transition voltage spectroscopy, and tunneling barrier height. *J. Am. Chem. Soc.* **133,** 19189–97 (2011).

141. Bagrets, A., Arnold, A. & Evers, F. Conduction properties of bipyridinium-functionalized molecular wires. *J. Am. Chem. Soc.* **130,** 9013–8 (2008).

142. Li, Z. *et al.* Conductance of redox-active single molecular junctions: an electrochemical approach. *Nanotechnology* **18,** 044018 (2007).

143. Stipa, P. Radical cations from dipyridinium derivatives: a combined EPR and DFT study. *Spectrochim. Acta. A. Mol. Biomol. Spectrosc.* **64,** 653–9 (2006).

144. Soler, J. M. *et al.* The SIESTA method for ab initio order- N materials simulation. *J. Phys. Condens. Matter* **14,** 2745–2779 (2002).

145. Ferrer, J. *et al.* GOLLUM: a next-generation simulation tool for electron, thermal and spin transport. *New J. Phys.* **16,** 093029 (2014).

146. Widawsky, J. R. *et al.* Length-Dependent Thermopower of Highly Conducting Au–C Bonded Single Molecule Junctions. *Nano Lett.* **13,** 2889–2894 (2013).

147. Brooke, C. *et al.* Resonant transport and electrostatic effects in single-molecule electrical junctions. *Phys. Rev. B* **91,** 1–9 (2015).

148. Pires, E. Electrical Conductivity of Single Organic Molecules in Ultra High Vacuum. (2013). at <http://orca.cf.ac.uk/56796/1/2013piresejphd.pdf>

149. Leary. Single Molecule Conductance of Dithiahexyl-Aryl Compounds. (2008). at <http://pcwww.liv.ac.uk/~nichols/documents/docs/Edmund Leary PhD Final thesis book EL (2).pdf>

150. Akamatu, H., Inokuchi, H. & Matsunaga, Y. Electrical Conductivity of the Perylene–Bromine Complex. *Nature* **173,** 168–169 (1954).

151. Naarmann, H. *Polymers, Electrically Conducting, in Ullmann's Encyclopedia of Industrial Chemistry.* (Wiley-VCH Verlag GmbH & Co. KGaA, 2000). doi:10.1002/14356007.a21_429

152. Melby, L. R. *et al.* Substituted Quinodimethans. II. Anion-radical Derivatives and Complexes of 7,7,8,8-Tetracyanoquinodimethan. *J. Am. Chem. Soc.* **84,** 3374–3387 (1962).

153. Dhar, D. N. The Chemistry of Tetracyanoethylene. *Chem. Rev.* **67,** 611–622 (1967).

154. Wudl, F., Wobschall, D. & Hufnagel, E. J. Electrical conductivity by the bis(1,3-dithiole)-bis(1,3-dithiolium) system. *J. Am. Chem. Soc.* **94,** 670–672 (1972).

155. Ferraris, J., Cowan, D. O., Walatka, V. & Perlstein, J. H. Electron transfer in a new highly conducting donor-acceptor complex. *J. Am. Chem. Soc.* **95,** 948–949 (1973).

156. Jerome, D., Mazaud, A., Ribault, M. & Bechgaard, K. Superconductivity in a synthetic organic conductor (TMTSF)2PF6. *J. Phys. Lettres* **41,** 95–98 (1980).

157. Nič, M., Jirát, J., Košata, B., Jenkins, A. & McNaught, A. *IUPAC Compendium of Chemical Terminology.* (IUPAC, 2009). doi:10.1351/goldbook

158. Mulliken, R. S. & Person, W. B. *Molecular complexes.* (John Wiley and Sons Inc., 1971).

159. Benesi, H. A. & Hildebrand, J. H. A Spectrophotometric Investigation of the Interaction of Iodine with Aromatic Hydrocarbons. *J. Am. Chem. Soc.* **71,** 2703–2707 (1949).

160. Merrifield, R. E. & Phillips, W. D. Cyanocarbon Chemistry. II. 1 Spectroscopic Studies of the Molecular Complexes of Tetracyanoethylene. *J. Am. Chem. Soc.* **80,** 2778–2782 (1958).

161. Dewar, M. J. S. & Thompson, C. C. Π-Molecular complexes—III: A critique for charge-transfer, and stability constants for some TCNE-hydrocarbon complexes. *Tetrahedron* **22,** 97–114 (1966).

162. Frey, J. E. *et al.* Charge-Transfer Complexes of Tetracyanoethylene with Alkyl and Aryl Derivatives of Sulfur, Selenium, and Tellurium. *J. Org. Chem.* **60,** 2891–2901 (1995).

163. Xu, B., Fichou, D., Horowitz, G. & Garnier, F. Preparation of charge-transfer complexes based on thiophene and paraphenylene oligomers as electron donors. *Synth. Met.* **42,** 2319–2322 (1991).

164. Abu-Eittah, R. & Al-Sugeir, F. Charge-transfer interaction of bithienyls and some thiophene derivatives with electron acceptors. *Can. J. Chem.* **54,** 3705–3712 (1976).

165. Aziz, E. F. *et al.* Localized Charge Transfer in a Molecularly Doped Conducting Polymer. *Adv. Mater.* **19,** 3257–3260 (2007).

166. Armarego, W. L. F. & Chai, C. L. *Purification of Laboratory Chemicals*. (Butterworth-Heinemann, 2003).

167. Davis, A., Tran, T. & Young, D. R. Solution chemistry of iodide leaching of gold. *Hydrometallurgy* **32,** 143–159 (1993).

168. Umeno, A. & Hirakawa, K. Fabrication of atomic-scale gold junctions by electrochemical plating using a common medical liquid. *Appl. Phys. Lett.* **86,** 143103 (2005).

169. Drzaic, P. S., Marks, J. & Brauman, J. *Gas Phase Ion Chemistry, vol. 3*. (Academic Press, 1984).

170. Chen, E. C. M. & Wentworth, W. E. A comparison of experimental determinations of electron affinities of pi charge transfer complex acceptors. *J. Chem. Phys.* **63,** 3183 (1975).

171. Zakrzewski, V. G., Dolgounitcheva, O. & Ortiz, J. V. Electron binding energies of TCNQ and TCNE. *J. Chem. Phys.* **105,** 5872 (1996).

172. Mock, R. S. & Grimsrud, E. P. Gas-phase electron photodetachment spectroscopy of the molecular anions of nitroaromatic hydrocarbons at atmospheric pressure. *J. Am. Chem. Soc.* **111,** 2861–2870 (1989).

173. Rocha, A. *et al.* Spin and molecular electronics in atomically generated orbital landscapes. *Phys. Rev. B* **73,** 085414 (2006).

174. Williams, D. B. G. & Lawton, M. Drying of organic solvents: quantitative evaluation of the efficiency of several desiccants. *J. Org. Chem.* **75,** 8351–4 (2010).

175. Vogel, A. I., Tatchell, A. R., Furnis, B. S., Hannaford, A. J. & Smith, P. W. *Textbook of Practical Organic Chemistry*. (John Wiley and Sons, 1989).

176. Carpita, A., Rossi, R. & Ceracini, C. A. Synthesis and 13C NMR Characterization of some pi-excessive Heteroaromatic Compounds. *Tetrahedron* **41,** 1919–1929 (1985).

177. Smeets, B. J. J., Meijer, R. H., Meuldijk, J., Vekemans, A. J. M. & Hulshof, L. A. Process Design and Scale-Up of the Synthesis of 2,2′:5′,2″-Terthienyl. *Org. Process Res. Dev.* **7,** 10–16 (2003).

178. Lukeš, V. *et al.* Structure, electronic and optical characterization of oligothiophenes terminated with (9H-fluoren-9-ylidene)methyl chromophores. *Synth. Met.* **157,** 770–778 (2007).

179. Bader, M. M., Pham, P.-T. T. & Elandaloussi, E. H. Dicyanovinyl-Substituted Oligothiophenes. *Cryst. Growth Des.* **10,** 5027–5030 (2010).

180. Lin, J. *et al.* Efficient synthesis of RITA and its analogues: derivation of analogues with improved antiproliferative activity via modulation of p53/miR-34a pathway. *Org. Biomol. Chem.* **10,** 9734–46 (2012).

181. Komiya, S. *et al. Synthesis of organometallic Compounds.* (John Wiley and Sons, 1997).

182. Bauerle, P., Wuerthner, F., Goetz, G. & Effenberger, F. Selective synthesis of α-substituted oligothiophenes. *Synthesis (Stuttg).* 1099–1103 (1993). at <http://www.thieme-connect.com/ejournals/abstract/synthesis/doi/10.1055/s-1993-26009>

183. Bauerle, P., Wuerthner, F. & Heid, S. Einfache Synthese von 3-(omega-Halogenalky)thio- phenen als Grundbausteinen fir funktionalisierte Thiophene und Polythiophene. *Angew. Chemie* **102,** 414–415 (1990).

184. Tran, T. K. *et al.* Structural control of the horizontal double fixation of oligothiophenes on gold. *Chemistry* **14,** 6237–46 (2008).

185. Haiss, W. *et al.* Wiring nanoparticles with redox molecules. *Faraday Discuss.* **125,** 179 (2004).

186. Tang, J., Zhang, X., Zhu, H. & Luo, S. Synthesis of bis[ω-(acetylthio)alkyl]bipyridinium dibromide and bis[ω-(mercapto)alkyl]bipyridinium dibromide derivatives. *Guizhou Shifan Daxue Xuebao* **24,** 98–102 (2006).

187. Seidler, A. *et al.* The synthesis of π-electron molecular rods with a thiophene or thieno[3,2-b]thiophene core unit and sulfur alligator clips. *Tetrahedron Lett.* **54,** 2795–2798 (2013).

188. Neenan, T. X. & Whitesides, G. M. Synthesis of high carbon materials from acetylenic precursors. Preparation of aromatic monomers bearing multiple ethynyl groups. *J. Org. Chem.* **53,** 2489–2496 (1988).

189. Soria-Castro, S. M. & Peñéñory, A. B. Efficient Cu-catalyzed base-free C-S coupling under conventional and microwave heating. A simple access to S-heterocycles and sulfides. *Beilstein J. Org. Chem.* **9,** 467–75 (2013).

190. Horcas, I. *et al.* WSXM: a software for scanning probe microscopy and a tool for nanotechnology. *Rev. Sci. Instrum.* **78,** 013705 (2007).

191. Hong, W. *et al.* An MCBJ case study: The influence of π-conjugation on the single-molecule conductance at a solid/liquid interface. *Beilstein J. Nanotechnol.* **2,** 699–713 (2011).

192. Sabater, C., Untiedt, C., Palacios, J. J. & Caturla, M. J. Mechanical Annealing of Metallic Electrodes at the Atomic Scale. *Phys. Rev. Lett.* **108,** 205502 (2012).

193. Yoon, H. J. *et al.* Rectification in Tunneling Junctions: 2,2'-Bipyridyl-terminated n-Alkanethiolates. *J. Am. Chem. Soc.* (2014). doi:10.1021/ja509110a

Acknowledgements

I would first and foremost like to offer my appreciation and special thanks to my supervisor Professor Simon J. Higgins for his advice, patience and support throughout my PhD. His enthusiasm and motivation were always pushing me forward and this definitely made me a better chemist. I would also like to thank my secondary supervisor Professor Richard J. Nichols and Professor Emeritus Don Bethell for useful discussion and advice, and for their constant help during the last few years. Much appreciation goes to the rest of the research group, both past and present, with special mentions going to Dr. Phil Donovan and Dr. Carly Brooke for helping me at the beginning of my PhD, and to David Costa Milan and Robert Smith for being amazing labmates and great friends.

This thesis has been written in its present form thanks to the help of our collaborators, Professor Colin J. Lambert, Dr. Iain Grace and Sara Sangtarash of Lancaster University and Dr Martin Elliott and Dr. Ellis Pires of Cardiff University. To them I must express my gratitude for their hard work.

The life of a PhD student is not only between the laboratory walls, and during these years I met a number of people that made me feel welcome in Liverpool, slowly making this city really feel like home. Special thanks go to Stirling, Sam, Ulysses and Nathan for their friendship, and for generally being fantastic human beings.

I would like to thank my family, and in particular my mother and my father for their constant love and support throughout my education; I hope I can be half the fantastic person you are.

Final thanks go to the most important person in my life. Alessandra, I couldn't have done this without you, your love, your help, your support, your kindness and your patience.

Afterword

To conclude, I would like to quote Titus Lucretius Carus, with a couple of excerpts from his didactic poem *De Rerum Natura* (English translation by William Ellery Leonard).

Humana ante oculos foede cum vita iaceret
in terris oppressa gravi sub religione,
quae caput a caeli regionibus ostendebat
horribili super aspectu mortalibus instans,
primum Graius homo mortalis tollere contra
est oculos ausus primusque obsistere contra;
quem neque fama deum nec fulmina nec minitanti
murmure compressit caelum, sed eo magis acre
inritat animi virtutem, effringere ut arta
naturae primus portarum claustra cupiret.

Whilst human kind throughout the lands lay miserably crushed
before all eyes beneath Religion – who
would show her head along the region skies,
glowering on mortals with her hideous face –
a Greek it was who first opposing dared
raise mortal eyes that terror to withstand,
whom nor the fame of Gods nor lightning's stroke
nor threatening thunder of the ominous sky
abashed; but rather chafed to angry zest
his dauntless heart to be the first to rend
the crossbars at the gates of Nature old.

In Lucretius' poem, the Greek man who first opposed the superstitious beliefs, prejudices and fears that were crushing mankind is Epicurus. As a philosopher who firmly believed in

empiricism, materialistic atomism and egalitarianism, he is generally considered one of the fathers of the scientific method. Epicureans had a preoccupation with science that was not disinterested, their aim was not knowledge for its own sake. As stated by Lucretius, Epicurus wanted to use science for the higher ends, to liberate men from what stands in the way of their happiness. He believed that only the study and understanding of the physical world, of nature and nature's laws can bring peace of mind. In his philosophy, unravelling the complexity of nature leads to better ethics and fuller humanity.

Hunc igitur terrorem animi tenebrasque necessest
non radii solis neque lucida tela diei
discutiant, sed naturae species ratioque.

This terror, then, this darkness of the mind,
Not sunrise with its flaring spokes of light,
Nor glittering arrows of morning can disperse,
But only Nature aspect and her law.

Science makes mankind free.

Andrea Vezzoli

Liverpool, 27/05/2015